Molecular scale dynamics of T cell immunological synapse components by advanced and super-resolution fluorescence microscopy

Ashdown, George

Awarding institution:
King's College London

Molecular scale dynamics of T cell immunological synapse components by advanced and super-resolution fluorescence microscopy

A thesis presented for the degree of

Doctor of Philosophy

by

George W. Ashdown

KING'S College LONDON

Department of Physics

and

Randall Division of Cell and Molecular Biophysics

2017

Abstract

Cortical actin forms a central role in the reorganisation and heterogeneity of plasma membrane (PM) components of T cells. During T cell activation, actin remodelling aids formation of the stable interface between cells known as the immunological synapse; this interface is a dynamic event where actin plays a key role in forming and translocating protein microclusters for sustained signalling. Cortical actin creates a dense meshwork at the synapse periphery, possibly acting as a barrier against molecular trafficking to the synapse interface. Additionally, actin flows in a retrograde manner towards the relatively actin-poor synapse centre, driving transmembrane proteins inwards.

Here, fixed cell single molecule localisation microscopy was used to characterise the actin cortex upon T cell synapse formation. Live-cell structured illumination microscopy (SIM) was quantified using spatiotemporal image correlation spectroscopy (STICS), this demonstrated flow speed and directionality was dependent on balanced actin turnover and membrane order. Building on these results, two-channel SIM imaging was carried out, correlating actin flow with plasma membrane (PM) dynamics, as these systems are known to interact via transmembrane and linker proteins. The PM was shown to correlate with actin flow speeds and direction in an α-actinin dependent manner.

Sustained signalling during synapse formation requires protein delivery to the interface, relying on vesicle trafficking via different components of the cytoskeleton. As membrane order modulates protein clustering within the PM, it was investigated using the polarity-sensitive dye di-4-ANEPPDHQ whether this was also true of vesicles. Results here demonstrated vesicle lipid order negatively correlated with microtubule structures.

Finally, vesicle cargo was shown to correlate with different vesicle populations, based on their membrane order, demonstrating vesicle order may mirror the heterogeneous nature of the PM. These results demonstrate the complex biophysical processes that control the T cell immunological synapse are an amalgamation of cytoskeletal organisation, vesicle dynamics and membrane polarity.

Acknowledgements

Many have contributed to the completion of this thesis in their own way and without whom it would not have been possible. People talk about the PhD rollercoaster, the dreaded second year blues and depression during write-up, while it hasn't been plain sailing it is fair to say a lot of the drama has been successfully navigated thanks to the constant expert support, guidance and sometimes even encouragement from my supervisor, Dr. Dylan Owen. Dylan; thanks for giving me this chance, even if you didn't give me a chance in Janelia, playing pool.

Being the first member of the Owen group has been fantastic, seeing Dylan's team grow. As only the second full-time member to be leaving, I've been with most of you from the start; it's hard to describe how much I've enjoyed working with you all. So thanks are due to Juliette and Ruby for their personal support and coding wizardry. Mike, 'French' David and 'German' David; thanks for your discussions, either mid-pipetting or write-up, these were -mostly- a useful distraction. Finally to Dave, you literally smashed it out the park after joining, from initiating CRISPR to keeping me going during the write-up phase with much-needed coffee runs – just thanks. Special thanks also to Garth for showing me the T cell ropes, your patience at the start and support during our Janelia trip was invaluable.

I would also like to thank Prof. Maddy Parsons for being a great second supervisor, who, no matter how random the emails were, went answered. I also acknowledge the support and help from Prof. Andy Cope and his group; from giving me access to your lab early on in this journey, through to discussion, your expertise in Immunology and publication. Thanks to Prof. Paul Wiseman and Dr. Elvis Pandžić for their support when initiating the image correlation project.

Thanks in part to our Cope group collaborations; I met Christine. Without you none of this would have been possible, the calm exterior I've been donning over the past year is mostly down to your unwavering support. I look forward to returning the favour, with some trepidation, during your own PhD journey.

The love and support from my brother and sister, Arthur and Florence, has been much needed at times; you've been a valuable pair over the last 3 years and you'll be glad to hear I'm in London for the next 3, so there's still somewhere free for you to stay in London! Finally, special gratitude and appreciation goes to my Mum and Dad, for being awesome parents, pillars of support and for reminding me every now and again of something I once said… 'I'm not an academic'. Well folks, maybe for once in my life, I was wrong.

Acknowledgements of work

All work presented in this thesis is my own with the following exceptions:

- Fibre analysis code used for quantification of single molecule localisation data was written by Ruby Peters (PhD student, King's College London).
- Image correlation spectroscopy code was extended to perform vector directionality by Dr. Elvis Pandžić (University of New South Wales) and Michael Holden (MSc student, King's College London).
- CRISPR cell work was carried out by Dr. David Williamson (King's College London).
- Vesicle imaging and tracking using Jurkat T cells within Chapter 4 was carried out by Gary HM Soh (MRes student, King's College London).
- Analysis and some imaging of the three channel vesicle-cytoskeleton and vesicle-cargo interactions were performed by Nathan Day (MSci student, King's College London).

Table of Contents

List of Figures

Acronyms & Abbreviations

- 7KC 7-ketocholesterol
- APC Antigen presenting cell
- Arp2/3 Actin related protein subunits 2/3
- CD Cluster of differentiation
- Cdc42 Cell division control protein 42 homolog
- CF Correlation function
- CRISPR Clustered regularly interspaced short palindromic repeats
- cSMAC Central supramolecular activation cluster
- CTB Cholera toxin-B
- Cyto-D Cytochalasin-D
- Di dye Dialkylcarboncyanine
- Di-4-ANE 2-di-butylaminonaphthylethylpyridinium propyl-2-hydroxy-3-dimethyl-hydroxyethyl quaternary
- DOS Trans-4-Dimethylamino-4-(1-oxybutyl)stilbene
- DRM Detergent resistant microdomains
- dSMAC Distal supramolecular activation cluster
- dSTORM Direct Stochastic optical reconstruction microscopy
- EBP-50 Ezrin binding protein of 50 kDa
- EGTA Ethylene glycol tetraacetic acid
- EMCCD Electron multiplying charged coupled device
- ERM proteins Ezrin radixin moesin proteins
- ES Environmentally sensitive
- F-actin Filamentous actin
- FBS Fetal bovine serum
- FCS Fluorescence correlation spectroscopy
- FERM 4.1 protein Ezrin, Radixin, Moesin
- FRAP Fluorescence recovery after photobleaching
- G-actin Globular actin
- GADS GRB2-related adaptor downstream of Shc
- GAPDH Glyceraldehyde-3-phosphate dehydrogenase
- GFP Green fluorescent protein
- GLOX Glucose oxidase
- GM_1 Monosialotetrahexosylganglioside
- GP Generalised polarisation
- GPCR's G-protein coupled receptors
- GPI Glycosylphosphatidylinositol
- GRB2 Growth factor receptor-bound protein 2
- HBSS Hank's balanced salt solution
- HEPES 4-(2-hydroxyethyl)-1-piperazineethanesulfonic acid
- HIV-1 Human immunodeficiency virus-1
- ICAM-1 Intercellular Adhesion Molecule 1
- ICS Image correlation spectroscopy
- IL-2 Interleukin-2
- IMDM Iscove's Modified Dulbecco's Media
- IRIS Image reconstruction by integrating exchangeable single-molecule localization
- IRM Interference reflection microscopy
- ITAM Immunoreceptor tyrosine-based activation motif

- ITIM Immunoreceptor tyrosine-based inhibition motif
- kDa KiloDaltons
- LAT Linker for activation of T cells
- Laurdan 6-dodecanoyl-2-dimethylaminonaphthalene
- Lck Leukocyte specific protein tyrosine kinase
- LFA-1 Lymphocyte function-associated antigen 1
- MAL Myelin and lymphocyte protein
- MEA Cysteamine-Hydrochloride
- MES 2-(N-morpholino)ethanesulfonic acid
- MHC-II Major histocompatibility complex class II
- MTF Modulation transfer function
- MTOC Microtubule-organising centre
- MTT 3-(4,5-dimethylthiazol-2-yl)-2,5-diphenyltetrazolium bromide
- MβCD Methyl-beta-cyclodextrin
- NBD 4-Chloro-7-Nitrobenzo-2-Oxa-1,3-Diazole
- NK Natural killer cell
- NPF Nucleation-promoting factor
- OTF Optical transfer function
- PA Photoactivatible
- PALM Photoactivated localisation microscopy
- PBS Phosphate buffered solution
- PC Phosphatidylcholine
- PE Phosphatidylethanolamine
- PenStrep Penicillin Streptomycin
- PFA Paraformaldehyde
- PFS Perfect Focus System
- PI Phosphatidylinositol
- PIP2 Phosphatidylinositol 4,5-bisphosphate
- PIV Particle image velocimetry
- PKC-Θ Protein kinase C, theta
- PLCγ-1 Phospholipase C, gamma-1
- Prodan 6-Propionyl-2-Dimethylaminonaphthalene
- PS Phosphatidylserine
- PSF Point spread function
- pSMAC periphery supramolecular activation cluster
- PTEN Phosphatase and tensin homolog gene
- Rac2 Ras-related C3 botulinum toxin substrate 2
- ROI Region of interest
- RPMI Roswell Park Memorial Institute
- RT Room temperature
- SAF Super-critical angle fluorescence
- sCMOS Scientific complementary metal-oxide-semiconductor
- SHIP2 SH2-containing inositol phosphatase 2
- SIM Structured illumination microscopy
- SLP-76 SH2 domain-containing leukocyte phosphoprotein of 76kDa
- SM Sphingomyelin
- SMAC Supramolecular activation centre
- SNARE Soluble NSF attachment protein receptors
- STED Stimulated emission depletion
- STICS Spatiotemporal image correlation spectroscopy
- Syk Spleen tyrosine kinase

- T cell Thymus derived cell
- TCR T cell receptor
- TIRF Total internal reflection fluorescence
- TOI Time of interest
- WASp Wiskott-Aldrich syndrome protein
- WIP WASp interacting protein
- ZAP-70 Zeta-associated protein of 70 kDa
- α-actinin Alpha-actinin
- β-integrin Beta-integrin

Chapter 1 – Introduction

1.1. The immune system

Following an invasion of foreign substances such as a virus, bacteria or fungi, as well as malfunctioning cells of the host itself, subsets of cells and molecules within an organism can respond to contain or eliminate these via an immune response. This response is loosely split into two categories, innate and adaptive. Innate immunity is that which does not change over an organism's life whereas adaptive immunity evolves over the organism's lifespan in response to the presence of specific pathogens. The innate immune system begins with physical epithelial barriers such as the skin which blocks entry of pathogens, and extends to phagocytic cells (e.g. macrophages, neutrophils and others) and natural killer (NK) cells. NK cells can respond to infected host cells directly, making them a key mediator of innate defence against infected and cancerous cells.

Dendritic cells and macrophages are professional antigen presenting cells (APC's), which phagocytose pathogens and digest them via enzymatic activity to produce peptides for attachment onto specialised transmembrane proteins called the major histocompatibility complex Class II (MHC Class II). Peptide coated APC's are considered 'mature' and migrate through lymph vessels to lymph nodes for presentation to thymus-derived lymphocytes (T cells) which form part of the adaptive immune system. This presentation allows crosstalk between the innate and adaptive immune system (Reschner et al. 2008), and is vital for triggering T cells, allowing them to mount a response against foreign pathogens.

The adaptive immune system is considered to have two main branches, firstly humoral immunity, driven by B cells which (as well as being APC's) secrete antibodies for binding to toxins and pathogens, promoting their recognition and internalisation by phagocytic cells of the immune system such as neutrophils or macrophages. Antibodies can be membrane bound or secreted, with different populations, known as isotypes, expressed or released by B cells after exposure to antigens via their surface receptors (Aureli et al. 2016). They bind with a high degree of affinity and specificity to their molecular targets, based on their variable structure of 2 light and 2 heavy chain N terminal regions (Figure 1.1). Their constant C terminal regions allow them to interact with other cells of the immune system. As will be discussed later, the ability of antibodies to specifically bind to proteins makes them useful for labelling in fluorescence microscopy applications (i.e. immunostaining).

Secondly, cell-mediated immunity is orchestrated and implemented by different T cell subsets (discussed below). Due to T cells' requirement for APC's to migrate to lymphoid tissue for their

antigen presentation (Burnet 1976) and the required increase in number of a T cell population against a specific antigen (clonal expansion), the adaptive immune system takes longer (>12hrs) to activate than the innate system but it offers the advantages of specificity to individual pathogens and diversity to the range of infectious materials it can target, as well as the ability to confer long term immunity.

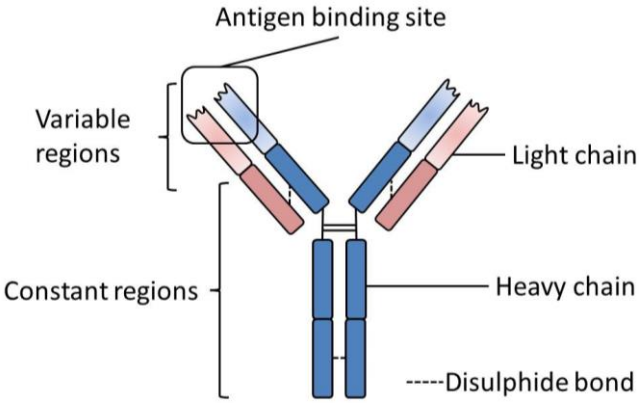

Figure 1.1 Basic structure of an antibody. Constant regions on the C terminus allow the antibody to interact with the cells of the immune system, while the variable regions on the N terminal heavy and light chain regions allow the antibody to vary its antigen binding domains.

After an infection has been eradicated, some stimulated T cells differentiate into memory T cells, which (via cytokine maintenance) remain in the system post-infection, displaying surface receptors against the original pathogen. This immunological 'memory' means pathogen reinfection can be abolished more efficiently (1-3 days) than the primary infection (5-7 days) as these memory cells can respond directly via clonal expansion; thus the immune system keeps pace with rapidly multiplying pathogens by increasing its own T cell cohort previously generated for that specific infection.

1.2. T cell activation and signalling

T cells originate from haematopoietic progenitor (stem) cells (Figure 1.2) that mature in the thymus, leading to different subsets classifiable by their membrane-bound cluster of differentiation (CD) molecules which divide their roles further; these include $CD4^+$ helper and $CD8^+$ cytotoxic T cell cohorts.

T cell triggering via APC contact can lead to a full adaptive immune response, improper triggering is indicative of autoimmune diseases including Crohn's disease, multiple sclerosis, and rheumatoid arthritis while a lack of T cells results in immunodeficient diseases such as severe combined immunodeficiency (Zeissig et al. 2015; Schofield et al. 2016; van der Burg & Gennery 2011). Characterising how T cells respond correctly while the events that lead to and from this decision are key to understanding what may cause the system to malfunction.

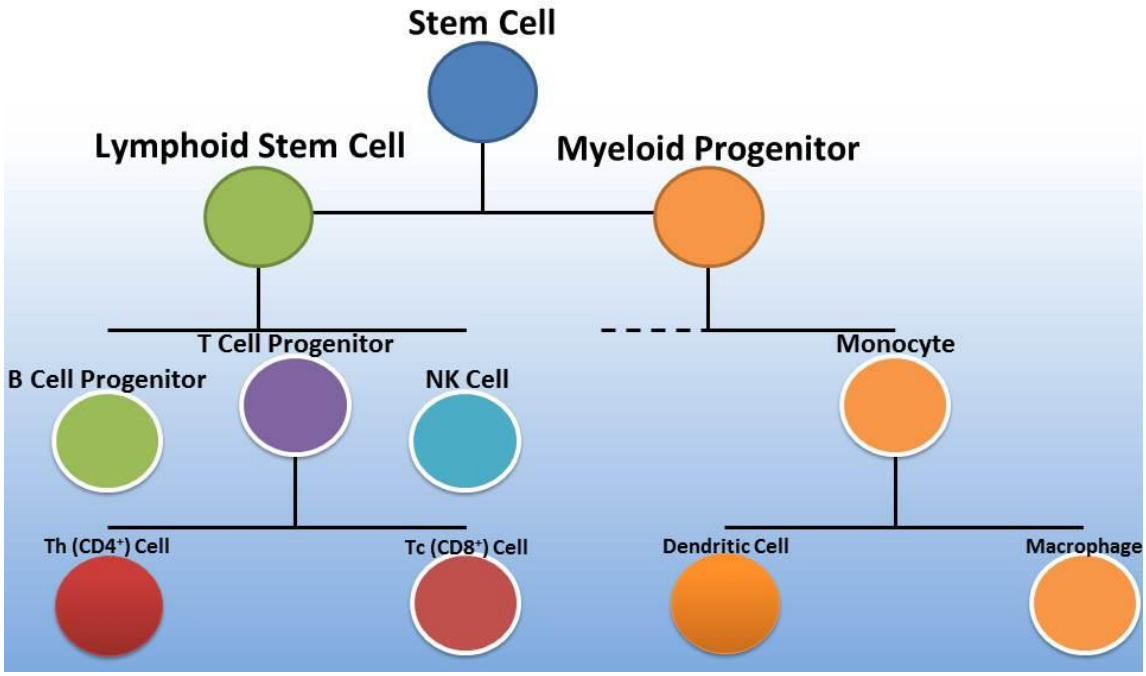

Figure 1.2 Simplified immune cell maturation tree. T cells are derived from stem cells, with $CD4^+$ helper and $CD8^+$ T cells both maturing from T cell progenitors. These cells are differentiated by molecules on their surface leading to specific functions.

T cell cohorts are characterised and triggered via their membrane bound T cell receptor (TCR), this heterodimeric structure recognises peptides bound to self-MHC molecules on the surface of APC's. The common structure is outlined in Figure 1.3**,** based on two transmembrane polypeptide chains named alpha (α) and beta (β) which are bound by a disulphide linker, each extracellular N terminus contains the variable binding region and constant domain. The variable region, derived from genetic recombination, gives TCR's the ability to recognise and bind different peptides.

When a pMHC binds to the TCR of a $CD4^+$ T cell it initiates an intracellular signalling cascade leading to secretion of the cytokine interleukin (IL)-2, which activates other cells of the immune system. As the TCR itself has no phosphorylation sites (or immunoreceptor tyrosine-based activation motif's; ITAM's) signal internalisation relies on the formation of the 'TCR complex' that includes two 100 amino acid long zeta- (ζ-) chains each with three ITAMs and four homologous CD3 proteins; two epsilon (ε), one gamma (γ) and one delta (δ), each with one ITAM and varying lengths between 44 and 81 amino acids (Abbas et al. 2012). These ITAM's are made up of a 4 amino acid sequences in the cytoplasmic tail of these proteins, these sites are believed to be unavailable for phosphorylation due to folding of the intracellular tails towards the plasma membrane prior to TCR recognition of antigens (Love &

Hayes 2010), once phosphorylated, the tyrosine residues within ITAM's form a docking site for other signalling proteins (see next section).

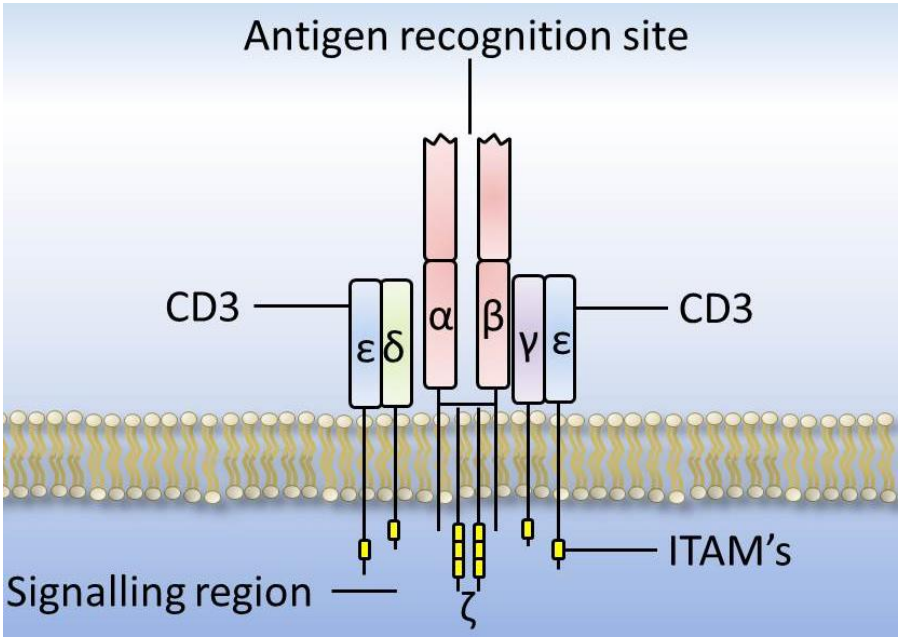

Figure 1.3 T cell receptor complex. The T cell receptor binds to the major histocompatibility complex via its variable antigen recognition region; this initiates phosphorylation of immunoreceptor tyrosine-based activation motif's (ITAM's) on the CD3 molecules, allowing signal internalisation to occur.

The signalling cascade which follows the binding of a TCR to a pMHC (Figure 1.4) begins with the phosphorylation of ITAM tyrosine residues via Src family kinases; including lymphocyte-specific protein tyrosine kinase (Lck). Upon ITAM phosphorylation by Lck, Syk family kinases such as ζ chain-associated 70 kDa tyrosine phosphoprotein (ZAP-70) dock onto these sites through Src homology (SH) 2 domain-phosphotyrosine interactions. ZAP-70 can then phosphorylate adaptor proteins such as the transmembrane Linker for activation of T cells (LAT), or cytosolic SH2-domain containing linker protein of 76 kDa (SLP-76) that act as molecular hubs, physically linking enzymes and forming signalling molecule complexes or 'signalosomes'. These scaffolding proteins can contain SH2 and SH3 domains for protein-protein interactions as well as tyrosine residue sites, targets of phosphorylation.

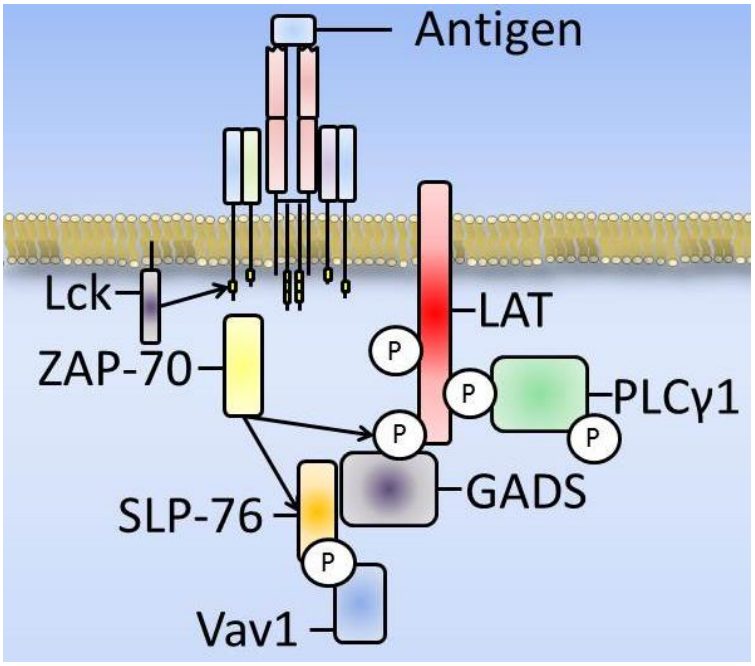

Figure 1.4 T cell signalling cascade after TCR engagement. After TCR complex formation following antigen binding, Lck mediated phosphorylation of ITAM residues creates docking sites for ZAP-70 and leads to phosphorylation of the scaffolding proteins LAT and SLP-76 allowing further protein-protein interactions.

Phosphorylated LAT 'signalosomes' include growth factor receptor-bound protein 2 (GRB2) and GRB2-related adaptor downstream of Shc (GADS). These bind Vav which activates actin reorganisation pathways and the enzyme phospholipase C, gamma 1 (PLCγ1) which leads to release of cellular calcium (Ca^{2+}) stores, important for gene transcription and eventually T cell activation. Further tuning of the signalling cascade is achieved through the costimulation by coreceptors such as CD4 on helper cells, and CD28 on all T cells. CD4 coreceptors are transmembrane proteins which link to the engaged antigen complex and, via their cytoplasmic domains, bring with them additional stimulatory molecules such as Lck. CD28, which binds to CD80 and CD86 molecules on APCs is key for T cell signalling as without it this signalling is anergic. CD28 is discussed in more detail later.

To stabilise cell-cell contacts, integrins (adhesion molecules) expressed on T cells (e.g. lymphocyte function associated antigen 1 [LFA-1]) and their ligands on APC's (e.g. Intercellular Adhesion Molecule 1 [ICAM-1]) bind to one another, and can themselves initiate signalling; increasing interaction longevity.

To balance this activation pathway there are other receptors which downregulate T cell activation, known as immunoreceptor tyrosine-based inhibitory motif's (ITIM's). Other negative regulators of T cell stimulation include CD43 and CD45, the former has been shown to reduce IL-2 production, and both are speculated to drive steric hindrance due to their large extracellular domains (Stockton et al. 1998; Chang et al. 2016), though this has been

challenged, with regulation thought to actually be driven by an intracellular mechanism (Tong et al. 2004). The following section will explore the molecular reorganisation required to balance T cell stimulation.

Much of our understanding of T cells comes from the use of the Jurkat cell lines (Schneider et al. 1977; Abraham & Weiss 2004); derived from a 14 year old male with acute T cell leukaemia, these cancer-cells express TCR, CD3 and secrete IL-2. The use of Jurkat T cells allows researchers to study the fundamental biophysics and TCR signalling during T cell stimulation and synapse formation.

Compared to primary T cells, Jurkat T cells do not possess the lipid phosphatases SH2-domain-containing inositol polyphosphate 5' phosphatase (SHIP2) and tensin homologue (PTEN) (Astoul et al. 2001; Shan et al. 2000; Wang et al. 2000), though the implications of these deficiencies are still poorly understood in the context of TCR signalling.

1.3. The immunological synapse

One of the most striking events to occur when a T cell is triggered through its TCR complex is the molecular and morphological repolarisation that leads to the formation of an immunological synapse. These rearrangements ensure a prolonged cell - cell junction between the T cell and APC which is speculated to have a variety of roles including signal sustainability, signal cessation, signal pathway integration, and polarised vesicle trafficking (Hashimoto-Tane et al. 2011; Valitutti et al. 1995; Lee et al. 2003; Varma et al. 2006; Campi et al. 2005; Ritter et al. 2015).

T cell activation follows a series of well characterised events over the course of 30 minutes, including the clustering of TCR complexes, reorganisation of cytoskeletal components, polarisation of the microtubule-organising centre (MTOC) and vesicle delivery towards the synapse interface (Monks et al. 1998; Sims et al. 2007; Ritter et al. 2015). To optimise the signalling of T cells, and balance the downstream cascade to ensure proper activation, certain molecules are segregated on, or perpendicular to, the plasma membrane into defined regions, known as supramolecular activation clusters (SMACs, (Monks et al. 1998)). Classically these regions are radially distinct, emanating from the cell centre as seen with activated $CD4^+$ and $CD8^+$ cells against B cells (Figure 1.5), though this spatial patterning is now thought to depend on the stimulus the T cell encounters (Thauland & Parker 2010). For example, multifocal TCR-pMHC clusters can be seen when activated T cells form synapses against dendritic cells, or double positive ($CD4^+$ and 8^+) cells against bilayers.

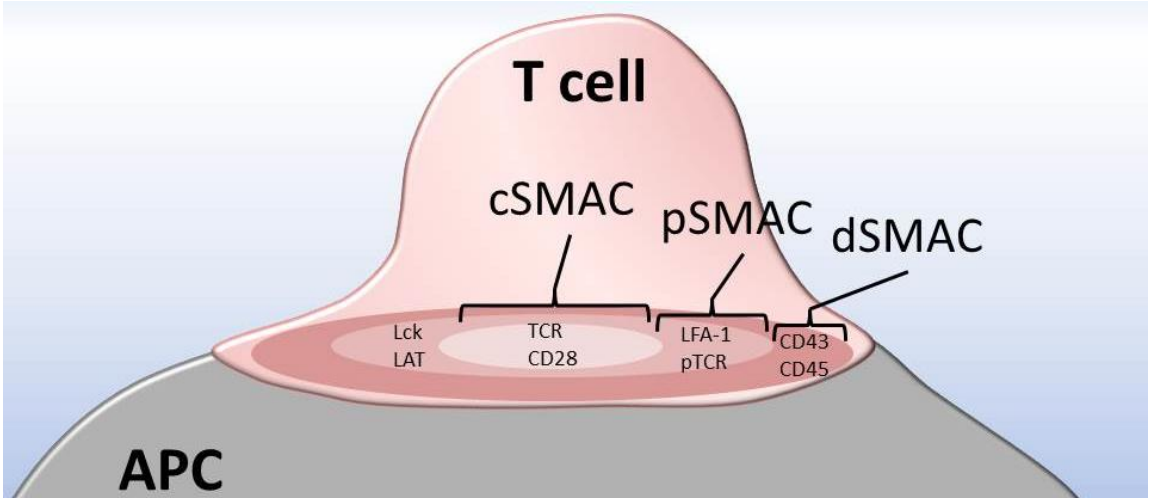

Figure 1.5 Molecular organisation of supramolecular activation clusters at the T cell synapse. Upon TCR engagement, the synapse forms distinct structural subregions which can be characterised by the segregation of molecules which reside there. Negative signalling factors such as cluster of differentiation CD43 and 45 are located at the synapse edge (dSMAC), phosphorylated signalling complexes such as the TCR complex and scaffolding molecules including LAT are situated in the peripheral zone (pSMAC), while the centre of the synapse (cSMAC) contains dephosphorylated clusters of TCR along with molecules dissociated from these TCR complexes including the costimulatory molecule CD28.

In the classical view of the synapse the cell edge or distal-SMAC (dSMAC) area contains a rich ring of filamentous- (F-) actin (a molecule discussed in the next section), along with membrane residing CD43 and CD45 (Leupin et al. 2000); the negative regulators of TCR signalling. Inside the dSMAC the peripheral-SMAC (pSMAC) region contains the integrin LFA-1 (Monks et al. 1998) which is important for the stability of the cell-cell contact. Upon ICAM-1 binding, LFA-1 recruits the actin-binding protein talin which (in NK cells (Mace et al. 2010)) recruits actin polymerising proteins, in both NK and T cells this is important for the stability of the synapse (Wernimont et al. 2011).

The central-SMAC (cSMAC) region is rich in molecules from and associated with the TCR complex including CD3, Lck (Monks et al. 1998) and the TCR costimulatory protein CD28, though these molecules no longer colocalise with TCR clusters (Yokosuka et al. 2008). The SMAC regions are also characterised by the relatively low distribution of cortical actin.

The low levels of cortical actin within the cSMAC permit the polarisation of the MTOC and associated vesicles, to the synapse centre (Ritter et al., 2015). The MTOC provides additional structural support to the cell, increases the sustainability of T cell signalling. Disrupting the motor protein mediated translocation of the MTOC was shown to reduce ZAP-70, LAT and Vav1 phosphorylation as well as their intracellular recycling (Martín-Cófreces et al. 2008). The MTOC also forms a filamentous highway for vesicle trafficking, mediated via dynein and kinesin

motor proteins (Sheetz & Martenson 1991). Vesicles are formed from cell membranes; in T cells they can contain signalling molecules including Lck, LAT, and components of the TCR (Soares et al. 2013). These molecules can be recycled via vesicles from the plasma membrane or released from intracellular pools to be trafficked to the plasma membrane (Das et al. 2004) making vesicle trafficking an important process in downregulating and recycling of synapse signalling.

Using kymograph analysis of T cells on lipid bilayers (Kaizuka et al. 2007) and (Yi et al. 2012) showed TCR clusters flowed inwards from the dSMAC with speeds between 8.4 ± 0.36 and 5.64 ± 0.96 µm / min, and slowed as they entered the pSMAC to 2.28 ± 0.36 µm / min. (Purbhoo et al. 2010) took microcluster dynamics further by observing the speeds of SLP-76 (2.2 µm / min), GADS (2.6 µm / min) and LAT (5.3 µm / min), showing that interactions between stationary ZAP-70 and vesicles containing LAT resulted in them slowing and being phosphorylated at these potential sites of signalosome formation.

Finally the cSMAC which was originally thought to be an active signalling site due to the accumulation of TCR, ZAP-70 and Lck is now known to contain dephosphorylated and downregulated signalling molecules which are endocytosed and possibly recycled back to the synapse periphery for sustained signalling; many of these findings were captured using high speed fluorescence microscopy.

Why a stable immunological synapse -including SMAC regions- form when TCR stimulation, Ca^{2+} flux and tyrosine phosphorylation all occur within seconds of TCR stimulation (before most molecular clustering has occurred) is still debated and reviewed by (Mitxitorena et al. 2015). Below is a summary of theories on immunological synapse formation, most involving structural reorganisation.

Table 1.1 Summary of theories for the formation of the stable immunological synapse

Role of Immunological Synapse	Function	Process	Reference
Signal modulation and sustainability: prolong signalling	Enhancement of weak / low affinity ligands through increased surface area.	Ligands produce cSMAC to enhance IL-2 production with CD28 co-stimulation. cSMAC depends on stimulation strength and regulates T-cell activation. Sustained signalling and cytokine production	Hasimoto-Tane et al., 2011
	Sustenance of TCR molecules from dSMAC.		Valitutti et
Signal cessation	Stop T cells from forming autoimmune response or over reacting to activator	cSMAC now seen as site of downregulation. TCR internalisation	Lee et al., 2003
Signal pathway integration	Increasing efficiency through colocalisation	Coalescence,TCR-CD3, CD2, CD28 signalling may integrate in ways not permitted by individual microclusters (signalosome)	
Exclusion zone	Increases stability of IS platform	By forcing membranes together at the site of cell-cell contact larger molecules (>15nm) are excluded; including	Leupin et al., 2000
Endocytosis site	Receptor internalisation and recycling	cSMAC is a site of dephosphorylated molecules including TCR, ubiquitin and vesicles	Varma et al., 2006; Campi et
Vesicle Trafficking / granule release	Endocytosis and exocytosis	Vesicles trafficked to the IS contain scaffolding molecules for signal internalisation, while secretion of molecules	Ritter et al., 2015
Seal / gasket	Reduced nonspecific damage to neighbouring cells	Seal formation around the target cell contains secretion to the site of the IS, reducing collateral damage	

As mentioned above T cell signalling occurs within seconds of TCR engagement, however to allow a full immune response, signal modulation and sustainability is required. This is particularly important for enhancing weak or low affinity ligands through serial TCR stimulation from the dSMAC and could be modulated by the increased surface area seen as T cells spread over the APC (Hashimoto-Tane et al. 2011; Valitutti et al. 1995). Cluster formation at the synapse interface increases integration of signalling molecules, potentially increasing signalling efficiency through coalescence of TCR-CD3 complexes, signalosomes and CD28.

Additionally signal cessation is important for reducing the chance of T cells initiating an autoimmune response. The cSMAC is now speculated as a site of downregulation where TCR is internalised (Lee et al. 2003). This site includes large amounts of receptor endocytosis and recycling, leading to increased downregulation by ubiquitin, vesicles (Campi et al. 2005; Varma et al. 2006) and dephosphorylated TCR. This agrees with the recent findings in $CD8^+$ T cells where vesicle trafficking and granule release occur here, encompassing both endocytosis and exocytosis. This vesicle trafficking to the synapse includes scaffolding molecules for signal internalisation, with secretion of molecules leading to activation of other immune cells and programmed cell death of infected cells (Ritter et al. 2015).

Synapse dissociation is the final stage of cell-cell contact and the least studied stage of the immunological synapse cycle, it represents a period of relative inactivity regarding signalling and internalisation of surface receptors including TCR for degradation by ubiquitination (Lee et al. 2003; Wiedemann et al. 2005).

1.4. The actin cytoskeleton

For cells to exert the forces required to maintain structure, change morphology and migrate, cytoskeletal components serve a pivotal role, permitting dynamic and sensitive rearrangement. The two main components of the cytoskeleton, actin and microtubules, both participate in these processes. Actin can form a variety of ATP dependent structures through the polymerisation and depolymerisation from its 2.4 nm x 5 nm monomeric form (known as globular- or G-actin) to its polymeric 7 nm diameter F-actin form, polymerised actin forms helical structures, preferentially in an anticlockwise ‘handedness’ (Tee et al. 2015).

Actin forms fibres through processes of nucleation, elongation and treadmilling (Figure 1.6). G-actin is constantly forming unstable dimer and trimer fragments after binding to ATP, longer fibres require a large amount of these fragments; for this cells rely on nucleation-promoting factors (NPF’s). Nucleation starts when three monomers join; forming a stable platform for fibre growth to occur, addition of actin monomers to this nucleated structure leads to its rapid elongation. This continues until monomeric actin reaches a critical concentration of G-actin:

for the pointed end this is 0.6 µM, while barbed end polymerisation continues until 0.1 µM, leading to steady-state treadmilling (Pollard et al. 2000).

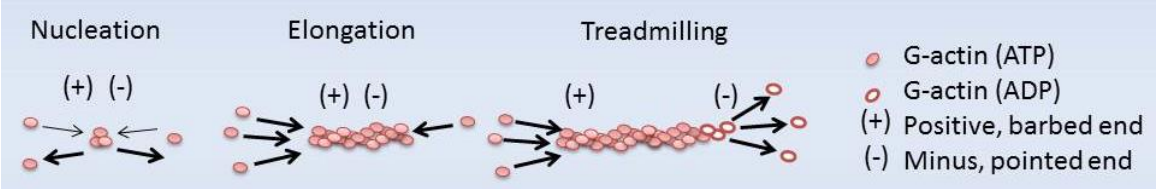

Figure 1.6 Actin nucleation and filament turnover. Spontaneous polymerisation of actin is limited due to unstable actin oligomers which have higher dissociation rates compared with association (depicted by black arrows). 'Nucleation' is aided by nucleation promoting factor proteins such as Arp2/3 and formins which provide nucleation sites and stabilise forming filaments. Once formed, an actin nucleus extends with additional monomers from the barbed (+) end and the pointed (-) end known as the 'elongation' phase. The final phase, 'treadmilling' occurs when a state of equilibrium is reached.

The G-actin pool is maintained by depolymerisation of actin from the pointed end of fibres after their transference to an ADP state, causing a conformational change and reducing its association to other actin monomers. This allows freed phosphorylated G-actin to be made available for polymerisation, this can occur through binding to and shuttling by profilin (Carlsson et al. 1977) and recognition by polymerising proteins, including formin (Wen et al. 2011).

Through polymerisation, actin generates forces between fibres as well as against the plasma membrane (Equation 1), driving cellular scale morphological changes including polarisation, protrusions and spreading (Mattila & Lappalainen 2008; Katsuno et al. 2015; Bunnell et al. 2001) down to molecular level protein clustering and segregation ((Chichili & Rodgers 2007; Pollard & Cooper 2009) (§1.5.4)). Both of these are important aspects of T cell migration, activation and synapse formation.

$$F = \frac{k_B T}{\delta} \ln(\frac{c}{c_{crit}})$$

Equation 1

Where k_B is the Boltzmann constant, T is temperature, δ is the radius of one actin monomer, c the concentration of G-actin and c_{crit} the critical concentration of G-actin.

1.4.1 Modulating actin polymerisation

Wiskott-Aldrich syndrome protein (WASp) is an NPF which is recruited after forming a complex with WASp-interacting protein (WIP) (de la Fuente et al. 2007) upon TCR engagement, the complex is formed through phosphorylation by PKCΘ (Sasahara et al. 2002) (itself activated by ZAP-70, SLP-76 and Vav1 (Herndon et al. 2001) (Figure 1.7). The WASp complex is then

shuttled to lipid ordered membrane domains where it mediates the cell division control protein 42 homolog (Cdc42) activation of the Actin related protein (Arp)2/3 complex (Sasahara et al. 2002).

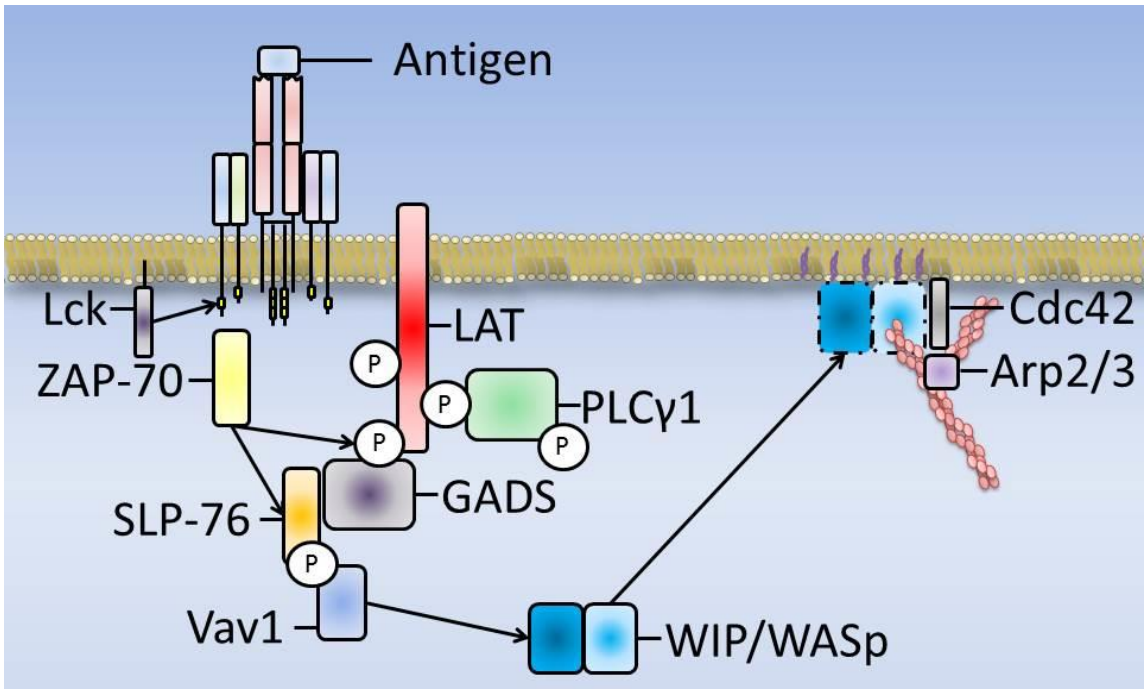

Figure 1.7 Actin polymerisation downstream of TCR engagement. After antigen recognition, the TCR complex leads to downstream signalling cascades resulting in the WASp/WIP complex phosphorylation by Vav1 leading to its association with ordered membrane components, allowing Arp2/3 driven actin polymerisation via Cdc42.

Arp2/3 is an assembly of 7 proteins which binds to a pre-existing or 'mother' filament and, due to subunits 2 and 3 mimicking an actin dimer, creates a nucleation site for a 'daughter' filament which polymerises off the side of the mother at an angle of 70 ° (Blanchoin et al. 2000). This increases polymerisation by increasing the number of free barbed ends. The PKCϴ phosphorylation which leads to the WASp-WIP-Arp2/3 complex formation is important for the total amount of F-actin at the synapse, IL-2 secretion and ultimately T cell activation (Sasahara et al. 2002; Sun et al. 2000).

Profilin binds to G-actin and increases barbed end polymerisation by recycling these monomers back to actin-ATP, it also negatively regulates the plasma membrane lipid phosphatidylinositol-3,4 biphosphate $(PI(3,4)P)_2$, therefore limiting its accumulation at the cell edge.

As with TCR signalling, negative regulators of actin polymerisation are an important set of balancing factors for maintaining a free pool of G-actin (Figure 1.8). Negative regulators of actin polymerisation include coronin-1 and cofilin-1; these molecules control polymerisation and enhance depolymerisation of actin respectively. Coronin-1 through binding to Arp2/3,

disrupting its activation, cofilin-1 through depolymerising fibres; both are preferentially located in the dSMAC of the T cell synapse through unknown mechanisms (Siegmund et al. 2015; Sims et al. 2007). Cofilin increases depolymerisation at the pointed end of filaments by changing the twist of F-actin's helical structure, it can be incorporated into the filament due to the increased flexibility of ADP-actin. These molecules are important regulators of steady-state F-actin formation in T cells, possibly controlling the structurally distinct areas seen during immune cell activation (Foger 2006; Eibert et al. 2004) and are implicated in correctly controlling vesicular release in NK cells during cell killing (Mace & Orange 2014).

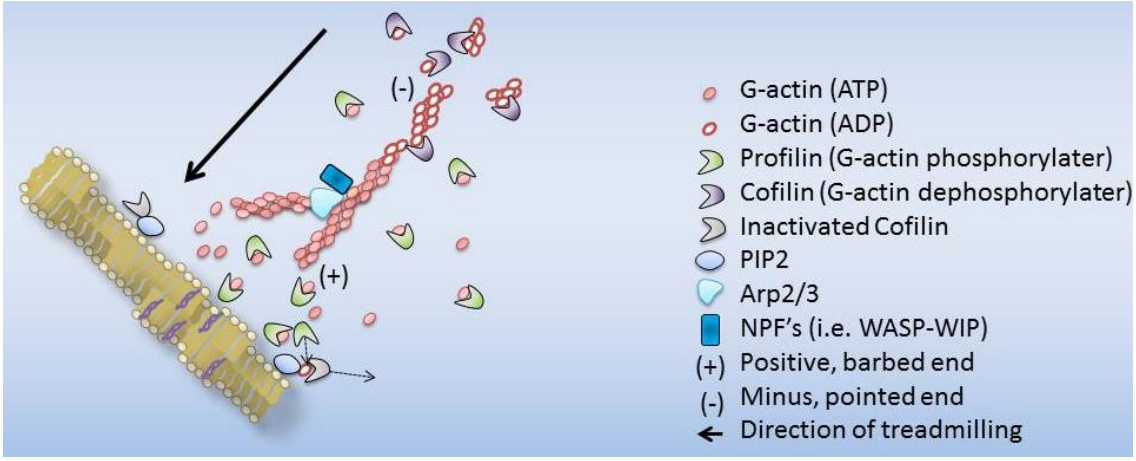

Figure 1.8 Molecules mediating actin polymerisation and depolymerisation. After nucleation and elongation of actin monomers, the resulting fibres enter a stage of turnover controlled in part by molecules that drive polymerisation such as profilin and actin related protein (Arp)2/3 as well as nucleation promoting factors (NPF's). Cofilin balances turnover of actin monomers by cleaving fibres, freeing G-actin to maintain the cytosolic pool concentration.

1.4.2 The role of actin at the synapse

In the context of the T cell synapse, actin is present during cell-cell engagement, synapse formation, stabilisation and finally dissociation. Depending on whether T cells are migrating or forming a synapse, actin can form elongated protrusions for penetrating endothelial tissue, filamentous arcs for corralling transmembrane proteins or dense meshworks for controlling cell migration and spreading upon TCR engagement.

Besides a structural role, actin dynamics are also important throughout the immunological synapse including organisation of membrane microdomains and complexes that initiate signalling cascades (Campi et al. 2005; Kaizuka et al. 2007; Yu et al. 2010; Yi et al. 2012). Actin dynamics redistribute and segregate signalling complexes into SMAC regions with actin rich regions sustaining cell-cell contact through peripheral ICAM-1 (Kumari et al. 2015), while the

actin-poor cSMAC allows vesicles linked to the MTOC to translocate to the immune synapse, necessary for signalling after the initial synapse formation and Ca^{2+} flux (Ritter et al. 2015).

To ready T cells for activation, cortical actin can act to transiently trap TCR complexes (F-actin increases led to reduced TCR mobility in ionomycin (increasing cytosolic Ca^{2+}) treated cells (Dushek et al. 2008)) which the authors speculate may allow scaffolding molecules to bind to the TCR for downstream signalling post-engagement. This is confirmed in studies which find WASp quickly co-localises with early TCR effector molecules including ZAP-70, LAT and SLP-76 (Bunnell et al. 2001; Barda-Saad et al. 2005). These colocalisations allow formation of relatively stable actin-based platforms, or actin rich areas, providing sustained signalling potential even in the presence of fast pMHC unbinding, as investigated by (Valitutti et al. 1995) where serial triggering of multiple TCR complexes by a small number of agonists is viable.

Actin reorganisation is also triggered through the T cells costimulatory molecule CD28, which increases actin polymerisation and actin protrusion (filopodia) assembly (Salazar-Fontana et al. 2003). CD28 also increases phosphorylation of the actin modulator Vav1, potentially via ZAP-70 (Wu et al. 1997), though this has been shown to be non-exclusive (Salazar-Fontana et al. 2003). Vav1's phosphorylation increases its association with LAT (Salojin et al. 1999), forming signalosomes which can then increase actin polymerisation further through Vav1's activation of the NPF Cdc42 (Salazar-Fontana et al. 2003).

Upon TCR engagement, T cells spread over their target following three temporal phases to establish a stable cell - cell contact. Firstly cell adhesion molecules (LFA-1 and ICAM) tether to each other to form a cell-cell junction, secondly the NPF WASp activation of Arp2/3 nucleation induces T cell spreading by F-actin polymerisation at the cell edge through actin branching (and with CD2 and CD28 costimulation, cofilin for SMAC formation) (reviewed (Samstag et al. 2003)), finally additional membrane from internal sources and the lamellipodia increases spreading further to engage around the target cell.

At the dSMAC where actin forms a dense meshwork and polymerisation is highest, proteins that drive these configurations are located, including NPF's. Here, those known to affect T cell synapse morphology and signalling are highlighted.

WASp and WASp-family verprolin-homologous protein 2 (WAVE2) are scaffolding proteins which provide a link between TCR engagement at the plasma membrane and the reconfiguration of G-actin (reviewed in (Takenawa & Suetsugu 2007)). WASp and WAVE2 bind with G-actin and Arp2/3 during TCR-dependent signalling, leading to increased actin polymerisation through increasing the number of free ends for G-actin to bind to (Krause et al.

2000). Recently WASp dependent actin-rich domains have been found at sites of TCR 'foci' (Figure 1.9; Kumari *et al.*, 2015). Making up less than 10% of the total actin at the synapse, as determined by a background filter, these foci are polymerised upon TCR stimulation. WASp dependent foci are sites of Phospholipase C, gamma 1 (PLC-γ1) activity, which metabolises $PI(4,5)P_2$ into IP_3 and diacylglycerol, increased IP_3 then leads to cytosolic Ca^{2+} release, agreeing with previous findings showing a loss of F-actin reduces PLC-γ1 phosphorylation in Jurkat T cells (Babich et al. 2012). 2-3 minutes after T cell activation WASp migrates to the dSMAC where it is thought to regulate the sustained actin flow at the cell periphery (Barda-Saad et al. 2005).

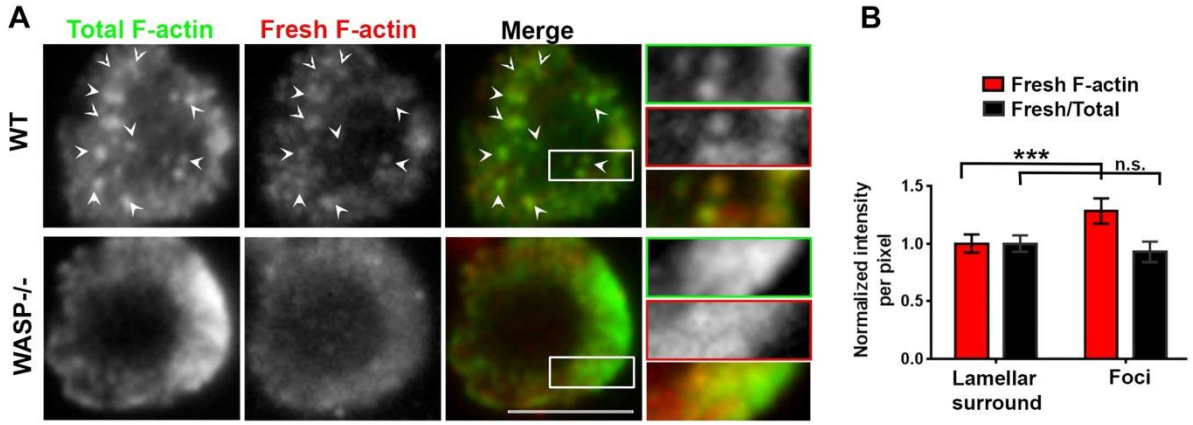

Figure 1.9 WASp dependent actin foci at the immunological synapse. A) Wild-type or WASp negative murine T cells, stimulated to form synapses on lipid bilayers exhibited different actin archetecture, with WASp negative cells lacking freshly polymerised actin rich foci (white arrows). This was quantified in B) (n = 20, p < 0.0001). Reproduced from Kumari et al. (2015). Scale bar = 5 µm.

Arp2/3 produces branched actin networks (reviewed by (Goley & Welch 2006)) which are important when forming both the actin foci (Kumari et al. 2015) and the actin-dense regions seen in the dSMAC (Yi et al. 2012). This dense meshwork is stabilised by formins and alpha (α)–actinin which create multi-filament bundles of F-actin (Figure 1.10; Esue *et al.*, 2008; Sjöblom, Salmazo and Djinović-Carugo, 2008). α-actinin forms an anti-parallel dimer which can bundle and cross-link fibres into many orientations due to its flexible neck region (Sjöblom et al. 2008). α-actinin has also been shown to cluster and drive movement of membrane receptors in lymphocytes (Hoessli et al. 1980) as it was observed using fluorescence microscopy to be enriched underneath clustered surface molecules (Geiger & Singer 1979). It may also have a regulatory or suppressive role in T cell activation, as silencing α–actinin increases IL-2 production and reduces F-actin accumulation at the immunological synapse (Gordón-Alonso et al. 2012).

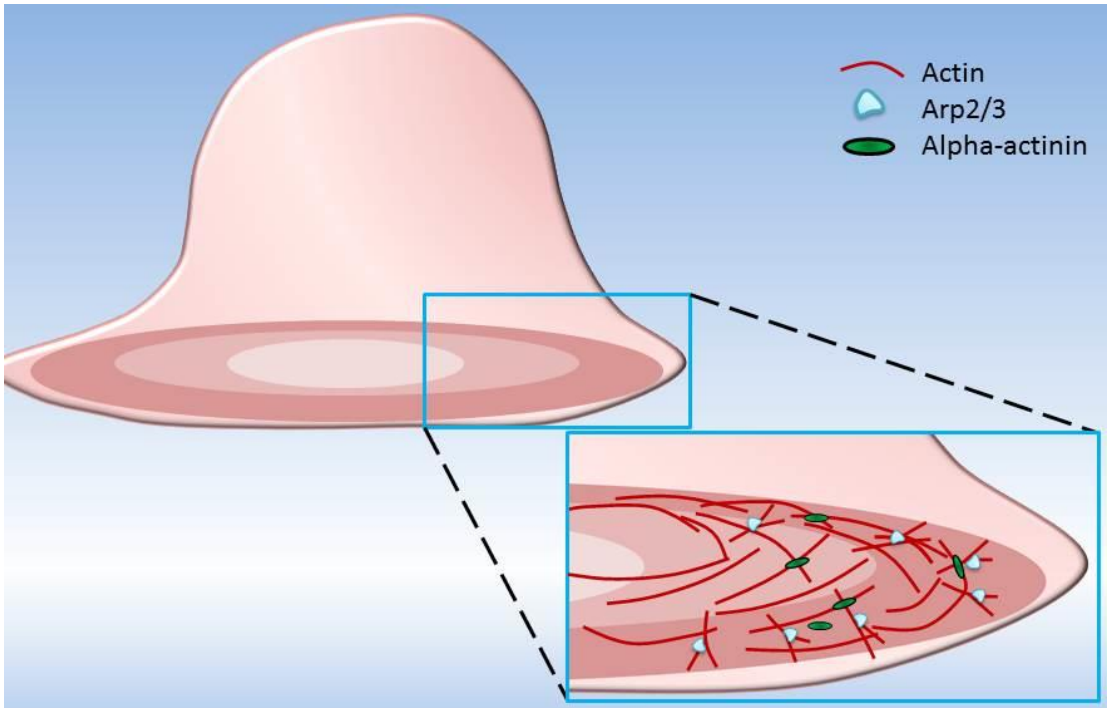

Figure 1.10 Cortical actin assembly at the immunological synapse. Arp2/3 driven polymerisation and branching creates a dense meshwork of F-actin at the synapse dSMAC with alpha-actinin crosslinking exhisting fibres.

Actin also has a role in reducing the lateral mobility of membrane residing proteins and increasing molecular clustering for signal amplification. Recently Köster et al. (2016) reported active flow is required to drive actin mediated clustering of glycosylphosphatidylinositol (GPI) anchored proteins in vitro, this agrees with previous modelling (Gowrishankar et al. 2012) and studies within T cells, where the diffusion of MHC, integrins and TCR microclusters were controlled by actin dynamics (Lavi et al. 2012; Comrie et al. 2015; Dushek et al. 2008). These dynamics therefore aid microcluster organisation and initiation of signalling cascades with cortical actin corralling and compartmentalising these signalling molecules.

Though this spatial information is accurate for a snapshot in time, signal modulation is a dynamic event where a huge amount of information can be gleaned from visualising the formation and regulation of the synapse through the temporal dimension. Much of the reorganisation and dynamics recently captured using live cell microscopy is due to the actin cortex. Actin (which is discussed in detail later) forms a meshwork juxtaposed to the membrane known as the cortex, generating forces and flow which modulate the molecular organisation of membrane residing proteins and of the membrane itself. The exclusion of the negative regulators CD43 and CD45 from TCR microclusters (Crites et al. 2014) and organisation to the dSMAC, is in part due to interactions with actin-binding proteins such as ezrin and moesin and also by their large extracellular domains. This permits phosphorylation and signalling to occur at the inner regions of the synapse through reduced cell-cell distances and reduced negative regulation of signalling complexes.

Away from these negative regulators, the pSMAC contains the active signalling platforms including the TCR-CD3 complex, the scaffolding proteins and the signalosomes. These proteins form microclusters in an actin dependent manner; clusters are believed to improve signalling strength and efficiency as multiple TCR complexes can transiently engage a single pMHC complex (Dushek & Coombs 2008; Ma et al. 2008).

Cluster dynamics mirror the flow velocities and directionality of the underlying actin cortex during synapse formation (discussed in the next section) though the Kaizuka and Yi findings disagreed on the dissipative nature of the microclusters-actin coupling with the latter group believing the connection to be more sustained.

Actin therefore generates and modulates signalling complexes during T cell activation, in part due to its dynamic nature. During T cell synapse formation the polymerisation of cortical actin drives cell spreading to create the cell-cell junction, the spreading phase eventually stops due to the containing role of the plasma membrane. As polymerisation of F-actin continues within the now fully spread cell, the actin starts flowing inwards, this flow is known as the retrograde flow.

1.4.3 Cell spreading and retrograde flow

As membrane residing signalling molecules and vesicles are both seen to congregate in the cSMAC of activated T cells it was speculated the retrograde flow, at least in part, corrals them there from the periphery. Retrograde F-actin flow and polymerisation has also been shown to correlate with relocalisation of proteins including ZAP-70 (Yokosuka et al. 2005) as well as TCR microcluster formation and downregulation (Varma et al. 2006). These findings highlight the corralling role of actin but also signal modulation either directly or through the modulation of proximal signalling proteins.

Extending actin beyond this transportation role for transmembrane proteins and vesicles via motor proteins, studies indicated F-actin dynamics also affect signalling, including that from the TCR (Valitutti et al. 1995; Kaizuka et al. 2007; Yu et al. 2010; Babich et al. 2012) in part due to spatial and temporal regulation of signalosome molecules themselves (Barda-Saad et al. 2005).

After T cell spreading polymerisation rates plateau, the actin within the dSMAC then starts flowing symmetrically inward towards the centre of the synapse in a polymerisation-driven manner (Babich et al. 2012; Yi et al. 2012). This actin flow and its force is important for regulating the spatial segregation of SMAC regions, including TCR centralisation and clustering at the cSMAC (Yu et al. 2010; Babich et al. 2012) via frictional coupling (Yu et al. 2010), driving

lateral mobility of TCR proteins (Kaizuka et al. 2007) and increased vesicle delivery through actin – driven microtubule repolarisation (Ritter et al. 2015).

During early TCR engagement where a small number of peptides are being presented it is important to drive T cells into an activated state through serial triggering, this has been hypothesized to occur through actin, where sheer forces are generated to create a conveyor-belt system of TCR-pMHC interactions (Ma et al. 2008). Grouping signalling molecules on the PM and keeping them separated from regulatory molecules until required, there is now speculation these may be laterally mobile or 'corralled' (Figure 1.11); bringing specific TCR-pMHC populations closer together and reducing tearing by excessive tension between dragged molecules (Ma et al. 2008; Kusumi et al. 2012).

Drug treatments which reduce motor protein activity or actin polymerisation, respectively decrease the clustered nature of integrins and disrupt the accumulation of TCR into the centre of the synapse (Yi et al. 2012). These findings agree with the active composite model (Köster et al. 2016) where myosin-actin driven dynamics aid molecular clustering in lipid bilayers such as the plasma membrane.

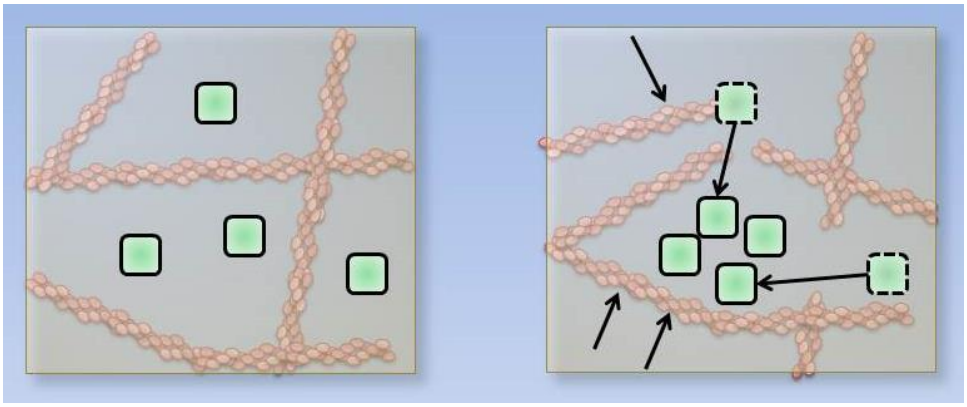

Figure 1.11 Cortical actin in modulating molecular lateral organisation and dynamics. Depending on actins (red fibres) ability to reorganise via motor proteins and polymerisation, molecules residing in the plasma membrane (green squares) can be segregated from each other or pushed together to form clusters.

Actin flow and microcluster signalling both diminish at the cSMAC; the mechanism for the coupling interaction is still unknown (Fooksman et al. 2010), as is the mechanism that keeps the cSMAC clear of actin. However signalling is down-regulated through the dissociation of CD28 and PKCΘ from TCR clusters (Yokosuka et al. 2008) as well as through the addition of ubiquitin (Varma et al. 2006).

To better understand these processes light-sheet microscopy was utilised (Ritter et al. 2015) to characterise F-actin flow in murine T cells during synapse formation. Findings showed actin depletion occurred after 1 minute of cell-cell contact, correlating with $PI(4,5)P_2$ depletion.

Cortical actin depletion was reported to occur because the exhibited retrograde flow continued up and backward towards the distal side, away from the site of the synapse (Figure 1.12).

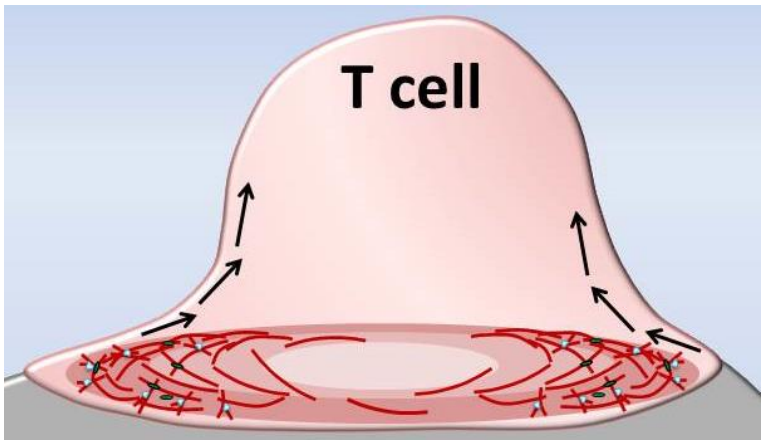

Figure 1.12 Flow of cortical actin at the synapse. Live-cell 3D imaging has highlighted the retrograde flow of actin at the synapse is the equivalent of 2D observations, with actin flowing both inwards and backward from the synapse periphery.

After TCR engagement and synapse stabilisation T cell disengagement and late stage synapse phases follow, these are poorly understood yet they are important for T cell deactivation, and for understanding how to negatively regulate incorrectly activated T cells. The cytoskeleton is believed to have a role in ending cell-cell interactions demonstrating the cytoskeleton is involved in the whole life-cycle of the T cell synapse. Molecules within the TCR signalosome are dissociated through various mechanisms (Bunnell et al. 2002), with SLP-76 trafficked away along microtubules using an unknown mechanism which was found to be negative for markers of endosomes or Golgi apparatus.

Understanding how microclusters form, are regulated, sustained and recycled will depend on fully characterising the synapse interface, particularly the plasma membrane.

1.5. Membrane biophysics

Membranes are planar bilayers that segregate interactions. The plasma membrane separates the cell interior for the surrounding environment. In its most basic form a lipid membrane a few nanometers thick, comprised of two leaflets of amphipathic lipids formed of a polar, hydrophilic head and two hydrophobic lipid tails. As the head groups are attracted to the polar water molecules and the tails are repelled this creates a stable but fluid two-leaflet structure of 7.5 – 10 nm (Hine 1999); Figure 1.13. This hydrophobic core also creates a semi-permeable structure for water-soluble molecules. The plasma membrane is comprised of lipids, proteins, glycolipids, glycoproteins and lipoproteins, and can contain water and ions.

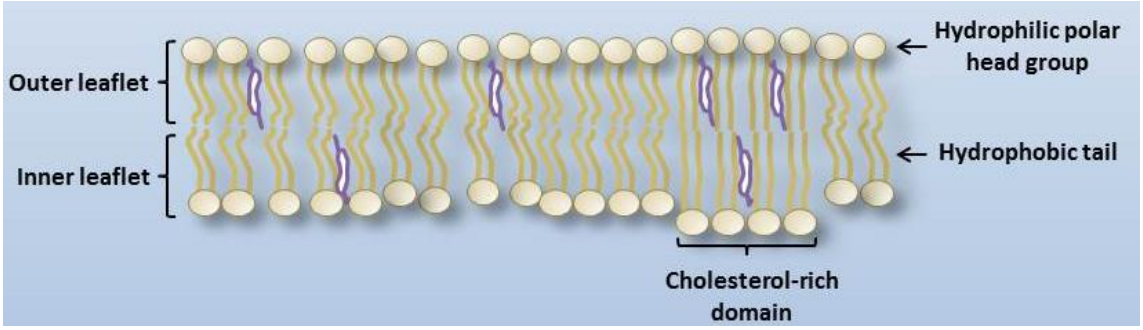

Figure 1.13 Basic structure of a lipid membrane bilayer. Lipids within the bilayer are formed of hydrophilic polar head groups and hydrophobic polar tails. The inner and outer leaflets are formed of different populations of lipids but both contain cholesterol (purple structure), which is one of the main components of lipid ordered domains.

1.5.1 Membrane structure and composition

Lipids within the outer leaflet of the membrane mainly contain phospholipids including sphingomyelin (SM) and phosphatidylcholine (PC), while the inner leaflet lipids (phosphatidylserine (PS), phosphatidylinositol (PI; including $PI(4,5)P_2$) and phosphatidylethanolamine (PE) possess head groups that are negatively charged resulting in a net negative charge of the cytosolic-facing plasma membrane.

Animal cells also contain glycolipids and cholesterol. Cholesterol is the most abundant sterol of the plasma membrane, and has a structural role in controlling membrane curvature, fluidity and permeability. Cholesterol can reside in both leaflets of the plasma membrane and increases packing density of these lipid regions and bilayer thickening via straightening of lipid hydrophobic tails (Olsen et al. 2013). This leads to an increased ordering of less well packed lipids, which is discussed in the next section.

The second major components of cellular membranes are membrane residing proteins (Figure 1.14), including glycoproteins and lipoproteins which are respectively formed from combinations of proteins and sugars or proteins and lipids. Proteins are targeted to the membrane from the endoplasmic reticulum via the Golgi apparatus through post-translational modifications including palmitoylation (the reversible covalent attachment of fatty acids - palmitic acid) and myristoylation (the covalent attachment of a myristoyl group) before trafficking via vesicles. The addition of hydrophobic structures increases protein affinity for the plasma membrane. Proteins make up 50 % of the membrane by weight (Cooper & Hausman 2013).

Anchored proteins attach to lipids, which increases their shuttling to the plasma membrane; this includes GPI-anchored proteins, which are anchored to the membrane via the GPI itself, with <40 % of these forming nanoclusters (Sharma et al. 2004). Proteins are also able to anchor

to the inner leaflet through either charge differences between the protein and the negatively charged inner membrane leaflet, or positively charged head groups of lipids within the extracellular leaflet.

Transmembrane proteins reside within the membrane itself, with portions exposed to both the cytosolic and exterior sides of the cell. Depending on the size of the cytosolic region of the protein it can then interact directly or indirectly with actin.

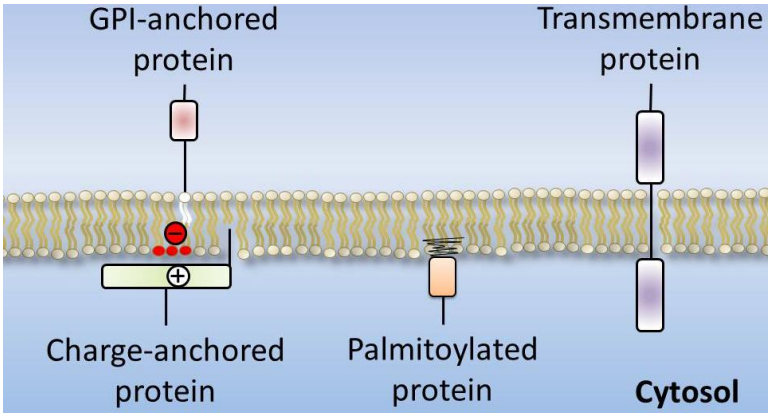

Figure 1.14 Different populations of membrane residing proteins. Glycosylphosphatidylinositol (GPI-) acts as a linker between the membrane and the anchored protein. Proteins with positive charge regions can associate with the plasma membrane due to the negative net charge of the inner leaflet. Proteins that are modified post-translation by the addition of for example palmitate are trafficked to the membrane inner leaflet. Transmembrane proteins span both leaflets and are permanently attached; the membrane-spanning portion is hydrophobic while the two protruding elements are hydrophilic.

1.5.2 Membrane order

Lipid tails have varying lengths and can be saturated or unsaturated fatty acids; the latter exhibit kinks from a double bond which disrupts packing, increases fluidity and permits the partial inclusion of water molecules into the leaflet. Saturated lipid tails provide the opposite. These saturated lipids are thought to coalesce, forming 'island' subregions within the membrane which exhibit different properties and may contribute an important role in compartmentalisation of membrane residing proteins, potentially increasing clustering of signalling proteins through these regions of increased molecular packing.

Different lipid tail compositions allow membranes to exist in one of three phases which determine its physical properties (Figure 1.15). Disordered, ordered and gel phase behaviours describe the lipid packing and lateral mobility at specific temperatures as well as the composition of the membrane. The liquid disordered phase exhibits highly mobile and irregularly packed lipids, with unsaturated tails kinked and interdigitated. Through the addition of sterols such as cholesterol, lipids exhibit increased packing compared to the liquid

disordered phase, though lipids are still relatively mobile – this is the ordered phase. Finally the gel phase represents solid lipid bilayers, with highly packed lipids demonstrating little movement – addition of cholesterol to the gel phase can also produce an ordered phase.

Along with membrane composition, phase behaviour can also change with temperature, as all lipids undergo a phase transition from gel to liquid at a certain 'melting' temperature. This induces a change in their hydrocarbon tails allowing them to freely diffuse within the membrane.

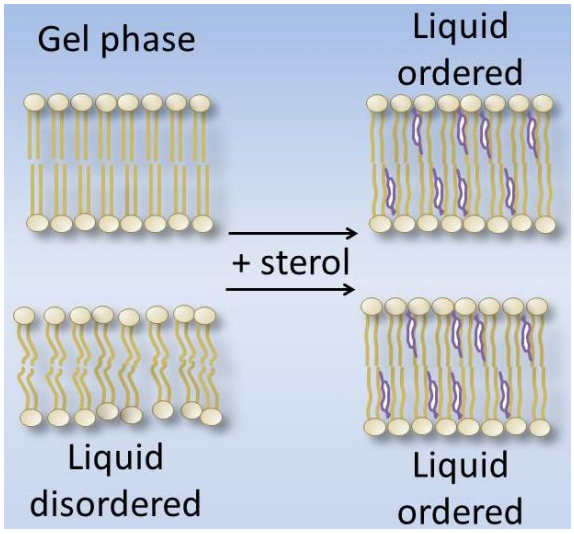

Figure 1.15 Phases of membranes. Sterols such as cholesterol can transition both gel phase and liquid disordered phase bilayer membranes to the ordered phase. This occurs through the respective disruption or ordering of the hydrophobic lipid tails due to sterol incorporation.

Cholesterol enriched domains also containing sphingolipids (e.g. sphingomyelin), forming ordered phases within the membrane due to the insertion of cholesterol which drives out polar water molecules and increases lipid packing. Cholesterol has also been shown, through its interactions with saturated lipids, to drive phase separation in regions made up of these lipids (Silvius et al. 1996).

Lipid ordered domains are reported to contain between 0.5 and 5 times more cholesterol than lipid disordered regions (Pike et al. 2002; Anchisi et al. 2013). The packing has been shown to induce lower molecular diffusion within these regions (Eggeling et al. 2009), where microscopy of individually labelled lipids was used. By reducing the levels of cholesterol within the sample using cholesterol oxidase, sphingomyelin lipids exhibited faster diffusion.

Alongside membrane composition, differences in membrane thickness can cause partitioning of transmembrane proteins based on their size, with proteins of different transmembrane-domain lengths matching the membrane thickness. This segregation can also occur during

hydrophobic matching; where proteins segregate based on their hydrophobic tail lengths as has been shown in G-protein coupled receptors (GPCR's) and soluble NSF attachment protein receptors (SNARE's) (Mondal et al. 2013; Milovanovic et al. 2015).

1.5.3 Techniques for imaging membrane order

Visualisation of membrane domains remains technically difficult, as the nature of lipids within a planar structure such as the membrane can be diffusive, with any changes made to the system for imaging reducing the validity of the measurements made. Below and Figure 1.16 summarise the minimally invasive techniques currently used.

Toxins which bind to cholesterol or lipids residing within ordered domains can be tagged with a fluorescent marker which can result in direct imaging of these domains; these toxins include Cholera toxin-B (CTB) which binds to the outer-leaflet membrane lipid monosialotetrahexosylganglioside (G_{M1}), enriched in lipid ordered compartments. However the toxin may bind to multiple G_{M1} lipids potentially causing artificial domains or to other glycosylated targets (Antes et al. 1992). Also, not all cells contain G_{M1}, limiting its use to specific cell types, including T cells and neurons.

To image lipids using light microscopy they must be labelled. Of all the techniques here this is the most direct way of imaging lipids, however depending on where the chromophore is situated on the lipid can greatly influence membrane distribution, incorporation and dynamics of the lipids themselves. For example cholesterol labelled with 4-Chloro-7-Nitrobenzo-2-Oxa-1,3-Diazole (NBD) at ring position 22 can demonstrate partitioning out of Lo domains (Ostašov et al. 2013).

Fluorescently tagged GPI's provide an alternative imaging method, as they reside in ordered regions of the outer-leaflet due to the inclusion of the glycolipid this has allowed the imaging and analysis of outer-leaflet partitioning and dynamics (Goswami et al. 2008; Saha et al. 2015). However a recent study claimed GPI-associated proteins do not attract other ordered membrane markers, and therefore do not reside in ordered regions of the membrane. Through micropatterning and immobilisation of GFP-GPI on a coverslip coated with antibodies against GFP, through fluorescence imaging the group reported other Lo membrane markers were not enriched in these regions (Sevcsik et al. 2015). However this assumes that immobilized GFP-GPI molecules are still markers of Lo domains, whereas these domains are believed to be transient in nature, exhibiting high lateral mobility and on spatial scales of nanometres not micrometres.

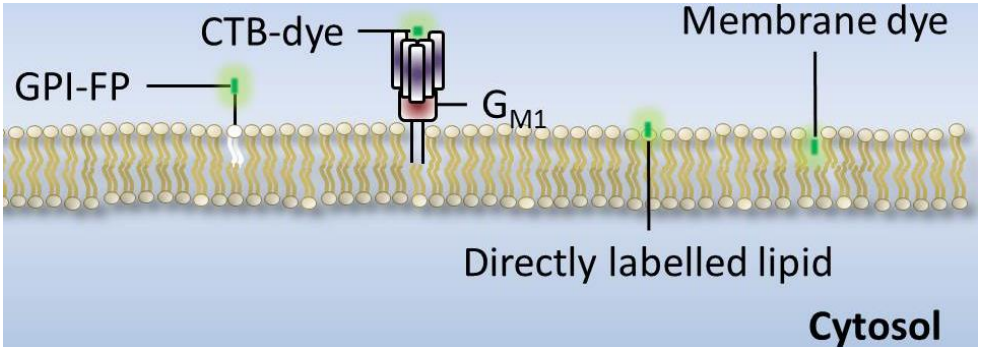

Figure 1.16 Modalities for labelling membrane lipids. From left to right GPI- anchors tagged with fluorescent proteins, cholera-toxin-B tagged with a molecular dye (such as Alexa Fluor; discussed in §2.2.1), lipids labelled directly or engineered to contain a fluorecent tag directly and membrane dyes. All report on specific regions and leaflets within the membrane as discussed in text.

Beyond labelling specific lipids, other techniques are available to image the membrane environment. Depending on their saturated acyl chain length, fluorescent dyes can segregate into different lipid domains, changing this length modulates the probes preference for selective membrane partitioning. This has been applied to chromophores that mimic lipid structure such as the dialkylcarbocyanines (DiO, DiI; Figure 1.17) which come with two hydrocarbon tails of various lengths and saturation states, segregating them out (C12:0, C16:0) or into (C20:0) Lo domains (Baumgart et al. 2007). However these are more complex interactions; as stated earlier hydrophobic and structural matching (including saturation status) dictates distribution, as reviewed by (Klymchenko & Kreder 2014).

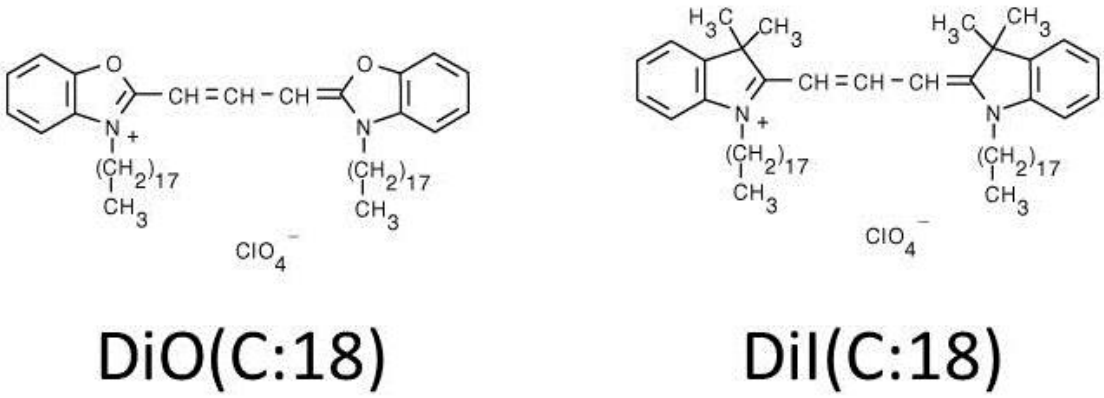

Figure 1.17 Structure of dialkylcarboncyanine (Di) dyes. The lipophilic structures contain two long hydrocarbon chains which mirror the structure of lipids, allowing them to preferentially insert into lipid bilayers.

Instead of relying on probes to partition into specific domains, environmentally sensitive (ES) dyes exhibit a shift in the fluorescent spectra, depending on the polarity of the surrounding environment (Figure 1.18a). They are hydrophobic and small in size so easily incorporate into the plasma membrane of cells on the scale of minutes, through incubation in solution. These

dyes are insensitive to protein packing within the membrane (Dinic et al. 2011), do not fluoresce strongly outside of the membrane itself and do not appear to interfere with cellular processes at labelling concentrations. Two commonly used ES membrane dyes are 6-lauryl-2-dimethylamino-napthalene (laurdan) and 2-di-butylaminonaphthylethylpyridinium propyl-2-hydroxy-3-dimethyl- hydroxyethyl quaternary (di-4-ANEPPDHQ; Figure 1.18b and §2.2.2).

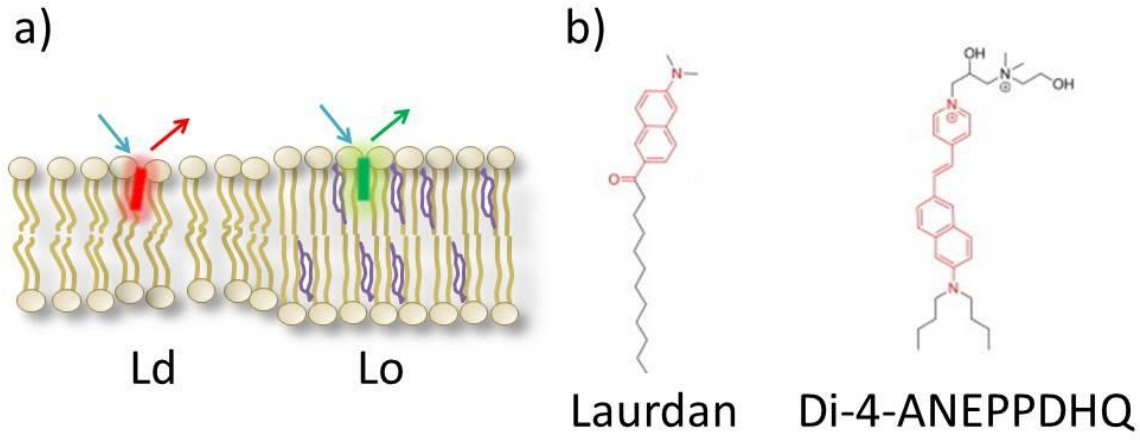

Figure 1.18 Polar sensitive dyes. a) depending on the orderedness of the membrane an ES dye resides in, they can exhibit a blue or red shift of fluorescence; red-shifted emission occurs in disordered domains. b) The molecular structure of laurdan and di-4-ANEPPDHQ with their dipole moments highlights in red.

These polar-sensitive (solvatochromic) dyes shift their dipole moment after excitation, resulting in a change to their emitted fluorescence. The large shift of laurdan's dipole moment is accredited to a charge transfer by the dialkyl amino group attached to one side of the naphthalene ring (Figure 1.18b) working as a donor of electrons to the carbonyl group. Voltage sensitive (electrochromic) dyes can sense the membrane potential and change their emission based on membrane polarity, making them sensitive to the inclusion of polar molecules such as water.

Limitations of imaging the plasma membrane with ES dyes for quantitative purposes include the varying signal that can be attributed to different dyes in different domains and orientations. For example depending on the dyes dipole moment dyes are more or less sensitive to absorbing excitation light (known as photoselection), changing their brightness. Environmentally sensitive dyes require carefully selected filters to separate the blue- and red-shifted fluorescent signal between channels for quantitative analysis. When using a widefield system the use of an image splitter is required, this adds the requirement of post-acquisition image alignment.

1.5.4 Membrane biophysics in models and cells

Cellular membranes contain a mixture of lipids and proteins which interact with each other, as well as with cytoplasmic and extracellular molecules to initiate signalling pathways across the lymphocyte membrane. How membranes are organised depends on environmental factors such as the lipid order phase of the membrane itself and the cytoskeletal cortex lying parallel and juxtaposed to the membrane (Machta et al. 2011; Mattila et al. 2016).

Protein and lipid organisation has generated multiple theories, starting with the fluid mosaic model (Singer & Nicolson 1972), where the PM is seen as a fluid environment with proteins and phospholipids distributed evenly and freely diffuse laterally (Figure 1.19a). This was developed into the lipid raft hypothesis (Simons & van Meer 1988; Simons & Ikonen 1997), with lipids partitioning into domains based on their order and membrane proteins preferentially partitioning into or out of these. Using detergents, centrifugation and biochemical analysis, subsets of proteins were extracted, but some 35 % remained within the membrane; residing within detergent resistant microdomains (DRM's), these lipids possessed saturated tails. The other 65 % are believed to follow free diffusion (Figure 1.19b) akin to the fluid mosaic model.

Limitations of detergent based analysis include the destruction of the sample, while detergents can themselves cause aggregation of lipids and proteins regardless of this Lo affinity (Lichtenberg et al. 2005). Additionally, different detergents can isolate different proteins based on the microdomains specific resistances (Schuck et al. 2003) and DRM studies are insensitive to quantification, as the percentage of proteins found in DRM's is not the same as in cells (Brown 2007).

Most of these early studies also use reductionist model membranes, made from unilamellar vesicles or bilayers, where diffusion is 10 – 100 times greater than that of cellular membranes, from the heterogeneity of lipid and protein distribution and the presence of the actin cortex indicating the systems lack complexity. There is also imaging and simulated evidence that proteins juxtaposed to and incorporated into the membrane can mediate order, as seen with actin and certain proteins roles in maintaining ordered domains (Dinic et al. 2013; Gómez-Llobregat et al. 2013).

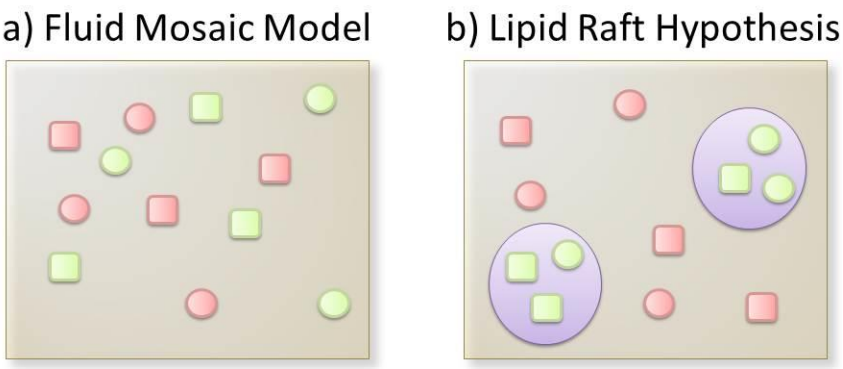

Figure 1.19 Theories of protein and lipid segregation within the cellular membrane. a) The Fluid mosaic model postulates that all molecules (green and red squares and circles) are freely diffusing within the membrane and homogeneously distributed. b) The Lipid Raft Hypothesis built on observations that some molecules (green) reside within detergent resistant membranes, postulating these molecular subsets segregate into Lo domains (purple).

Kusumi, Ike et al. (2005) built on these theories, introducing the picket fence model (Figure 1.20a), which introduced cortical actin interactions. Here a subset of molecules diffuse as normal in actin-poor regions of the cell but become transiently trapped when interacting with proteins located on the actin cortex in a juxtaposed manner. Proteins are freed into neighbouring zones when the actin fence-picket structures form holes for the diffusing proteins to jump over or through via 'hop diffusion'.

Hop diffusion was first characterised when the Kusumi group experimentally demonstrated single-molecule imaging with 25 µs time resolutions (Kusumi, Nakada, et al. 2005; Fujiwara et al. 2002). Hop-diffusion behaviour of proteins and lipids was described, with prolonged confined or stationary characteristics punctuated with 'hopping' to an adjacent region of the membrane. These confinements and hops were believed to be caused by transmembrane proteins interacting with the cortical actin layer. This was also found to modulate the dynamics of phospholipids; where these transmembrane protein 'pickets' temporarily confined lipid movement (Fujiwara et al. 2002). When not interacting with cortical actin, the motion of lipids and transmembrane proteins was Brownian in nature. These findings proposed neither cholesterol-rich domains nor extracellular regions of transmembrane proteins had any influence on these dynamics.

Another theory is the protein island model, based on findings in T cells by EM and live-cell single molecule data it proposes all proteins are segregated, into raft or non-raft clusters, both of which contain cholesterol, with minimal 'free' proteins in between. Lillemeier et al. (Lillemeier et al. 2006; Lillemeier et al. 2010) demonstrated these clustered regions, including LAT and TCR rely in part on the connecting cytoskeleton to form and stabilise (Figure 1.20b).

This agrees with the notion that cytoskeletal dynamics help drive membrane associated clustering as with the active composite model outlined below. Limitations of this work include the fixation of cells for EM imaging, and the 'deroofing' technique (ripping the top of the cell off) used to gain access to the interior and basal membrane of the cell, both of which can be prone to structural artefacts.

Until recently the two leaflets of the membrane were not known to interact with each other. However lipid clustering such as that seen within areas of increased lipid order has been shown to be mediated by leaflet mirroring between PS and GPI lipids residing on the inner and outer faces of cell membranes respectively. This mirroring takes place in an actin dependent manner (Figure 1.20c) through interactions between the lipids long acyl-chains (Raghupathy et al. 2015; Gowrishankar et al. 2012).

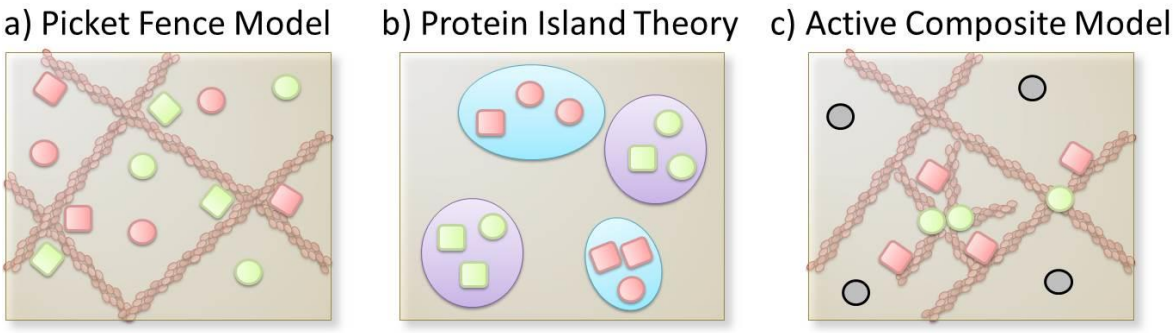

Figure 1.20 Extended theories of protein and lipid segregation within the cellular membrane. a) The Picket Fence Theory suggests the cortical actin layer (red fibres) situated juxtaposed to the membrane can interact with transmembrane proteins (red squares), forming pickets which can transiently trap and bind other molecules (green) which can be released during hop diffusion phases. b) The Protein Island Model states all proteins are segregated into different clusters of Lo (green) and Ld (red) proteins, unlike previous models there are no freely diffusing molecules other than those transitioning between two clusters. c) The Active Composite Model was developed to account for both the static actin cortex and active flow from dynamics actin asters (short fibres) with the latter required for aiding molecular clustering, these actin asters are driven by myosin motors to generate clustering of passive molecules (red squares) and are sustain by active molecules (green circles) while inert proteins (grey circles) are not involved in these dynamics.

The proposed active composite model splits proteins into three categories, inert (membrane dyes), passive (GPI-AP's) and active (e.g. TCR, BCR) based on their ability to interact with the actin cytoskeleton via varying acyl-chain lengths, saturation states or direct coordination of the actin itself (Figure 1.21). Actin asters drive protein clustering of active but also passive molecules which explains the clustering of GPI-AP's.

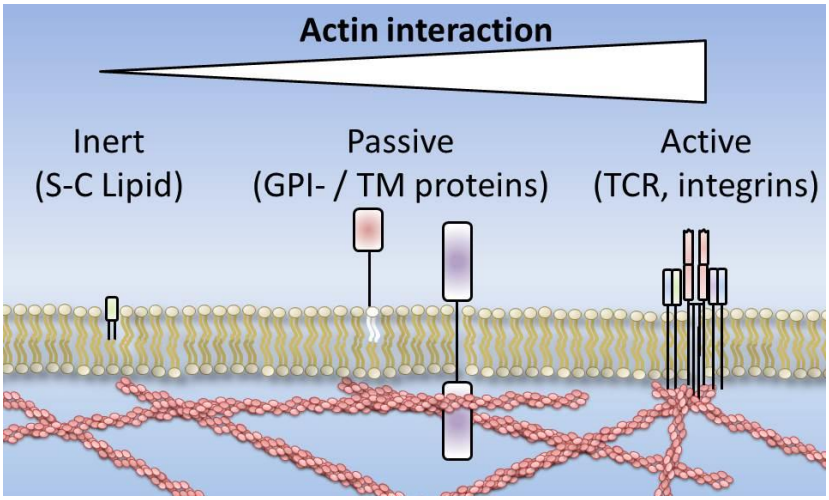

Figure 1.21 Active composite model. Cell surface molecules are classed by their ability to interact with the dynamic or static actin networks; 'Inert' molecules do not bind with dynamic actin but may couple with the static cortical meshwork (for example short-chain outer leaflet lipids). 'Passive' molecules bind directly or indirectly with dynamic actin but their dynamics do not affect the actin itself (for example GPI-AP's). 'Active' molecules are those whose dynamics can drive in part the actin filaments or motor proteins (for example TCR complex and integrins).

The active composite model was developed experimentally using supported lipid bilayers by Koster et al. (2016) to study actomyosin dynamics, providing evidence these forces are capable of driving membrane organisation of both actin binding and non-binding molecules, but did not report any bulk membrane flow in their system. Using GPI-AP's the group studied the effects of actin on the membrane when considered as a set of static crosslinked fibres and dynamic, short aster filaments.

1.5.5 Sub-synaptic vesicles

Cells maintain and recycle the molecular milieu of the plasma membrane through trafficking. Larger cargo molecules require vesicles during this process, originating and formed from lipids of the plasma membrane, Golgi or endoplasmic reticulum. Vesicle recycling can occur via receptor mediated endocytosis (e.g. clathrin coated pits [Figure 1.22]); forming indentations within the membrane before budding via dynamin, driven by actin and associated molecules. Incorporation back into the plasma membrane is initiated by vesicle-SNARE and target-SNARE proteins, which tether vesicles onto the membrane before its fusion occurs. Within activated T cells, molecules including SNAREs, vesicle associated membrane protein (VAMP)-7 and myelin and lymphocyte (MAL) protein aid trafficking of vesicles towards the synapse (Das et al. 2004; Soares et al. 2013), with these vesicles containing signalling proteins such as LAT (Larghi et al. 2013). Additionally, MAL was shown to help facilitate membrane order and MTOC distribution to the cSMAC, with mislocalisation causing redistribution of Lck and LAT to the pSMAC (Anton et al. 2011).

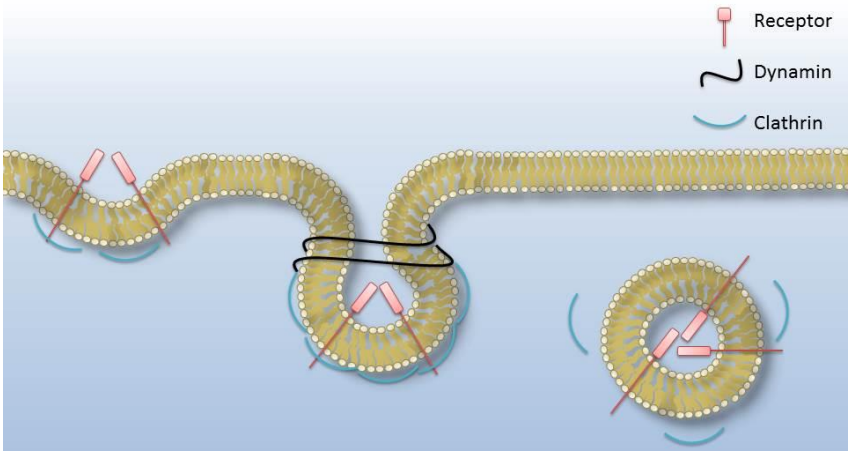

Figure 1.22 Receptor driven formation of vesicles. Vesicles form from the plasma membrane firstly through an indentation which is coated by clathrin from the cytoplasm, this structure then becomes an invagination which is budded off by molecules including dynamin. At this point the clathrin coat is shed and the vesicle is trafficked to the relevant cytosolic compartment.

Cargo delivery and distribution to and from the plasma membrane, particularly within the context of cell-cell junctions such as neurons and the immunological synapse is an important stage of cellular signalling. Spatiotemporal control of vesicles and their cargo allows replenishment of populations and sequential trafficking of new molecules to the interface, initiating different signalling events.

T cells require several hours of signalling (as seen by both Ca^{2+} flux and synapse polarity towards the APC) to initiate cytokine production and cell proliferation (Goldsmith & Weiss 1988; Lipkowitz et al. 1984)**.** For this to occur protein recycling is key, after initial engagement and dephosphorylation of plasma membrane bound TCR complexes, signalling is sustained through endocytosis at the cSMAC and rephosphorylation (Das et al. 2004). This also serves as a mechanism of transportation for TCR complexes to the synapse periphery, where continued signalling is observed (Varma et al. 2006). WASH, a member of the WASp family, has been found to drive actin polymerisation through its recruitment of Arp2/3 to vesicles containing TCR molecules (Derivery et al. 2009), WASH also interacts with tubulin; possibly indicating vesicles travelling along the MTOC can increase delivery speeds through actin dynamics.

Vesicle trafficking within cells including T cells can take two routes; firstly $Rab4^{+}$ vesicles recycle rapidly back to the plasma membrane along microtubules, secondly $Rab11^{+}$ vesicles situated further into the cell are clustered around the centrosome and move at longer time-scales, also along microtubules (Figure 1.23 (Mohrmann & van der Sluijs 1999; Ward et al. 2005)). TCR is contained in both sets of vesicles; but it could be speculated these early and late stage endosomes may also carry heterogeneous cargo such as LAT and Lck or negative signalling regulators for different stages of the T cell synapse.

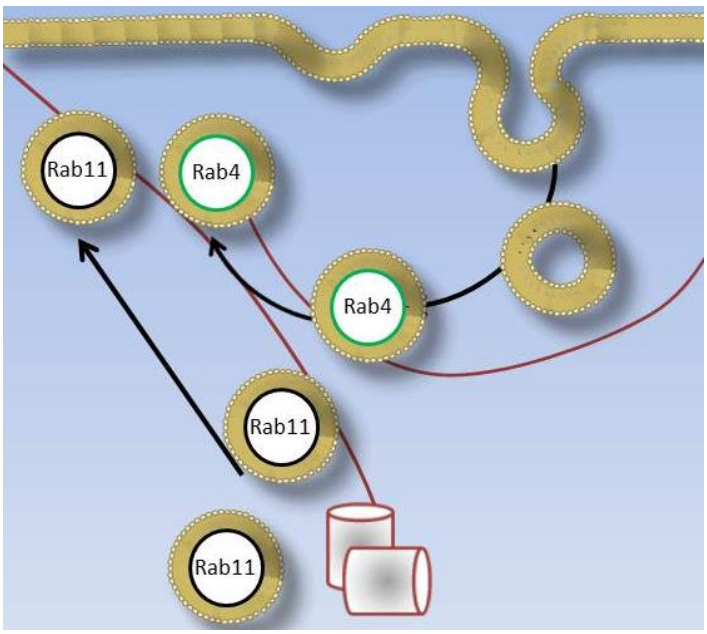

Figure 1.23 Vesicle transport based on Rab protein expression. Following endocytosis, Rab4+ vesicles are recycled quickly, while Rab11+ vesicles are transported from further within the cell. Both populations are transported along microtubules with Rab4+ vesicles recycled quickly, while Rab11 taking longer to reach the plasma membrane. As both have been shown to contain TCR this may be a mechanism to stagger the signalling process of T cell activation and immune response.

Beyond characterising recycling, studies have also investigated delivery of membrane-bound downstream molecules required for T cell activation. Vesicles and their cargo can be imaged with a membrane dye in cells co-expressing membrane-associated molecules such as LAT and SLP-76 (Purbhoo et al. 2010). The group and others have established a cytosolic pool of LAT overlays with cytoplasmic vesicles. pLAT (Bonello et al. 2004), along with Lck (Ehrlich et al. 2002) are recruited via vesicles to the synapse within 3 minutes of T cell activation, this coincides with the repolarisation of the MTOC network.

Work into LAT was extended by Williamson et al. (2011) who speculated vesicles may contain LAT for prolonged and dynamic signalling at the IS. The study found vesicular LAT was phosphorylated and therefore reasoned this population may represent an active signalling complex, through either interacting with the TCR complex at the plasma membrane or after LAT internalisation, where signalling could be continued.

Although LAT (upon palmitoylation) was shown via detergent extraction to reside in ordered membrane domains (Zhang et al. 1998), pLAT was only partially colocalised to G_{M1} in vesicles (Bonello et al. 2004), complicating the current view of cargo within endosomes. Whether these cargo segregate into different vesicles as they do with different plasma membrane domains is still unclear. Though, using fluorescent imaging it was demonstrated that LAT and Lck are

situated in distinct synaptotagmin-7 and Rab-containing endosomal pools respectively, with Lck colocalised with the lipid-raft associated MAL protein (Soares et al. 2013).

1.6. Interactions of actin and membranes

While cortical actin is juxtaposed to the plasma membrane it can also form transient or long-lived contacts with it, either through direct interaction or via binding and linker proteins. These interactions are also driven by actin polymerising proteins which tend to increase membrane order. The following section will summarise research investigating how actin corrals transmembrane proteins, membrane topology, organises some vesicle trafficking, and can become a barrier for membrane fusion.

1.6.1 Linker components between actin and membranes

Topological changes to the membrane such as protrusions (invadosomes) and ruffles which form during T cell migration and synapse formation are studied to investigate how spatiotemporal membrane organisation can lead to an effective immune response. Protrusions which are driven by actin and contain increased lipid order (Gaus et al. 2003) are also speculated to contain TCR complex proteins (Dinic et al. 2015) and therefore offer a mechanism for increased antigen recognition as T cells scan APC's (Sage et al. 2012). Membrane ruffles which -during NK cell synapse formation- dissipate from the synapse centre but remain at the distal regions, may be important for ligand binding and entry of larger receptors into the region (Benninger et al. 2009).

Ezrin, radixin and moesin proteins form the cytosolic ERM family which, depending on their proximity to $PI(4,5)P_2$ (Yonemura et al. 2002) can adopt two states; closed (inactive) or open (active) (Shabardina et al. 2016). ERM proteins act as linkers between the actin cortex through their actin binding C-terminus (Gautreau et al. 2000) and in T cells to the CD43, CD44 and ICAM-1 proteins (Yonemura et al. 1998) directly via their 4.1-ERM (FERM) domain N-terminus. They therefore preferentially localise to areas of actin-membrane proximity such as filopodia, protrusions and membrane ruffles. ERM's can also bind via the scaffolding protein ERM-binding phosphoprotein of 50 kDa (EBP-50) to the lipid raft associated C-terminal Src kinase (Csk)-binding protein (Cbp) in T cells, acting as a direct link between actin and lipid ordered domains and these negative regulators of immune synapse formation (Tomas et al. 2002; Itoh et al. 2002).

T cells only express ezrin and moesin (Shcherbina et al. 1999), both are phosphorylated upon TCR ligation and aid formation of the synapse, mediating accumulation and possibly actively corralling the negative regulator CD43 to the dSMAC (Allenspach et al. 2001; Delon et al. 2001; Roumier et al. 2001). Allenspach et al. found a dominant negative-ERM mutant which lacked

an actin binding domain, lowered IL-2 production in stimulated T cells via a reduced translocation of CD43 to the dSMAC (Figure 1.24). This ERM translation to the cell periphery may also account for topological changes through the synapse, with less actin linkages at its centre causing membrane ruffle reduction and increased cell-cell contacts. Overexpression of Cbp reduced the mobility of lipid rafts, halting synapse formation (Itoh et al. 2002), linking actin-membrane interactions to T cell activation.

Another actin-membrane protein, Filamin-A, is a molecular partner of CD28 which recruits lipid rafts to the immunological synapse via the cytoskeleton (Tavano et al. 2006), it also crosslinks F-actin and anchors plasma membrane residing proteins including β–integrins, and membrane receptors (reviewed in (Feng & Walsh 2004; Stossel et al. 2001). In Filamin-A depleted T cells PKCΘ exhibits reduced translocation from the cytosol to the plasma membrane with a dampening in IL-2 activation, though it did not affect proximal TCR signalling (Hayashi & Altman 2006).

As mentioned in §1.4.2., α–actinin crosslinks F-actin into parallel bundles but may also bind singular actin fibres to the membrane via zyxin and paxillin, (reviewed by Otey and Carpen, 2004) in the context of focal adhesions (Hampton et al. 2007) via β-integrin (Otey et al. 1990). Along with computer modelling that suggests crosslinking is most likely to occur when fibres are tangential to the plasma membrane (Kelly et al. 2006) these single 'monofilaments' bound to α-actinin may indicate actin-membrane protein linkages such as with actin protrusions (Figure 1.24). Vinculin and talin also interact with α-actinin and each other, forming adhesions, with the former binding to Arp2/3, increasing actin polymerisation and the latter binds to β-integrin. Gordon-Alonso et al. (2012) found α-actinin inhibited HIV-1 entry, potentially through creating and maintaining the dense meshwork to halt the virus's internalisation.

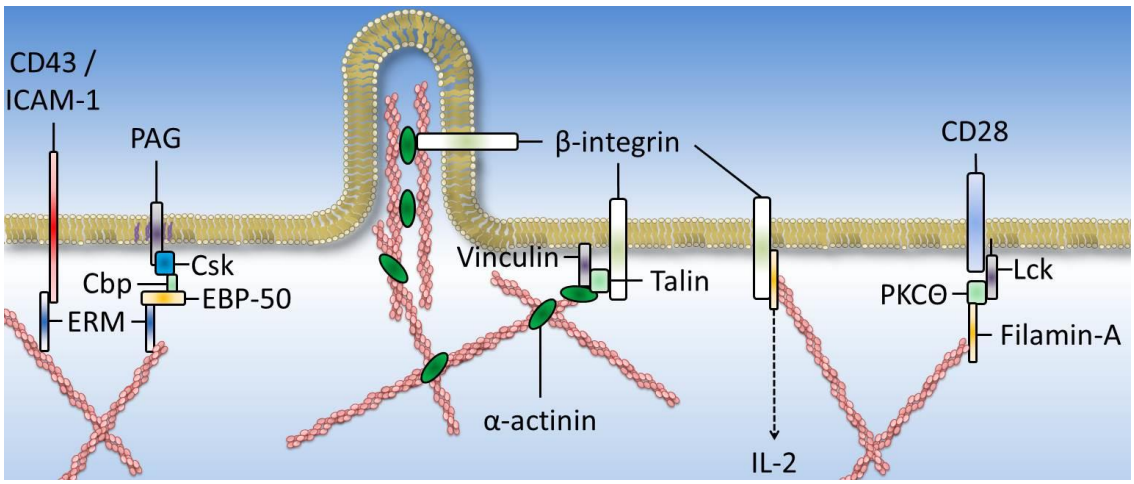

Figure 1.24 Actin-membrane linker proteins. Ezrin and moesin of the ERM family link actin to negative regulators of T cells CD43 and PAG, as well as the integrin ICAM-1, all of which translocate to the synapse periphery in an ERM mediated manner. A-actinin bundles and crosslinks F-actin forming protrusion and interacts with vinculin and talin at integrin sites. A partner of the costimulatory protein CD28; Filamin-A crosslinks F-actin and recruits lipid rafts and PKCΘ to the synapse, leading to increased IL-2 production.

1.6.2 Regulation of clustering

To initiate and sustain intracellular signalling, membrane associated molecules must be co-ordinated and clustered to generate specific downstream responses. Protein clustering within the membrane environment can be broadly controlled by three factors; lipid-protein, protein-protein (self-clustering) and actin-protein interactions. Lipid-protein interactions were outlined in §1.6.1.

Protein-protein clustering of membrane associated proteins occurs through direct self-interactions, as can be seen within the TCR signalling pathway this is usually through binding of proteins after a scaffolding protein binding site is phosphorylated. This phosphorylation can change the conformational state of adaptor proteins, leading to binding domains becoming available for protein-protein interactions.

Binding domains are regions within the protein sequence which allow interactions with other molecules, particularly relevant to T cell signalling are the SH2, SH3 and FERM domains. SH2 domains are generally located on enzymes such as PLC-γ and recognise phosphorylated tyrosine residues on adaptor proteins such as LAT. SH3 domains recognise proline rich domains, which are located on GRB2 and tyrosine kinases such as Lck, they are also found on proteins that regulate the cytoskeleton. FERM domains are located within ERM proteins and are therefore associated at the cytoskeleton-membrane interface.

As shown in Figure 1.24 actin-driven clustering can occur through direct interactions with membrane-associated proteins or indirectly through linker proteins.

Another factor that is speculated to control the microenvironment of protein clusters, particularly at cell-cell interfaces is the kinetic segregation model (Davis & van der Merwe 2006). At the immunological synapse proteins are thought to be included or excluded based on their size (Figure 1.25), with larger downregulation molecules such as CD45 being forced out of the tight junction, this has been shown experimentally in NK cells (Cartwright et al. 2014) and within GUV's (Schmid et al. 2016). Cartwright et al. found shorter dextrans (>4 nm) were able to freely move within the synapse whereas taller dextrans (>10 nm) were restricted to peripheral regions, this exclusion was partially controlled by the actin cytoskeleton as its disruption reduced this spatial exclusion.

Schmid et al. studied the spatial distribution of proteins with varying sized extracellular component within GUV's on supported lipid bilayers. Clusters of longer proteins were found to coincide with membrane bending or ruffles which were required to accommodate the larger molecules. Interestingly the study also highlighted lateral crowding as a contributing factor to the larger molecules exclusion (examples would include CD45 and ICAM-1 which are 40 nm), with smaller molecules (such as TCR-pMHC at 13 nm) packing membrane compartments and forcing longer/larger molecules out.

However this hypothesis has been called into question with the finding from T cells, where large transmembrane molecules such as CD43 are actively excluded from the synapse interface by ERM proteins and actin dynamics (Allenspach et al. 2001; Tong et al. 2004).

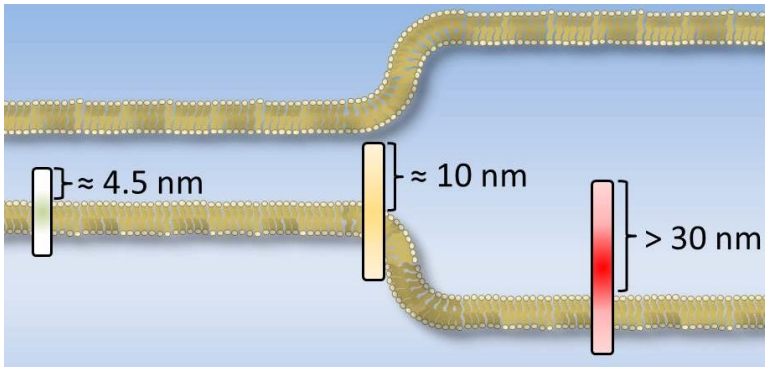

Figure 1.25 Principles of kinetic segregation model. Due to the tight junction created between membranes through receptor and ligand binding, as well as actin polymerisation, proteins of a cetain extracellular size cannot penetrate particular regions, these include junctions such as the immunological synapse, where excluded molecules are thought to include downregulatory molecules such as CD45, while upregulatory molecules such as TCR arepermitted to enter.

Protein clustering is potentially also controlled through actin and its interaction with membrane bound proteins such as LAT or activated WASp which act as sites of enhanced signalling and actin polymerisation (Sherman et al. 2016; Kumari et al. 2015). The picket fence

and active composite models both attribute cortical actin and its flow to increased clustering (Kusumi, Ike, et al. 2005; Köster et al. 2016). By reducing actin polymerisation or halting its flow, organisation and clustering of an actin-membrane protein engineered from the actin binding domain of ezrin is stopped, with membrane-bound molecules returning to spatial randomness (Köster et al. 2016).

The actin binding protein ezrin is known to cluster upon TCR and CD28 ligation, coalescing lipid ordered regions of the membrane (Tomas et al. 2002) which, along with TCR complexes (Dinic et al. 2015), have been shown by electron microscopy to accumulate with actin (Valensin et al. 2002; Lillemeier et al. 2006). This process could indirectly coalesce proteins associated with these raft-like structures as liquid ordered domains are stabilised by actin (Viola & Gupta 2007; Dinic et al. 2013), or directly with ERM proteins and their ability to link transmembrane proteins to the actin cortex (Niggli & Rossy 2008; Neisch & Fehon 2011). Interestingly, overexpressing ERM proteins in T cells reduces TCR clustering at the synapse of cell-cell interfaces (Roumier et al. 2001). As ezrin relocates negative regulators (CD43, CD44) away from TCR complexes and the synapse centre, this may demonstrate a mechanism for enhanced TCR clustering, where cell-cell contacts need to be tight to allow TCR microclusters to form.

According to the modelling work of Machta et al. (2011) the underlying actin cytoskeleton may limit the maximum size that membrane lipid domains can form; and that long-lived membrane order fluctuations are reduced by membrane-actin coupling, actin movement and actin flow. They predict 20 nm lipid order domains at sites found between cortical actin, where disordered domains are located preferentially to actin-membrane binding sites. This agrees with experimental finding in supported lipid bilayers by Koster et al. (2016) who found actin filaments were located around Lo domains, limiting their size through a barrier action.

These findings highlight contradicting evidence from in vivo experiments where actin has been found to be crucial for the formation and maintenance of Lo domains in T cells. By reducing phosphoinositides (which links actin to the membrane via ERM proteins) through phenylarsine oxide, the number of actin-membrane attachment points were reduced and with it the orderedness of the membrane itself (Dinic et al. 2013).

Overall, functional protein signalling at the membrane is partially driven by spatiotemporal heterogeneity and segregation. The actin cytoskeleton appears to have a direct role in organising and maintaining this clustering in T cells, as well as the stability and molecular structure of the T cell synapse.

However there is still some debate as to the role of the interaction between the actin cortex and the plasma membrane, including how the cytoskeleton directly or indirectly modulates liquid order within the membrane; possibly leading to protein clustering. Additionally, how proteins crucial for synapse signalling are trafficked, by interactions with the cortex itself either through its role as a barrier for vesicle delivery or as a corralling mechanism as with the picket fence model, are yet to be elucidated.

1.7. Aims for this study

To capture and quantify the nanometer scale biophysics within the T cell immunological synapse in relation to the cytoskeleton; this will advance current research using conventional imaging and analysis methods by reducing the artefacts such as an ensemble effect from imaging and user bias from manual tracking.

This method will then be to used to correlate these cytoskeletal dynamics to components within the plasma membrane, using two-channel imaging and cross-correlation analysis; this will provide evidence for or against the hypothesis that flowing or static actin and the plasma membrane can interact either directly or indirectly – as speculated by the active composite model and picket-fence theory.

Finally, to understand part of the mechanism for molecular recycling and delivery at the immunological synapse, this project will quantify the biophysical properties of the sub-synaptic vesicular population within T cells. This will include the membrane order of the vesicles themselves, their dynamics and the cargo they contain – building on previous research into vesicular cargo and dynamics to combine these into a more coherent model in the context of membrane order.

Chapter 2 – Introduction II

2.1. Fluorescence

Fluorescence is a subset of luminescence; the process of light emission by a molecule. Fluorescence describes the emission of visible or invisible radiation from a molecule that has absorbed electromagnetic radiation of a shorter wavelength; this relies on the excited molecule remaining in the same system state (e.g. singlet [S] or triplet [T]).

Singlet and triplet states refer to the spin or angular momentum of the excited electron, while intersystem crossing refers to the flipping of the electrons spin (spin conversion) leading to singlet – triplet exchange. As spin conversion has a low probability of occurring, intersystem crossing is rare, however when this event does occur these molecules enter a state of high chemical reactivity often resulting in photobleaching. Upon intersystem exchange (e.g. S to T, or vice versa, followed by relaxation to the ground state) this becomes the second process of luminescence, phosphorescence. It is also possible for the electron to interchange back to S1 from T1, and then relax, leading to delayed emission of a photon.

Fluorophores (molecules that exhibit fluorescence properties) normally reside in a non-fluorescing or ground state (S0); an electron is raised to an excited state (S1) after absorbing a quantum of light possessing a certain quanta of energy. The different energy states a molecule can reside in may be depicted on a Jabłoński diagram (Figure 2.1). After *t* amount of time (which depends on the duration of the non-radiative relaxation to the lowest vibrational state of S1) an electron drops from S1 back to S0 and a photon may be emitted with a lower energy state than the excitation wavelength, thus exhibiting red-shifted spectra. Energy loss is due to the vibrational nature of the S1 state with this spectral change is known as Stokes shift (Figure 2.2).

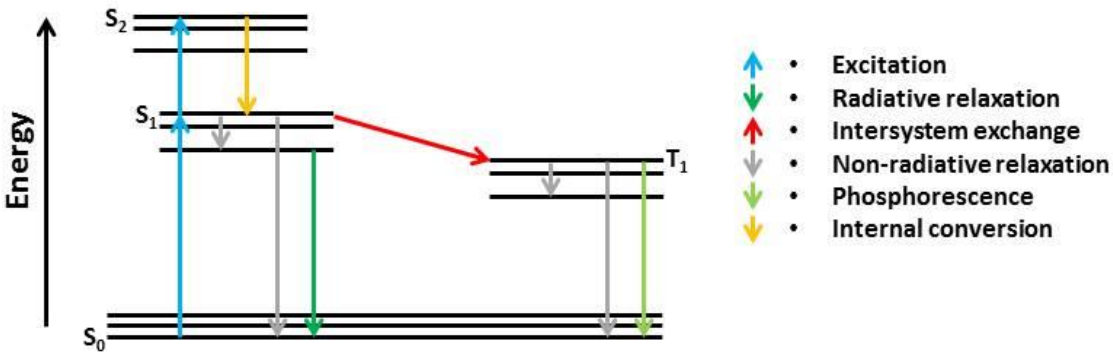

Figure 2.1 Jabłoński diagram. Depicting the main radiative and non-radiative transition states a molecule enters after residing in different energy states, these states are arranged vertically regarding energy levels and horizontally by spin multiplicity. The main process used during fluorescence microscopy is the radiative relaxation between S_1 and S_0, while some super-resolution techniques discussed later exploit intersystem crossing.

Fluorescence intensity depicts the number of photons emitted and is expressed as the quantum yield through a ratio measurement compared to the number of photons absorbed (the extinction coefficient) by the molecule. The quantum efficiency therefore describes the quality of the molecules as a fluorophore and its efficiency as a reporter for fluorescence imaging. The commonly used organic fluorophore enhanced (E)GFP has a quantum yield of 0.6 compared with the dye cyanine [Cy]5 whose quantum yield is 0.18 (Pawley 2006). Assuming the quantum yield is a fixed measurement, the overall intensity of the image, or pixels within an image, can allow researchers to quantify the number of emitting fluorophores and therefore their concentration.

The average time an electron spends in S1 before returning to S0 is known as the fluorescene lifetime, this lifetime is an important chararcteristic as it can be used as a reporter for the local environment, such as the refractive index surrounding the fluorophore. When fluorescence lifetime is used instead of fluorescence intensity this allows researchers to report on different materials or samples with different lifetimes, even when these materials are excited by the same wavelengths.

Extinction coefficient is a molecules ability to absorb light at a given wavelength (λ), when imaging this fluorescence output, it can be used to report on the number of fluorophores within the sample as this brightness is proportional (at a specific wavelength) to the excitation coefficient and the quantum yield.

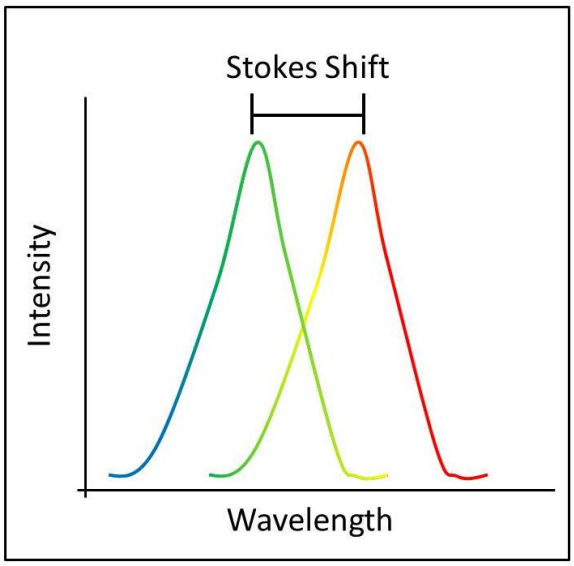

Figure 2.2 Stokes shift. In conditions where a molecule absorbs a photon of a certain energy to enter the S_1 state, before returning to the S_0 state upon releasing a photon, this photon will have a lower energy than the excitatory photon, as such a shift in energy and therefore wavelength occurs.

2.2. Fluorophores and fluorescence microscopy

Fluorescence microscopy has become one of the most widely used tools in research, due to the fact 1) fluorophores exhibit specific excitation and emission spectra so selective excitation and detection of subpopulations of fluorophores allows multi-channel (colour) imaging in the same sample. 2) Fluorescent labels can be conjugated onto antibodies for binding to specific molecules, or genetically encoded into cells via DNA transfection. 3) Organic fluorophores such as dyes are small (200 – 1000 Daltons) and depending on concentrations are normally non-toxic at levels needed for visualisation using microscope imaging. 4) Light is comparatively non-invasive. 5) Images can be analysed quantitatively.

2.2.1 Different types of fluorophores

Fluorophores can be grouped into dyes, proteins and synthetic nanocrystals.

Fluorescent dyes such as fluorescein were some of the first fluorescent compounds to be utilised for fluorescent imaging, and have since been bioconjugated to biotin or antibodies (e.g. fluorescein isothiocyanate [FITC], AlexaFluor (Panchuk-Voloshina et al. 1999) and Cy dyes). These dyes have been engineered to excite and emit at a range of wavelengths allowing multiple targets to be labelled and imaged within the same sample. Some dyes exhibit high affinities for specific structures such as the plasma membrane and are small enough in size compared to organic proteins (AlexaFluor = 1.3 kDa) to reduce perturbation of the labelled system. However for more targeted staining or for those dyes not possessing a specific affinity, they must be conjugated to an antibody, when labelling a specific protein, namely

immunofluorescence. This increases a dyes affinity but also their size as two antibodies are required; a primary (targeting the protein of interest) and the secondary (conjugated to the fluorophore and targeting the primary) antibody.

2.2.2 Environmentally sensitive dyes

2.2.2.1 Solvatochromism and photophysics

Depending on their environment and the light incident upon them fluorophores can exhibit different spectral phenomena in part due to photophysics and solvatochromism.

Photophysics at the single molecule level can be seen with fluorophore blinking between the on fluorescing and off non-fluorescing states and is thought to be due to transient intersystem crossing to triplet or dark states especially when illumination powers are increased as this increases the probability that the fluorophore will enter a non-emitting state. Triplet states are higher-energy and last longer (< minutes) (Turro et al. 2010) making them susceptible to reducing or oxidising species (Vogelsang et al. 2008). The presence of molecular oxygen in solution will react with molecules in this higher energy state leading to permanent photobleaching. By reducing oxygen levels in the system and the durations of this S and T state switching it is possible to reduce the probability of photobleaching.

Solvatochromism is defined as the process where a solvent's polarity changes the emission spectra of the fluorophore. As mentioned above fluorophores follow the Stokes shift principle, this is true when the molecule is in a vacuum, however upon solvent interactions this can be modified.

As the emission wavelength of a fluorophore depends on the energy gap between the S0 and S1 states, any change in the excited state by reorientation of solvent molecules can shift the fluorescence wavelength emitted. These changes can be due to, amongst others, solvent polarity or viscosity, rigidity of the local environment, and probe conformational changes (Lakowicz 2006). A polar fluorophore with a large dipole moment exhibits larger red-shifted emission when in more polar environments, such as a membrane system with increased polar water molecules.

Fluorophores will typically possess a larger dipole moment in S1 compared to S0, in an environment containing increased polar molecules the S1 energy levels are reduced due to these environmental polar molecules reorientating around the fluorophore. The greater the number of polar molecules the larger the effect; resulting in a lower energy S1 state of the fluorophore, leading to lower energy or red-shifted emitted photons to be released (Lakowicz

2006). As is covered in the next section this is useful for characterising the phase state of the plasma membrane.

Dyes can also sense temperature and viscosity based on the transition time taken between excitation and molecular relaxation, at lower temperatures emission spectra become blue-shifted due to a mismatch between the relaxation time and photon emission. This is because the solvent becomes more viscous leading to an increase in its reorientation time. pH sensitivity leading to emission shifts or inactivation ('on' or 'off' states) are also seen in certain dyes, caused by suppression of the electron transfer via photoinduction or by charge transfer (Han & Burgess 2010).

2.2.2.2 Environmentally sensitive dyes

Dyes which exhibit solvatochromism as discussed above include 6-Propionyl-2-Dimethylaminonaphthalene (Prodan), trans-4-Dimethylamino-4-(1-oxybutyl)stilbene (DOS) and dyes used in this study; Laurdan and di-4-ANEPPDHQ (Parasassi et al. 1991; Jin et al. 2005; Obaid et al. 2004). Laurdan (Figure 2.3a) excites at 405 nm, exhibiting a 70 nm red-shift (Parasassi et al. 1991) in fluorescence emission when residing in disordered domains such as cholesterol poor domains of the plasma membrane. Di-4-ANEPPDHQ (Figure 2.3b) excites at 488 nm and has a blue-shifted emission of around 60 nm when residing in less ordered environments (Jin et al. 2005). This shift is due to greater penetration of polar molecules such as water into the membrane environment which leads to interactions with the chromophore, and not due to other factors such as protein packing or pH shifts (Dinic et al. 2011; Parasassi et al. 1991).

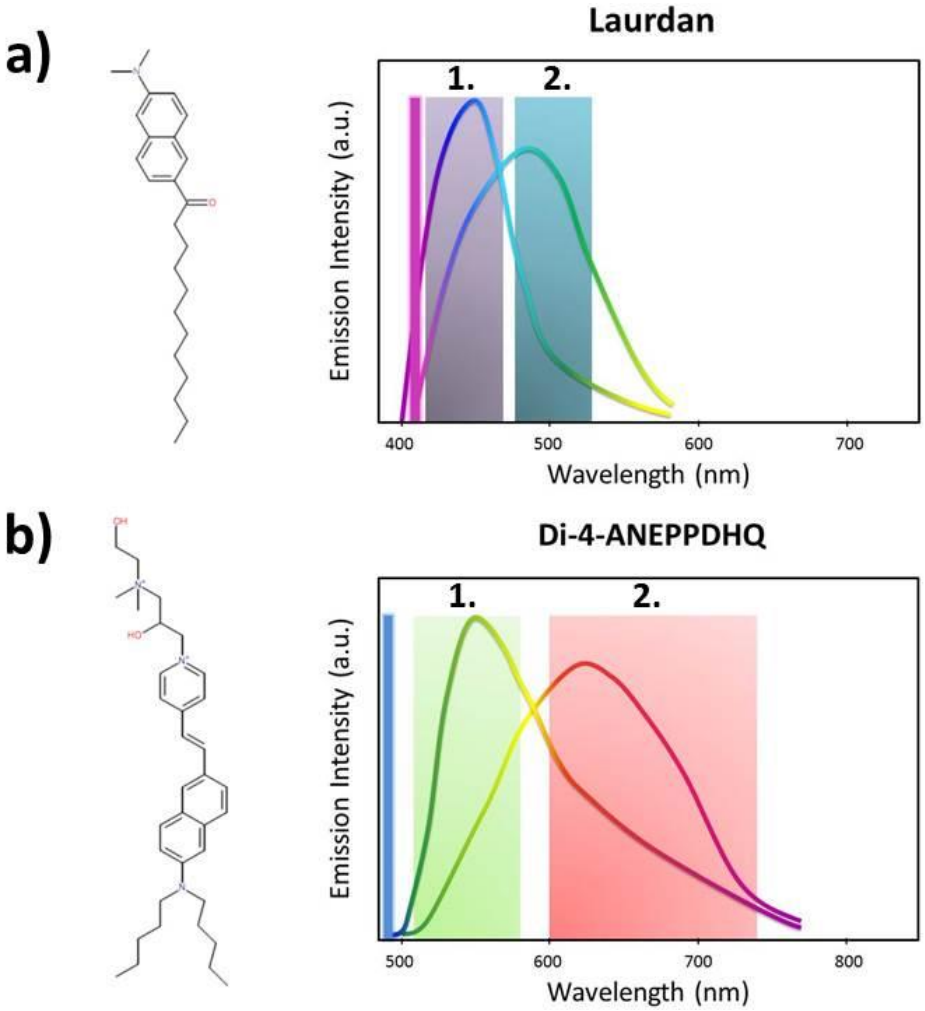

Figure 2.3 Structure and spectra of Laurdan and Di-4-ANEPPDHQ. a) After excitation by 405 nm light Laurdan exhibits -depending on membrane orderedness- a blue (1; ordered) or red (2; disordered) shifted emission. b) Di-4-ANEPPDHQ follows the same emission shifts as Laurdan but is excited by 488 nm light.

Application of environmentally sensitive (ES) dyes has been widespread within the imaging sciences, with use in characterising phase order within synthetic unilamellar vesicles, the plasma membrane of cells and whole organisms such as in zebrafish (Aguilar et al. 2012; Golfetto et al. 2013; Dylan M. Owen, Magenau, et al. 2010). Both dyes report lipid order but at different depths of the membrane, with Laurdan's chromophore residing in the polar head region of the membrane while di-4-ANEPPDHQ's chromophore aligns with the hydrophobic tails of the surrounding lipids. This may make di-4-ANEPPDHQ less sensitive to the environment surrounding the cell, instead reporting on the order of the hydrophobic region, while Laurdan may be more sensitive to the peripheral environment closer to the headgroups.

Di-4-ANEPPDHQ is less prone to flipping into the inner leaflet of the membrane due to its two positive charges but also preferentially resides in lipid disordered domains generating more signal in these regions due to different QY's, emission filter widths and camera sensitivities. These can be accounted for through standardising signal with the use of neutral density filters

and applying a calibration ('G') factor. For quantification of these dyes in different environments a normalised method termed Generalised Polarisation (GP) analysis was introduced (Equation 2), which expresses the intensity of fluorescent dye populations residing within ordered or disordered environments as a ratio:

$$GP = \frac{I_B - GI_R}{I_{B+}GI_R}$$

Equation 2

Where I_B = Intensity under which wavelength 'B' (blue-shift), I_R = Intensity under which wavelength 'R' (red-shift), G is the calibration factor; to account for intensity differences between the two channels, a G factor is set (Equation 3). This is undertaken by imaging the dyes in solution and taking the ratio measurement:

$$G = \frac{GP_{ref} + GP_{ref}GP_{mes} - GP_{mes} - 1}{GP_{mes} + GP_{ref}GP_{mes} - GP_{ref} - 1}$$

Equation 3

Where GP_{mes} is the GP value in solution and GP_{ref} is the reference value of the dye in solution; for Laurdan this is 0.207 (Gaus et al. 2006), while for di-4-ANEPPDHQ a value of -0.85 is chosen (Owen et al. 2011).

This analysis can be applied to microscope images on a pixel by pixel basis giving advantageous resolutions compared to alternative methods such as DRM and lipidomic analysis for studying membrane lipid composition, in a manner which is independent of probe concentration.

2.2.2.3 Use in microscopy

ES dyes have been applied to quantitatively analyse the lipid order of T cells and synapses before. Through the use of Laurdan, it was shown that upon TCR stimulation through membrane patching, ordered membrane components were aggregated; with increased local lipid order of resting Jurkat and primary human T cells. These domains accumulate and are stabilised by sites of increased actin accumulation upon T cell stimulation, with costimulation by CD28 increasing sustainability of membrane lipid order (Dinic et al. 2015; Gaus et al. 2005). Other signalling molecules known to reside in and possibly generate ordered membrane domains include LAT, Lck, and Fyn, these findings came from depletion of membrane cholesterol with methyl-β-cyclodextrin (MβCD) which resulted in reduced condensation of ordered domains (Gaus et al. 2005).

Lipid order has also been shown to determine the activation state of $CD4^+$ T-cells, using di-4-ANEPPDHQ to characterise higher lipid order resulted in cells forming more stable synapses and increased proliferation while lower lipid order reduces these parameters (Miguel et al. 2011). Lipid order at the whole synapse scale has also been studied using di-4-ANEPPDHQ; with increased order reported at the synapse periphery during coverslip and cell-cell activation (Dylan M. Owen, Oddos, et al. 2010). As these peripheral regions are populated by active signalling microdomains and are known to be juxtaposed by a dense actin meshwork this points to further actin-membrane interactions, in the context of membrane order.

Imaging multiple molecules of interest requires their serial labelling and staining with different antibodies, for imaging with dyes this normally requires samples to be fixed. Fluorescent proteins are genetically engineered and permit live sample imaging, first isolated in the 1960's from the *Aequorea Victoria* jellyfish, the bioluminescent blue-emitting protein named aequorin and the original green fluorescent protein (GFP; (Shimomura et al. 1962)).

GFP has also been genetically engineered to increase its excitation-emission spectra which, along with further discoveries of red-shifted fluorescent proteins, allows for multiple targets to be imaged within the same sample. Compared to Alexa Fluor, fluorescent proteins are relatively large in size (≈ 25 kDa) but remain beneficial for live-cell imaging, as their genetic sequence can be inserted within a protein of interest and, through transcription, can produce a fluorescent fusion construct to be expressed by the organism itself. As the proteins are expressed as a 1:1 ratio within the target molecule this allows quantitative imaging to be carried out (Patterson et al. 1997).

Fluorescent proteins consist of an α-helix core surrounded by a β-barrel protein structure containing the chromophore, chromophores exist within the β-barrel which reduces its sensitivity to the surrounding environment, making it more resistant to photobleaching.

Fluorescent proteins have been further engineered to permit photoconversion or photoactivation derivatives, that is, fluorophores which are activated via a specific wavelength of light from a non-fluorescing state or change their emission spectra.

Quantum-dots (Bruchez et al. 1998) are a group of synthetic nanometre sized crystals which exhibit wide absorption spectra, primarily based on their diameter and composition (Alivisatos 1996; Jaiswal & Simon 2004) and are highly resistant to photobleaching. However being synthetic they must be made biocompatible for use during *in vivo* studies, and require an antibody coat to target the molecules of interest during imaging. Due to their relatively large

size they are also more difficult to incorporate into the sample and may be more susceptible to perturbing the system of interest.

2.2.3 Widefield, confocal and TIRF microscopy

At a fundamental level, a fluorescence microscope is an optical detector that uses light to excite fluorophores and record any emitted light as information through an objective lens and a detector (e.g. electron multiplier charged coupled device [EMCCD] camera). While this system can detect single molecules, resolving these individual molecules is rarely achieved using conventional techniques.

Widefield microscopy (Figure 2.4a) describes the simultaneous illumination of the whole field of view, which lends itself to fast imaging. This illumination however can lead to increased photobleaching and phototoxicity as the full sample (including outside of the optical plane) is being illuminated and with it any fluorophores. Furthermore thick (>2 µm) specimens will generate a high degree of background away from the plane of interest due to this whole-sample illumination; also limiting the technique when imaging in 3D.

To reduce this limitation, optical sectioning can be employed so illumination light only excites fluorophores within a specific image plane. This reduces fluorescent signal from those fluorophores not residing within the plane of interest and therefore reduces the background level of fluorescence, improving contrast of those molecules in focus.

Confocal light scanning microscopy uses excitation light limited to a selective volume of illumination and (when used in combination with a pinhole in front of the detector) selective detection. This form of optical sectioning helps form the final image by decreasing the number of fluorophores being excited in the x, y plane (Figure 2.4b). This range of sectioning is determined by the pinhole size and the objective lens, along with the wavelength of light being used (discussed in the next section).

The reduced sized ‘spot’ of illumination can then scan across and through the sample via moveable mirrors to form an image of all fluorophores in two or three dimensions. Depending on the size of the sample being imaged, this scanning method can prolong the time taken to acquire data compared to widefield methods.

TIRF microscopy (Axelrod 1981) is an extension of widefield acquisition which selectively excites fluorophores at a refractive index interface, such as that at the coverslip-sample (Figure 2.4c)

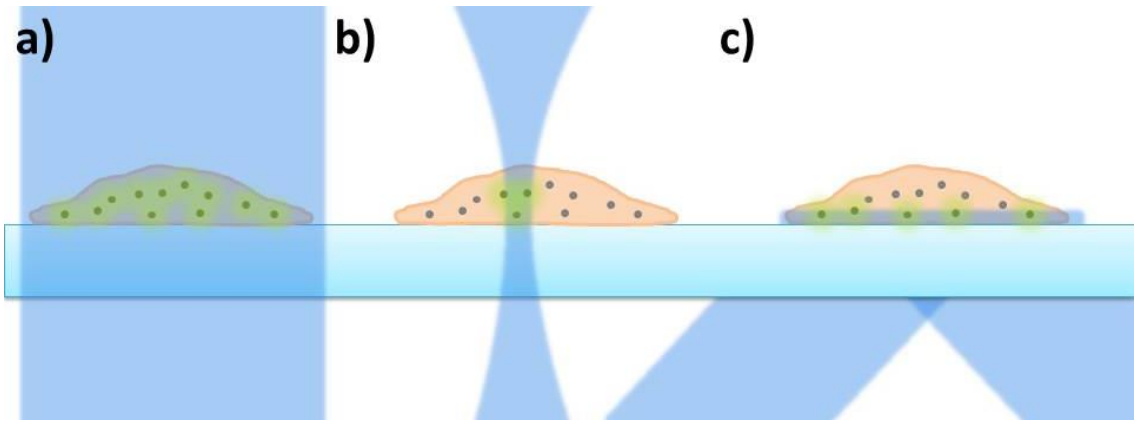

Figure 2.4 Different far-field microscopy modalities. Depicted are a) widefield, b) confocal and c) total internal reflective fluorescence (TIRF) set-ups, the excitation beam (blue) illuminates the sample in different methods, giving information on fluorophore locations. Widefield illumination excites the full sample, confocal illumination reduces the illumination volume to improve signal to noise, as does TIRF illumination.

The selective illumination of TIRF reduces background fluorescence from within the sample and photodamage from excess illumination while improving the signal-to-noise ratio making it easier to detect single molecules compared to widefield and confocal methods. This is achieved by angling the illumination beam beyond the critical angle (Equation 4) defined as:

$$\theta_C = sin^{-1}(n_2/n_1)$$

Equation 4

Where Θ_C = the critical angle, n_1 = the refractive index of the first medium (coverslip), n_2 = the refractive index of the second medium (water, cell cytoplasm).

As there is a refractive index mismatch between the coverslip and the sample total reflection of the laser occurs (Figure 2.5). However an evanescent wave possessing the same frequency as the excitation beam propagates across the coverslip, and penetrates into the sample before exponentially decaying (Equation 5 & Figure 2.6). This is advantageous versus standard widefield imaging as only a 100 – 200 nm section of the sample is illuminated; limiting photodamage to within the illuminated section as well as increasing the signal-to-noise ratio. In this sense TIRF imaging is a form of optical sectioning, as the evanescent wave decays exponentially from the interface as:

$$I_z = I_o e^{-z/d}$$

Equation 5

Where I_z is the intensity perpendicular to the interface, I_o is the intensity at the interface (where z = 0) while the penetration depth d of the illumination wavelength is given by Equation 6:

$$d = \frac{\lambda}{4\pi}\sqrt{n_2^2 sin^2\theta - n_1^2}$$

Equation 6

Where λ is the wavelength of the excitation light.

The penetration depth of the evanescent wave is affected by the excitation wavelength (longer wavelengths increase the penetration depth), the incident angle (shallower angles reduce the penetration depth) and the refractive index mismatch of the coverslip – sample (greater mismatches increase the wave depth).

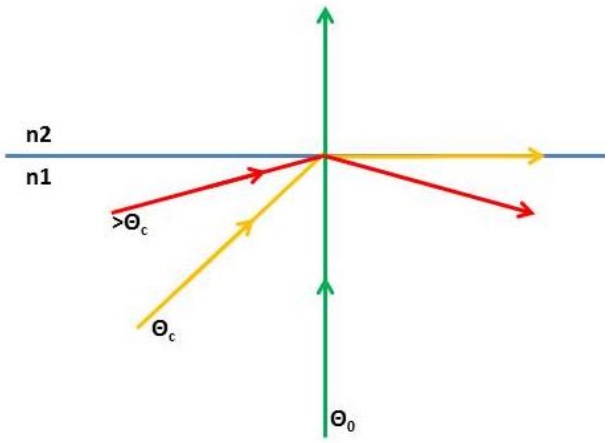

Figure 2.5 Reflective properties of light at a refractive index interface between two non-uniform media. Light, when incident upon the mismatched interface of two refractive indexes (n1 and n2) can, when the wavefront has no angle relative to the interface, will pass straight through (Θ_0, green arrow), when the wavefront is angled at the critical angle (Θ_C, yellow arrow) light is propagated along the mismatch, while beyond the critical angle (>Θ_C, red arrow) light is totally reflected.

A consideration of TIRF imaging is the polarisation of the light, that is, the vector direction of the electric field. With TIRF microscopy, the evanescent wave expresses the same polarisation as the incident beam, which can be either 's' or 'p' polarised. S-polarised light vectors remain normal to the plane or incidence, p-polarised light is maintained in the incidence plane (into the z-axis); resulting in nonzero longitudinal 'cartwheeling' intensity (reviewed by Axelrod, 2001). This allows p-polarised light to distinguish structural irregularities such as vesicle formation or ruffling of a stained membrane. This means, due to the orientation of a dye such as DiI, which positions itself parallel within the membrane and has its transition dipole

moment orientated parallel to the membrane; indentations within the stained membrane can be specifically excited with p-polarised light. Polarized excitation can be quantified by ‘p’ over ‘s’ polarised light.

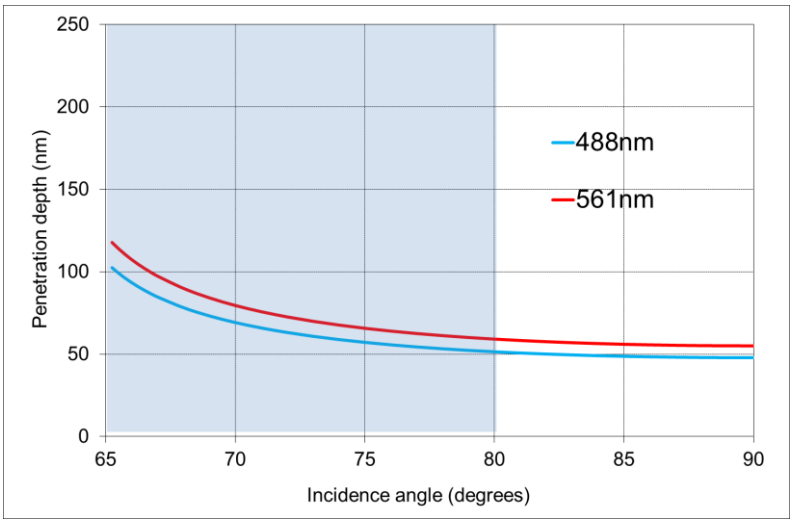

Figure 2.6 Penetration depth of the evanescent wave as a function of the incident angle of light. Evanescent wave penetration depth depends on the angle of incidence and the wavelength of incident light, the plot demonstrates shorter wavelengths lead to lower penetration depths, as do higher incident angles.

Compared to widefield imaging (Figure 2.7a) the resulting TIRF image (Figure 2.7b) has improved contrast and optical sectioning of fluorophores close to the coverslip-sample interface, enabling better resolution of structures.

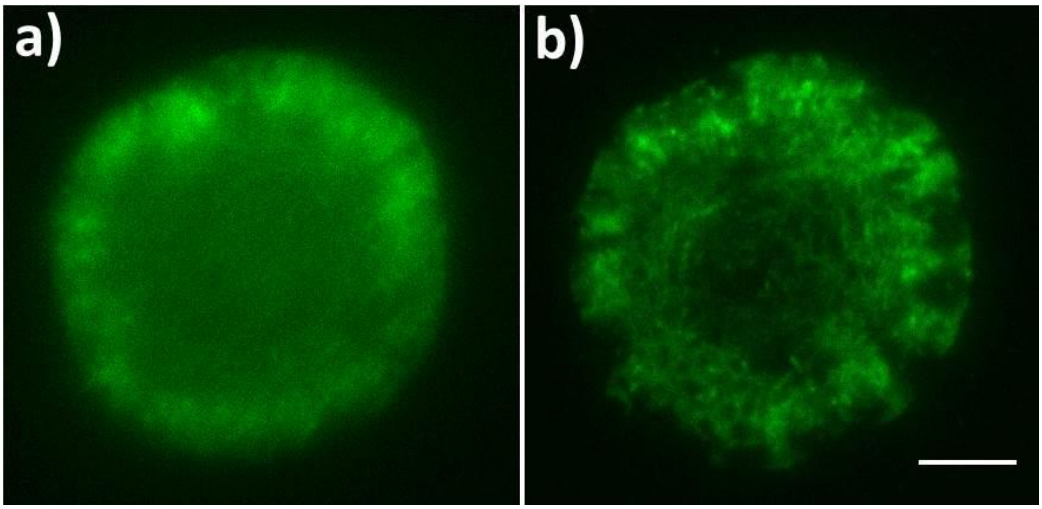

Figure 2.7 Fluorescent imaging using widefield or total internal reflective fluorescence modalities. a) Depictes a T cell forming a synapse against a stimulatory coverslip using widelfield imaging technqiues, with the actin network labelled with GFP. b) Shows the same cell imaged in TIRF, with only GFP fluorophores residing within the evanescent wave being detected. Scale bar = 5 µm.

Alternatives to TIRF imaging include super-critical angle fluorescence (SAF) imaging, like TIRF this technique can detect fluorophores at or linked to surfaces. By using an aspherical lens the sample is illuminated and emitted light (the majority of which emanates through the objective above the critical angle) is detected. As with TIRF this means molecules are detected when residing within ≈ 200 nm above the surface, due to the approximately exponential relationship between distance from the coverslip and signal. This technique has also been extended to 3D super-resolution (Deschamps et al. 2014), using single molecule localisation. By rejecting the under-critical angle signal from the sample this technique can be utilised for optical sectioning (Axelrod 2001), however by combining the super- and sub-critical signal the axial positions of fluorophores can be determined.

SAF is limited by its relatively technical set-up compared to TIRF microscopy, the technique is also (as with TIRF) limited by its axial range. Additionally, to exclusively select the fluorescence beyond the supercritical angle is difficult due to diffraction at the circular objective (Deschamps et al. 2014) with improved imaging requiring advanced and expensive objectives. This method of selecting only a subset of photons also means loss of detected signal from the sample, reducing image quality.

2.2.4 Spatial and temporal resolution

Imaging with light limits techniques to finite spatial and temporal dimensions. To spatially resolve point-like objects such as fluorophores, emitted photons are recorded as intensity distributions, convolved through the 3D point spread function (PSF) of the microscope to form the final image.

The diffraction limit was defined by Abbe, Rayleigh and others around the beginning of the 1800's. As light from a point source becomes convolved by a lens, the intensity profile at the detector is spread, appearing as a circular Airy diffraction pattern, with a peak intensity approximately following a Gaussian distribution surrounded by a 'dark' ring (Figure 2.8a). The Airy disk (Equation 7) was described by George Airy in 1834 (Airy 1834):

$$d_{airy} = \frac{1.22\lambda}{n \sin \alpha}$$

Equation 7

Where λ is the wavelength of the light, n the refractive index of the medium and α the half-angle of the collected light from the point object (see Figure 2.9).

The PSF generates a representation of the source object exhibiting dimensions of around 250 nm laterally and 500 nm axially. This is derived from the Fourier transform of the point object

emanating from the lens, imaging through the focal plane of the PSF gives an Airy disk pattern. The size of the Airy disk is important for resolving two point objects close to each other. When two fluorophores reside at a distance smaller than the radius of the first ring they are considered unresolvable due to the Airy disks overlapping (Figure 2.8c). The distance from the central peak to the first minima or 'dark' Airy ring is described in Equation 8 as:

$$d_{x,y} = \frac{\lambda}{2NA}$$

Equation 8

Where NA is the numerical aperture of the objective lens (Equation 9) which describes the cone of light it can be propagated to and received from the sample:

$$NA = n\ sin(\alpha)$$

Equation 9

Where n is the refractive index of the medium between the lens and the sample, and α is the half-angle of the objectives light cone or opening angle, also see Figure 2.9.

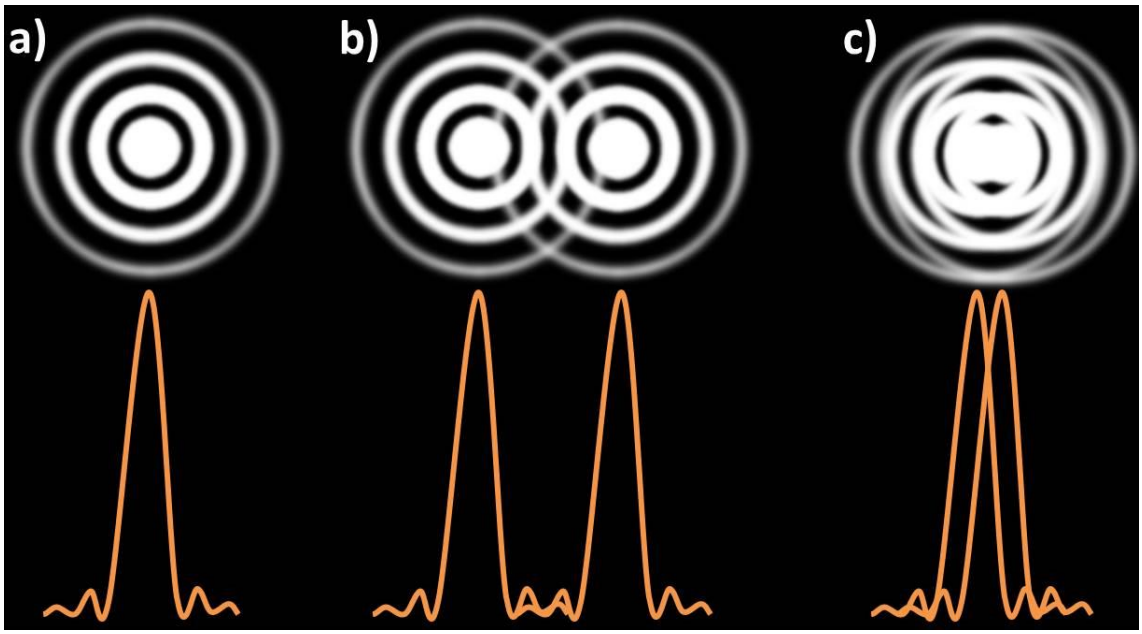

Figure 2.8 Airy disk pattern and resolution limit. a) Single Airy disk and below its 2D intensity distribution, when two emitters are detected within a distance their Airy disks are overlaid to different extents (b) they can interfere with each other through constructive interference, when emitters are close together their Airy disks are further overlaid and the peaks become unresolvable and are imaged as a single entity (c).

High NA objective lenses use an immersion oil to reduce the mismatch between refractive indices, thereby improving their ability to resolve smaller structures. These lenses exhibit a greater range of illumination and acquisition 'angles', obtaining higher spatial frequencies in

Fourier space. Higher NA lenses achieve higher spatial resolution as they gather more light from the wider angles of their light cone and can therefore define smaller point sources (Figure 2.9) as defined in Equation 8.

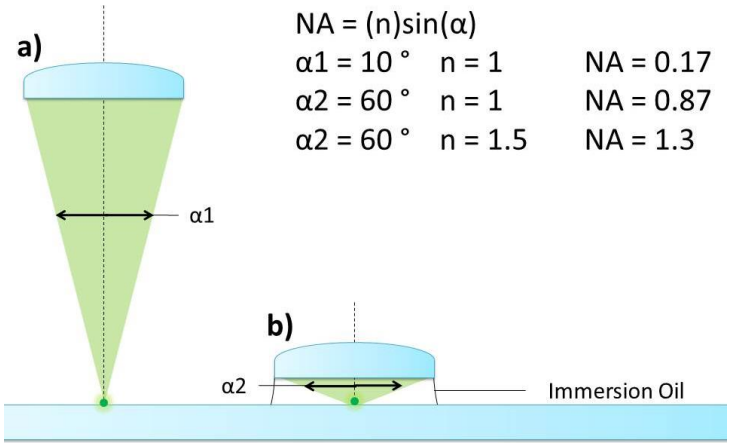

Figure 2.9 Numerical aperture (NA) of a lens. The number of angles a lens can collect photons from a point source is described by its NA, moving the lens further from (a) or closer to (b) the sample decreased or increases these angles; described as α, allowing more light to be collected, adding immersion oil which has a higher refractive index (n) than water also increases the NA.

This ability of a lens to distribute and collect light is known as the optical transfer function (OTF). The OTF is a Fourier transform of the PSF, (Figure 2.10), where images are broken down into component frequencies and phases with lower spatial frequency information towards the centre of the Fourier image and higher frequencies towards the periphery. When a PSF is represented by Fourier transform a circle is observed, with the circular edge of the OTF demonstrating the objectives cut-off frequency beyond which additional or higher information cannot be resolved. The OTF is defined as the ratio between specimen contrast (Equation 10; for a series of parallel black and white lines this would be considered regions of 100 % contrast) and image contrast as a function of spatial frequency, limited by the NA of the lens. The specimen contrast (modulation) is defined as:

$$Modulation = \frac{I_{max} - I_{min}}{(I_{max} + I_{min})}$$

Equation 10

Where I_{max} is the maximum intensity displayed from a repeating structure and I_{min} the minimum intensity found within the same specimen

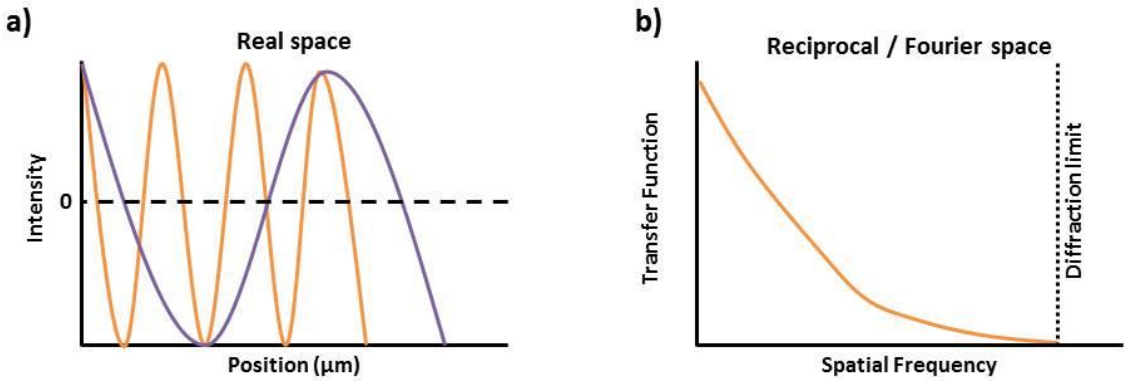

Figure 2.10 Optical transfer function (OTF) of a lens. When collecting non-coherent fluorescence through a lens a) Two profiles of high (orange) and low (purple) frequency information can be described in real space, b) the profile of summated component frequencies via Fourier transform, multiplied by the microscopes point spread function, creates the OTF, where the diffraction limit (dotted line) shows the frequency limit of the optical system. The lines profile characterises how efficiently each spatial frequency is transferred and thus how much contrast is preserved at each spatial frequency through the objective lens.

Enhancement of the spatial resolution of light microscopy can incorporate several strategies. For 3D widefield imaging these strategies can include post-acquisition deconvolution; reconstructing the sample based on the pre-determined PSF of the microscope allowing out-of-focus light from labelled structures to be correctly reassigned, improving signal-to-noise and therefore image contrast and resolution.

2.2.5 Labelling Density

When looking to optimise the imaging of structures, labelling density needs to be considered. This is described by the Nyquist-Shannon sampling theorem where continuous information is represented by discrete data; as with digital images representing a sample. This sampling is depicted in Figure 2.11 with the black dots representing detected fluorophores on the underlying sample (orange line). When sampling once per structure (Figure 2.11a) the reconstructed signal (purple line) represents an inaccurate depiction. To preserve the information, imaging at Nyquist sampling is usually set to twice the frequency of the structure (Figure 2.11b), thus, if a resolution of 20 nm is desired labelling is required every 10 nm. An increase beyond the Nyquist limit is described as oversampling, and is useful for super-resolution imaging of structural components such as actin fibres as a sample can be fully reconstructed from the increased information and reduced noise.

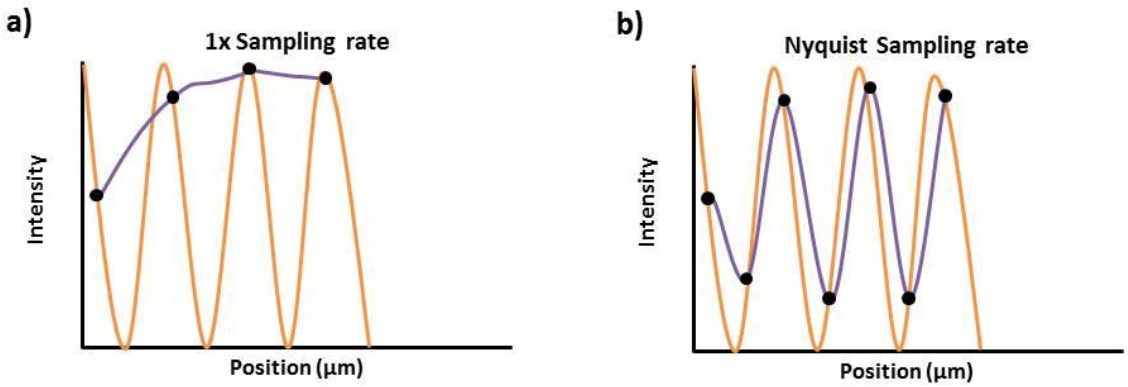

Figure 2.11 Nyquist sampling rate. Depicted are two scenarios: a) shows undersampling (purple) of a structure (orange) based on the Nyquist-Shannon rate while b) shows sampling at this rate of twice the spatial frequency of the sample - leading to a more accurate sample reconstruction.

2.3. Super-resolution microscopy

As resolution is a measure of the minimum distance two objects can be separated, dictated by the diffraction limit of light, any method that can circumvent this limit is said to contain super-resolution information.

2.3.1 Introduction of methods

'Super-resolution' improves the resolution of far-field light microscopy imaging beyond the diffraction limit. Most techniques allow researchers to gain access to molecular level details, permitting the imaging and organisation at nanometre resolutions. Modalities can be grouped by how fluorophores are detected, i.e. separated temporally, single molecule localisation microscopy (SMLM); including photoactivatable localisation microscopy (PALM, (Betzig et al. 2006)), direct stochastic optical reconstruction microscopy (dSTORM, (Heilemann et al. 2008), image reconstruction by integrating exchangeable single-molecule localisation (IRIS, (Kiuchi et al. 2015)), point accumulation for imaging in nanoscale topography, (PAINT, (Jungmann et al. 2014) or ground state depletion microscopy followed by individual molecule return (GSDIM, (Fölling et al. 2008). Alternatively fluorophores can be detected through spatial separation with structured illumination microscopy (SIM, (Gustafsson 2000)) and stimulated emission depletion (STED, (Hell & Wichmann 1994)). These techniques are summaried in Table 2.1.

SMLM relies on detecting and localising fluorophores that are fluorescing stochastically, through imaging fluorophores as they transition between S and T states of molecules, or through localising individual molecules as they transition between dynamic and bound states (Figure 2.12). These images are collected using a widefield system, usually with TIRF to improve the signal-to-noise ratio. Raw PALM, dSTORM and IRIS data all represent a series of diffraction limited images, each containing sparse subsets of fluorophores PSFs, the position of each emitter is localized by fitting a 2D Gaussian profile to this. Centres of mass are then

localised resulting in the pointillist dataset. The reported difference in resolution between these techniques (i.e. PALM reports improved 'resolution' compared to dSTORM) is due in part to the excitation wavelengths used for the probes. PALM excitation of 561 nm will achieve 200 nm resolution (for a 1.4 NA lens) compared with dSTORM excitation of 647 nm, achieving 231 nm resolution.

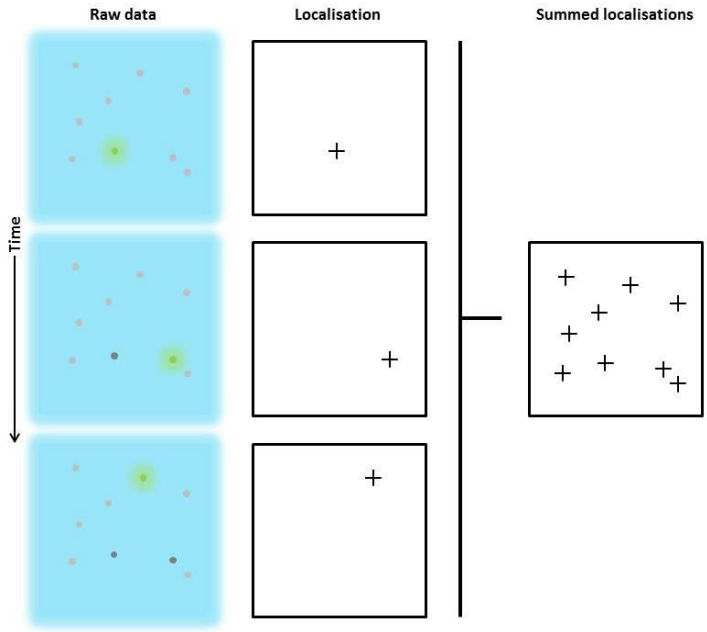

Figure 2.12 Concept of SMLM imaging. Raw data contains emission from only a sparse subset of fluorophores, these can then be localised frame by frame as different molecules are identified. Imaging continues until enough fluorophores are localised to be summed and form a representative final image of the sample.

STED microscopy is based on a confocal setup where a second (depletion) beam of a longer wavelength is tuned to selectively reduce the excitation spot below the diffraction limit. The depletion beam has a toroidal (doughnut) shape which drives neighbouring molecules into the S0 state by stimulated emission, the probability of a fluorophore switching between the S1 and S0 states is proportional to the power of the depletion beam (Harke et al. 2008). As users can tune the spot-size of their excitation beam below the diffraction limit by increasing the laser power the PSF of the microscope is reduced below the diffraction limit, while molecules within the toroidal beam return to the S0 state without being detected (Figure 2.13).

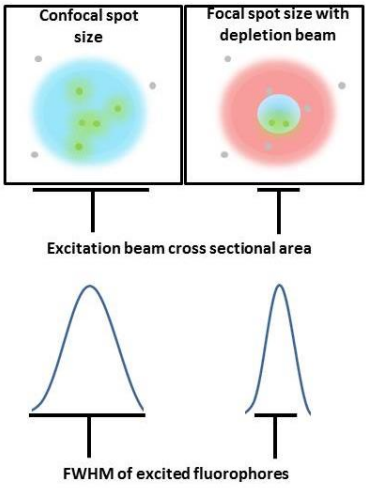

Figure 2.13 STED concept. STED imaging improves the spatial resolution of the microscope, compared to standard confocal imaging, with the addition of a second depletion beam. After initial excitation of fluorophores within the diffraction limited focal spot, the toroidal STED beam drives any excited molecules residing within its path into a nonfluorescing state. This essentially limits the size of the focal spot and therefore the resolution of the microscope.

Stimulated emission occurs when an excited electron interacts with a photon of a specific energy, forcing the electron into a lower energy state. Dropping into this lower energy state results in the release of a photon but of the same energy as the original 'depletion' photon; preventing the fluorophore from spontaneously relaxing and emitting fluorescence. This depletion beam was originally timed to pulsed at 250 ps after the pulsed excitation beam of 80 ps (Hell & Wichmann 1994) to allow depletion of the molecules surrounding the centre of the PSF, this is technically challenging both in terms of beam alignment, generation of the pulses with the correct timing and the high laser powers required (100 – 300 MW / cm^2). Therefore the technique was extended to use a continuous wave STED beam, which has the benefit of being less technically challenging and results in less exposure of the sample to high power pulses of light (Willig et al. 2007) but results in lower resolutions compared with pulsed-STED.

Due to the laser powers involved and the driven emission states required for STED imaging, all these methods rely on the fluorescent molecule possessing the ability to switch between states many thousands of times, giving them resistance to photobleaching. The STED library was further extended to use gated-STED, which can utilise the continuous wave excitation of the fluorophore (for improved resolution) or pulsed excitation (for reduced photodamage). This excitation is followed by a pulsed de-excitation beam and gated detection (Vicidomini et al. 2013). Gated- STED has the obvious disadvantage of reduced signal from the sample due to the gating and selective detection from emitted photons.

SIM imaging, like STED, structures the excitation light at the sample to access higher frequency information. This structured illumination is formed through a diffracting grid allowing the 1st order beams to be focused onto the sample, which due to constructive and destructive interference, creates areas of high and low illumination. As it is based on a widefield system with no pinhole, it has the advantage over STED and confocal imaging that no fluorescence information is rejected and lost. In the following sections the techniques used in this thesis are covered in greater theoretical and practical detail.

Table 2.1 Summary of super-resolution techniques

Imaging modality	Microscope system	Lateral resolution [Calculation]	Temporal resolution	Compatible probes	Original Reference
PALM	Widefield	10 nm (60 nm live cell) [Structure width]	25 s	Photoactivatable fluorophores	(Betzig et al. 2006; Shroff et al. 2008)
dSTORM	Widefield	20 nm [Object separation]	3 mins	Standard organic fluorophores	(Rust et al. 2006; Heilemann et al. 2008)
IRIS	Widefield	20 nm 50 nm resolution [Structure width]	≈ 10 minutes	Standard organic fluorophores	(Kiuchi et al. 2015)
PAINT	Widefield	< 10 nm / 16 nm [FWHM / object separation]		Standard organic fluorophores	(Jungmann et al. 2014)
GSDIM	Widefield	30 nm		Rhodamine and organic fluorophores	(Fölling et al. 2008)
STED	Confocal	106 nm / 160 nm (62 nm live cell) [FWHM / Object separation]	28 fps	Any (with ↑ photostability)	(Hell & Wichmann 1994; Westphal et al. 2008)
SIM	Widefield	$\frac{\lambda}{2}$ [FWHM]	1 – 2 fps	Any	(Gustafsson 2000)

2.3.2 SMLM

dSTORM utilises the blinking photophysics of fluorophores to temporally resolve sub-diffraction limited molecules via induced dark- and triplet-states. dSTORM offers advantages over other methods with the use a standard organic fluorophores which, compared with photoactivatable probes, have greater photostability and improved quantum yield; improving localisation precision due to an increase in the signal-to-noise ratio (see §2.3.3.).

By spontaneous and stochastic switching, of a subset of molecules in each frame are localised as they reside outside the diffraction limit of each other. As discussed in §2.3.1., 'blinking' arises from a fluorophores conversion into the dark-state by high power laser illumination and then held there in a stable off state ranging from milliseconds to minutes due to their local chemical environment. Modulating this environment can photoreduce organic fluorophores used with dSTORM (e.g. Alexa Fluor and ATTO dyes), for example in the presence of an electron donor like cysteamine-hydrochloride (MEA), fluorophores are quenched from the excited state to the dark states before the release of a photon (Figure 2.14).

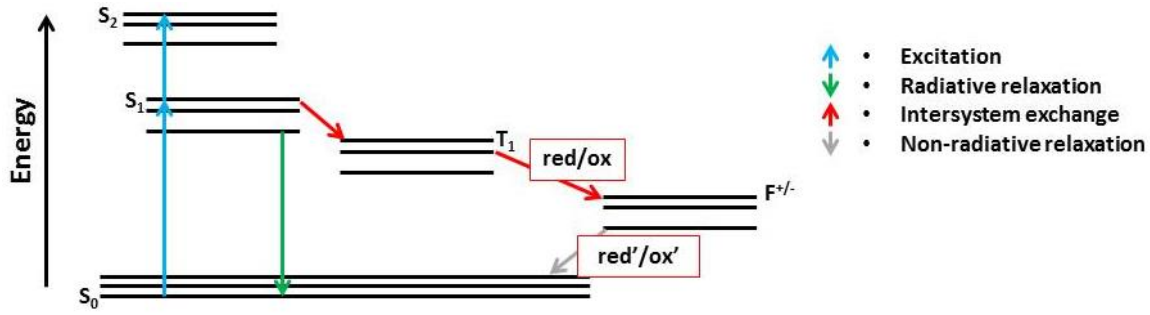

Figure 2.14 Extended Jabłoński diagram with fluorophores in the presence of a redox buffer. As before fluorophores can enter higher energy states through excitation by a photon. When decaying via the highly reactive triplet state in the presence of a redox/glox buffer it is rapidly depleted by reducing or oxidising agents respectively forming a radical cation or anion ($F^{+/-}$). These states are then depleted by the remaining reducing or oxidising agent; leading to S0 recovery.

By reducing the density of detectable molecules and allowing photons from single emitters to be captured (Figure 2.15), these localisations are used to build up and image over time, reconstructing the underlying structure.

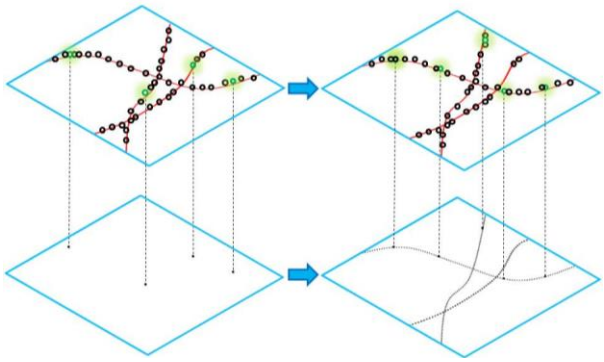

Figure 2.15 STORM concept After labelling the sample, a sparse subset of these fluorophores are localised in each frame, over time this leads to a complete map of the structure being built up through plotting these molecular positions to form the final image.

Fluorophore switching speeds and photostability are influenced by pH and oxygen levels within the imaging buffer environment and must be stabilised to ensure a limited number of fluorophores are emitting per image frame (Dempsey et al. 2011). As oxygen is the primary source of photobleaching in fluorophores through free-radical build-up or direct interaction, lowering reactive oxygen levels through glucose oxidase (GLOX) and catalase can reduce free-oxygen in the imaging media through conversion to gluconic acids (Ha & Tinnefeld 2012) therefore extending fluorophore lifetimes (Aitken et al. 2008; Ha & Tinnefeld 2012).

In contrast to STORM, PALM (Betzig et al. 2006) requires no imaging buffer to localise sparse fluorophores, instead utilising fluorophores with photoactivatable properties, such as photoactivatable- (PA-)GFP (Patterson 2002). These molecules reside in an inherently dark-state but are rendered sensitive when illuminated by a specific wavelength of light (e.g. 405 nm), they can then be excited and imaged as normal with (for PA-GFP 488nm) excitation light. To maintain the sparse population of fluorophores for SMLM reconstruction methods the activation laser is kept low and turned on for a short period of time so only a subset of molecules are stochastically switched on. Additionally the excitation light is turned up high, so activated molecules are irreversibly bleached, reducing fluorophore signal density within each image frame.

IRIS also requires no imaging buffer to localise sparse fluorophores, relying on the transient binding of protein fragments (Figure 2.16). At nanomolar concentrations this creates a raw dataset akin to other SMLM techniques. As the probe transiently binds for set periods of time before dissociating from its target back into the imaging solution, the same protein can be tagged and imaged multiple times, limiting its use as a quantitative tool to specific situations (Jungmann et al. 2016) but improving its use for structural imaging as Nyquist sampling conditions are easily met. As the probe is not fixed onto the sample or required to be

photobleached there is a larger supply of the probe making it more practical for longer imaging periods.

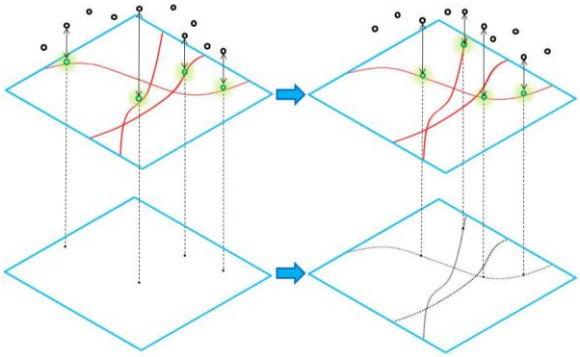

Figure 2.16 IRIS concept. Unlike PALM or STORM where the structure is labelled, with IRIS the label resides in solution and transiently binds to the structure. When the frame rate of acquisition is matched to the binding time of the probe, bound molecules are visualised above the background of suspended probes which follow Brownian motion.

An advantage of IRIS imaging is that any fluorescent probe can be attached to the protein fragment as localisation is not dependent on fluorophores photophysics for blinking, so blue-shifted fluorophores can be used to free the red-shifted channels usually favoured by probes for dSTORM imaging. Additionally, as the localisation of sparse bound probes reside in solution there is a greater stock of fluorophores for acquiring information over time, this allows the concentration of the probe to be easily changed and optimised for different samples based on the density of the protein of interest. The suspension based probe also allows it to be washed out so it can be replaced with a different probe for serial acquisitions. The longer acquisition times also allow for more selective filtering so only the best localisations form the final image; which improves the resolution of the imaged structures. The main disadvantage of the technique is the availability of probes to specific targets, which is still limited. There is also difficulty in quantifying images due to the possibility that probes may bind multiple times to the same targeted protein; essentially mimicking the multiple blinking issues when quantifying STORM images.

2.3.3 SMLM reconstruction

Point sources of light imaged by a microscope are represented as a fixed PSF or Airy pattern, to extract their true positions each fluorophore must be individually localised. Images captured by a camera are pixelated (Figure 2.17a), therefore emitters are localised down to nanometre scales by analysing how the intensity spread over multiple pixels (Figure 2.17b). For example an emitter positioned exactly in the centre of a pixel will result in a near symmetrical decay of intensity in neighbouring pixels, while any asymmetry in pixel intensities will be due to the

emitters position away from this 'centre pixel'. This allows emitters residing within the diffraction limit of each other to be precisely localised (Figure 2.17c).

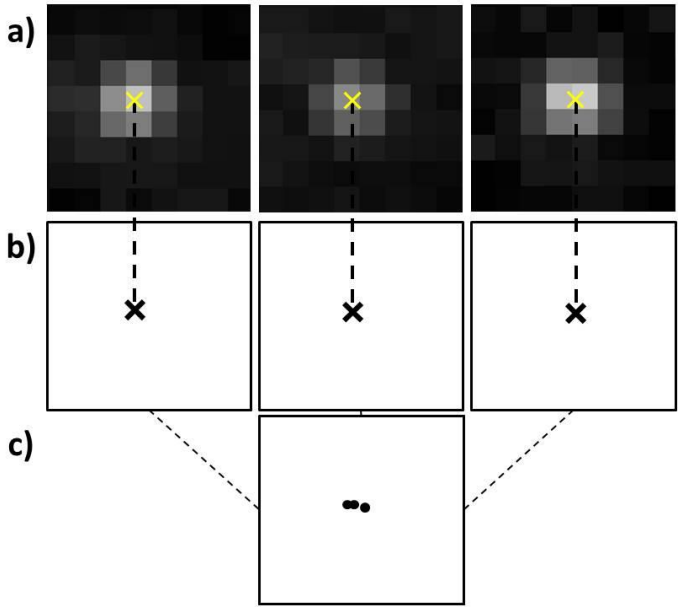

Figure 2.17 Nanometre localisation of emitters through pixel intensities. a) Raw data of single emitters overlaid with yellow crosses for approximation of molecule positions. b) These co-ordinates can be extracted from the raw data and (c) plotted to create a pointillist dataset, with diffraction-unlimited localisation precision.

To localise enough fluorophores to build up a representation of the sample many thousands of frames are required, as each frame must contain emitted photons from fluorophores residing outside the diffraction limit of each other. Molecules can be localised to nanometre precisions (depending on background levels, Figure 2.18) based on recording emitted photons, as each photon is an independent reporter of the fluorophores spatial position (x_t, y_t) multiple photon positions are recorded to build up a distribution over time (Figure 2.19). The more photons collected from each emitter increases the precision with which each centre of mass can be calculated.

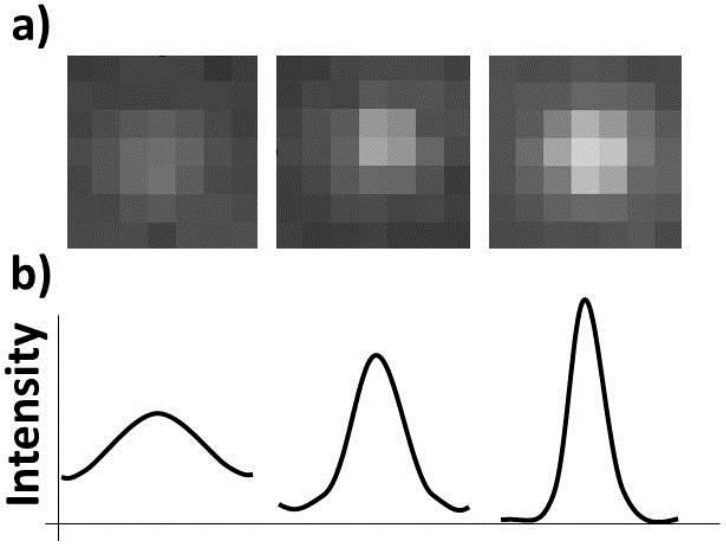

Figure 2.18 Photons collected from emitters modify localisation precision. a) Compared to background levels the number of photons (brightness) from each emitter influences the intensity distributions (b) leading to the strength of the Gaussian generated and therefore the localisation precision.

These positions are then fitted, usually to a curve based Gaussian function to establish the centre of mass. The localisation precision of each emitter (Equation 11) is given as the spread of estimates $x_{t,s}$ and contains a level of uncertainty and can be defined as the standard deviation (σ_x):

$$\sigma_x = \sqrt{\frac{1}{n-1}\sum_{i=1}^{n}(x_{t,s} - \bar{x}_t)^2}$$

Equation 11

Where *n* is the number of estimates or detected photons.

As mentioned above, high quantum efficiencies (the probability for a specific fluorophore to emit a photon upon excitation) links directly to the ability to localise the centroid of molecules (Thompson et al. 2002), in zero background conditions this can be calculated from Equation 12:

$$\Delta x = \frac{\sigma}{\sqrt{N}}$$

Equation 12

Where Δx is localisation precision, σ the standard deviation of the (PSF) and N is the number of collected photons

However imaging data contains noise (signal originating from either the background [out of focus light] or shot noise from the camera), which reduces the precision of this localisation. Thompson et al. (2002) considered these two factors to generate Equation 13:

$$((\Delta x)^2) = \frac{\sigma^2 + \frac{a^2}{12}}{N} + \frac{4\sqrt{\pi}s^3b^2}{aN^2}$$

Equation 13

Where *a* represents pixel size, *s* the shot noise and *b* the background noise.

Precision can also be expressed as the full width at half maximum (FWHM) of a detected localisation (Equation 14), expressed as the standard deviation (σ_x) of these:

$$FWHM = 2\sigma\sqrt{2\ln(2)}$$

Equation 14

Localisation precision is spread due to factors beyond the acquired photon counts, these added variables include the background noise from out-of-focus fluorophores, the pixel size of the camera, sample drift, and PSF deformation (such as with refractive index (RI) differences) and label displacement (Figure 2.19). After localising each fluorophore in the dataset it is possible to represent these using the list of x, y co-ordinates to generate a pointillist image.

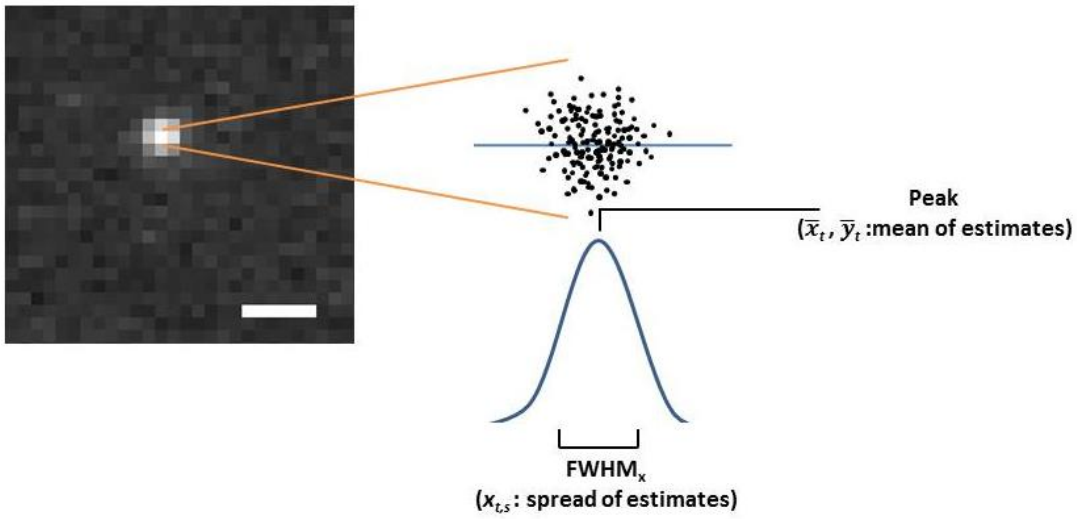

Figure 2.19 Localisation precision of a single emitter. Insert is a raw image showing the fluorescence of a single emitter during SMLM imaging (Scale bar = 1 µm). Each black spot to the right of the image represents individual localisation estimate over multiple frames, after calculating the spread of estimates and fitting a Gaussian peak to this data a centre of mass for the molecules position can be calculated.

Raw pixelated data stacks (Figure 2.20a), are improved by localisation methods, a qualitative example of this improvement is to compare to summed images of the entire data stack (Figure

2.20b). Localisation methods output *x, y* coordinates which each represent the estimated position of a detected fluorophore. These can then be plotted to give a pointillist, reconstructed image (Figure 2.20c).

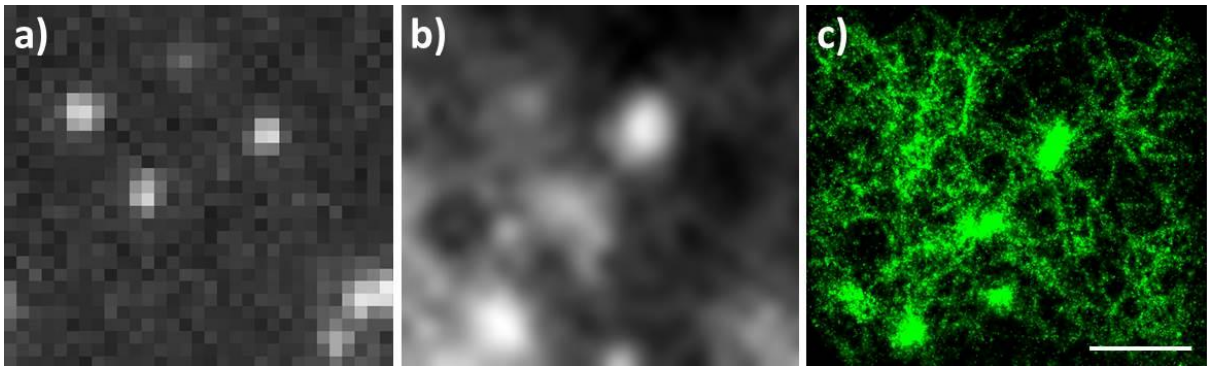

Figure 2.20 SMLM image reconstruction. After collecting an image stack of sparse emitters (a), these can be represented as an average intensity projection (b) to approximately demonstrate the diffraction limited data, or - through reconstruction software- as a pointillist image (c) where each point represents the localisation of a single emitter. Scale bar = 1 µm.

2.3.4 SIM & SIM-TIRF

While imaging in fixed cell has been achieved using STED microscopy, including within the context of F-actins reorganised within the NK cell synapse (Rak et al. 2011) it is known that signalling proteins and cellular events are modulated not only spatially but temporally. As such live-cell super-resolution microscopy was developed to map processes through time, the importance of live-cell imaging was apparent when investigating the role of actin during vesicle trafficking to the plasma membrane as covered in §1.5.5. (Wollman & Meyer 2012).

As discussed earlier most live-cell super-resolution techniques are based around the spatial separation of fluorophores. SIM was realised around the millennium (Heintzmann & Cremer 1999; Gustafsson 2000). When coherent light is diffracted through a grating pattern (Figure 2.21) it interacts with itself, causing structured illumination at the sample through constructive and destructive interference. In standard SIM imaging three beams are focused at the sample, the 0^{th} and 1^{st} order diffraction beams, this creates a chessboard pattern of high and low intensities within x, y and z planes.

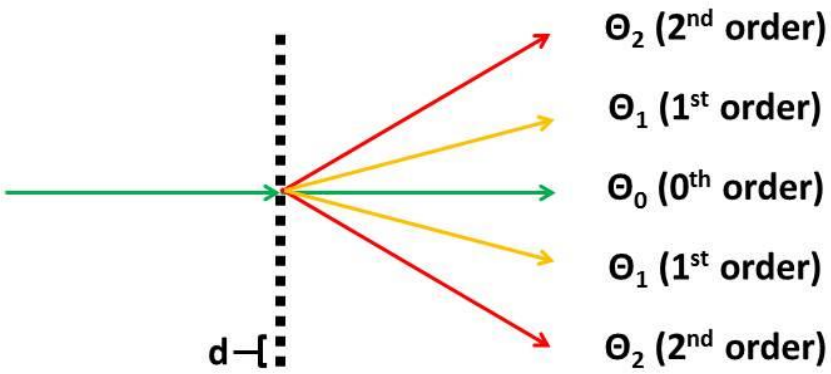

Figure 2.21 Diffraction of coherent light through a diffraction grating. When a coherent light source is incident onto a diffraction grating with the distance (d) between the elements matched to the wavelength of light used, diffraction occurs. Here a single point of the incoming wave is shown, when an incoming wave diffracts through the grating intensity is modulated due to constructive and destructive interference of the beam.

Diffraction gratings are described through Equation 15; these are patterned with regular components to generate a diffraction pattern:

$$m\lambda = \mathrm{d}(\sin\theta_m + \sin\theta_i)$$

Equation 15

Where θi is the light incident angle, d the distance between elements of the grating pattern (see Figure 2.21), and θm is the order number (i.e. θ_0).

As with TIRF, TIRF-SIM is based upon translating a laser beam up the side of the objective so it is incident upon the coverslip – sample interface, beyond the critical angle. However as there are two 1st order beams, one travelling up either side of the objective, they counter-propagate, interfering with each other constructively and destructively at the sample, creating an evanescent wave which follows a sinusoidal pattern (Figure 2.22a).

A polarizer is used and rotated with the diffraction grating to maintain *s* polarization for maximum pattern contrast. The resulting sinusoidal pattern is described in Equation 16, and represents a high contrast periodicity of around 200 nm for 488 nm light. Contrast is enhanced when using the TIRF configuration as the signal is limited to the 75 – 100 nm evanescent wave, TIRF-SIM is also light-efficient as 80 % of the laser power is diffracted into the 1st order beams and no light from the sample is rejected by a pinhole, as it uses a widefield setup.

Due to the high-frequency periodicity of the illumination light overlaid with the sample, the result is a downmodulation of the image, known as Moiré fringes (Figure 2.22b). These represent regions of higher spatial frequency, generating a lower spatial frequency in the overlap.

$$I(r) = I_0(1 + \cos[k_0 \bullet r + \varphi])$$

Equation 16

With k_0 representing the radius of the OTF support region in Figure 2.23a and ϕ the illumination pattern phase. Much of the following is explained more intuitively in Fourier space, with images transformed from real into reciprical or frequency space through Equation 17:

$$F(\omega) = \int_{-\infty}^{\infty} f(t)e^{-i\omega t}dt$$

Equation 17

Where t is the variable time in seconds, F is the Fourier transform of the function.

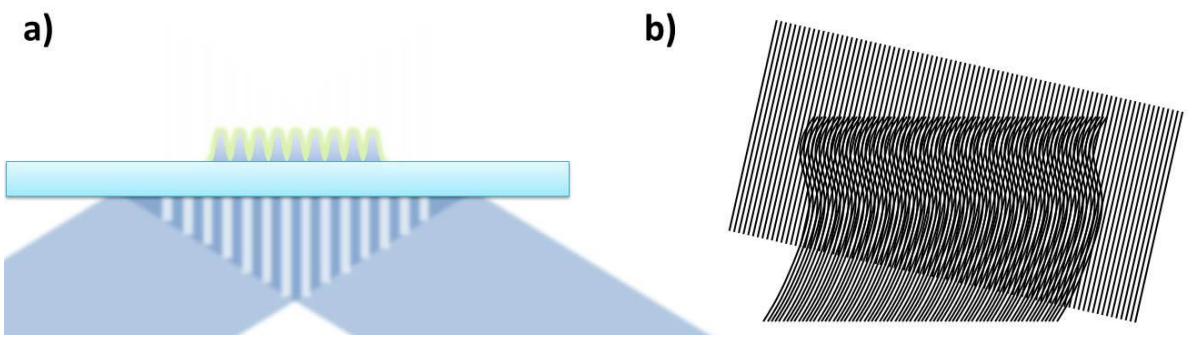

Figure 2.22 Structures illumination and Moiré fringe concept. a) Two opposing 1st order beams constructively and destructively interfere with each other; by insuring TIRF conditions are met this interference extends to the evanescent wave at the coverslip-sample interface, generating a sinusoidal illumination pattern. b) When this high-frequency pattern is overlaid onto a fluorescent sample containing high-frequency information, this is down modulated to lower-frequency information in the form of Moiré fringes.

If the illumination pattern is known the unknown underlying structure (i.e. the distribution of fluorescing molecules) can be mathematically recovered from these (Equation 18). For example the fluorescence emission (E) in real space (r) is determined by:

$$E(r) = (D[r] \bullet I[r]) \otimes PSF(r)$$

Equation 18

Where D(r) is fluorophore concentration and all are convolved (⊗) by the PSF. Taking the Fourier transform of this function creates Equation 19:

$$\tilde{E}(k) = \left(\tilde{D}[k] \bullet \tilde{I}[k]\right) \otimes OTF(k)$$

Equation 19

As mentioned in §2.2.4 the OTF of a lens is limited by it NA and is therefore a fixed value, where higher spatial frequencies cannot be collected. However as Moiré fringes are coarser than the underlying sample or illumination pattern, their spatial frequency is shifted into the support region (or OTF) of the objective lens and detected due to frequency downmodulation (Jost & Heintzmann 2013). The higher resolution information within these fringes is mixed with the lower frequency information and can be retrieved after reconstruction to create an image with twice the resolution of standard widefield microscopy. SIM is limited to halving the diffraction limit using linear methods as the formation of the structured illumination pattern is still required to pass through the objective lens, meaning the periodicity is still limited by diffraction.

This limit can be overcome by using nonlinear methods such as saturated SIM (SSIM); here concepts follow that of STED microscopy as fluorophores switch between S and T states. Unlike STED however fluorophores are illuminated with a non-Gaussian illumination pattern (hence saturated SIM). This leads to finer illumination patterns, introducing higher Fourier frequencies and displaying a sharper contrast. The lateral resolution is improved due to much finer Moiré fringes; sub-50 nm resolutions have been achieved using both polystyrene beads and live samples (Rego et al. 2012; Li et al. 2015) though like STED this technique can theoretically offer unlimited resolution improvement.

When represented in reciprocal or Fourier space a sinusoidal pattern is described as three circles (the origin and the direction; Figure 2.23b) with the distance from the origin being proportional to the line spacing of the striped pattern. If the illumination pattern is half the wavelength of light used then these points will reside at the edge of the lenses OTF (Figure 2.23c). When describing spatial frequencies in Fourier space it is termed k-space (Equation 20) giving the maximum observable resolution.

$$k_0 = \frac{\lambda}{2NA}$$

Equation 20

SIM imaging at frequency k_1 results in the sum and difference frequencies $k + k_1$ and $k – k_1$ (the constructive and destructive Moiré fringes), effectively increasing the OTF of the lens from k_0 to $k_1 + k_0$ (visualised as black dots peripheral to the lens OTF in Figure 2.23c). This gives a new resolution limit of $2k_0$ translating to double the resolution limit of the microscope, but in a

single direction corresponding to the orientation of the grating pattern. To gain isotropic resolution enhancement the diffraction pattern is shifted by a third of the period ensuring the sample is uniformly illuminated by the end of the three lateral shifts, with three 120° rotations filling in the missing information beyond the OTF's support region for each orientation.

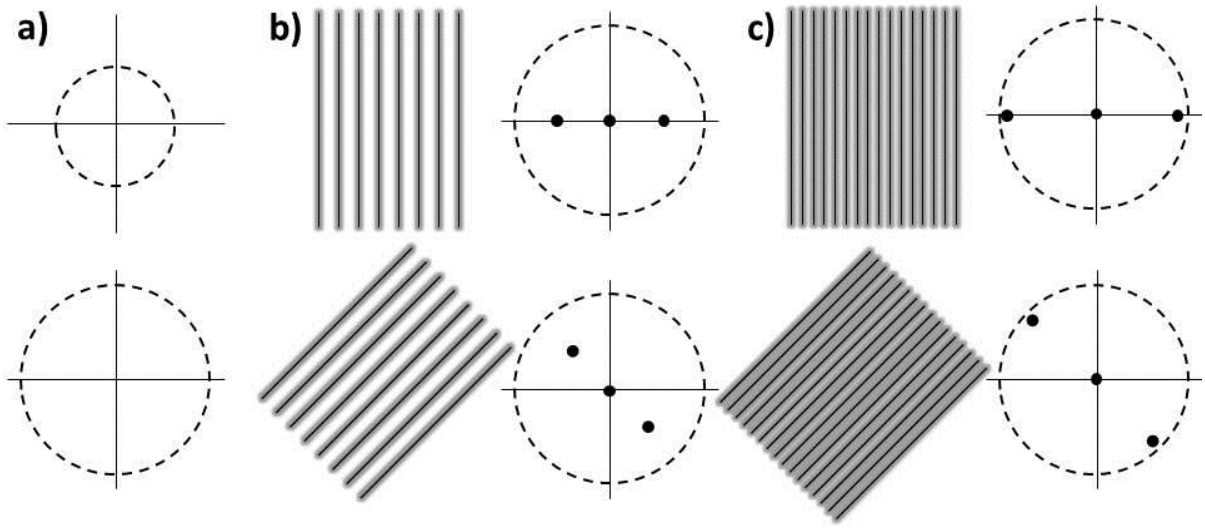

Figure 2.23 Optical transfer functions in reciprocal space. OTF profiles of a low NA objective (a, top) versus high NA objective (a, bottom), b) and c) depict how a sinusoidal patterns orientation and frequency is characterised (black dots). These describe the origin and frequency of the pattern and can be used to describe more complex images such as a fluorescent sample.

2.3.5 SIM reconstruction

Image reconstruction occurs after processing the nine raw images to extract the three information components; the resulting image contains data extending beyond the OTF of the lens.

As pixel intensity is proportional to the fluorophore concentration and the known sinusoidal or standing wave illumination pattern, the Fourier transform corresponds to three peaks, resulting in three Fourier-derived objects. Two of these peaks are displaced or downmodulated in Fourier space, allowing them to enter the OTF of the lens and form part of the raw image. This allows higher resolution information to be extracted and shifted back to their original positions, after an inverse Fourier transform this creates an image containing previously unattainable information (Figure 2.24).

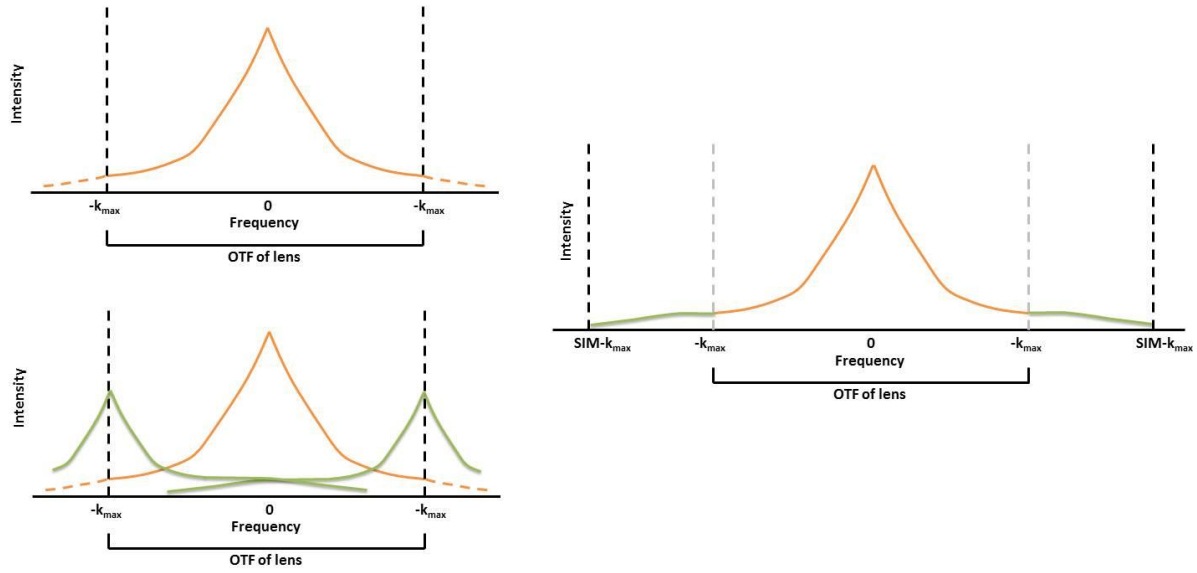

Figure 2.24 Lateral resolution enhancement. When structured illumination of sample information (orange) is described in Fourier space, additional information (green) is also present at the 1st order positions, providing additional higher frequency information within the OTF support region, after reconstruction this essentially extends the resolution (right) by reassigning this information back to its original position.

Image data is Fourier transformed before a cross-correlation is applied to estimate the constant direction of the grating before the components are separated and shifted to their original positions in the image.

2.3.6 Correlation approaches

How cells co-ordinate sites of heterogeneity such as the plasma membrane is not fully understood. But the implications are thought to be important for processes such as signalling efficiency; including that at the immunological synapse.

Correlative methods, unlike tracking methods (such as speckle tracking; (Watanabe & Mitchison 2002)) do not rely on identifying and following individual fluorophores through time and space. As such correlative spectroscopy offers tools for capturing molecular transportation, diffusion and interactions, in densely labelled samples where signal from multiple fluorophores overlaps. Correlative techniques do not therefore rely on selective labelling strategies; while tracking requires labelled molecules to be sparse enough for software to identify and trace individual paths.

By using pixels as reporters of fluorophore density, correlating these intensity fluctuations over time and/or space provides information on speed and/or directionality of labelled molecules. ROI's or times of interest (TOI's) are selected to extract information on the direction and speed of fluorescent markers, tagged to molecules of interest. Correlation techniques include

fluorescent correlation spectroscopy (FCS; (Magde et al. 1972)), particle image velocimetry (PIV; (Grant 1997)) and image correlation spectroscopy (ICS; (Petersen et al. 1993)). The techniques share a basic workflow, where fluorescent signal is captured through time and correlated either through time, space or both to extract information. For example FCS was originally used to demonstrate DNA-drug binding and investigating protein interactions and membrane dynamics (Wawrezinieck et al. 2005), while ICS has been used to study the distribution of membrane receptors (Petersen et al. 1993).

Classically, FCS utilises a static detection volume, exciting the sample with a confocal based illumination (Figure 2.25a). Fluorescent fluctuations are measured as intensity peaks from fluorophores moving in and out of the excitation volume. As the illumination volume can be moved to any area of the sample, measurements can be made in 3D space, with laser powers orders of magnitude less than fluorescence recovery after photobleaching (FRAP) experiments and with temporal resolutions ranging from microseconds to minutes.

Recorded datasets are analysed via an autocorrelation (Equation 21), where the intensity reading *I* at timepoint *t* is compared with a timelagged intensity reading *τ*. The resulting output autocorrelation defines recorded intensity similarities over time.

$$G(\tau) = \frac{(\delta I[t]\delta I[t+\tau])}{(I[t])^2} = \frac{(I[t]I[t+\tau])}{(I[t])^2} - 1$$

Equation 21

Where *G(τ)* is the correlation function and *δI[t]* is the intensity deviation about the mean. The denominator here is the most commonly used as it is normalized, meaning the correlation at τ = 0, G(0) is the initial autocorrelation amplitude and is inversely related to the number of particles within the excitation volume. Correlated data can then be fitted to a nonlinear least squares algorithm; such as the Levenberg-Marquardt algorithm in Equation 22:

$$x_v^2 = \frac{\sum_i([y(x_i) - y_i]^2/\sigma_i^2)}{v}$$

Equation 22

Where $y(x_i)$ are the fitting values, y_i are the data point values and σ_i is the standard deviation of point *i*. *v* is the number of significant datapoints which equals the number of free parameters. The nanoscale dynamics of the data can then be determined by the distribution of the curve; standard Brownian motion subjected to thermal diffusion is given by the autocorrelation curve of Equation 23:

$$G(\tau) = G(0)\frac{1}{(1+\left[\frac{\tau}{\tau_D}\right])(1+\beta^{-2}[\frac{\tau}{\tau_D}])^{\frac{1}{2}}} + G(\infty)$$

Equation 23

Where β is the axial to radial ratio of the observation volume given by the PSF of the system, and τ_D is the average molecular dwell time. $G(\infty)$ is the subsequent correlation amplitude after long lags. τ_D can be used to recover the diffusion coefficient using Equation 24:

$$D = \frac{\omega_{xy}^2}{4\tau_D}$$

Equation 24

Where ω is the area of interest (i.e. the illuminated regions). In cases where diffusion is non-Brownian Equation 25, the anomalous diffusion coefficient α becomes a free function as mean squared displacement is no longer proportional to time:

$$G(\tau) = G(0)\frac{1}{(1+[\frac{\tau}{\tau_D}]^{\alpha})(1+\beta^{-2}[\frac{\tau}{\tau_D}]^{\alpha})^{\frac{1}{2}}} + G(\infty)$$

Equation 25

After correlating the intensity of the signal at timepoint t with various time scales ($t\Delta$), the correlation function (CF) can be plotted to show correlation times and diffusion coefficients depending on the shape of the correlation curve. For example where slower diffusion is present, the curve will shift rightwards as signal is correlated for longer through time (Figure 2.26).

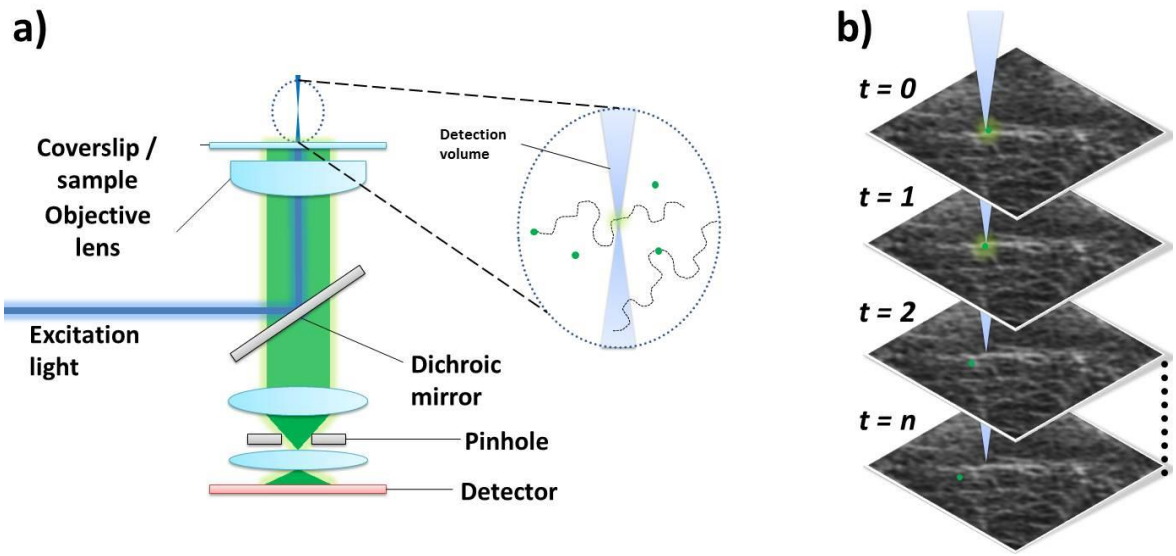

Figure 2.25 Fluorescence correlation spectroscopy set-up and temporal correlation concept. a) The detection volume of FCS is determined by the PSF of the microscope, usually the beam is set to a fixed position within the sample as fluorescent molecules enter and exit the excitation path (b), resulting in fluctuations of detected fluorescence and a temporal correlation.

Until now FCS has been described when imaging diffusion in 3D space, however when imaging confined diffusion such as within the plasma membrane, considerations must be made for events close to a refractive index boundary such as the coverslip-sample interface. The detection volume will be susceptible to deviations, which must be characterised before measurements are made. Characterisation and calibration of the correlation curve is made using a reference dye of a known concentration in solution or by using a known diffusion coefficient, both of which are dependent on temperature.

Due to the static nature of the observation point, FCS suits fast moving molecules that enter and exit this focal point freely. As the illumination volume is described by the PSF of the microscope this volume is reduced when using a high NA lens; however it remained diffraction limited until a recent extension of FCS was reported, incorporating a STED beam (Honigmann et al. 2014). This allowed the beam to be tuned below the diffraction limit for super-resolution detail of nanoscale dynamics at the plasma membrane. However this set-up is demanding, in terms of physical alignment, correct analysis and with the stresses placed on the sample; as with STED microscopy depletion laser powers must be higher to tune the excitation volume down to the desired size.

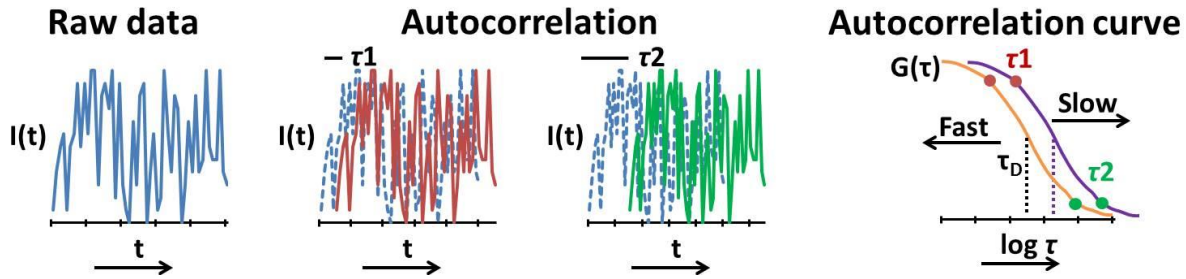

Figure 2.26 Auto-correlation analysis of FCS data. Correlating the intensity fluctuations of the raw data with itself over shorter time lags (τ1) gives a higher correlation while longer time lags (τ2) will exhibit reduced correlation. Once the correlation function (G(τ)) is plotted over time (autocorrelation curve), the point at half the maximum amplitude gives the correlation time τ_D (dotted black line). Depending on the speed of molecular diffusion this curve will remain correlated to the reference image for shorter timelags (faster diffusion, orange line) or longer (slower diffusion, purple line).

All FCS techniques above temporally correlate datasets, to extend FCS for spatial analysis a scanning detection beam is used to study the spatio-temporal dynamics of membranes (Ruan et al. 2004). The outputs from these experiments resemble kymograph scans with the x axis representing the path of the beam (usually a circle) and the y axis plotting multiple passes, hence they are referred to as 'carpets' of fluorescence intensity.

Correlating 2D data can also be achieved with PIV and ICS methods, which provide net flow speed and/or directionality, in PIV this is achieved by raster scanning an image at time t*n* over image t*n+1* to deduce pixel similarities. Where the correlation is highest (i.e. the structure is identified) object displacement between the two images is found, a vector is then generated to characterise these flow dynamics (Figure 2.27).

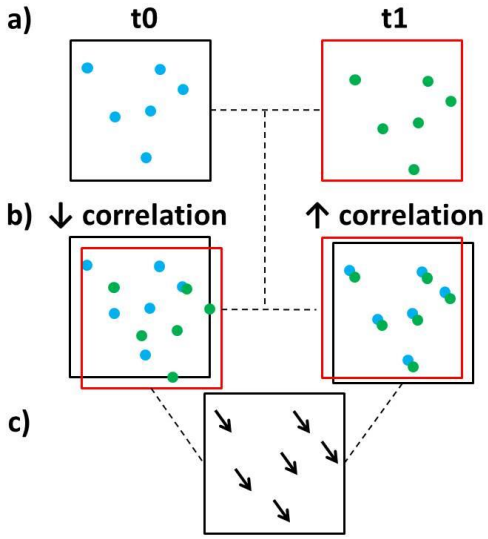

Figure 2.27 Schematic of Particle Image Velocimetry (PIV). a) Two images are taken of a sample containing detectable molecules, such as fluorophores. b) these two images are overlaid and translated to establish which shift generates the highest correlation. c) From this analysis vectors of each 'interrogation window' can be plotted, showing flow direction and speed based on the correlations lateral displacement.

PIV was originally developed for imaging fluid dynamics containing 'seeded' molecules; through illumination of a sample using a sheet of light these seeds were correlated to produce an estimate of the samples kinetics. As PIV it essentially a pattern-matching approach it relies on both the structures maintaining their shape when translating through space, and also on the signal translating across the detectors; (i.e. not moving through the z plane). Both PIV and ICS rely on sufficient signal from the sample, requiring the observation 'window' to be large enough to contain adequate spatial information for a reliable correlation of fluorescent intensity above noise.

ICS encompasses a series of techniques for detecting fluorescence and correlating pixel intensity in space or time. Originally extended from scanning-FCS to widen the correlative power through *x, y* space (Petersen et al. 1993) this technique can use confocal or widefield modalities, with the latter possessing the advantage of sampling faster for larger fields of view compared to scanning methods. ICS also has the advantage of sampling and correlating signal from entire fields of view (Figure 2.28); making this method more suited to studying larger events and slower or quasi-static diffusive populations. Compared to speckle tracking, ICS has no issues with shorter lifetime events as it does not track individual speckles but the fluorescent signal as molecules flow within ROI's. This does mean however it may miss subtleties of nanoscale molecular events.

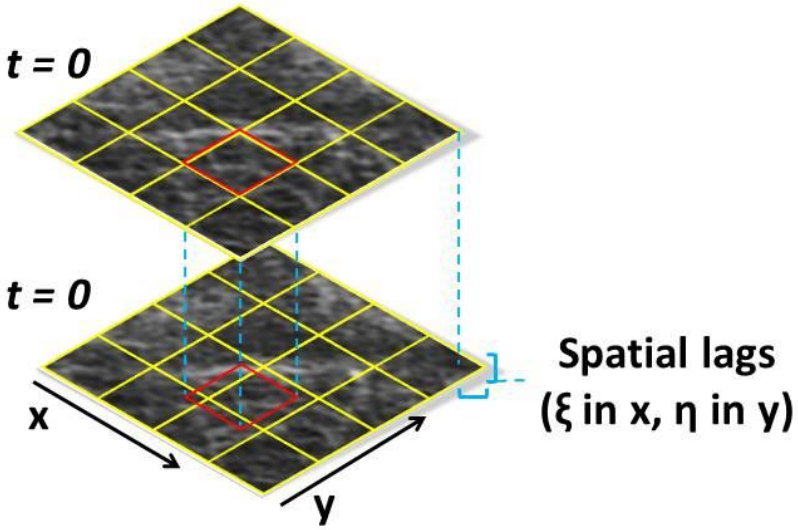

Figure 2.28 Spatial correlation of imaging data. Correlation of a dataset with itself (autocorrelation) at timepoint t will yield perfect correlation; by shifting the second image relative to the reference image by ξ and η results in a spatial correlation.

ICS measurements correlate fluorescent fluctuations (δi; Equation 26), defined as the difference of pixel intensity in time and space against the mean:

$$\delta i_a(x,y,t) = i_a(x,y,t) - [i_a]$$

Equation 26

Where δi signifies the difference between pixel intensity at a single point in space and time versus the mean intensity, a indicates the channel and $[i_a]$ the average. This mean can define a spatial mean of a region of interest or a temporal mean for a single pixel through time.

As with most imaging modalities, sampling at the Nyquist-Shannon criteria is recommended, with good signal-to-noise for detected molecules and analysing photostable emitters over longer time courses; as bleaching reduces the signal which can be used for correlation. ICS correlates signal within a subregion of interest; as such the sampling time must be fast enough to capture flow while they remain within the ROI.

2.3.7 STICS, STICCS

One limitation of the FCS and ICS techniques are their insensitivity to flow direction, by incorporating correlation of fluorescence fluctuations temporally as well as spatially both flow speed and directionality of molecular populations can be quantified, can generated for cellular length scales. Spatio-temporal ICS (STICS; (Hebert et al. 2005)) builds on previous techniques by calculating flow velocities and diffusion through temporal correlation and directionality through spatial correlation. STICS correlates the similarity of pixels in comparison to

neighbouring pixels, by correlating pixels in space through time this provides flow directionality and velocity.

STICS cross correlates pairs of images separated by time interval τ. An increasing width through time of the Gaussian shaped CF peak is an indicator of diffusion while translation of the peak demonstrates flow. The STICS CF is given in Equation 27:

$$G_{STICS}(\xi,\eta,\tau) = \frac{(I[x,y,t]I[x+\xi,y+\eta,t+\tau])}{(I[x,y,t])^2} - 1$$

Equation 27

After a ROI is selected the dataset is analysed to produce a space-time CF stack; showing spatial correlation as a function of time. This output depends on the nanoscale dynamics and fluorophore photophysics, with spatial fluctuations arising from variations in fluorophore concentrations in space while temporal fluctuations are detected as variations at a single point over time. For zero time lag (τ = 0) each image autocorrelates with itself spatially (Figure 2.29, left; Equation 28), with the maximum intensity distribution at zero spatial lags, displaying a Gaussian (as this is the PSF profile of the microscope system).

$$r_a(\zeta,\eta,\tau) = 0$$

Equation 28

Where r_a = detected channel, ζ and η = spatial lags and τ = time lags.

As immobile objects remain at the centred location, with amplitude determined by their density, they can obscure mobile objects if the acquisition has limited τ (Figure 2.29, middle). These immobile and diffusive populations can be filtered out either by removing Fourier frequencies associated with these static populations or using an immobile object filter which employs a user defined sliding TOI through the data stack, removing any fluorescent population static for this time period.

To form a high and smooth CF within each subregion, the correlation relies on multiple signal fluctuations, this represents a trade-off between correlating a high (or low) number of molecules per subregion to generate the CF within < (or >) minute length timescales. As such it remains advantageous to image for prolonged periods of time to ensure improved characterisation of the correlated flowing population.

Datasets with longer time lags (τ > 1) evolve different CF's over time (τ0 to τ2 ≠ τ0 to τ3). For detected flow the CF $r_a(\zeta,n,\tau)$ is fitted to a Gaussian peak using nonlinear least-squared methods (Petersen et al. 1993). These peaks then translate from the zero spatial lags (central)

origin as a function of time (Figure 2.29, right). This can be represented as a vector map demonstrating the speed and directionality of this flow (Figure 2.30).

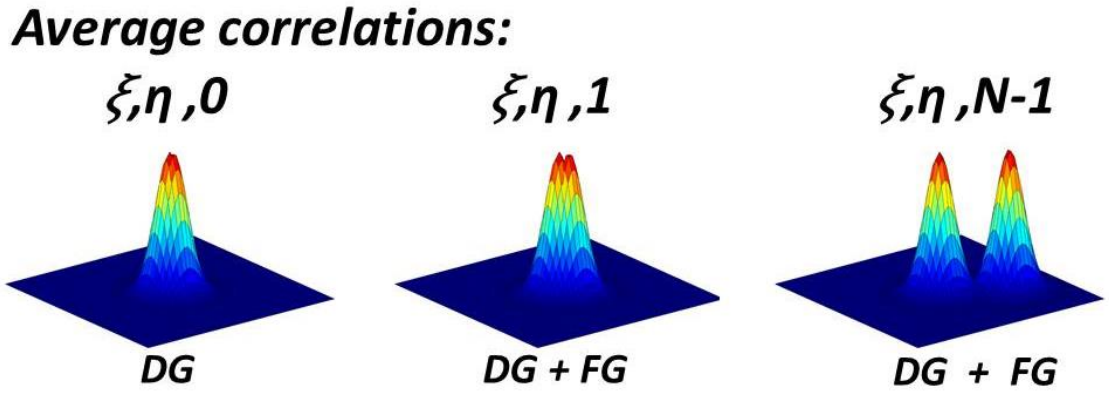

Figure 2.29 Correlation functions from a microscope. Depicted are diffusive (DG) and flowing (FG) populations correlated with increasing time lags from left (autocorrelation) to right, the Gaussian distribution is due to the PSF of the microscope spanning over multiple pixels.

Disadvantages of STICS include the assumption of a 2D sample; as such acquisitions should be taken in as thin an optical plane as possible; such as with TIRF. As STICS relies on correlating signal through a finite ROI (pixel bins) frame integration times should be kept short for higher temporal resolutions, ensuring fluorescent fluctuations (i.e. the movement of molecules) do not shift too quickly so as to move out of this ROI, which would hinder the software's ability to correlate molecules and reduce data reliability.

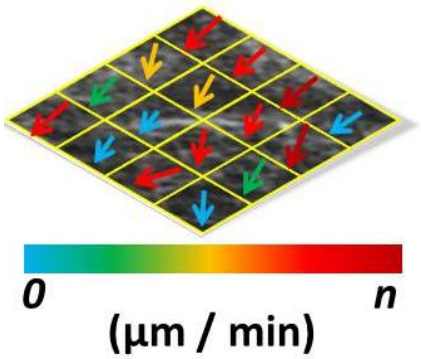

Figure 2.30 STICS vector outputs. For each subregions exhibiting flow, STICS analysis will generate a vector describing the speed (colour) and directionality (orientation) of flow.

Further considerations for STICS over traditional ICS methods include the possible use of a sampling rate above the Nyquist-Shannon criteria, as smaller pixel sizes provide greater information for the algorithm. As STICS correlates spatial fluctuations of signal, the number of fluctuations relies on the image ROI and the PSF of the microscope. To increase the number of molecules within an ROI, this subregion size is traditionally increased, however this reduces

the number of generated vectors (Wiseman 2013). One way around this could be to instead reduce the pixel size.

STICS can be extended for two-channel cross-correlation (STICCS) imaging, for quantitative comparison of flow between two molecular populations labelled with spectrally separated fluorophores. For this method accurate alignment between the channels is essential, as well as minimal channel transition times for optimal correlation. In unaligned channels this would result in an apparent spatial lag between the two populations, if translated relative to each other this could result in directional biases of cross-correlated flow. Minimising the transition time between channels is also important as STICCS does not yet account for delays leading to offset fluorescent signal between channels, as the analysis relies on (cross-) correlating channel(s) within each subregion, delays leading to fluorescent populations leaving a specific subregion would reduce the strength of the (cross-) CF.

STICCS builds on single channel correlation spectroscopy by analysing data recorded in two channels; this enables the labelling and analysis of two molecular species, where a strong correlation indicates these species are co-transported, moving in a complex. Equation 29 extends single channel correlations by incorporating a second channel (b) to enable cross-correlation analysis:

$$\delta i_{a/b}(x,y,t) = i_{a/b}(x,y,t) - [i_{a/b}]$$

Equation 29

Cross-correlation between the two channels can occur in space, time or both (Figure 2.31), Equation 30 calculates this space-time CF, based on the intensity fluctuations recorded.

$$r_{ab}(\zeta,\eta,\tau) = \frac{([\delta i_a(x,y,t)\delta i_b(x+\zeta, y+\eta, t+\tau)]_{xy})_t}{(i_a)_t(i_b)_{t+\tau}}$$

Equation 30

Where ζ, η and τ are the spatial and temporal lags or shifts in space and time between pixels.

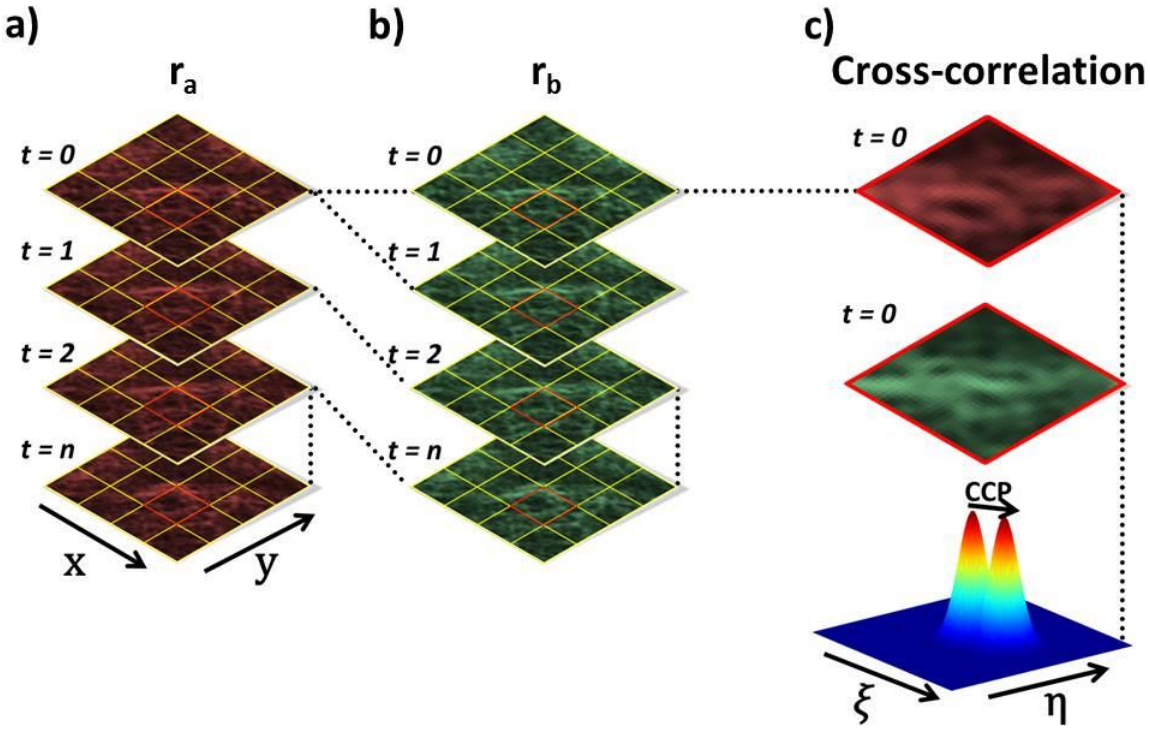

Figure 2.31 Cross-correlation analysis. The two-channel variant of STICS is shown, with both datasets (a and b) being correlated separately but also cross-correlated both spatially (r_a t0 – r_b t0) and temporally (r_a t0 – r_b tn) (c). This outputs information on how similar the flows are between channel r_a and channel r_b, described in the cross-correlation output peaks (CCP).

STIC(C)S analysis has been used to reveal the speed and directionality of various membrane residing proteins and their cross-correlation dynamics with cortical actin, α-actinin and integrins (Hebert et al. 2005) and demonstrated an actin-integrin linkage in murine cells (Brown et al. 2006). Brown and colleagues imaged channels simultaneously and found actin and α-actinin demonstrated correlated flow in images collected at 10 s intervals for 100 images. The study then went on to show integrins and their associated proteins were correlated both for speed and directionality, highlighting actins role in mediating cell adhesion and migration proteins at the plasma membrane. Additionally two potential linkage sites where identified, where the actin-α-actinin or the integrin can disconnect to regulate cell dynamics.

Recently, studies using high- and super-resolution imaging with particle and time resolved ICS (PICS, trSTICS) have been described (Semrau & Schmidt 2007; Pandžić et al. 2015). These techniques analyse single particle tracking and SMLMS data respectively, permitting nanometre and millisecond spatial and temporal resolutions. PICS offers the advantage over classic single particle tracking by not breaking down if multiple trajectories overlap.

All aforementioned ICS techniques to this point, assume detected fluctuations arise from nanoscale dynamics, rather than the photophysics of the fluorophore. However the photophysics of fluorophores are known to fluctuate due to environmental factors and photobleaching. k-space ICS (kICS; (Kolin et al. 2006)) offers several advantages over real-space ICS as data is analysed after Fourier transformation. This makes it insensitive to fluorophores which exhibit blinking or bleaching and the PSF of the system does not need to be measured before analysis.

Depending on the biological system being studied, correlation techniques can offer various advantages. The incorporation of super-resolution imaging and correlative methods is an interesting new area, as most cellular processes involve the spatial and temporal modulation of various proteins including those controlled by the actin cytoskeleton. The combination of live-cell techniques may answer questions involving spatio-temporal organisation of molecular scale dynamics, possibly within the context of the T cell synapse.

Chapter 3 – General methods

3.1. Cell culture

Jurkat clone E6.1 T cells (ATCC, USA) were cultured in flasks containing Roswell Park Memorial Institute (RPMI) 1640 medium (Thermo Fisher, USA) supplemented with 10 % fetal bovine serum (FBS; Thermo Fisher, USA) and 1 % Penicillin Streptomycin (PenStrep; Thermo Fisher, USA), at 37 °C in a 5 % CO_2 environment. Cells were split every 2-3 days to a confluence of 3 x10^5 cells / mL and were not allowed to grow beyond 8 ×10^5 cells / mL.

Primary T cells were isolated from human blood using a peripheral blood mononuclear cell isolation protocol. Blood was diluted 1:1 with room temperature (RT) phosphate-buffered saline (PBS; Thermo Fisher, USA) and carefully layered on top to 15 mL of Lymphoprep® (StemCell Technologies, UK); this was then centrifuged at 515 ×G with no brake at ambient temperature for 20 minutes to create a sucrose gradient. T cells were then pipetted out and resuspended twice in PBS, at 260 ×G for 15 minutes. The pellet from the second spin was then resuspended in Iscove's Modified Dulbecco's Media (IMDM; Thermo Fisher, USA) supplemented with 10 % FBS and 1 % PenStrep to a density of 5 ×10^6. 1 µg / mL phytohaemagglutinin or antibodies against human CD3 (Cambridge Bioscience, UK) were then added to stimulate the T cells and drive clonal expansion. Cells were passaged after 48 – 72 hrs to a density of 2 ×10^6 cells / mL and imaged within 2 weeks.

3.2. Transfections

For Jurkat T cells transient transfection of fluorescent proteins was achieved via electroporation 24 hrs prior to imaging. To ensure optimal cell health and logarithmic growth phase cells were split 48 hrs prior to imaging (24 hrs prior to transfection). For cells electroporated with the Gene Pulsar Xcell electroporation system (BioRad, USA), 4 × 10^6 cells were pelleted at 327 ×G for 5 min and washed in an equal volume of pre-warmed OptiMem electroporation media (Thermo Fisher, USA). After re-pelleting, cells were resuspended in 500 µL of fresh, prewarmed OptiMem and pipetted into the cuvette along with 2-5 µg of the required plasmid(s). The cuvette was inserted into the electroporation system and pulsed with 250 V and 900 Ω capacitance for an exponential decay of ≈ 20 ms. Cells were then carefully pipetted into 5 mL equilibrated RPMI supplement.

Primary human T cells and Jurkat T cells were transfected using the Amaxa (Lonza, USA) Nucleofector® protocol 24 hrs prior to imaging. 1 ×10^6 cells were pelleted at 327 ×G for 5 min and resuspended in 100 µL RT Nucleofector® solution (Lonza, USA), 2 µg plasmid DNA was added and cell solution pipetted into a cuvette. Primary human T cells were electroporated

using the T-023 program for stimulated T cells (or high viability X-01 program for Jurkat T cells) and left for 10 mins at RT before resuspending in 1 mL equilibrated IMDM (or for Jurkats, RPMI) supplement.

For imaging the actin cytoskeleton LifeAct-GFP (Ibidi, Germany), LifeAct-mCherry or GFP-actin (both gifts from Prof. Maddy Parsons) plasmids were used. Membrane was imaged using GPI-GFP (gift from Dr. David Albrecht) while MAL-mCherry (gift from Dr. Helena Soares) or α–actinin-mCherry (Davidson lab) were used to image the vesicle sorting protein and actin-crosslinking protein respectively.

3.3. Formation of immunological synapses

To engineer T cells to form an immunological synapse, CD3 and CD28 were crosslinked through the use of antibodies. #1.5 8-well Labtek (NUNC, Germany) coverslips were used for SIM imaging, while 8-well Ibidi (Ibidi, Germany) coverslips were used for all other imaging. These were coated the day before synapses were to be formed, with 200 µL of PBS containing 1 µg / mL of human αCD3 and 1 µg / mL of human αCD28 (BD Bioscience, USA) antibodies. Coated coverslips were placed at 4 °C overnight. Prior to adding cells coverslips were gently washed once with RT PBS to remove any antibodies still in suspension and 37 °C Hanks' Balanced Salt Solution (HBSS; Thermo Fisher, USA) was added.

For fixed cell experiments 1 mL of cells were pelleted at 260 ×G for 5 minutes and resuspended in 1mL HBSS, 100-200 µL of cell solution was then pipetted onto the coated coverslips to form synapses in the incubator. After the required time period cells were fixed for 20 mins with 4 % paraformaldehyde (PFA; Electron Microscopy Sciences, USA) in PBS or for actin imaging cytoskeletal buffer (10 mM MES [2-(N-morpholino)ethanesulfonic acid] at a pH of 6.1, 5 mM Magnesium Chloride, 5 mM EGTA [Ethylene glycol tetraacetic acid], 150 mM Sodium Chloride and 5 mM glucose, with a final pH of 7.0) before being washed in PBS.

For live cell experiments coated coverslips were placed in the microscopes pre-heated incubation chamber, 200 µL of cells were then pelleted and resuspended as above in HBSS supplemented with 20 mM HEPES (4-(2-hydroxyethyl)-1-piperazineethanesulfonic acid; Thermo Fisher, USA) before being pipetted into one of the 8-well chambers.

3.4. Fixed cell staining

3.4.1 dSTORM and IRIS staining

Cells fixed as in §3.3. were permeabilised for 5 mins with cytoskeletal buffer containing 0.1 % Triton-X-100 (Sigma-Aldrich, Germany) at room temperature. For dSTORM imaging autofluorescence was quenched with PBS containing 0.1 % sodium borohydride (Sigma-

Aldrich, Germany) for 7 mins, washed once in PBS before F-actin was labelled using the F-actin binding toxin phalloidin conjugated to AlexaFluor® 647 (Thermo Fisher, USA), added as a 1:40 dilution with PBS overnight at 4 °C. Prior to imaging the sample was washed in PBS before the dSTORM buffer (Metcalf et al. 2013) was added, based on a reducing-oxidising buffer system it consists of 3 components: an enzyme solution (20 µg/ml catalase, 4 % Tris (2-carboxyelthyl) phosphine hydrochloride, 50 % glycerol, 25 mM potassium chloride, 20 mM pH 7.5 Tris-hydrochloride and 1mg/ml glucose oxidase in diH_20). Glucose solution contained 100 mg/ml glucose and 10 % glycerol diluted in diH_2O. The reducing solution was made up as 1M Cysteamine-Hydrochloride (MEA) in diH_2O.

These were all stored at -20 °C in aliquots until needed, with the enzyme and glucose solutions stored for a maximum of 6 months while the reducing solution was made fresh on the day of imaging. 50 µL of the enzyme solution, 400 µL of the glucose solution and 100 µL of reducing solution were mixed together with 450 µL PBS just before imaging to preserve catalytic and enzymatic activity. To reduce the effect of oxidation which significantly shortens the buffers lifetime the wells were filled and the tops covered.

For IRIS imaging cells were fixed and permeabilised as above before RT Image-iT FX Signal Enhancer (Thermo Fisher, USA) was added for 30 mins. After washing with PBS, a solution containing 0.5 nM of an Atto-655 dye conjugated (through maleimide chemistry via the N-terminal cysteine) to a modified LifeAct peptide was added in PBS. LifeAct was modified as it has a natural binding time of 400 ms (Riedl et al. 2008), for SMLM imaging the modified version exhibits -on average- a 50 ms binding time (Kiuchi et al. 2015) this permits faster data collection, as frame rates are matched to the binding time to optimise collected signal and acquisition speed.

3.4.2 Immunofluorescent staining

Jurkat T cells were fixed 10 minutes after stimulation, with cytoskeletal buffer and 4 % PFA, before being permeabilised at RT for 10 minutes with 0.01 % lysolecithin (Sigma-Aldrich, Germany) in PBS. Compared to permeabilisation with Triton-X-100 for SMLM imaging, this method creates transient membrane pores, allowing improved imaging of membrane residing structures such as membrane proteins and pre-stained cytosolic vesicles. Next samples were blocked for 1hr at 37 °C with 2 % bovine serum albumin (Sigma-Aldrich, Germany) and 0.2 % fish skin gelatin (Sigma-Aldrich, Germany) in PBS before adding antibodies and labels.

For 3-channel imaging of vesicles and actin, phalloidin was added as in §3.4.1, at a 1:200 dilution for 1 hr at RT. After washing three times with PBS cells were imaged.

Microtubules were labelled through incubation for 1 hr at RT with the α–tubulin mouse anti-human antibody DM1A (Thermo-Fisher, USA), followed by labelling with the secondary antibody rabbit anti-mouse conjugated to Alexa Fluor 647 (Life Technologies, USA). After washing three times with PBS cells were imaged.

LAT was imaged by incubation of mouse anti-human primary (Cell Signalling Technology, USA) for 1 hr at RT, followed by labelling with a rabbit anti-mouse secondary conjugated to Alexa Fluor 647 (Life Technologies, USA) for 1 hr at RT. After washing three times with PBS cells were imaged.

3.5. Environmentally sensitive dye staining

Jurkat or Primary T cells were stained with 5 µM di-4-ANEPPDHQ (Thermo Fisher, USA) for 20 minutes to allow dye internalisation; dye stocks were kept at -20 °C at 5 mM in DMSO. Cells were then centrifuged at 327 ×G for 5 minutes and resuspended in HBSS + 20 mM HEPES to reduce the amount of dye in the plasma membrane while leaving internal membranous components including vesicles stained. Cells were then pipetted onto a stimulatory coverslip for imaging at 3-4 $\times 10^5$ cells / mL.

For 3-channel imaging cells were then fixed and stained as in §3.4.2.

3.6. Live-cell drug treatments

Drug treatments were carried out on Jurkat T cells when imaging F-actin, to establish polymerisation rates or membrane order and their respective roles on synapse formation and stability. Drug treatments were also used on Jurkat and primary T cells during vesicle tracking experiments to establish the cytoskeletons role in vesicle trafficking and distribution.

5 minutes after contact with a stimulatory coverslip, drugs were added directly to the cell-containing wells and imaged as with control experiments.

Cytochalasin-D (cyto-D; Cambridge Bioscience, UK) inhibits actin polymerisation in several ways; first it binds to the fast growing barbed end of F-actin with a 6:1 affinity versus the pointed end (Wegner 1976) and blocks G-actin dissociation (Brown & Spudich 1981), secondly it is believed to sever F-actin fibres (Schliwa 1982). At concentrations of 2 µM cyto-D achieves 79 % capping of F-actin, reduces actin elongation by 88 % and reduces membrane ruffling (Yahara et al. 1982).

Jasplakinolide (Cambridge Bioscience, UK) enhances the rate of actin nucleation and decreases the number of oligomers required for actin fibre formation from four down to three subunits.

This increases both F-actin polymerisation and stabilisation; the latter taking around 3 minutes (Bubb et al. 2000).

7-ketocholesterol (7KC, Santa Cruz Biotechnology, USA (Lyons & Brown 1999)) is a cholesterol oxide, it differs from cholesterol by the addition of a ketone functional group, modelling suggests this 7K group tilts the molecule parallel to the bilayer / water interface (Massey & Pownall 2005) reducing its ability to coalesce and pack as efficiently as cholesterol. By using in combination with methyl-beta-cyclodextrin (MβCD, Sigma-Aldrich, Germany) which reduces the level of cholesterol in the membrane and acts as a carrier of 7KC, it can disrupt membrane lipid order and potentially clustering of proteins within these ordered domains.

Nocodazole (Source Biosciences, Lifesciences, UK) is a microtubule modulating drug which has been shown to slow the elongation phase and velocities, and reduces microtubule turnover (Vasquez et al. 1997). It is therefore used in T cells to disrupt MTOCs polarisation, which polarises vesicles to the synapse.

For disruption of the motor protein myosin IIA, blebbistatin (Santa Cruz Biotechnology) was used. Blebbistatin is a small molecule inhibitor which slows phosphate release and preferentially binds to the active site, disrupting ATPase activity (Kovács et al. 2004); blocking the motor proteins ability to move along cytoskeletal fibres.

Stock solutions of Cyto-D (10 mM), Jasplakinolide (1 mM), Nocodazole (10 mM) and blebbistatin (10 mM) were made up in ethanol or DMSO. For the 7KC, 15 mg/ml was dissolved in ethanol, and 50 mg/ml MβCD heated to 80°C in PBS, 7KC was slowly added to the heated MβCD solution over 30 minutes to a final concentration of 1.5 mg/ml 7KC (3.4 mM 7KC stock). Drugs stocks were aliquoted and stored in centrifuge tubes at -20°C until the day of the experiment where they were thawed and diluted to working concentrations.

To ensure drug treatments were not lethal MTT assays (Sigma Aldrich, Switzerland) were performed on Primary human T cells. MTT (3-(4,5-dimethylthiazol-2-yl)-2,5-diphenyltetrazolium bromide) is a dye that turns from yellow to a purple formazan due to enzymatic conversion in viable cells, providing a direct indicator of cell death based on absorbance of formazan illumination at 570 nm. 2×10^7 cells were suspended in 100 µL PBS with relevant drug doses, incubated for 1 hour with 10 µL MTT solution at 37 °C. 100 µL of a solubilisation solution was added to each well to dissolve the formazan crystals and mixed well. Absorbance was then recorded using a Victor 1420 plate reader (Wallac, EG&G, USA). Treatments were performed in triplicate alongside negative and DMSO controls (where cells were treated with 50/50 v/v DMSO).

3.7. Microscope setup

3.7.1 SMLM

dSTORM and IRIS imaging was performed on an N-STORM system (Nikon, Japan) using a 100× 1.49 NA CFI SR Apochromat TIRF objective and iXon3 EMCCD camera (Andor, UK). A quadruple bandpass cube was selected (Chroma, USA) for both IRIS and dSTORM imaging techniques, allowing 405, 488, 561 and 647 nm light through to the sample. Once the sample had been focused using brightfield illumination and a synapse forming cell was found the 647 nm laser was set to 1 % so the TIRF angle could be found by walking the illumination beam to the edge of the objective. TIRF was confirmed by focusing above and below the sample to ensure only florescence at the coverslip-sample interface was detected. To reduce axial drift Nikons Perfect Focus System (PFS) was enabled. An ROI of 256 × 256 pixels was selected which for the EM-CCD camera used (Andor, UK) with a pixel size of 160 nm gave a 40.9 μm^2 field of view.

After finding a suitable cell, dSTORM imaging was initiated by setting the 647 nm laser power to 100 % (167 mW at the fibre tip) for ≈ 5 seconds to check for sample suitability by observing label blinking photophysics and ensuring a sparse enough subset of molecules were activated before starting the acquisition itself. The 405 nm laser was then set to automatically increase in intensity during acquisition up to 75 % laser power (22.3 mW at the fibre), responding to changes in the number of localisations the software detects per frame. Frame rates were set to 20 ms with acquisitions lasting 50,000 frames (15 mins).

For IRIS imaging the 647 nm laser was set to 50 % laser power (83.5 mW at the fibre). Frame rates were set to 50 ms to match the binding time of the LifeAct peptide with acquisitions lasting 20-50,000 frames taking 20-40 mins. Camera settings for both imaging modalities were set to maximise the sensitivity of the system; the EM Gain Multiplier to 300 with a Conversion Gain of 3.

Data was reconstructed using the Nikon Elements Imaging Software (NIS) STORM package which allows the fitting of overlapping peaks. Using a Gaussian localisation method of detection the software scans the image with a 5 × 5 pixel subregion to subtract local background maxima and fitting a Gaussian to find the centroid of each detected emitter (principle by (Thompson et al. 2002)). Candidate molecules must then fulfil brightness selection criteria (minimum and maximum signal counts) which were manually set to 3000 and 65535 for dSTORM and IRIS. Minimum and maximum molecule width was set to 200 nm–400 nm, balancing filtration of noise without letting overlapping molecules through which decreases localisation precision. These settings resulted in >1 $\times 10^6$ and >2 $\times 10^6$ molecules detected for dSTORM and IRIS respectively.

A drift correction utilising autocorrelation was applied to correct for gradual displacement of the sample over time.

3.7.2 SIM

Two SIM systems were used during this study for single- and two-channel imaging; the NSIM system (Nikon, Japan) and a custom-build SIM system (Janelia Farm, USA) respectively. The NSIM system uses a physical grating block to generate the 1st order diffraction beams required to generate the structured illumination pattern at the coverslip-sample interface (Figure 3.1). While this works well for single-channel data it is not designed for interchanging between illumination wavelengths as the physical grate spacing is wavelength specific so requires changing for imaging additional channels which is prohibitive for fast live-cell events. As such two-channel data was acquired on a system where the diffraction beams are generated by a spatial light modulator (SLM) which can be switched via a current to generate beams for different illumination wavelengths at rates compatible for live-cell samples (Figure 3.2).

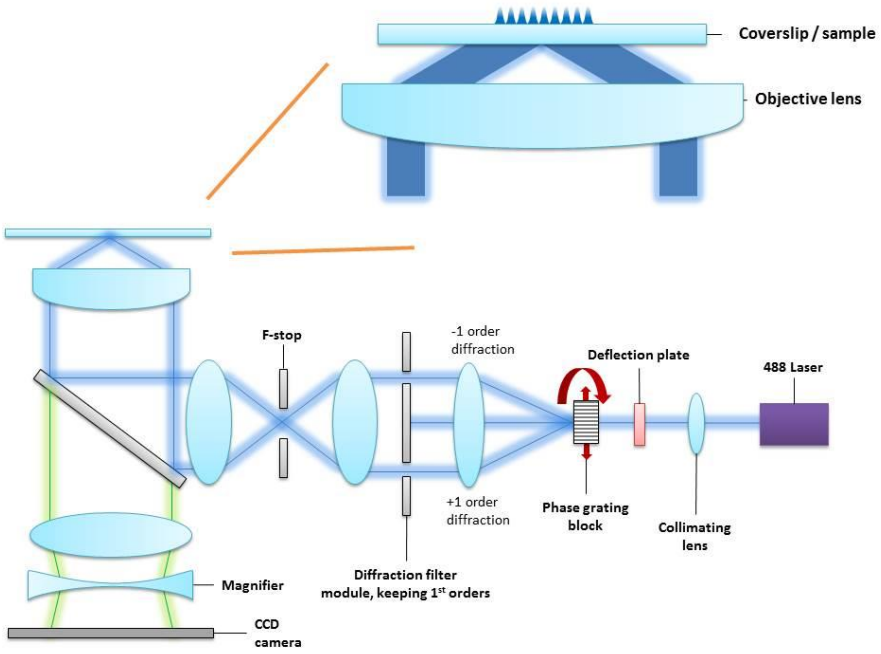

Figure 3.1 TIRF-SIM set-up for single channel imaging. Excitation light passes through a phase grating block matched to the wavelength of light to generate diffraction beams with the 1st order beams selected by the diffraction filter. These beams are then passed through the back aperture of the objective to create TIRF conditions, the beams interact constructively and destructively to form a sinusoidal illumination pattern.

The NSIM system was fitted with a 100× 1.49 NA CFI Apochromat TIRF objective (Nikon, Japan), for single-channel imaging the 488 nm TIRF specific phase grating block was placed in the path of the illumination beam. The iXon3 EMCCD camera (Andor, UK) was used with the EM Gain Multiplier set to 300 and a Conversion Gain of 1. After enabling the PFS, the 488 nm

laser was set at 10 % power (0.2 mW at the back focal plane) and an ROI of 512 × 512 pixels was selected, with a pixel size of 60 nm for a 30 μm^2 field of view.

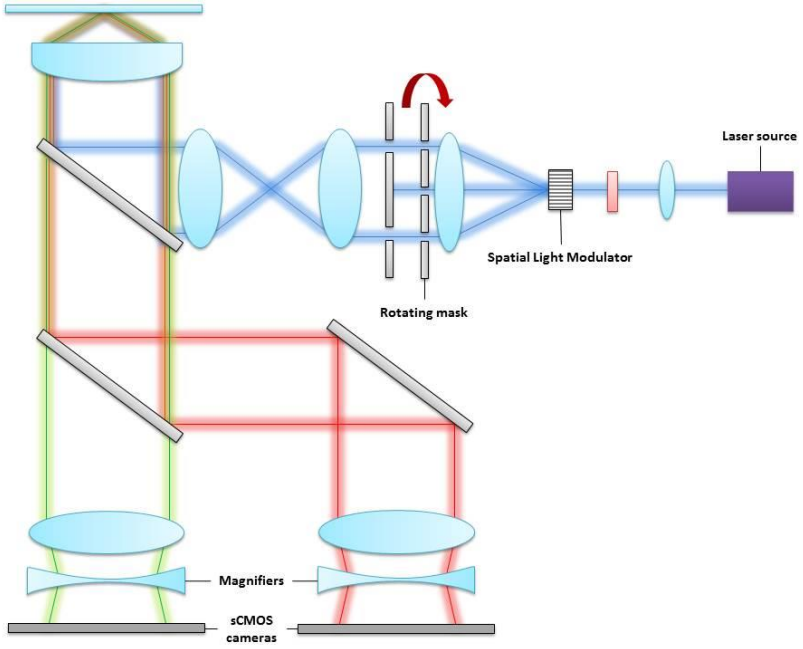

Figure 3.2 TIRF-SIM set-up for multi-channel imaging. Excitation light passes through a spatial light modulator matched to the wavelength of light to generate diffraction beams with the 1st order beams selected by the diffraction filter and rotating mask. These beams are then passed through the back aperture of the objective to create TIRF conditions, forming a sinusoidal illumination pattern. Two-channel imaging is achieved by separating the emitted light onto two sCMOS cameras.

Prior to imaging live samples 100 nm TetraSpeck fluorescent beads (Thermo Fisher, USA) were imaged to ensure the structured illumination pattern was providing optimal sample illumination and reconstruction, images were reconstructed and the FWHM measured. NSIM datasets were reconstructed through the NIS Elements Analyze software (v4.2, Nikon, Japan), achieving a pixel size of 30 nm and an image size of 1024 × 1024. The illumination pattern contrast (illumination modulation contrast, IMC) and high resolution noise suppression (HRNS) were both set to the default of 1. IMC distinguishes the stripes from the structured illumination pattern while HRNS can be used to crop the higher resolution information from the Fourier transform (FFT); for the value of 1 this led to most of the higher frequency information remaining in the final image, for improved resolution.

For two-channel data image reconstruction was achieved using a custom written program, resulting in a final pixel size of 30 nm, with datasets aligned using an algorithm in Priism (UCSF, USA).

For multi-channel imaging a custom-build system based on a Zeiss Axio Observer.Z1 inverted microscope (Zeiss, Germany) was used. An Olympus 100× 1.49 NA objective (Olympus, Japan)

was used, with 488 and 561 nm laser excitation set to 8 and 20 % (≈ 0.4 and 1 mW at the back focal plane). To minimise channel cross-talk a narrow band GFP filter (515/30 nm) and long pass orange/red filter (568 nm) were used, with signal split by a dichroic mirror and collected serially on two separate sCMOS cameras. Images were acquired using the same exposure time and frame rate settings as the single channel data.

Prior to imaging, the incubators of the NSIM and custom-build systems (Tokai Hit, Japan and Okolab, Italy respectively) were set to 37 °C and allowed to equilibrate for at least 1 hr, for NSIM imaging an objective heating collar was also set to 37 °C and distilled water added to a reservoir to maintain humidity around the sample, for the custom-build system the in-built humidifier was switched on.

3.7.3 Multi-channel live-cell TIRF

Vesicle imaging for tracking was performed on a widefield microscope (Nikon, Japan) with an environmental chamber equilibrated to 37 °C; excitation light was passed through a 1.49 NA 60x Apo-TIRF oil immersion objective lens (Nikon, Japan) under TIRF illumination conditions.

Two-channel di-4-ANEPPDHQ data was collected using a Sapphire 488 50 mW laser (Coherent, USA) set to 50 % laser power (1.6 µW at the back focal plane) illumination and emitted light was split using a 488 band pass dichroic mirror (Semrock, USA). Emitted light from the two-channels was split using an OptiSplit III image splitter (Cairn, UK) placed in the emission path (Figure 3.3), for selective filtering of the ordered (542 / 50 nm) and disordered (660nm long pass) channels (Semrock, USA). To account for discrepancies in brightness due to filter selections the disordered channel was fitted with a neutral density (ND) filter and both channels fitted with lenses to correct for differences in the channel path lengths.

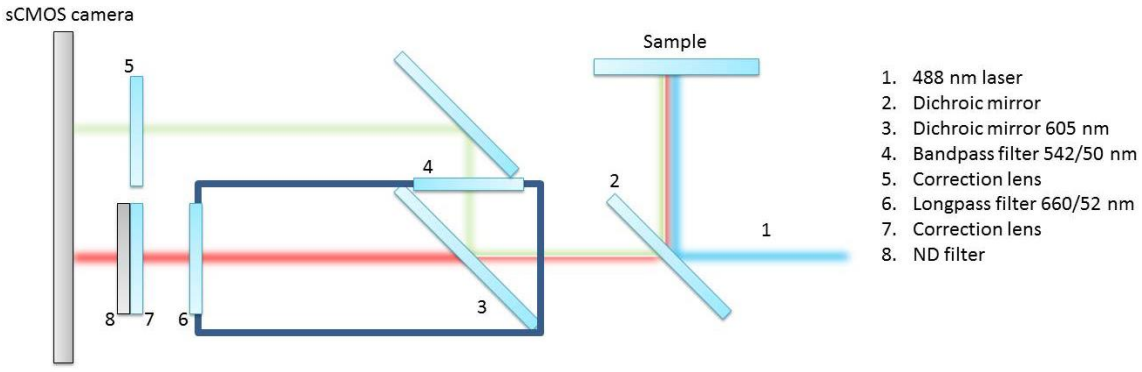

Figure 3.3 OptiSplit filter set-up for two-channel imaging with Di-4-ANEPPDHQ. Emitted light form the sample is passed through a dichroic mirror before entering the splitter cube, here a second dichroic mirror splits the emitted light into blue and red shifted fluorescence. Each channels spectra is then cleaned up by a band- and longpass filter respectively, before passing through a correction lens and for the red-shifted channel a neutral density filter to maintain intensity parity between the channels.

GP analysis was then undertaken, extracting order information for each pixel using an ImageJ plugin as described previously (Owen et al. 2011). The ratiometric measurement is given in Equation 31 for GP analysis:

$$GP = \frac{I_B - I_R}{I_{B+} I_R}$$

Equation 31

Where I_B = Intensity under which wavelength 'B' (blue-shift) is observed, I_R = Intensity under which wavelength 'R' (red-shift) is observed. (B+R equate to ordered and disordered membrane domains).

After analysis the grayscale GP images were combined with the merged ordered-disordered raw images; with the latter used to track individual vesicles. Vesicles were tracked semi-automatically using Imaris (v 8.4.0, Bitplane, UK), the merged channels were used to identify vesicle 'spots' in each frame, these were identified using an estimated x, y diameter of 2 µm with a background subtraction and a filter 'quality' of ≈ 2; based on visual inspection. For tracking of these vesicles through time the autoregressive motion algorithm with tracks being plotted when spots from neighbouring frames (through setting a maximum frame gap size of 0) move a maximum distance of 4 µm.

3.7.4 IRM imaging

Interference reflection microscopy (IRM) was performed with assistance from Dr. Deborah Keller at Imperial College London. IRM is a technique for qualitatively assessing the distance of a sample from the glass interface, such as with a cell on a coverslip. Polarised light is angled and reflected as with TIRF imaging but not beyond the critical angle, thus letting an amount of light to penetrate the sample. Below the critical angle, the ratio of reflected versus non-reflected light is calculated (Equation 32) as the square of the Fresnel reflection coefficient:

$$r_{ab} = \frac{(n_a - n_b)}{(n_a + n_b)}$$

Equation 32

As a cell in media, close to the coverslip will have at least two RI mismatches, two partially coherent beams are reflected and therefore interfere with each other. This results in an image where intensity depends on the amount of interference between the beams, and therefore the path difference between them (Equation 33). This path difference is given by:

$$d = 2n_2 h cos\Theta$$

Equation 33

Where *h* is the vertical distance between the points. The working distance of the system is limited to half λ, as it depends on the interference of the illumination light, making it akin to the depth of the evanescent wave in TIRF.

Imaging was performed on a confocal LSM-510 system (Zeiss, Germany) using a 60x water objective; Jurkat T cells were dropped onto stimulatory coverslips as before and imaged forming synapses using the 561 nm laser.

3.7.5 Confocal imaging

3-channel imaging within §6.3-6.4 was carried out on a Nikon A1R confocal microscope (Nikon, Japan). Fixed samples, stained for membrane order with di-4-ANEPPDHQ and labelled for secondary structures (outlined in §3.4.2 and §3.5) with AlexaFluor-647 were located by brightfield illumination with the Plan Apo VC 100× 1.4NA oil objective, before imaging sequentially using the 488 nm laser for di-4-ANEPPDHQ, splitting the emission spectra using the microscopes 525/50 nm and 595/50 nm filters. The 642 nm laser was used for imaging the labelled cytoskeleton, with the 700 nm LP filter in the emission path. A 3× zoom was selected providing a pixel size of 80 nm for the 512 × 512 image. 488 nm and 640 nm laser powers were set to 10 % and 10-15 % respectively. PMT gain for the green, red and far red channels was set to 70, 1 and 6 High Voltage.

Multi-channel files were split in ImageJ (Schneider et al. 2012) and GP analysis on the green / red channel pairs carried out. Green/red merges were then used to manually select ROI's containing individual vesicles, before overlaying these ROI's onto the GP image to quantify vesicle membrane order. The same ROI was then overlaid on the far-red image to quantify signal intensity for the cytoskeleton. These intensities were then analysed to investigate any correlation between membrane order and the presence of cytoskeletal components at these vesicle sites.

3.8. Fibre tracing analysis

To extract quantitative information about the structure of fibres from pointillist datasets an analysis technique based on Ripley's K(r) analysis was implemented. Classical Ripley's K(r) is a statistical function (Equation 34) which analyses clustering by counting the number of neighbours (*n)* within a distance (*r*) of each localisation (*j*), *N* is given as:

$$N_j = \sum_{i=1}^{n} \delta_{ij}$$

Equation 34

Where δ_{ij} = 1 if the distance between two points, *i* and *j* is less than *r*, otherwise this is 0. For example in Figure 3.4 the selected localisation *j* will have a score of 2 based on distance *r*.

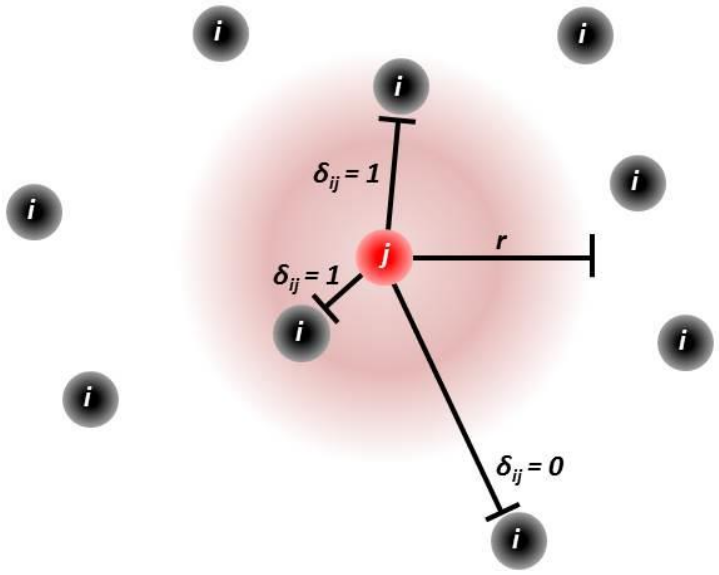

Figure 3.4 Schematic of Ripley's K(r) analysis of pointillist data. From a selected datapoint *j*, any neighbouring points (*i*) within a radius (*r*, red area) are counted. This output can then be used to describe the local density of points about each point.

From this the K(r) function (Equation 35) can be found using the density of the region *ρ*.

$$K(r)_j = \frac{\sum_{i=1}^{n} \delta_{ij}}{\rho}$$

Equation 35

Where $\rho = \frac{n}{Area}$. This is used to detect and assess distribution heterogeneity of areas in space. Deviations of spatial homogeneity are concluded to be significant if compared and different from a randomly distributed set of points (i.e. complete spatial randomness (CSR) [or the homogeneous Poisson process]). The expected value for *K(r)* when the distribution is homogeneous is πr^2. Therefore, the K-function is typically linearised (Equation 36) to give the L-function:

$$L(r) = \sqrt{\frac{K(r)}{\pi}}$$

Equation 36

The circular ROI works well but is also limited to clustered data, for fibre analysis this was extended. Here the ROI was segmented into 5 ° steps or wedges to create angularly defined cluster scores; if localisation (*j*) is assumed to lie on a labelled fibre, it will have peak localisations (*i*) at two points around the angular segmentation, 180 ° apart. Analysis of fibrous structures will therefore reveal a peak at 180 °. This was used to determine the fibrous nature of actin in different regions of the immunological synapse.

3.9. STICS analysis

STICS analysis is based on correlating fluorescent fluctuations through space over time. The subregion area in pixels gives the ROI size the algorithm uses to correlate fluorescent signal. For data containing more defined structure or with slower moving fluctuations this subregion can be made smaller as there are more fluorescent molecules to correlate, which remain in the ROI for multiple frames. Subregion shift refers to the number of pixels the ROI is translated before the next CF is applied; overlap between subregions gives greater vector consistency.

Maximum time lag, which limits the number of time lags to be analysed, was set at the default of 20, so after temporally correlating 20 frames the analysis is ended.

As depicted in Figure 2.29 flowing correlated signal can be covered by the central diffusive Gaussian, especially when there is a high proportion of this population. To reduce any potential masking effect, the immobile object filter can be applied. Designed to remove immobile fluorescent populations prior to analysing the flowing fluorescent signal, this number (given in frames) removes fluorescent signal remaining static for this period of time or longer. The setting used in this study (Table 3.1) has been shown to work for slower moving and large fluorescence signals, as it is based on subtracting serial frames from the frame being analysed.

To reduce artefactual and spurious vector calculation, as can be generated with large structures or noisy data, outlier criteria are applied to terminate analysis within these subregions: a beam radius threshold; where larger structures exceeding the set radius are aborted (based on the PSF of the microscope), an appropriate beam width setting is important for fitting the CF as it is one of the autocorrelation function fitting parameters. When global image noise correlation is comparable to the height of the local flowing correlation these subregions are aborted as this can disrupt the robustness of the CF. Finally when vectors exhibit deviation from neighbouring vectors, especially when there is significant overlap of the

subregions as denoted by the subregion shift, they are aborted, as they should exhibit similar directions. For this thesis all outlier criteria were kept at their respective default settings.

Table 3.1 Image correlation settings for different image datasets.

	Actin and α–actinin analysis	Plasma membrane and cross-correlation analysis
Subregion size (and shift) in pixels	8 × 8 (1)	16 × 16 (4)
Maximum time lag	20 images	20 images
Immobile removal	Moving average, 21 frames	Moving average, 21 frames
Outlier criteria: - Beam radius threshold - Correlation local maximum - Vector mismatch threshold	 - 0.8 - 0.5 - 3	 - 0.8 - 0.5 - 3

After applying the settings in Table 3.1 to the datasets, a polygonal ROI was selected. To ensure correlation reliability when analysing the synapse dSMAC the selection was made without crossing the cell boundary (that is, without imaging the extracellular space).

3.10. Extraction of velocities and directionality

To extract velocity information, the speeds of each subregion were recorded from the vector map data, given either as a mean for scatter plots or as individual subregions for histogram plots. Directionality information was extracted by manually establishing a seed point, which in this case was the cell centre (Figure 3.5). The seed point allowed each vector to be assigned a value of angular deviation (Φ), with a vector being considered retrograde when it was orientated within a 90 ° cone (45 ° deviation) from the assigned cell centre (solid black lines in figure).

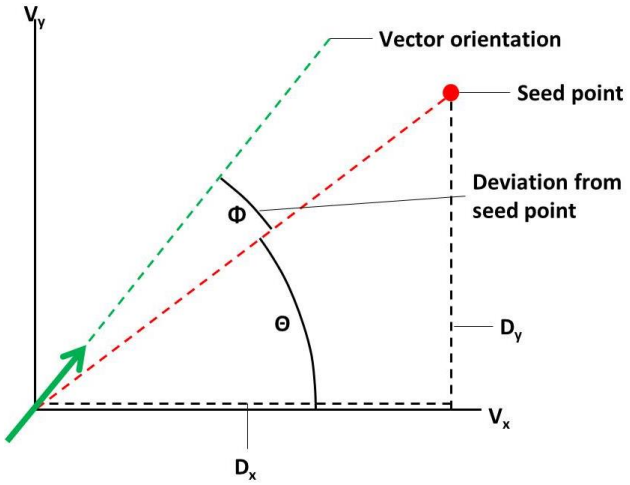

Figure 3.5 Parameters required for calculating vector orientation versus seed point. V_x, V_y STICS outputs are rotated by Θ before calculating Φ which provides each vector with its deviation from the user defined seed point, in this study the centre of the synapse forming cell.

As STICS outputs directionality information as fixed vertical and horizontal components (V_x and V_y) Θ must first be calculated to rotate each V_x, V_y pair so V_x was orientated towards the seed point with V_y perpendicular. Using a rotation matrix this was achieved through Equation 37:

$$\begin{bmatrix} V_{xcorr} \\ V_{ycorr} \end{bmatrix} = \begin{bmatrix} \cos\Theta & -\sin\Theta \\ \sin\Theta & \cos\Theta \end{bmatrix} \begin{bmatrix} V_x \\ V_y \end{bmatrix}$$

Equation 37

Where V_{xcorr} and V_{ycorr} are the rotated versions of V_x and V_y. From Figure 3.5 it can be seen Θ is calculated as in Equation 38:

$$\Theta = \tan^{-1}\left(\frac{D_y}{D_x}\right)$$

Equation 38

D_x, D_y (dotted black lines in Figure 3.5 derived from Equation 39) were found by utilising four output parameters from the STICS algorithm, the distance of the vector to the image edge (x_1/y_1), and the distance of the seed point to the image edge (x_0/y_0)

$$D_x = x_1 - x_0$$

$$D_y = y_1 - y_0$$

Equation 39

Each rotated vectors deviation from the seed point (Φ) could then be calculated via Equation 40:

$$\Phi = \cos^{-1}(\frac{V_r}{V})$$

Equation 40

Where V_r is the radial velocity and V the velocity vector. This gave angles in the range of 0 – 180 °, one final correction was to reverse these so the code outputted smaller angles for more retrograde vectors.

3.11. Statistical analysis

All statistical analysis was carried out in GraphPad Prism (v5.04, GraphPad Software Inc., La Jolla California, USA). All data is reported as the mean ± standard deviation, with two-tailed Student t-test analysis for condition comparison, with confidence intervals set to 99%. Correlation analysis of vesicle GP values and track characteristics used the Pearson correlation function, assuming a Gaussian distribution.

Chapter 4 – F-actin structure and dynamics within the immune synapse with super-resolution methods

4.1. Introduction

The organisation and dynamics of molecules at nanometre scales are important for cellular processes as these changes modulate cellular responses, including at the immunological synapse. Studies have previously shown F-actin forms a dense ring at the dSMAC region of the synapse, and that after initial spreading, F-actin begins a retrograde flow back towards the synapse centre (Figure 4.1 (Babich et al. 2012; Yi et al. 2012)). Actin forms filamentous arcs for corralling transmembrane proteins and dense meshworks, controlling cell migration and spreading upon TCR engagement. Actin dynamics are important for organising membrane microdomains and complexes that initiate signalling cascades (Campi et al. 2005; Kaizuka et al. 2007; Yu et al. 2010; Yi et al. 2012).

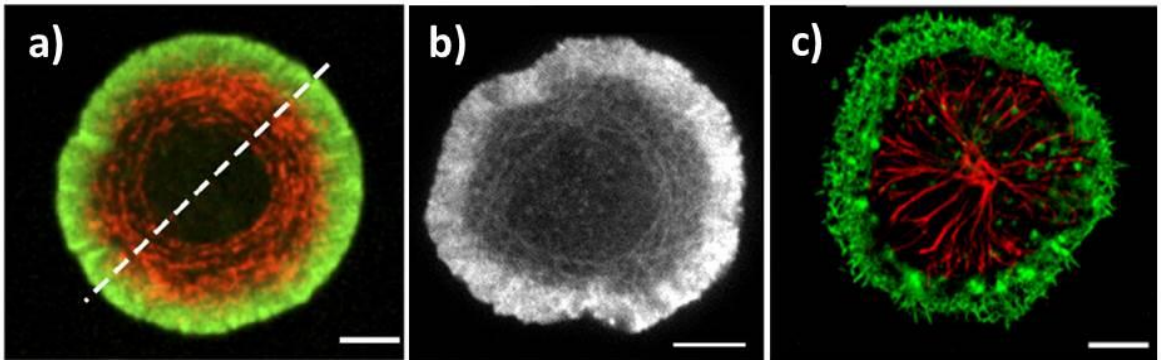

Figure 4.1 Previous imaging of F-actin at the T cell immunological synapse. Representing findings from a) Babich et al., 2012, with actin in green, and myosin (a motor protein) in red, b) Yi et al., 2012, c) Ritter et al., 2015, with actin in green and microtubules in red. Scale bars = 5 µm.

In this chapter nanoscale architecture of the F-actin cortex during synapse formation is characterised using dSTORM with fixed Jurkat T cells and IRIS imaging with fixed Jurkat and primary human T cells. IRIS images show nanometre resolved actin fibres and are analysed to quantify fibre orientation within different synaptic regions. Extending these findings, the novel combination of STICS analysis is applied to live T cells imaged by TIRF-SIM.

To date, most live-cell imaging has used diffraction-limited modalities and quantified data using tracking or single-line kymograph analysis (Babich et al. 2012; Yi et al. 2012; Yu et al. 2010). These methods have provided useful results as to how components of the F-actin cortex behave, however both techniques are comparatively selective with speckle tracking only quantifying a labelled subset of molecules and kymographs relying on manually analysing the

brightest labelled molecules for tracing through 1D single-pixel line profiles. Additionally, as a two-dimensional ROI is reduced to a one-dimensional axis for kymograph analysis there is a complete loss of spatial information along the second axis. This has the disadvantages of making analysis insensitive to molecules crossing the ROI, and multiple molecules residing within the same line profile are indistinguishable. It also leads to a loss of information as particle speeds are underestimated, with only movement along the line-profile of the kymograph counts towards reported velocity. Finally analysis is time consuming when taking multiple manual measurements.

The use of super-resolution imaging for both fixed- and live-cell analysis offers several advantages over conventional fluorescence microscopy. SMLM is particularly useful for studying the extremely dense F-actin meshwork at the synapse periphery. Results within this chapter are then extended to live cell super-resolution and correlation analysis, providing an extension to current tracking techniques, as higher resolution (through smaller pixel sizes) SIM data affords better sampling of fluorescence from individual fibres. This compares with –in the case of diffraction limited microscopy- an ensemble of many fibres potentially with diverse flow properties being summed and a loss of information.

STICS was applied to live-cell TIRF-SIM data for characterisation of molecular flow in T cells during immunological synapse formation, offering potential visualisation and quantification of actin structures summated during standard imaging methods. As mentioned in §3.9, STICS correlates signal, ideally sampled at or below Nyquist-Shannon conditions and when combined with super-resolution datasets (where the spatial sampling rate is greatly enhanced), these correlation strengths are improved.

Correlation strength is similar to the enhancements seen in STED-raster ICS (Hedde et al. 2013), but with TIRF-SIM-STICS offering the additional spatial dimension. The CF depends on the number of characterised fluctuations; at around the square root of fluctuations sampled. Additionally the number of fluorescent entities within the focal volume is inversely proportional to the CF amplitude (G(0) = 1/n). These two factors are improved upon applying STICS to super-resolution imaging as more spatial fluctuations are sampled (to the detriment of faster fluorescent species) and a smaller focal volume will theoretically increase the CF's amplitude.

4.2. Investigating F-actin structure at the synapse

For nanoscale imaging of F-actin within the T cell synapse, dSTORM was applied to fixed cells which had formed a synapse against a stimulatory coverslip. Mean localisation precision of detected fluorophores was 5.2 ± 2.2 nm (Figure 4.2, n = 3). This localisation precision is a

result of the brightness of the dye combined with the high laser powers used and the thresholding during post-acquisition analysis, which selected molecules, based on a brightness criteria.

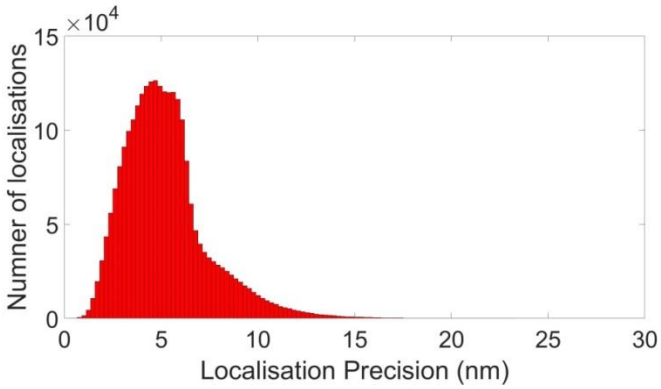

Figure 4.2 Localisation precision of dSTORM datasets. A histogram demonstrating the distribution of individual localisations with a mean precision of 5.2 ± 2.2 nm (n = 3).

Figure 4.3a-c demonstrates the capabilities of dSTORM for resolving AlexaFluor 647-phalloidin bound to actin structures, capturing the distribution of cortical actin at the T cell synapse. The representative cell shows the actin-dense dSMAC region, while towards the synapse centre this cortical actin diminishes to bundled and individual fibres, including punctate structures.

Figure 4.3d shows quantification of the relative labelling density and therefore density of the actin cortex by radial intensity profile analysis with a user-defined cell centre. This confirms qualitative observations of the imaging data that F-actin creates a dense meshwork at the dSMAC and quickly dissipates towards the pSMAC and cSMAC regions where actin forms less dense structures in agreement with previous literature (Babich et al. 2012; Yi et al. 2012; Ritter et al. 2015). Resolving individual actin structures of the T cell synapse is particularly challenging for fluorescence imaging due to the differences in density of actin between the dSMAC meshwork and the sparser cSMAC.

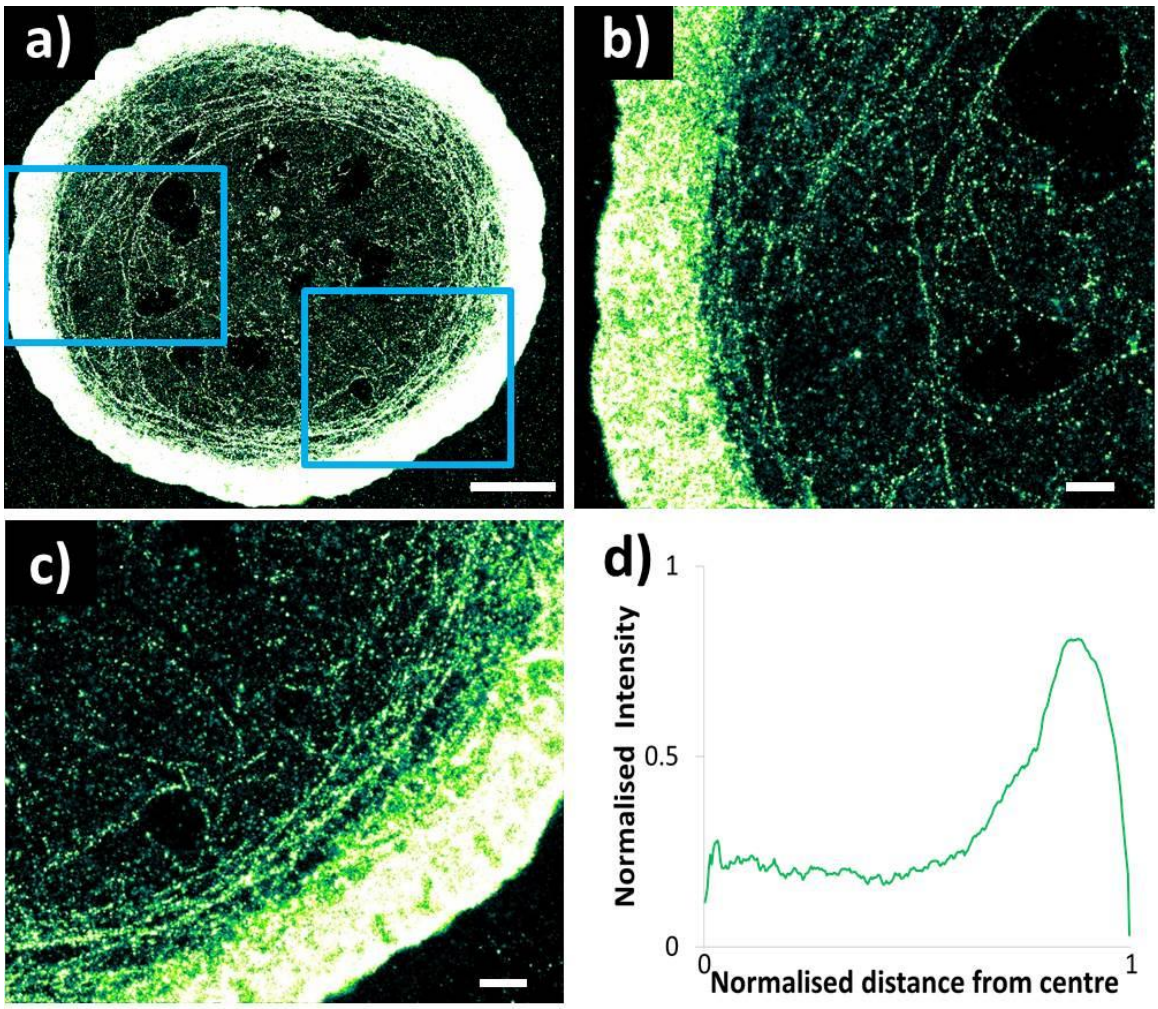

Figure 4.3 F-actin structures at the T cell synapse labelled by AlexaFluor 647-phalloidin imaged by dSTORM. dSTORM images show the organisation and congregation of F-actin during synapse formation and some filamentous structure can be seen, however ROI's show discontinuous filaments and less structure in the actin-rich dSMAC. Scale bar in a) = 5 µm, b) and c) = 1 µm. d) Radial intensity profile of F-actin distribution (n = 3).

This data demonstrates dSTORM is not optimal for resolving individual fibres which exhibit dense bundling and crossing, as with those at the leading edge of migrating cells which are akin to the dSMAC of synapses (Figure 4.4; (Svitkina & Borisy 1999)). dSTORM is also sub-optimal for imaging elongated or fibrous structures such as F-actin, due to the long binding times of phalloidin there is essentially a finite number of fluorophores which can be localised per actin monomer. During image acquisition this makes visualisation of continuous and densely organised structures difficult. Another limiting factor is steric hindrance; the probe may not be able to bind due to its size, hindering other molecules from binding to neighbouring sites of the actin filament.

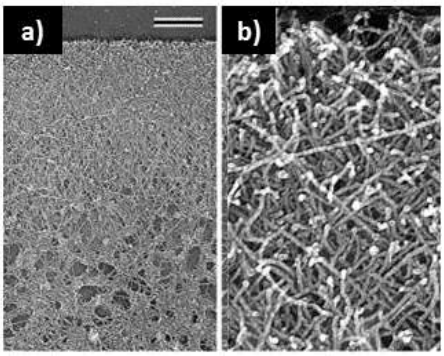

Figure 4.4 Electron microscopy images of actin. Images are of the leading edge of migrating keratocyte cells from Svitkina and Borisy, (1999). Images show the dense meshwork and crosslinked fibres of actin. Scale bar 1 µm.

To circumvent these limitations IRIS imaging was carried out. Figure 4.5a plots the mean localisation precision of 12.0 ± 5.4 nm (n = 5) for the same thresholding as for dSTORM data, interestingly molecules are less precisely localised compared to dSTORM imaging. As fluorophore localisation is reliant on the transient binding of the probe, IRIS utilises lower excitation powers which may return less photons per molecule, directly affecting localisation. The binding to F-actin of modified LifeAct is itself less stable than phalloidin, possibly resulting in low precision due to increased binding mobility (i.e. reduced binding stability). Probe photophysics may also contribute; with the phalloidin Alexa Fluor dye exhibiting a slightly improved quantum yield (0.33) compared to the Atto dye used for IRIS (0.3). Additionally, due to the majority of the IRIS probe residing in suspension these molecules will contribute to an increased background compared to dSTORM imaging.

IRIS does however offer the advantage of prolonging the imaging capacity to hours compared to dSTORM which generally offers less than an hour before molecular populations are depleted due to image buffer degradation. This allows researchers to be more selective in their thresholding to improve mean localisation precision (Figure 4.5c and e); but to the detriment of the final reconstructed images, with reduced localisation numbers, leading to unresolvable actin fibres (Figure 4.5d and f). This leads to reduced fibrous structure being visible, and additional artefacts being present, as can be seen in Figure 4.5d and f where apparent illumination inconsistencies are occurring.

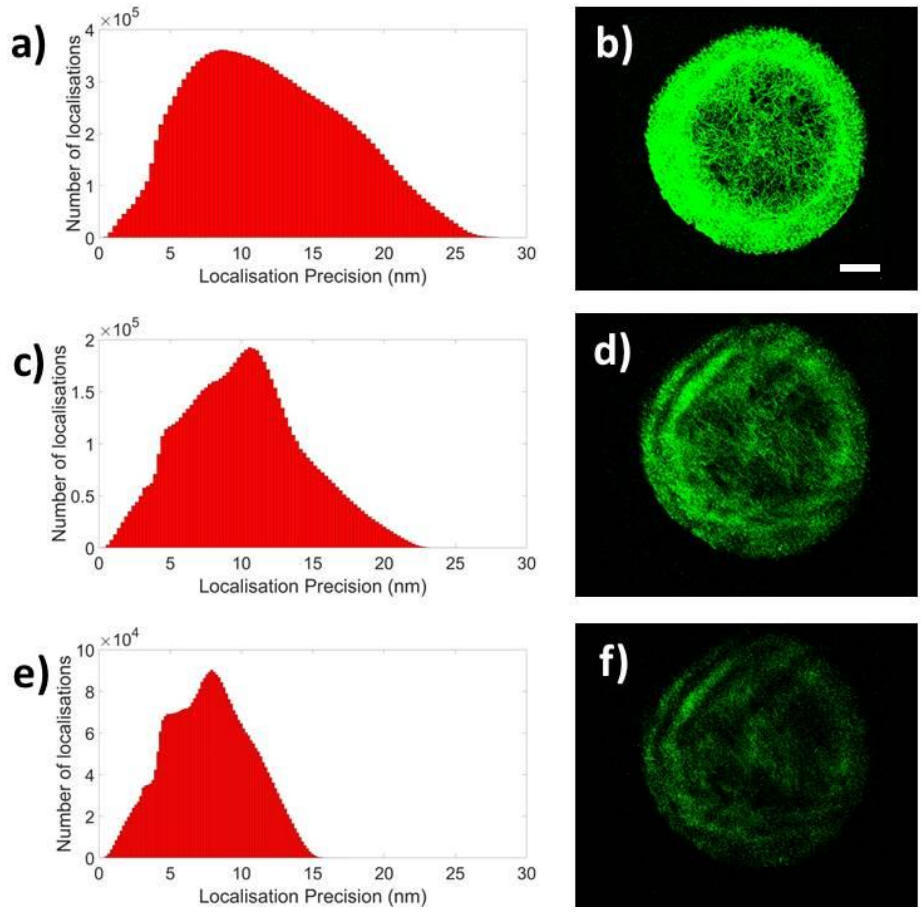

Figure 4.5 Localisation precision of IRIS datasets. The precision of individual localisations and their respective output images with varying thresholds between 3000 (a, b), 6,500 (c, d) and 10,000 (e, f) gave a distribution mean of 12.0 ± 5.4, 9.6 ± 4.2 and 7.0 ± 2.9 nm, but also reduced the resolvable structure of the F-actin network (n = 5). Scale bar = 5 µm.

Figure 4.6 shows how IRIS can better visualise the F-actin cortex with the same reconstruction settings as dSTORM. Due to the increased number of available fluorophores (as the probe is freely diffusing in solution) this allows for longer acquisition times before the probe population is depleted and its concentration can be modified to suit the sample being imaged. For example a concentration of 0.5 nM IRIS probe offered a greater number of localisations per frame (94 ± 51) compared to dSTORM (32 ± 17).

IRIS images provide further insight into the molecular organisation of the actin cortex during T cell synapse formation. Datasets demonstrate resolvable fibrous arcs within the pSMAC, emanating from the dSMAC in both 5 minute (Figure 4.6a-c) and 10 minute (Figure 4.6d-f) synapses; these form part of the dense meshwork and become sparse before giving way to more punctate actin structures within the cSMAC, particularly within the 10 minute synapse. 5 minutes after contact with the stimulatory coverslip, fixed samples exhibited F-actin was still present within the cSMAC, by 10 minutes the cSMAC region is almost devoid of such structures. However, these were replaced by punctate actin structures which may account for

the relative increase of fluorescence intensity within the mature synapse centre (Figure 4.7 green line). This data correlated well with findings that actin clears and enables MTOC polarisation at around 7 minutes (Ritter et al. 2015). Punctate actin structures within the cSMAC have not yet been characterised but they could represent actin foci (Kumari et al. 2015), regions of actin mediated endocytosis or actin-rich regions which contain cell adhesion molecules.

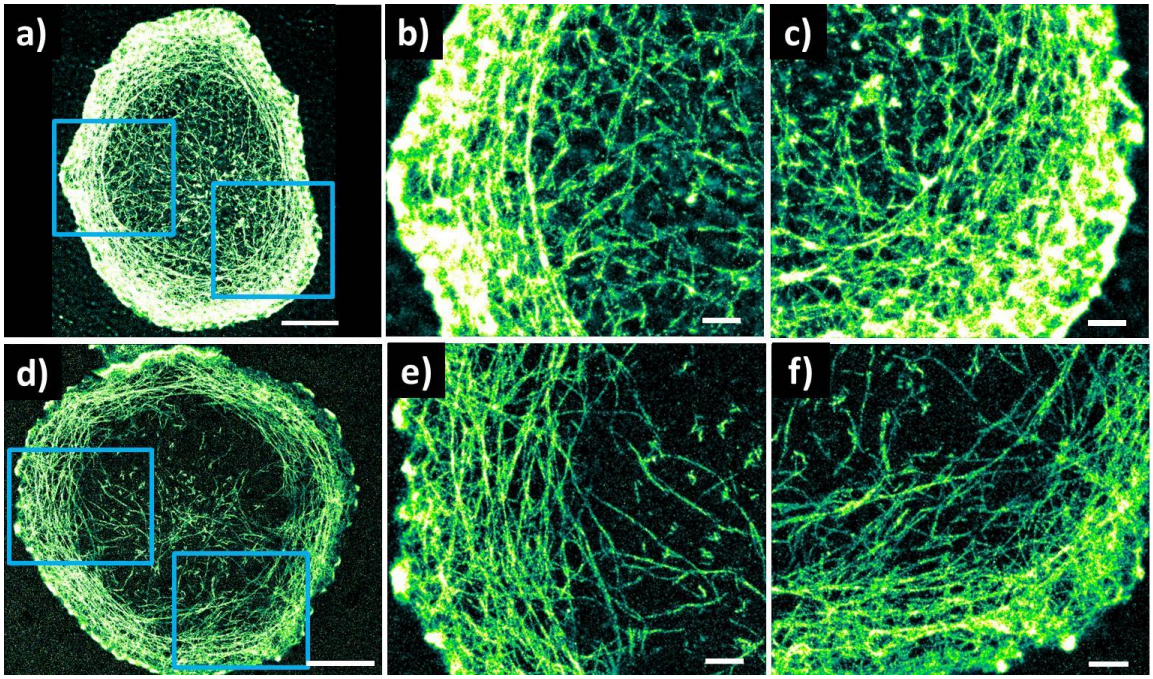

Figure 4.6 IRIS imaging of F-actin structure within the T cell synapse. All images show F-actin labelled by a modified LifeAct-647 probe, through transient binding and sequential localisations, this allows single molecules to be localised a-c) show a T cell synapse, fixed 5 minutes after contact with a stimulatory coverslip d-f) show a synapse fixed 10 minutes after stimulation. Scale bar in a) and d) = 5 µm, b, c, e and f) = 1 µm.

Interestingly, Figure 4.7 also demonstrates a shift in peak intensity of actin towards the synapse centre with the peak translating inwards within the 10 minute synapses. The peak within 5 minute synapses is higher and narrower; signifying more actin within the dSMAC. This may be indicative of cells still spreading during these early time points; leading to higher concentrations of actin within this region due to polymerisation.

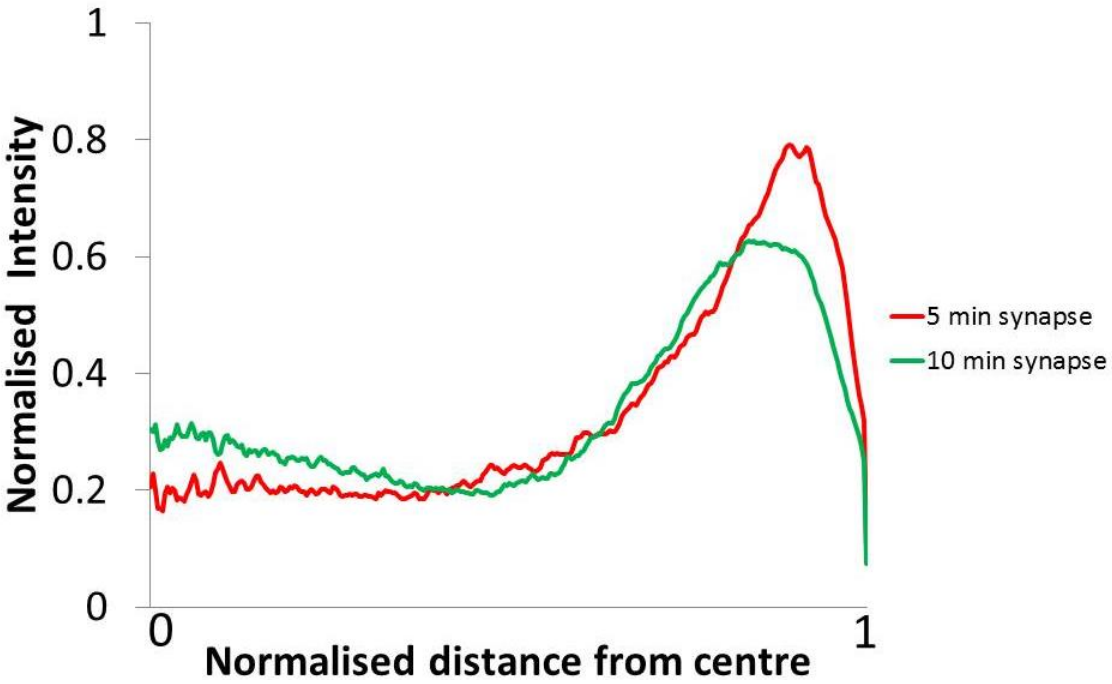

Figure 4.7 Radial intensity profile of F-actin distribution. Jurkat T cells imaged by IRIS microscopy after fixing 5 minutes and 10 minutes post-stimulation were analysed by radial intensity profiles, where pixel intensities from the cell centre to the cell periphery were quantified, these data showed an increase in pixel intensity towards the synapse periphery, indicating increased actin density (n = 5 cells, both conditions).

IRIS imaging was repeated in primary human T cells (Figure 4.8), data exhibited an actin dense periphery as with Jurkat T cells. Interestingly these synapses contained holes prevalent throughout the interface (Figure 4.8a-c) rather than a large actin depletion zone in the centre, with actin localisations demonstrating near homogeneous density relative to the dSMAC (Figure 4.8d). F-actin structures were more akin to asters as previously reported during in vitro experiments (Köster et al. 2016). These structures are similar to those found in $CD8^+$ and NK cells (Murugesan et al. 2016; Brown et al. 2011), Murugesan and colleagues also noted similar differences between Jurkat T cells and primary mouse cells, with far smaller cSMAC regions devoid of F-actin.

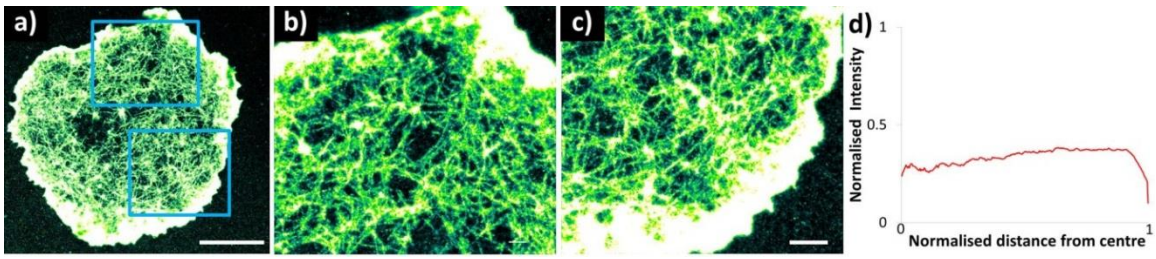

Figure 4.8 F-actin structures within the 10 minute synapse of primary human T cells, labelled by a modified LifeAct-647 probe and imaged by IRIS. Scale bar in a) = 5 µm, b) and c) = 1 µm. d) Radial intensity profile of F-actin distribution, demonstrating relatively homogeneous actin distribution compared to Jurkat T cells (n = 4 cells).

These differences were quantified through a modified version of Ripley's-K function, coded by Ruby Peters (Owen lab), which allows the analysis of fibre orientation and linearity. Figure 4.9 depicts two T cells (Jurkat [Figure 4.9a] and primary human [Figure 4.9b]) each with three 3 × 3 µm ROI's highlighted for analysis; one each for the dSMAC (1), pSMAC (2) and cSMAC (3). These plots represent the fibrous nature of the pointillist data by selecting a 200 nm ROI around each point and segmenting this into steps of 5 °. By counting the points within each segment this results in line plots describing the orientation of neighbouring points (with Angle '0-5' aligned to the y axis of the image). Randomly oriented fibrous data or clusters result in flat line plots (due to the homogeneous nature of localisation distributions), while more fibrous data result in a peak around 180 °, as can be seen for the pSMAC regions.

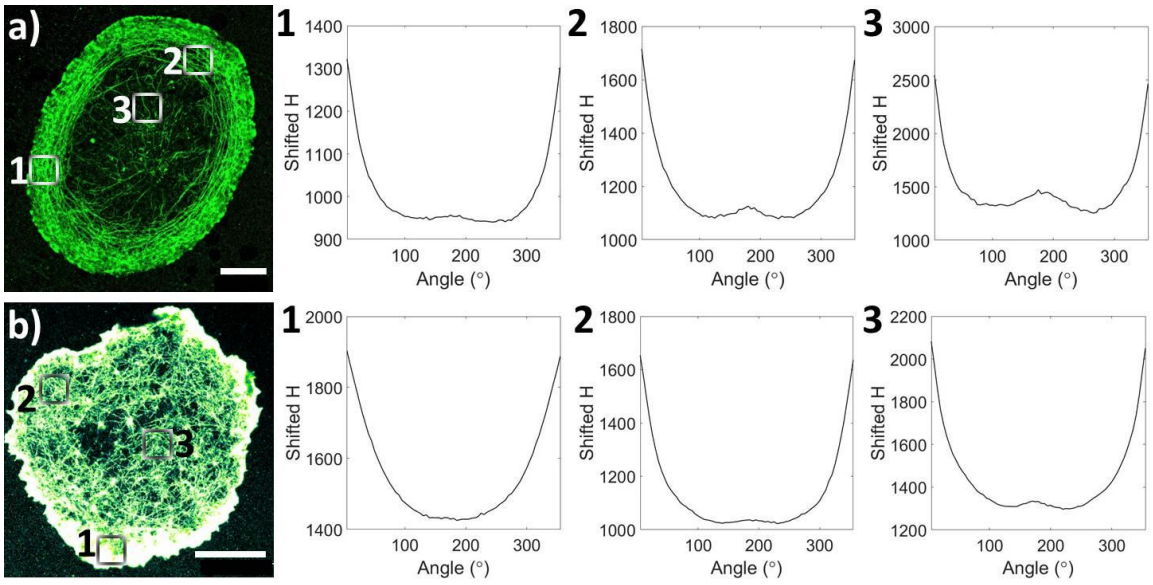

Figure 4.9 Quantification of pointillist data by fibrous spatial point patterns. To further clarify the changes seen between different SMAC regions of cells, as well as between Jurkat and primary cells, data was analysed using a novel variant of Ripley's(K) analysis. a) Jurkat and b) primary human T cells with the cortical actin network labelled; 3 × 3 µm regions of the dSMAC (ROI 1), pSMAC (ROI 2) and cSMAC (ROI 3) were selected for analysis; 1-3 plot the orientation of fibres from the pointillist data. Scale bar = 5 µm.

Together this data demonstrates Jurkat T cell synapses contain an actin rich dSMAC, which gives way to a less actin rich but more organised pSMAC, which are visualised and quantified as radial arcs. Finally images show the actin poor cSMAC which contains randomly orientated fibres and punctate structures. However in primary human T cells actin forms a more homogeneous distribution with multiple actin poor 'holes' within the central regions. These actin structures are also seen to be orientated more randomly.

4.3. Live cell microscopy (TIRF-SIM)

While nanoscale structures can be characterised with SMLM techniques, they are still limited to static or slow moving events especially with regard to structural information where localising enough fluorophores to form a meaningful image is challenging. However, understanding how structures such as the actin cortex dynamically modulate cellular and molecular scale events requires capturing their movement. Characterisation of cortical actin meshwork dynamics was achieved through TIRF-SIM microscopy.

4.4. Spatial and temporal resolution

The spatial resolutions of both the commercial Nikon NSIM and custom build SIM systems were characterised using the 488 nm channel, first 100 nm fluorescent beads were used on the NSIM system, giving FWHM measurements of 120 nm (Figure 4.10).

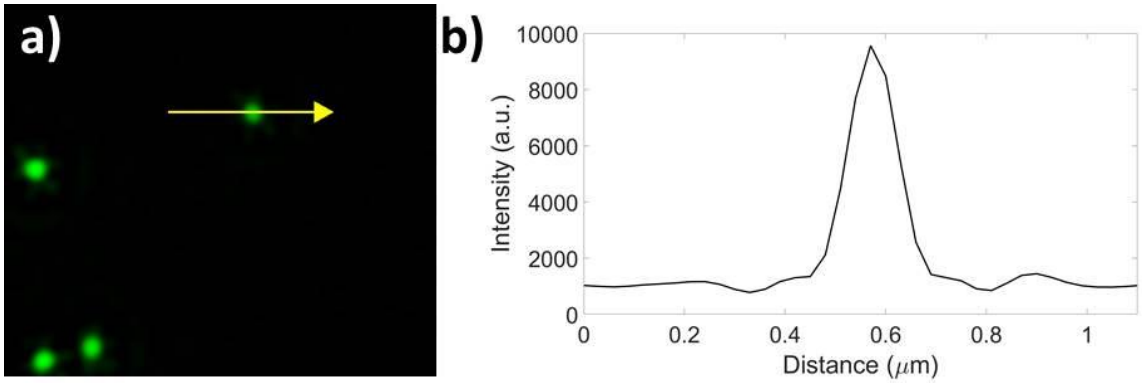

Figure 4.10 Characterisation of SIM resolution with fluorescent beads. a) Reconstructed SIM data was analysed by measuring the full width at half the maximum intensity. b) After plotting a line profile this was shown to provide a resolution of 120 nm.

Next FWHM measurements of individual actin fibres at the Jurkat T cell immunological synapse, labelled with LifeAct-GFP were measured from Nikon N-SIM system datasets (Figure 4.11), giving (100.1 ± 11 nm, n = 10). These resolution discrepancies are possibly due to the respective size of F-actin (7 nm) and the fluorescent beads (100 nm).

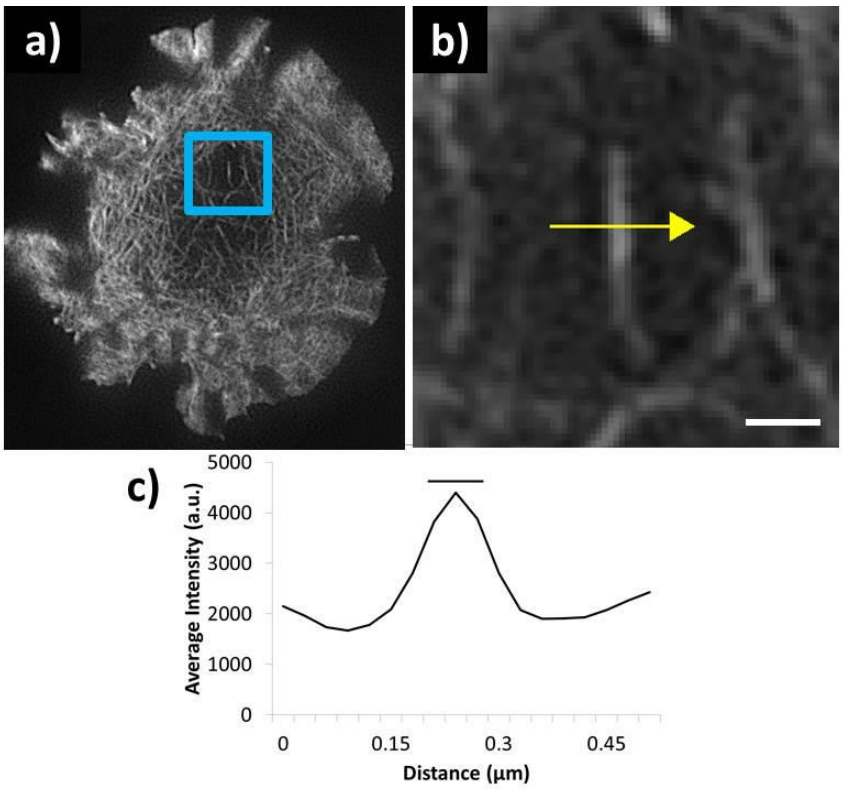

Figure 4.11 FWHM measurements for the NSIM system. a) Representative data and b) zoomed regions of Jurkat T cells expressing LifeAct-GFP and forming synapses against a stimulatory coverslip. To test the resolution capability of the SIM system the FWHM of single actin fibres within cells were measured after reconstruction. c) FWHM profiles of the N-SIM system gave average resolutions of 100.1 ± 11.0 nm for actin fibres (n = 10). Scale bars = 1 µm.

The custom-build system provided a FWHM of 98.6 ± 12.4 nm (n = 10) for individual fibres using the 488 nm channel (Figure 4.12) and 111.7 ± 15.6 nm for the 561 nm channel, this difference in resolution between 488 and 561 nm illumination was to be expected as the diffraction pattern is generated by matching the periodicity to the wavelength of light being used.

As live-cell imaging incorporates temporal information, the temporal resolution is also important to characterise. Imaging F-actin labelled with LifeAct-GFP was carried out using an exposure time of 50 ms, which provided good signal-to-noise of raw frames before reconstruction and no obvious 'blurring' of the F-actin structure which would arise from fluorescent signal moving through two intensity maxima of the structured illumination during the acquisition of the nine raw frames. SIM requires the reconstruction of these nine raw frames to produce an isotropically resolved image, the 50 ms acquisitions plus the inter-frame delays arising from the physical shifts and lateral reorientation of the grating block in the NSIM system. This resulted in a final reconstructed frame rate of 1.05 per second or 63 frames per minute. For consistency during data analysis this frame rate was repeated for the custom-build

microscope, though due to the faster reorientation provided by the SLM unit the 9 raw frames were acquired in around 0.5 s requiring a 0.5 s pause before collecting the next 9 frames.

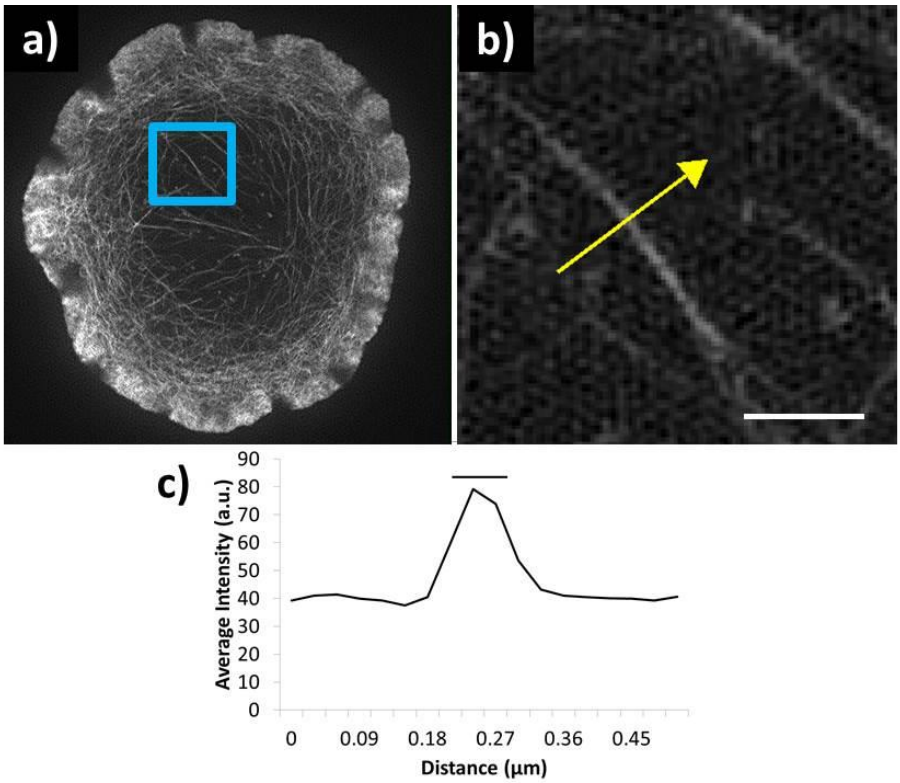

Figure 4.12 FWHM measurements for the custom build system. a) Representative data and b) zoomed regions of Jurkat T cells expressing LifeAct-GFP and forming synapses against a stimulatory coverslip. To test the resolution capability of the SIM system the FWHM of single actin fibres within cells were measured after reconstruction. c) FWHM profiles of the custom built system giving 98.6 ± 12.4 nm (n = 10) for the green channel and 111.7 ± 15.6 nm (n = 10) for the red channel. Scale bars = 1 µm.

4.5. Validation of STICS on TIRF-SIM data

The rationale for using TIRF-SIM data for STICS analysis, compared to conventional light microscopy is the additional spatial sampling rate available. To robustly correlate spatial signal fluctuations per analysed subregion (i.e. to increase the number of fluorophores to be correlated) traditionally requires increasing the correlation subregion size; however this reduces the spatial resolution of the vector maps generated. By reducing the pixel size this limitation is circumvented, therefore retaining or even reducing the subregion size without reducing the strength of the CF. This provides a greater number of vectors and therefore more flow information per image, giving the potential to visualise sub-diffraction structures such as different actin populations.

To ensure any high resolution noise artefacts from the SIM reconstruction were not interfering with the STICS analysis, raw images were reconstructed using various high resolution noise suppression (HRNS) settings (Figure 4.13a, f, k), leading to the representative Fourier

transforms being 'clipped' of their higher resolution data in a linear manner (Figure 4.13b, g, l). This firstly removed any artefacts associated with high resolution noise when using the default setting of 1 but degrades the resolution to conventional fluorescence microscopy levels when this was increased to 5. Running a Student's t-test on the data revealed neither the flow speeds (Figure 4.13d, i, n) nor directionality (Figure 4.13e, j, o) were significantly different between control and the reduced resolution data (p = 0.27 [HRNS 2.5] and 0.09 [HRNS 5]).

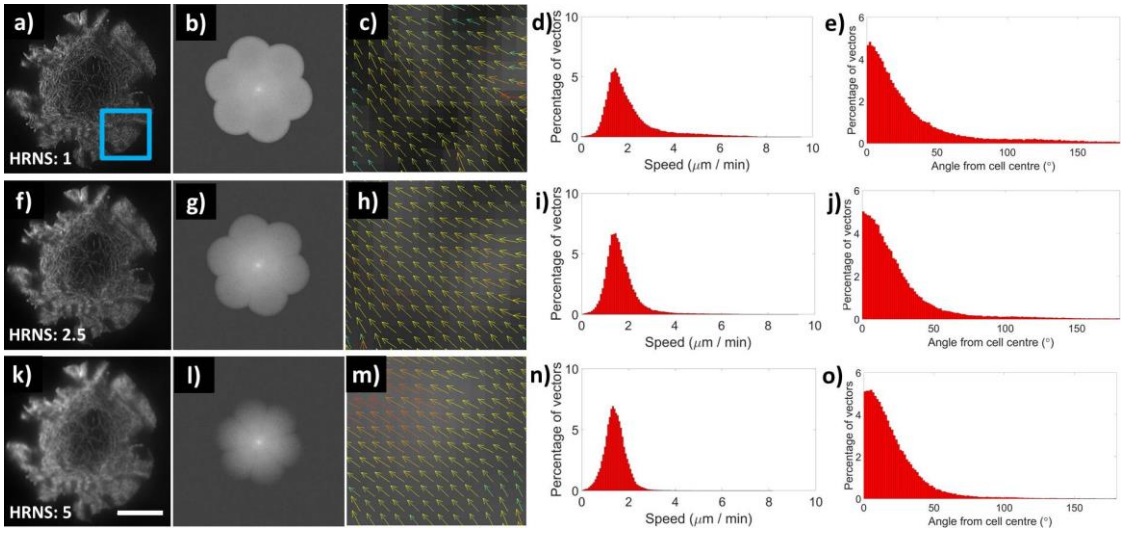

Figure 4.13 Image correlation analysis following high resolution noise suppression (HRNS) settings for TIRF-SIM reconstruction. To demonstrate analysis is insensitive to spatial filtering, HRNS was applied to SIM images during reconstruction (a, f, k), this reduced the resolution in a linear manner as denoted by Fourier transform (b, g, l). Following correlation spectroscopy (c, h, m), velocities were measured for the three HRNS conditions (d, i, n) giving 2.0 ± 0.6, 1.6 ± 0.3 (p=0.27 relative to control), 1.4 ± 0.2 µm / min (p=0.09 relative to control). Directionality was also measured (e, j, o), with mean angles of 30.4 ±14.1, 24.2 ±5.3, 20.9 ±0.6 °, retrograde flow measuremens gave 79.6, 86.4, 90.9 % (n = 5).

This result is in line with a potential limitation of using diffraction limited microscopy for dense datasets, where a summation of individual molecules are reported in each pixel and therefore multiple fluorophore dynamics are binned and correlated; with the net flow being reported. This has also been demonstrated using conventional TIRF microscopy and STICS analysis of F-actin flow in Jurkat T cells, where a subregion size matched to the size used for SIM imaging resulted in a spurious vector map. Using TIRF-SIM and STICS together allows the heterogeneous nature of a greater number of molecules to be correlated at lower densities per pixel; providing additional information versus diffraction limited microscopy.

4.6. Actin control data – speed and directionality

Imaging and analysis of F-actin flow within the T cell synapse was carried out on the N-SIM, due to the comparatively low laser powers used and the small penetration depth of the TIRF-SIM evanescent wave (75 nm), datasets up to 10 minutes could be recorded with no apparent

photobleaching or perturbation of cell architecture. For STICS analysis, datasets lasting 1 minute were adequate for detecting and correlating flow.

F-actin labelled with LifeAct-GFP was imaged (Figure 4.14a), correlated and quantified; the generated vector maps (Figure 4.14b) gave flow speed as 1.63 ± 0.46 µm/min (n = 24; Figure 4.14c). STICS analysis of TIRF-SIM datasets agree with previous studies using kymograph and tracking methods to quantify subpopulations of F-actin retrograde flow at the synapse ((Yi et al. 2012; Kaizuka et al. 2007; Yu et al. 2010; Babich et al. 2012); see Table 4.1).

Table 4.1 Previous quantification of F-actin retrograde flow

	Speed (um / min)	Region analysed	Method	Cell type	Notes
Yi et al., 2012	6.3 2.4	dSMAC pSMAC	Kymograph	Jurkat on bilayers	Analysis demonstrated a reduction in speeds from the dSMAC to pSMAC
Babich et al., 2012	5.4	dSMAC	Kymograph	Jurkat on glass	
Yu et al., 2010	5.2	d- and pSMAC	Speckle analysis	Jurkat on bilayer	Figure 4 shows slowing in pSMAC versus dSMAC Actin velocity decreases around confined TCR clusters
Kaizuka et al., 2007	19.2	dSMAC	Speckle analysis	Jurkat on bilayers	TCR movement most abundant during 1st 10mins. TCR 2-fold slower than measured actin flow
Burnette et al., 2011 (NCB)	4.2 maximum	Leading edge (LP)	Speckle flow kymograph	PtK1 cell	Show actin flow changes in migrating cells of protrusion-retraction cycle

The combination of TIRF-SIM and STICS offers the advantage over previous techniques of whole-sample quantification for molecular scale dynamics. Another advantage over alternative

tracking or correlative methods is the added directional information given within each subregion. Extraction of flow orientation for each subregion was extracted as described in §3.10. This confirmed the majority of F-actin was flowing in a retrograde manner (Figure 4.14d) with 72.9 % of vectors orientated within a 90 ° arc of the synapse centre and a mean angle of 40.8 ± 23.35 °.

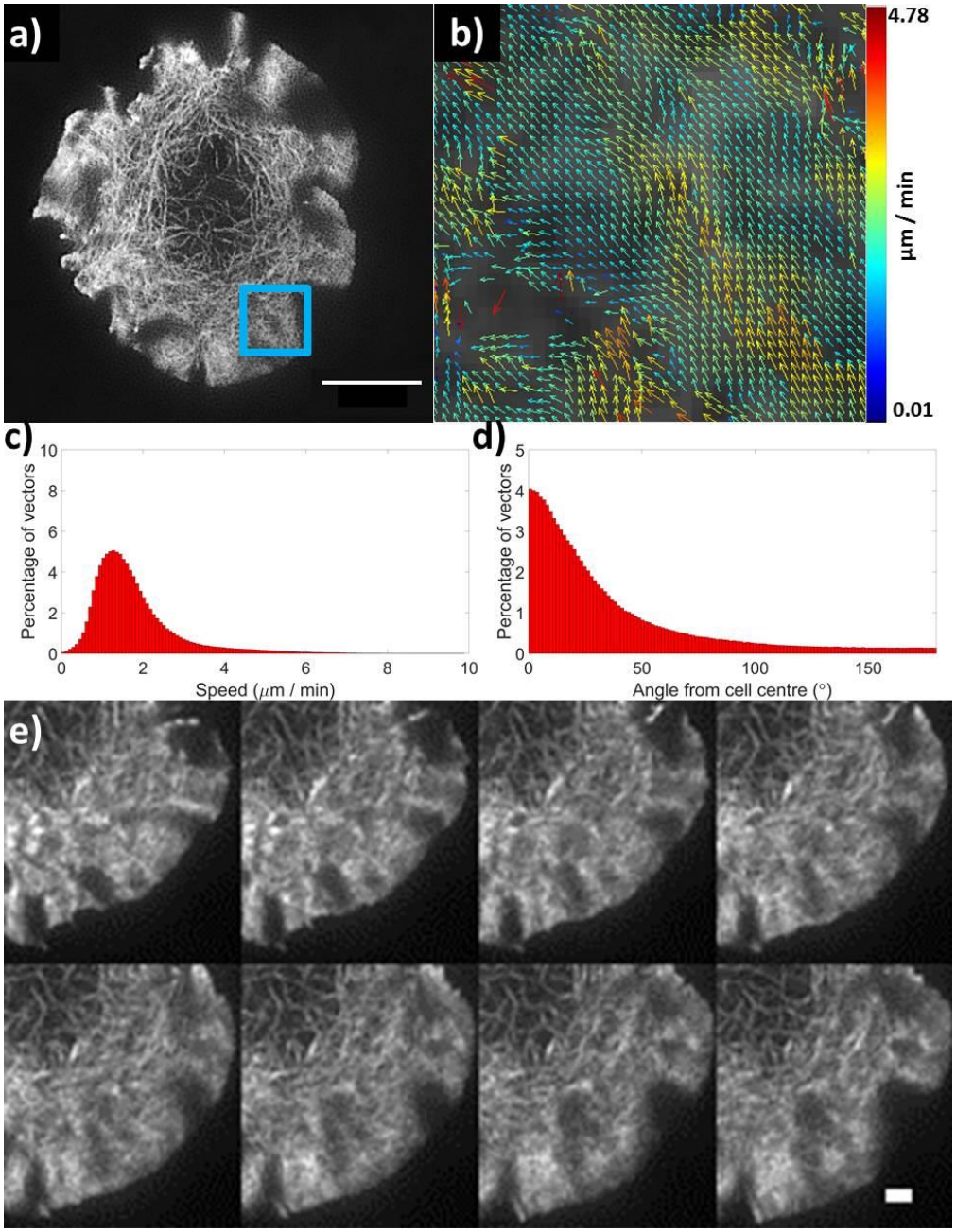

Figure 4.14 TIRF-SIM datasets analysed by image correlation. a) F-actin in Jurkat T cell forming immunological synapse is labelled by LifeAct-GFP, after STICS analysis vector maps (b) are generated from selected ROI's in the distal region of cell synapse and displayed as histograms reporting mean speed (c, 1.63 ± 0.46 µm) and mean flow directionality (d, 40.8 ± 23.35 °). A montage of 8 frames from the dataset in a) is shown in e) running from top left to bottom right, with increments of 5 frames, demonstrating labelled actin structures exhibit retrograde flow. n for c) and d) = 24, scale bars = 5 µm (for a) and 1 µm (for e).

Flow data was also represented as a rose plot (Figure 4.15a), where each bin represents vectors within a 1 ° range and each lines length corresponds to the number of vectors within that range. Retrograde flow information was plotted against the distance from the cell centre (Figure 4.15b) relative to the area of each cells region of interest. This showed a reduction in retrograde flow as the vectors approached the inner regions of the synapse. Together these results indicate that the highly organised retrograde flow is most present within the dSMAC, where actin density is highest, agreeing with previous findings using kymographs (Yi et al. 2012; Babich et al. 2012).

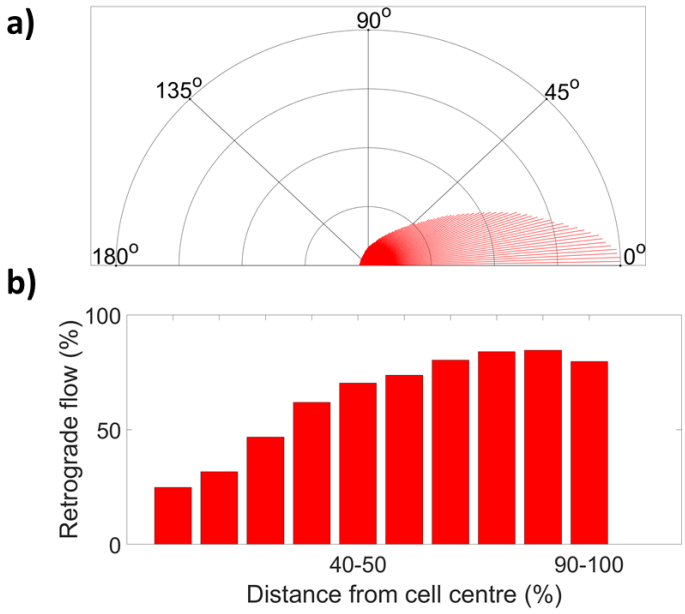

Figure 4.15 Rose plot and retrograde flow over distance. To further characterise the retrograde flow of F-actin retrograde flow was plotted on a rose plot (a), demonstrating the distribution of vectors over all angles. (b) Plots the percentage of retrograde vectors as a function of distance from the cell centre, relative to the area of the region of interest selected.

One drawback of using LifeAct is that it labels F-actin by binding to multiple monomers (Riedl et al. 2008), which could transiently stabilise F-actin structures and modulate polymerisation and depolymerisation rates. As such monomeric actin labelled with GFP offers the advantage of labelling F-actin without these transient binding events. STICS characterisation of the flowing F-actin cortex using TIRF-SIM was repeated using monomeric-actin labelled with GFP (Figure 4.16a). The generated vectors (Figure 4.16b) gave actin flow velocities of 2.15 ± 0.76 µm/min (Figure 4.16c); with 74.9 % of vectors retrograde in nature with a mean angle of 35.7 ° (Figure 4.16d).

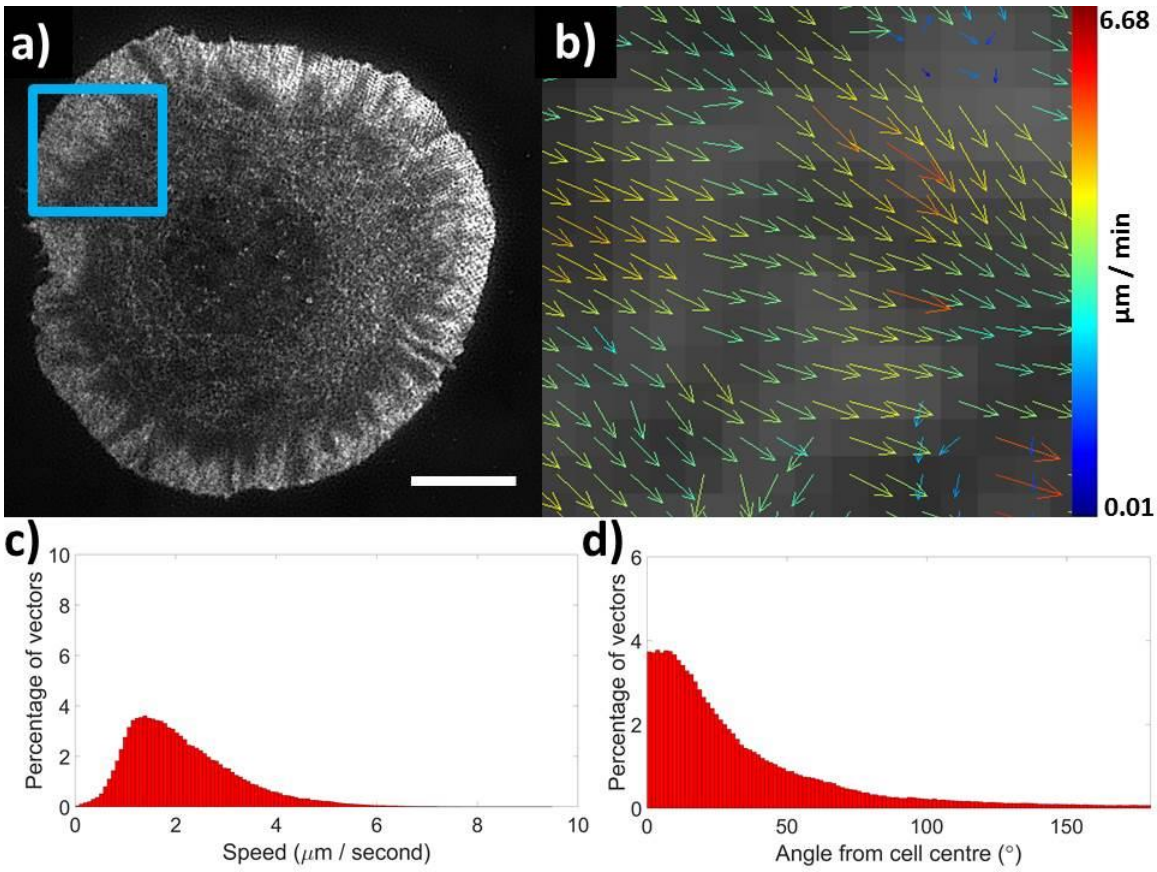

Figure 4.16 Image correlation of GFP-actin imaged by TIRF-SIM in Jurkat T cell forming immunological synapse. a) F-actin in Jurkat T cell forming immunological synapse is labelled by actin-GFP, following STICS analysis vector maps (b) are generated from selected ROI's in the distal region of cell synapse and displayed as histograms reporting mean speed (c, 2.15 ± 0.76 µm) and mean flow directionality (d, 35.7 ± 15.1 °). n = 13, scale bar = 5 µm.

These results along with velocities from primary human T cells expressing LifeAct-GFP are shown in Figure 4.17. Jurkat T cells expressing GFP-actin exhibited faster flow velocities compared to LifeAct-GFP expressing cells ($p = 0.01$). Primary human T cells expressing LifeAct-GFP were non-significant compared to Jurkat T cells expressing either LifeAct-GFP ($p = 0.1$) or actin-GFP ($p = 0.19$).

The difference between the LifeAct and actin-GFP expressing cells could be due to several factors. Firstly, LifeAct binds transiently to multiple actin monomers, potentially stabilising or crosslinking existing fibres and modulating flow. Secondly, GFP-actin expressing cells have by definition higher levels of monomeric actin available to polymerise; this will prolong the time cells can retain the faster elongation phase of actin polymerisation, before G-actin is depleted to the steady-state treadmilling phase.

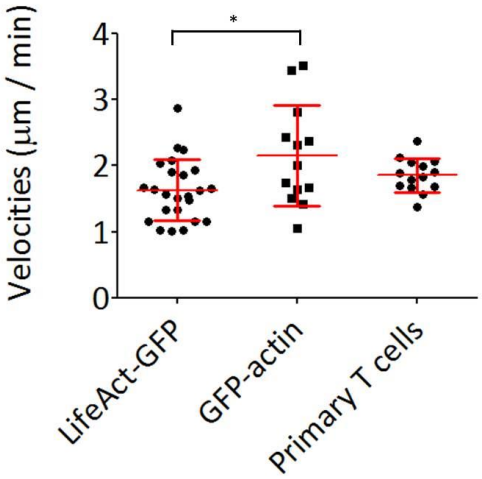

Figure 4.17 Comparison of Jurkat T cells expressing LifeAct-GFP or GFP-actin and Primary human T cells expressing LifeAct-GFP. LifeAct-GFP expressing Jurkat T cells exhibited slower flow speeds compared to actin-GFP expressing Jurkat T cells (p = 0.01), n = 24, 13 and 14.

To confirm STICS analysis does not correlate non-flowing (i.e. stationary or diffusive) fluorescence from TIRF-SIM datasets the cSMAC regions of Jurkat T cells exhibiting signal from static and diffusive F-actin were imaged and analysed (Figure 4.18a & b). Compared to dSMAC regions, the cSMAC did not exhibit net flow directionality (Figure 4.18c) with 28.3 % of vectors exhibiting retrograde flow towards the synapse centre.

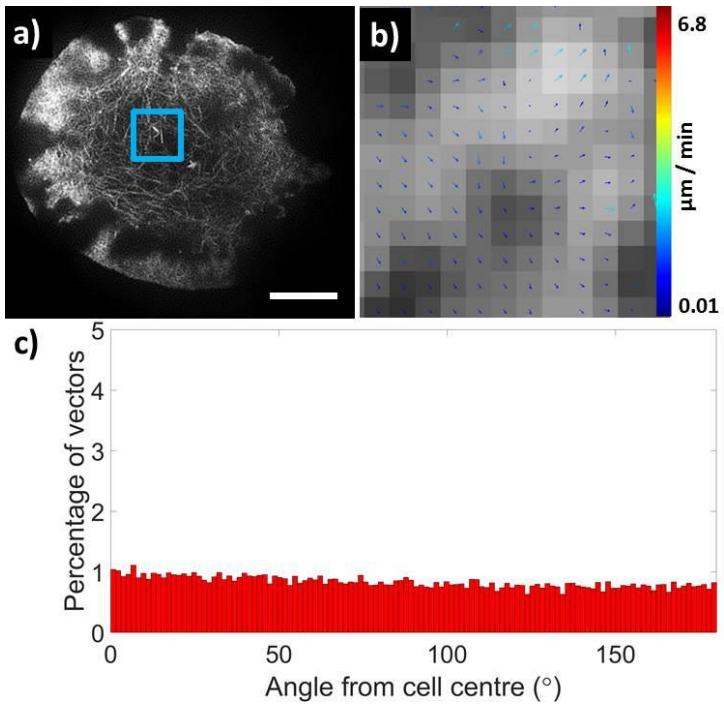

Figure 4.18 Retrograde actin flow does not continue into the cSMAC. After imaging F-actin in LifeAct-GFP expressing Jurkat T cells with TIRF-SIM (a) and selecting ROI's within the synapse centre for STICS analysis (b) it was shown any detected flow was undirected in these regions (c, n = 5). Scale bar = 5 µm.

Finally Jurkat T cells were transfected with LifeAct-GFP for actin visualisation and dropped onto an uncoated coverslip to represent resting condition. Imaging by TIRF-SIM (Figure 4.19a) and analysis by STICS (Figure 4.19b), demonstrated resting cells had significantly less retrograde flow compared to controls ($p < 0.05$, 72.2 ± 13.9 °, n = 3, 38.4 % retrograde; Figure 4.19c).

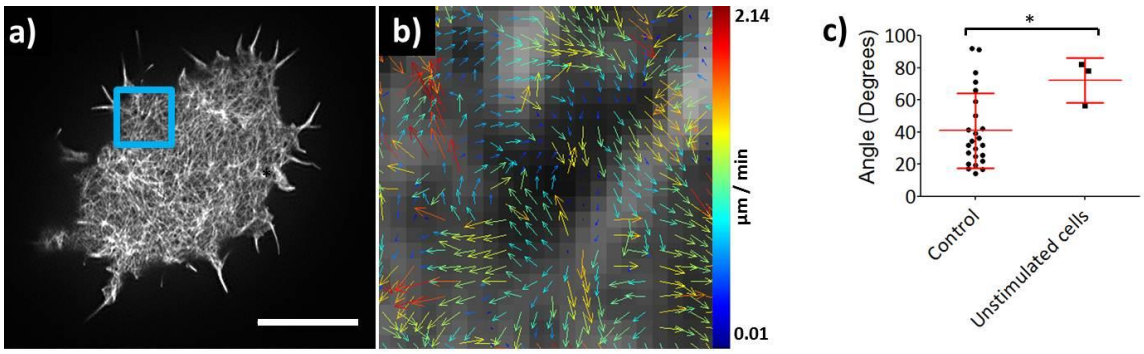

Figure 4.19 Jurkat T cell mean actin flow angle comparison. a) Jurkat T cells were imaged by TIRF-SIM against an uncoated coverslip, b) after STICS analysis vector maps demonstrated limited retrograde flow which was confirmed by quantitation. c) Compared to control cells stimulated on a coverslip coated with antibodies against CD3 and CD28 (n = 24), unstimulated cells (n = 3) had less directed inward flow ($p < 0.05$).

Together these results demonstrate STICS does not correlate any artefactual features of TIRF-SIM imaging, as generated vectors from samples with static signal exhibited no directed flow.

4.7. Discussion

In this chapter the nanoscale architecture of cortical actin was imaged using two SMLM methods, both dSTORM and IRIS of Jurkat T cells demonstrated a rich ring of F-actin at the dSMAC, which quickly diminished towards the synapse centre. Though dSTORM has been applied to elucidate many nanoscale structures before, including actin, and has been shown here to provide more precise localisations, the labelling process leads to a reduced number of fluorophores becoming attached to the structure of interest. This can limit the number of localisations captured by the detector in regions of dense structure such as the dSMAC of the T cell synapse. This is especially true if multiple fluorophores are activated within the diffraction limit of each other at the same time; causing them to be merged or rejected by post-acquisition analysis. This problem can be circumvented through modulating the laser powers and imaging buffer to reduce the number of fluorescing molecules, however this will prolong the time taken to image the structure of interest.

As can be seen in Figure 4.3**,** dSTORM of F-actin; even of distinct fibres within the cSMAC region, are visualised as discontinuous, partly due to the labelling and detection efficiencies of the imaging method. The technique was therefore extended to use IRIS, a method which improved the number of localisations and therefore better represented the continuous

structure of the actin cortex (Figure 4.6) partially due to the transient binding of the fluorophore.

Punctate actin structures within the cSMAC; particularly in the 10 minute synapses were visualised and may represent WASp mediated actin 'foci' which have been shown to be TCR-rich signalling territories (Kumari et al. 2015) and could be exhibiting relocation towards the synapse centre as has been seen with TCR microclusters (Kaizuka et al. 2007). This may be important for TCR downregulation and recycling for sustained signalling at the pSMAC (Varma et al. 2006; Das et al. 2004).

Due to the dynamic nature of the F-actin cortex and its importance in modulating the T cell synapse structure and signalling through time (Campi et al. 2005; Varma et al. 2006; Kaizuka et al. 2007; Yu et al. 2010; Yi et al. 2012), this imaging was then extended into the temporal dimension. Flow speed and directionality of cortical F-actin was analysed by image correlation spectroscopy, in combination with structured illumination this allowed nanoscale subregions to be imaged and quantified.

In line with previous observations and analysis by kymographs and speckle analysis (Babich et al. 2012; Yu et al. 2010; Kaizuka et al. 2007) the majority of F-actin flowed in a retrograde manner towards the synapse centre of Jurkat and primary human T cells. However these results improve previous methods by allowing whole fields of view to be analysed and therefore all fluorescence from flowing populations is quantified. Additionally, 2D STICS analysis of super-resolution imaging provided extensions in the spatial dimension, compared to kymographs; with improved fluctuation sampling and increased CF amplitudes compared to conventional microscopy.

Table 4.1 shows previously quantified actin flow during synapse formation from kymograph and speckle analysis using various experimental conditions. Compared to both LifeAct-GFP and GFP-actin results presented in this chapter (Figure 4.14 & Figure 4.16), analysis of the dSMAC region from previous studies agrees with F-actin flow speeds. The slightly slower speeds exhibited could highlight STICS correlating overall fluorescent signal; including that from dimmer structures, rather than selection of brighter structures, which are tracked through manual selection in kymograph analysis. As pixel intensity correlates with number of fluorescent molecules and actin retrograde flow is linked to the number of actin monomers, these brighter structures will contain more actin and could therefore exhibit faster polymerisation and retrograde flow dynamics.

Changes to retrograde flow with distance to the synapse centre were also demonstrated (Figure 4.15b), with a reduction of net directionality closer to the synapse centre. This correlates with previous findings that actin flow speed along with signalling microclusters also reduces towards the synapse centre (Yi et al. 2012). These results suggest polymerisation rates and flow speeds are a factor in the 'orderedness' of directionality, where lower speeds are associated with the pSMAC at sites dominated by myosin II motor dynamics, leading to more spurious flow directions.

The combination of TIRF-SIM and STICS techniques could be applied to any biological sample which resides close to the coverslip-specimen interface which exhibits molecular flow. This could include investigating coverslip proximal nanoscale dynamics of cells undergoing migration or division or dynamics of proteins or lipids labelled and residing close to or within the plasma membrane.

Though this combination of techniques can be applied to various samples it is limited by some factors. The temporal resolution of SIM microscopes is inherently limited by the time taken to acquire the 9 raw frames which make up the reconstructed image. As such any molecules of interest moving across the sinusoidal illumination pattern faster than the reorientation will create blurring artefacts. Additionally, regions of homogeneous signal can create 'honeycomb' regions of signal due to the raw images lacking contrast, while transforming data into and back from Fourier space can generate high resolution noise.

TIRF-SIM is inherently a 2D imaging modality, while this is advantageous for STICS analysis which assumes a 2D dataset; it is designed for capturing structures close to the coverslip-sample interface and cannot be used for analysis of 3D samples.

As with SIM, STICS represents a trade-off between spatial and temporal information; as the size of the correlation subregion along with the dynamics and size of the fluorescent sample influences how sensitive STICS is to different flowing populations. Larger and / or faster fluorescent signals require larger subregions for them to be captured and correlated before leaving a ROI. However larger ROI's reduces the information gained per dataset, as less CF's are produced and therefore fewer vectors.

Overall these results demonstrate the structural and temporal organisation of F-actin during formation of the T cell synapse utilising super-resolution imaging techniques and quantitative analysis.

Chapter 5 – TIRF-SIM-STICS for characterising flow modulation and actin-membrane cross-correlation

After validating the combination of TIRF-SIM and STICS analysis for quantifying F-actin flow, the technique was used in combination with drug treatments to analyse the actin cortex within the dSMAC regions of the T cell immunological synapse, elucidating actin's role in its formation and stability. Firstly, small molecule drugs which modulate the polymerisation and stability of actin fibres were used to investigate how changing the rates of actin polymerisation determined this quantifiable flow. Next blebbistatin, which inhibits myosin II motors, was used to investigate whether myosin motor proteins changed flow rates or directionality in the dSMAC. Finally, the role of membrane order for cortical actin flow within the dSMAC was investigated using 7KC, which reduces lipid order within the plasma membrane.

Actin and the plasma membrane are thought to interact, via ERM and transmembrane proteins, including those forming signalling microclusters and those within lipid ordered membrane regions such as LAT and the TCR (Lillemeier et al. 2006; Dinic et al. 2015). It was therefore hypothesised this retrograde flow may be conveyed to components of the membrane itself through these linkers. This was investigated by, firstly, staining and imaging the membrane with the lipophilic dye DiO during synapse formation, and using actin-modulating drugs to establish whether any observed flow was driven by actin polymerisation.

To assess any correlation between cortical actin and the plasma membrane, the novel combination of two-channel TIRF-SIM imaging with cross-correlation analysis was carried out. This was applied to the data which resulted, for the first time, in a correlation between the two systems' flow speeds and directionality. The actin-crosslinking protein α-actinin was studied as a possible modulator of actin flow and organisation. It is known to be enriched under, and drive clustering of, membrane receptors in lymphocytes (Hoessli et al. 1980; Geiger & Singer 1979) while silencing α–actinin reduced F-actin accumulation at the immunological synapse (Gordón-Alonso et al. 2012). Finally, membrane topography was investigated with IRM imaging, giving information on the 3D structure of the plasma membrane.

5.1. Drug treatments – cell viability

To characterise and quantify how modulating the polymerisation rates of actin or disrupting the membrane order of cells changed the F-actin flow speeds and directionality, treatments which affect these parameters were used as described in §3.6. To assess the toxicity of the dosages used here, an MTT assay was performed using primary human T cells cultured under

standard conditions. MTT assays use the dye 3-(4,5-dimethylthiazol-2-yl)-2,5-diphenyltetrazolium bromide, that turns from yellow to a purple formazan upon enzymatic conversion in viable cells. This leads to increased absorbance at 570 nm, indicating cell viability, while increased cell death is indicated by reduced absorbance. Incubation times of 1 hr gave viable cells time to convert the dye. Figure 5.1 shows, when compared to controls (absorbance value = 1.28 ± 0.14), the viability of cells was reduced within a 50/50 v/v dilution of DMSO (absorbance value = 0.51 ± 0.09, $p < 0.005$), while treatments used at their respective concentrations were not cell lethal for cytochalasin-D (Cyto-D; absorbance value = 1.22 ± 0.13, $p = 0.66$), jasplakinolide (jasp; absorbance value = 1.14 ± 0.04, $p = 0.17$) or 7KC (absorbance value = 1.18 ± 0.11, $p = 0.38$).

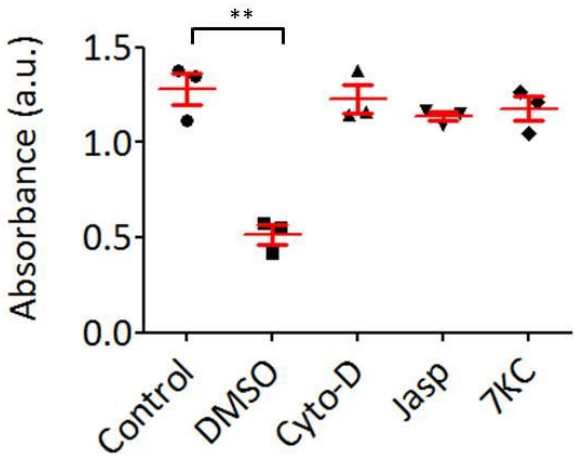

Figure 5.1 Cell viability assay of drug treatments. Primary T cells were incubated with drugs or DMSO for 1 hour prior to measuring the absorbance, where high absorbance indicates higher cell viability. Compared to control, cytochalasin-D ($p = 0.66$), jasplakinolide ($p = 0.17$), and 7KC ($p = 0.38$) were all nonsignificant, while DMSO treatments exhibited significant reduction in absorbance and therefore increased cell death ($p < 0.005$). ** $p < 0.005$.

Compared to actin-modulating treatments where concentrations are well characterised, there is less standardisation for lipid order modulating drugs such as 7KC. As such a drug dose response curve was produced for concentrations ranging from 2 µM to 20 µM. Cells stained with di-4-ANEPPDHQ, resting on a coverslip, were imaged on the Nikon confocal A1R at 0, 5, 10 and 20 minute intervals.

By collecting 2 channel data (Figure 5.2a-d), GP analysis of the plasma membrane (as described in §2.2.2) was achieved through selection of ROI's at the membrane (Figure 5.2e-h).

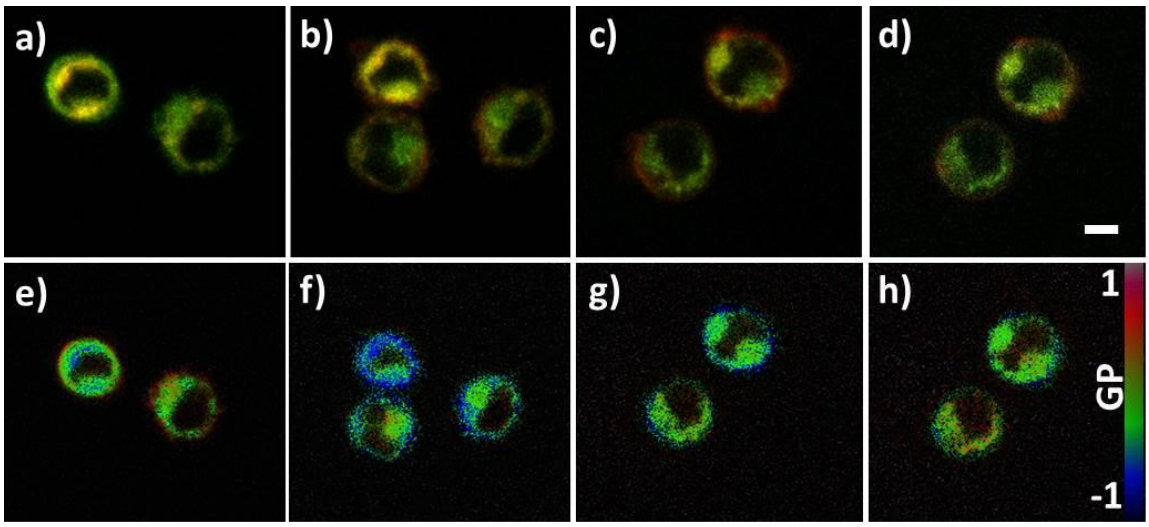

Figure 5.2 Membrane order disruption in Jurkat T cells following 7KC treatment. Ordered (green) and disordered (red) channels are merged at a) 0, b) 5, c) 15 and d) 20 minutes after 20 µM 7KC treatment. These images were quantified with GP analysis, providing order values of the same timepoints (e-h). Scale bar = 5 µm.

Figure 5.3 shows quantification by GP analysis for different 7KC dosages through time. After 20 minutes incubation time, compared to control cells (GP = 0.31 +/- 0.08), 7KC did not cause a significant reduction in in plasma membrane order after 2 µM treatment to (0.14 +/- 0.14, $p = 0.29$), but both 10 µM and 20 µM treatments did (-0.26 +/- 0.15, $p < 0.001$ and -0.13 +/- 0.1, $p < 0.005$; n = 3 per condition).

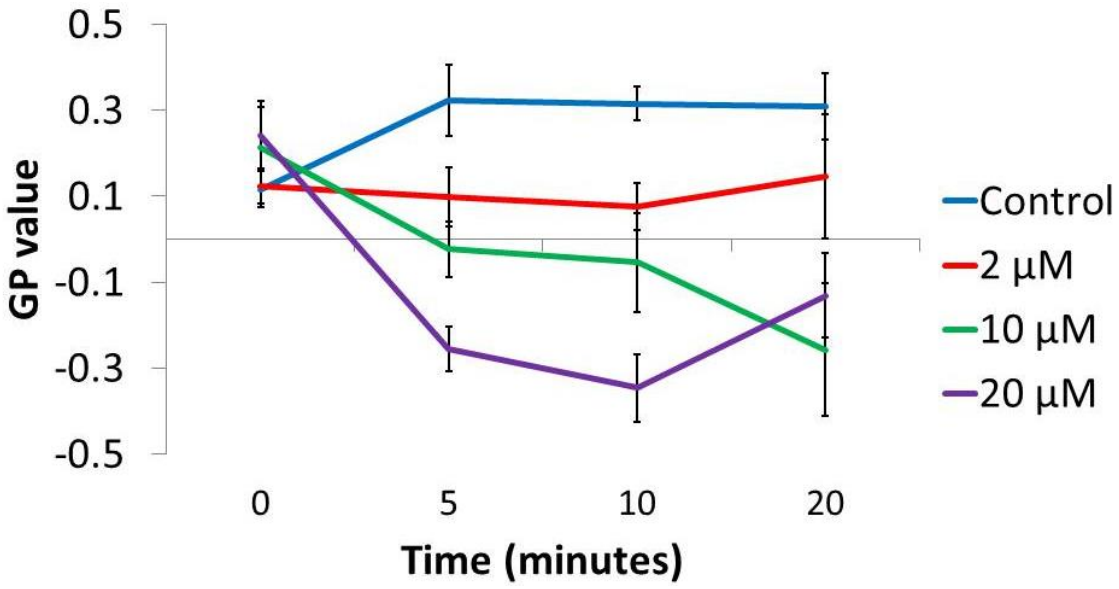

Figure 5.3 Dose response curve for 7KC in Jurkat T cells over time. Compared to controls the lipid order of the plasma membrane (as measured by GP analysis) was unaffected by lower (2 µM) doses, upon higher (10 & 20 µM) treatments the membrane order was significantly disrupted after 5 minutes with this disruption maintained for 20 minutes, n = 3.

In conclusion, and based on these experiments, we selected 2 µM for cyto-D and jasplakinolide treatments, and both 10 and 20 µM for 7KC drug treatments to better characterise the effects of membrane order on T cell synapse formation and stability. The MTT assay showed cells remained viable during these treatments, consistent with those dosages used in the literature for cyto-D [1 – 5 µM; (Forscher & Smith 1988; Henson et al. 1999)] and jasplakinolide (1 µM; (Babich et al. 2012)).

5.2. Modulating actin dynamics at the immunological synapse

To quantify rate changes in F-actin flow speeds and directionality, drug treatments were performed on cells forming synapses. These drug treatments reduce or increase actin polymerisation rates, or disrupt membrane lipid order. STICS provided quantification of treatment effects on cortical F-actin dynamics, allowing analysis of regions within the dSMAC. Figure 5.4**,** Figure 5.6 and Figure 5.10 show speed and directionality results after Jurkat T cells were treated with each drug, during immunological synapse formation.

Compared to controls (1.63 ± 0.46 µm) cyto-D (2 µM) treated cells showed significantly reduced F-actin retrograde flow at the dSMAC (0.99 ± 0.27 µm/min $p < 0.001$, $n = 10$), this was expected as retrograde flow has been confirmed to be driven by actin polymerisation (Babich et al. 2012). However the additional directionality information provided by STICS showed compared to control conditions (72.9 % retrograde vectors with a mean angle of 40.8 ± 23.35 °) the flow was also significantly scrambled by cyto-D. Upon treatment, fewer vectors were orientated towards the synapse centre (Figure 5.4) with 53.5 % of vectors being retrograde in nature and a mean vector angle of 63.7 ± 21.0 ° ($p = 0.01$).

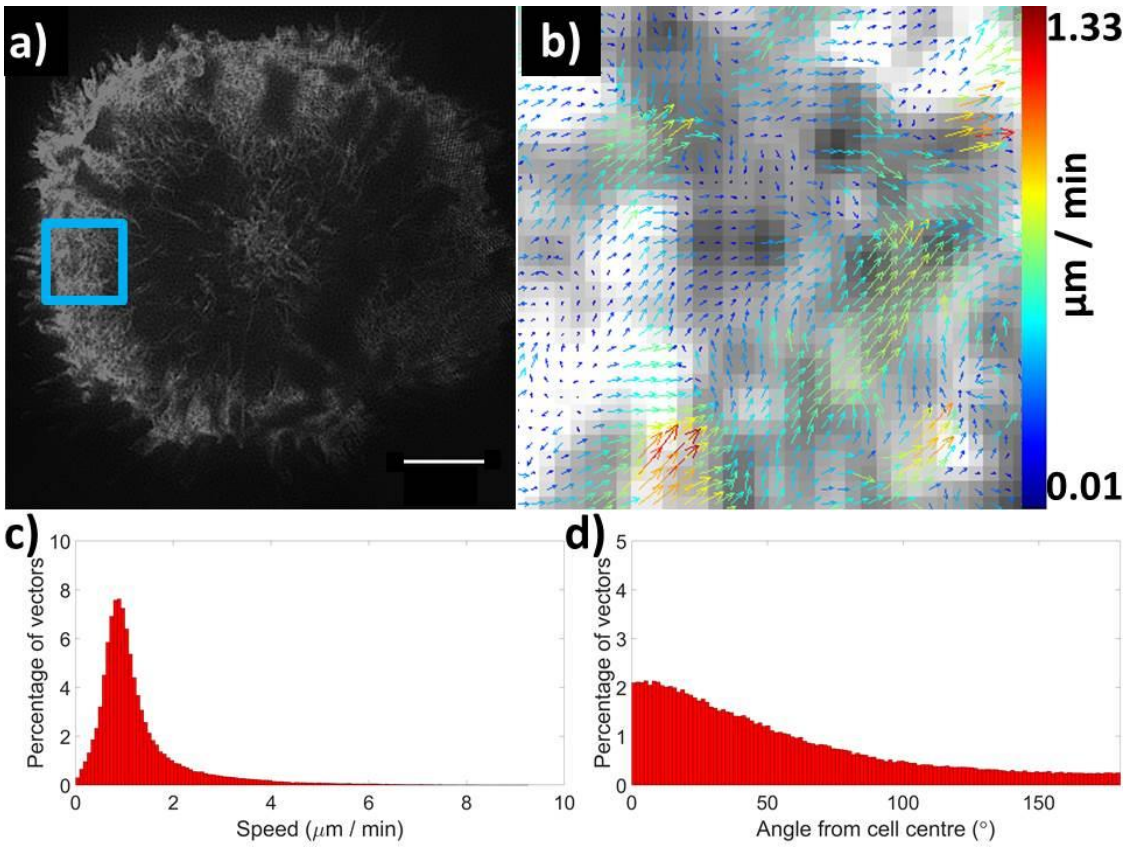

Figure 5.4 Image correlation of F-actin flow in Jurkat T cell after cytochalasin-D treatment. After imaging (a), STICS vector maps (b) are from the ROI selected from the distal region of the cell synapse and displayed as histograms reporting on individual vector speed (c) and flow directionality (d, n = 10, scale bar = 5 µm).

To investigate whether increased disruption of flow speed created more disordered flow, directionality cell mean flow speeds were plotted against average angles (Figure 5.5), demonstrating a non-significant correlation (r^2 = 0.03, p = 0.6).

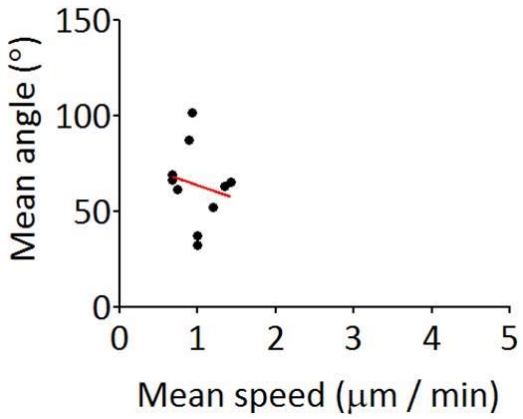

Figure 5.5 Correlation between cell average flow speeds and mean angle of F-actin after cytochalasin-D treatment. The negative correlation (r^2 = -0.03) between increased F-actin flow speed and more ordered cortical actin directionality was non-significant (p = 0.6).

Jasplakinolide (2 µM) showed a non-significant increase (to 2.07 ± 1.06 µm/min $p = 0.06$, $n = 27$) in F-actin flow speed (Figure 5.6). As mentioned in §3.6, jasplakinolide increases actin polymerisation but also stabilises pre-existing fibres. As cells contain a finite pool of G-actin, slower flow speeds may be due to lower G-actin reserves owing to longer jasplakinolide exposure, while faster flows could be indicative of cells which still have G-actin available. In most cases however the direction of flow was significantly scrambled (56.9% retrograde, 61.1 ± 27.5 ° $p < 0.01$) indicating a drug induced increase in polymerisation rates leads to erroneous system flow. This was confirmed when mean flow speeds were plotted against average angles for individual cells (Figure 5.7), demonstrating a significant positive correlation ($r^2 = 0.18$, $p < 0.05$).

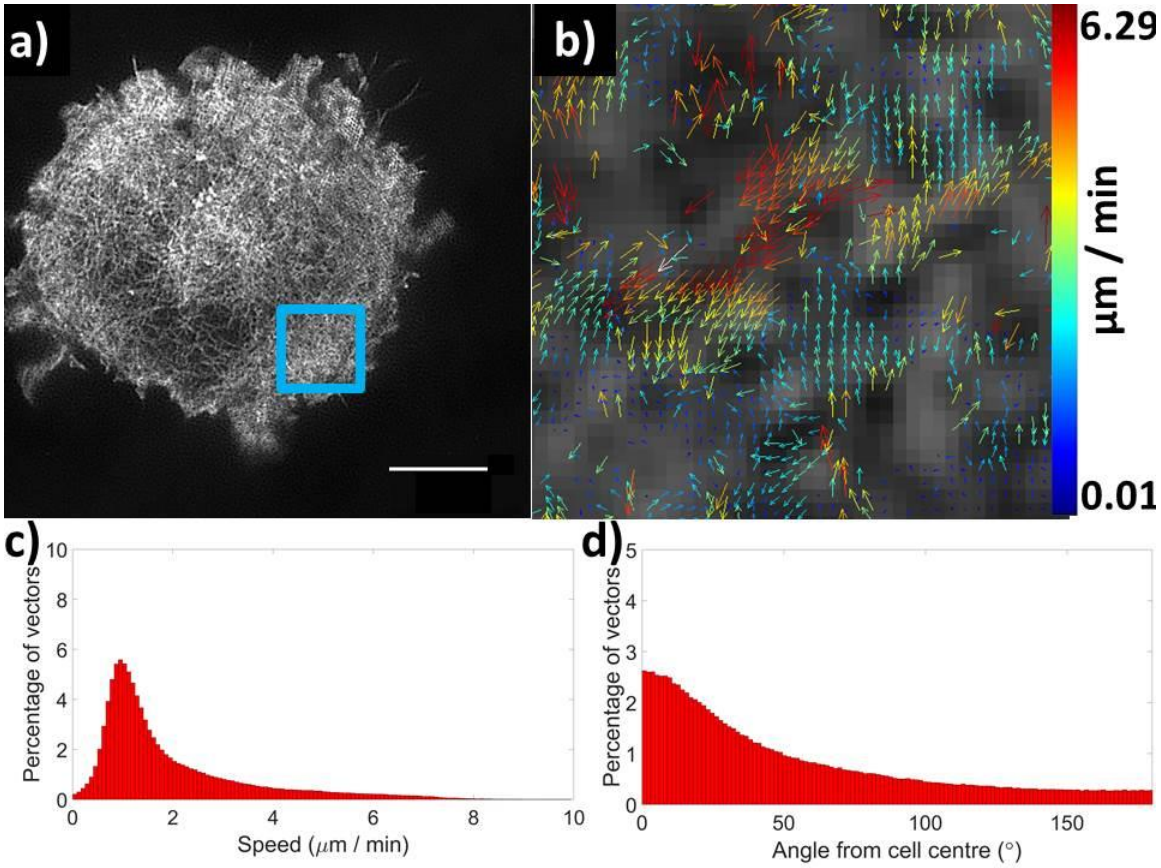

Figure 5.6 Image correlation of F-actin flow in Jurkat T cell after jasplakinolide treatment. After imaging (a), STICS vector maps (b) are from the ROI selected from the distal region of the cell synapse and displayed as histograms reporting speed (c) and flow directionality (d, n = 27, scale bar = 5 µm).

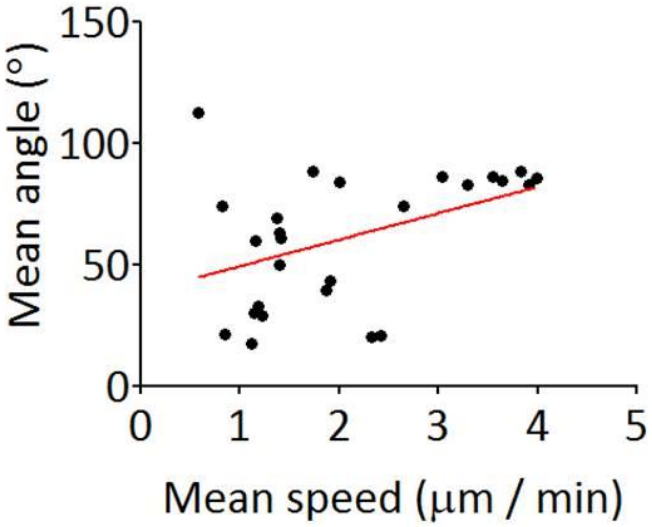

Figure 5.7 Correlation between cell average flow speeds and mean angle of F-actin after jasplakinolide treatment. The positive correlation (r^2 = 0.18) between increased F-actin flow speed and disruption of cortical actin directionality was significant (p < 0.05).

Summarised results from actin modulating drugs and control conditions from §4.6 are shown in Figure 5.8. Drug treatments had varying effects on the flow speed and directionality of F-actin. Velocities were reduced when cyto-D was added and increased after the addition of jasplakinolide. Directionality was shown to be linked with the rate of actin polymerisation and possibly the levels of G-actin, with any drug induced deviation of F-actin speed resulting in a scrambling of retrograde flow.

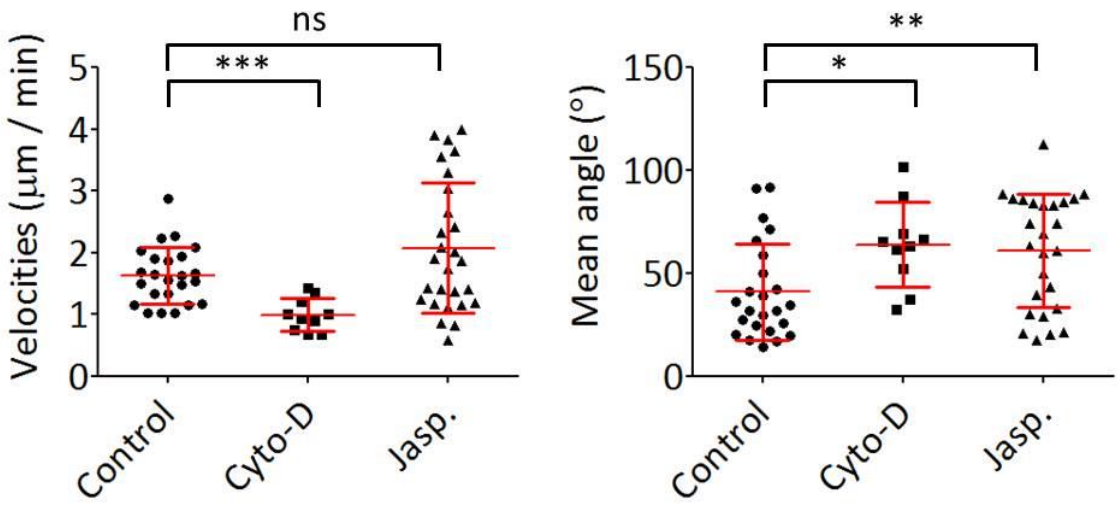

Figure 5.8 Scatterplots of mean cell velocities (left) and angles (right) for F-actin in the dSMAC. Compared to control cells, cytochalasin-D treated cells had significantly slower (p < 0.001) average speeds and significantly increased mean angles (p = 0.01), as did jasplakinolide (p < 0.01), however increasing actin polymerisation and stabilising actin fibres had no significant effect on the flow speed (p = 0.06). ns = non-significant, * p < 0.05, ** p < 0.005, *** p < 0.001.

The rate of actin polymerisation is therefore regulated, maintaining the directionality of retrograde flow seen within the T cell synapse. Additionally, modulating actin polymerisation has a striking effect on the synapse architecture, with the cortex unable to consistently maintain the classic actin rich periphery or actin poor synapse centre. This is reiterated in Figure 5.9, showing radial plots of control cells, where the characteristic dSMAC peak in actin signal intensity is diminished upon cyto-D or jasplakinolide treatments.

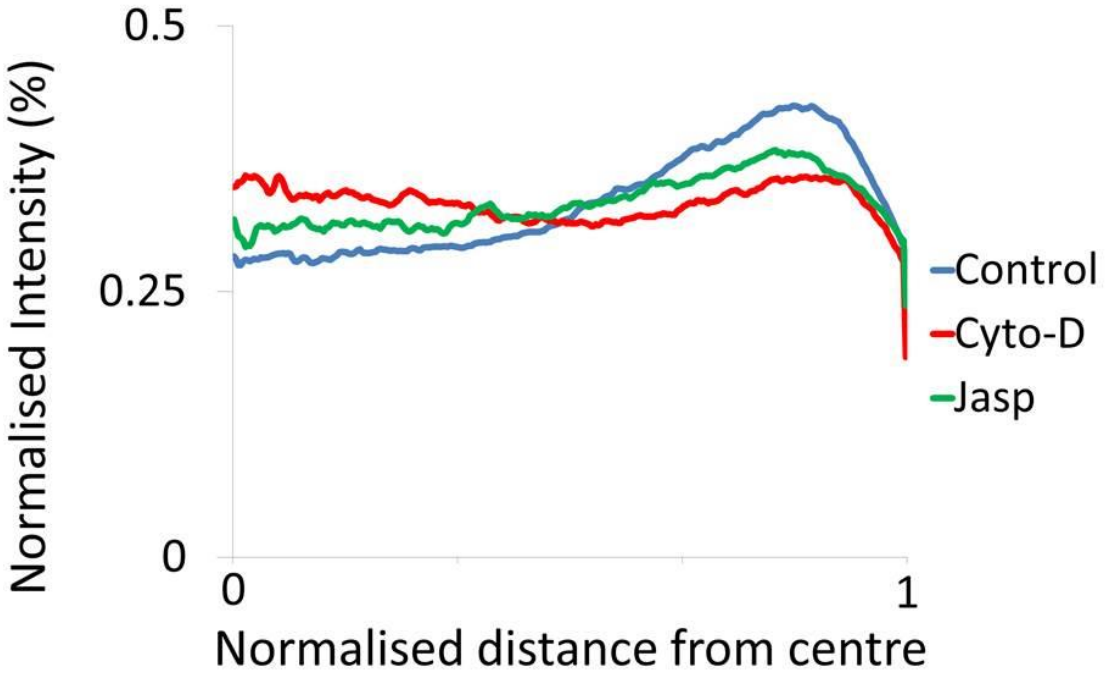

Figure 5.9 Radial profile plots of actin at the immunological synapse following actin modulating treatments. Images from TIRF-SIM data were analysed for actin intensity and normalised against total signal for comparison between treatments. Control cells exhibited the characteristic peak around the dSMAC region while, following cytochalasin-D and jasplakinolide treatments, these peaks were reduced with actin distributed more homogeneously through to the cSMAC. n = 10.

The data here signify a role of actin turnover in synapse architecture, with disruption or increases in actin polymerisation reducing the retrograde flow of the actin network, and changing the overall distribution of cortical actin. For the first time, these drug treatments were used in combination with TIRF-SIM and STICS analysis to better characterise the retrograde flow speed and directionality, providing detailed insight within nanometre scale subregions.

5.3. Modulating actin dynamics through membrane order and motor proteins

Through transmembrane proteins, the actin cortex and plasma membrane are thought to interact with each other (Kusumi, Ike, et al. 2005). Actin modulating proteins such as talin and WASp (when activated by $PI(4,5)P_2$), and transmembrane proteins including LAT and the TCR

complex, preferentially occupy lipid ordered membrane domains (Saarikangas et al. 2010; Dinic et al. 2015; Owen et al. 2012). Disrupting the actin cytoskeleton leads to a reduction of membrane lipid order and declustering of order-dependent signalling molecules including Lck (Chichili et al. 2012). Additionally, the actin rich membrane of the dSMAC has been shown to be more ordered than the synapse centre (Dylan M Owen et al. 2010). It was therefore reasoned that disruption of these domains could modulate actin polymerisation, or reduce the highly orchestrated retrograde nature of the flow.

As membrane order corresponds to lipid packing, these regions may have higher viscosities and membrane-actin interactions may result in slower or faster actin flow. This was demonstrated for diffusion of the transmembrane protein LAT, in cells exhibiting different liquid ordered domains (Owen et al. 2012), whether this is also reflected in the cytoskeleton as it drags transmembrane proteins through more or less viscous regions is unknown. To test this hypothesis, the order disrupting molecule 7KC was used. When adding 10 µM 7KC to Jurkat T cells forming an immunological synapse to disrupt membrane packing and therefore lipid order no significant difference was observed, compared to control conditions (Figure 5.10) for either speed (1.61 ± 0.49 µm/min, $p = 0.88$, $n = 24$) or directionality, with 73.8 % of vectors retrograde in nature and a mean angle of 35.6 ± 10.3 ° ($p = 0.32$).

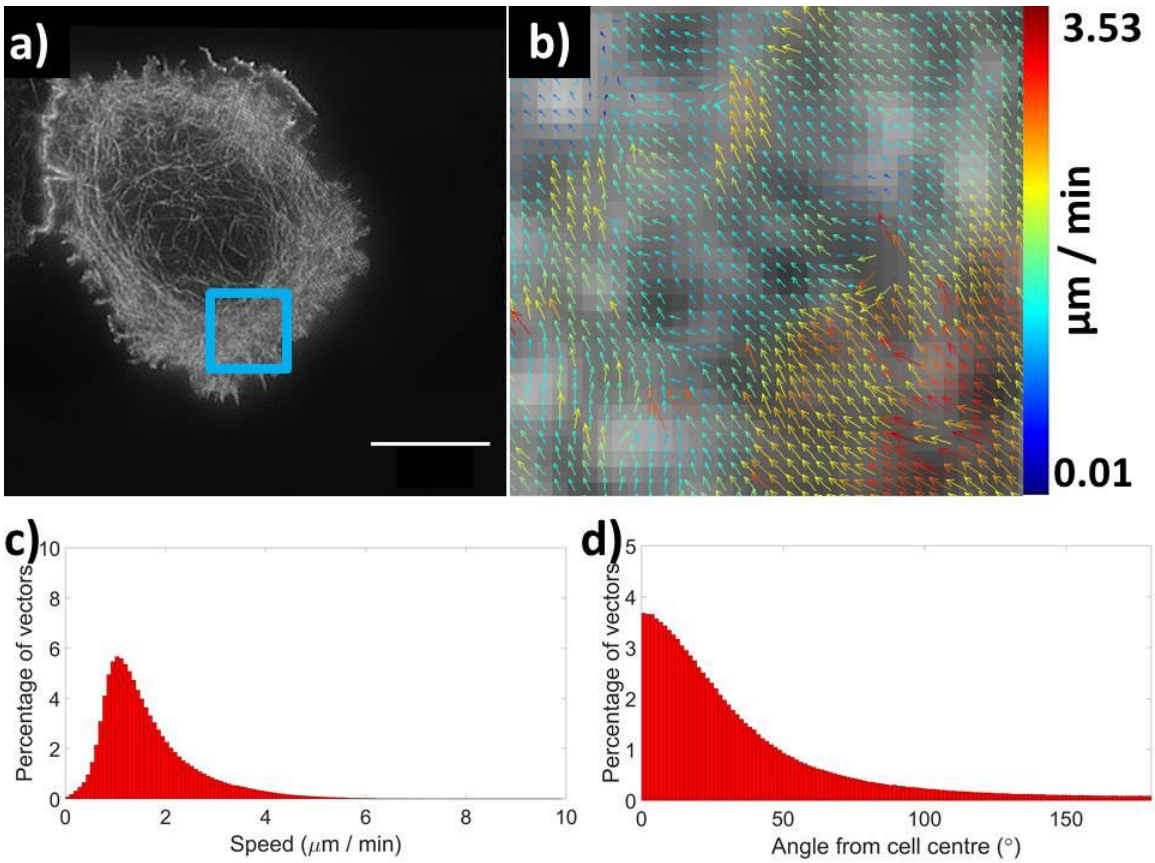

Figure 5.10 Image correlation of F-actin flow in Jurkat T cell after 10 µM 7KC treatment. After imaging (a), STICS vector maps (b) are from the ROI selected from the distal region of the cell synapse and displayed as histograms reporting speed (c) and flow directionality (d, n = 24, scale bar = 5 µm).

However, with the addition of 20 µM 7KC (Figure 5.11) cells exhibited increased actin flow speeds (2.1 ± 0.22 µm/min $p < 0.03$, n = 7) but a non-significant reduction in retrograde flow; mean angle 51.8 ± 12.1 ° ($p = 0.25$) with 56.6 % of vectors retrograde in nature.

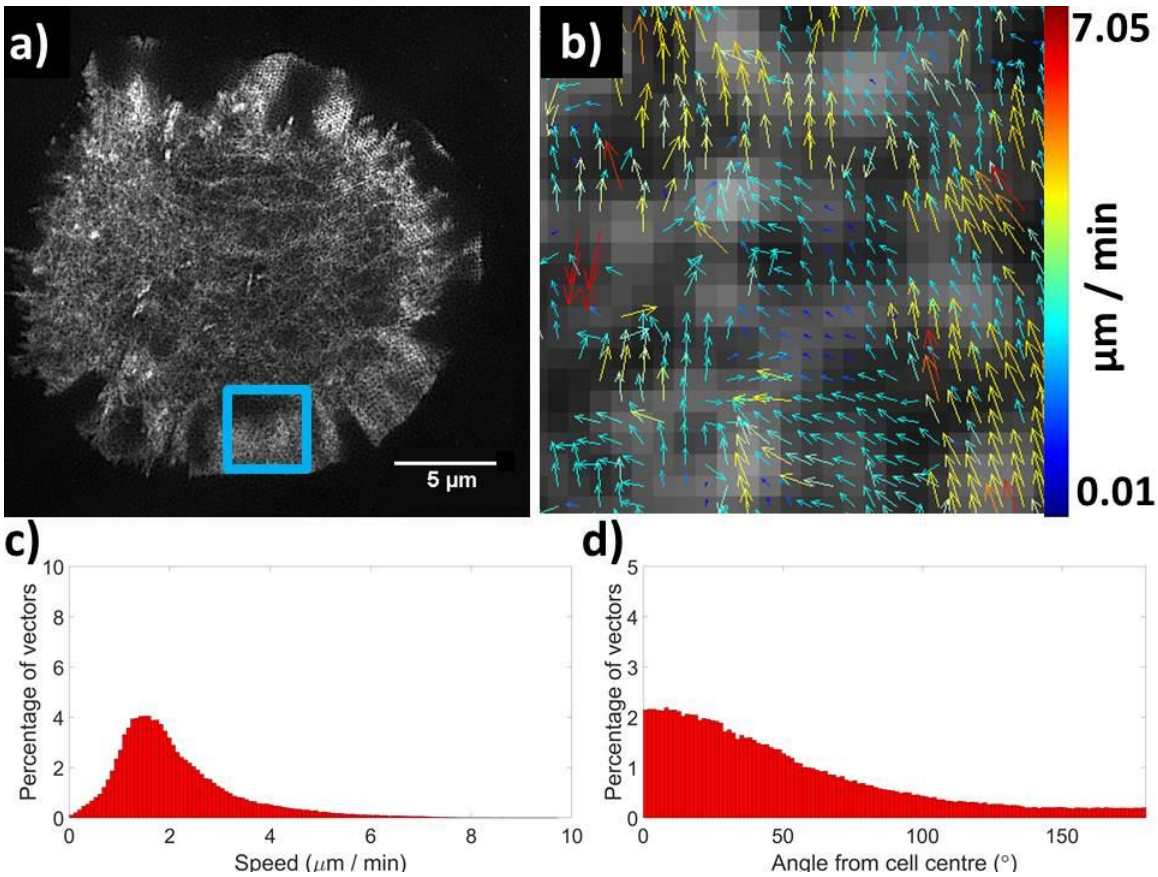

Figure 5.11 Image correlation of F-actin flow in Jurkat T cell after 20 µM 7KC treatment. After imaging (a), STICS vector maps (b) are from the ROI selected from the distal region of the cell synapse and displayed as histograms reporting speed (c) and flow directionality (d, n = 7, scale bar = 5 µm)

To assess the distribution of actin within cells treated with 7KC, radial profiles were plotted (Figure 5.12). Here a dose dependent response was observed, with 10 µM 7KC treated cells exhibiting increased peak intensity within the dSMAC region of the synapse and less actin present in the synapse centre. 20 µM treated cells had a more homogeneous distribution of actin compared to both controls and 10 µM 7KC treated cells. This may indicate a disruption of the localisation of actin polymerisation machinery such as WASp, which is known to reside within more ordered regions of the plasma membrane when mediating with actin polymerisation proteins Arp2/3 and Cdc42 (Sasahara et al. 2002).

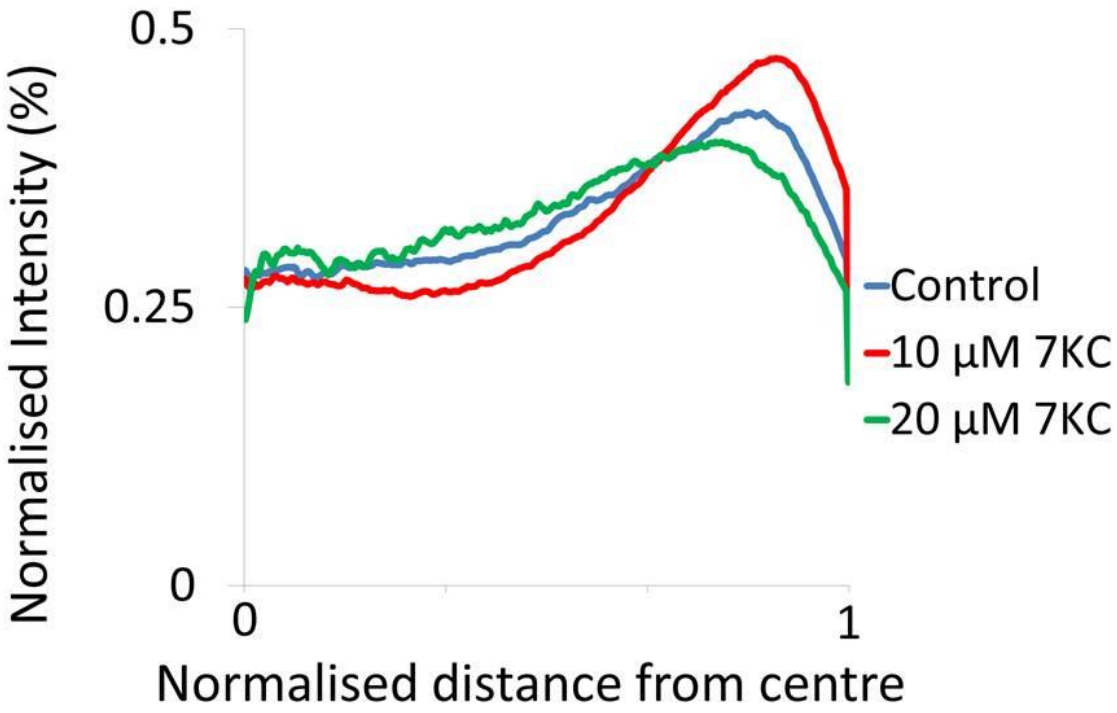

Figure 5.12 Radial profile plots of actin at the immunological synapse following membrane order disruption. Images from TIRF-SIM data were analysed for actin intensity and normalised against total signal for comparison between treatments. Control cells exhibited the characteristic peak around the dSMAC region while, following 10 µM 7KC treatment, these peaks were increased with actin distributed more towards the dSMAC (n = 10). After 20 µM 7KC treatment, cells exhibited a reduced dSMAC peak compared to both controls and 10 µM 7KC cells (n = 7).

Another potential mechanism for modulating transmembrane protein and actin flow is the motor protein myosin IIA. This molecule drives the retrograde flow of so called acto-myosin arcs; the tangential fibres present in the pSMAC (Yi et al. 2012). However as myosin IIA is not located in the dSMAC (Yi et al., 2012 & Figure 4.1a, §4.1), it is not believed to contribute to flow speeds within the dSMAC (Babich et al. 2012).

To test this hypothesis Jurkat T cells were treated with the same concentration of blebbistatin, a myosin IIA inhibiting drug, as previous studies (50 µM; (Babich et al. 2012; Yi et al. 2012)). In line with previous studies, cells were dropped onto a stimulatory coverslip after 30 minutes incubation time with the drug and formed a synapse as before; with flow speeds captured using TIRF-SIM and STICS analysis. As blebbistatin is inactivated with 488 nm light (Sakamoto et al. 2005), actin was imaged using LifeAct-mCherry and 561 nm excitation light. Compared to control speeds (3.26 ± 0.55 µm/min, n = 12) and directionality (59.6 ± 14.5 °, p = 0.05, n = 16) with 51.3 % of vectors retrograde (imaged on the same day), blebbistatin treated cells exhibited no speed changes (2.73 ± 0.80 µm/min, p = 0.06, n = 16) or directionality (69.9 ± 12.2 °, p = 0.05, n = 16) with 39.5 % of vectors retrograde in nature.

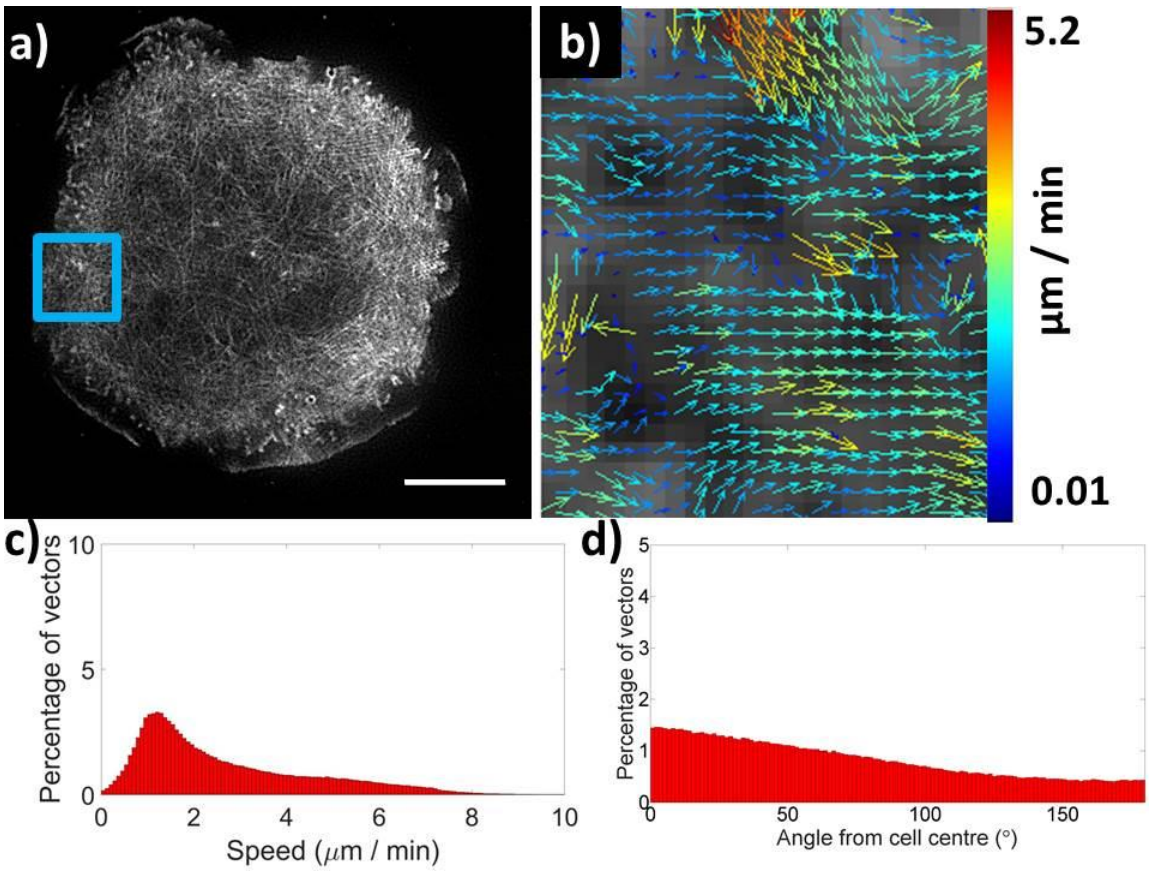

Figure 5.13 Image correlation of F-actin flow in Jurkat T cell after 50 µM blebbistatin treatment. After imaging (a), STICS vector maps (b) are from the ROI selected from the distal region of the cell synapse and displayed as histograms reporting speed (c) and flow directionality (d, n = 16, scale bar = 5 µm).

These results of membrane order and motor protein disruption are summarised, compared to their respective controls in Figure 5.14. 7KC at higher concentration had an effect on actin flow speed within the dSMAC but not its directionality. Inhibiting myosin IIA activity had no effect on actin flow within the dSMAC, when compared to same-day controls ('Control (b)') imaged with LifeAct-mCherry for consistency. Differences in speeds between LifeAct-GFP and LifeAct-mCherry may be due to multiple reasons: mCherry is not as bright as GFP, and imaging with 561 nm excitation light reduces the resolution of the reconstructed SIM image. Together these factors will reduce image contrast and may introduce noise into the data before analysis, leading to increased erroneous vectors or less robust generation of CF's which may be rejected by the STICS quality control filter (as described in §3.9). Briefly, where image noise correlation is similar to the flowing correlation, subregions are aborted and when vectors exhibit deviation from neighbouring vectors, they are aborted.

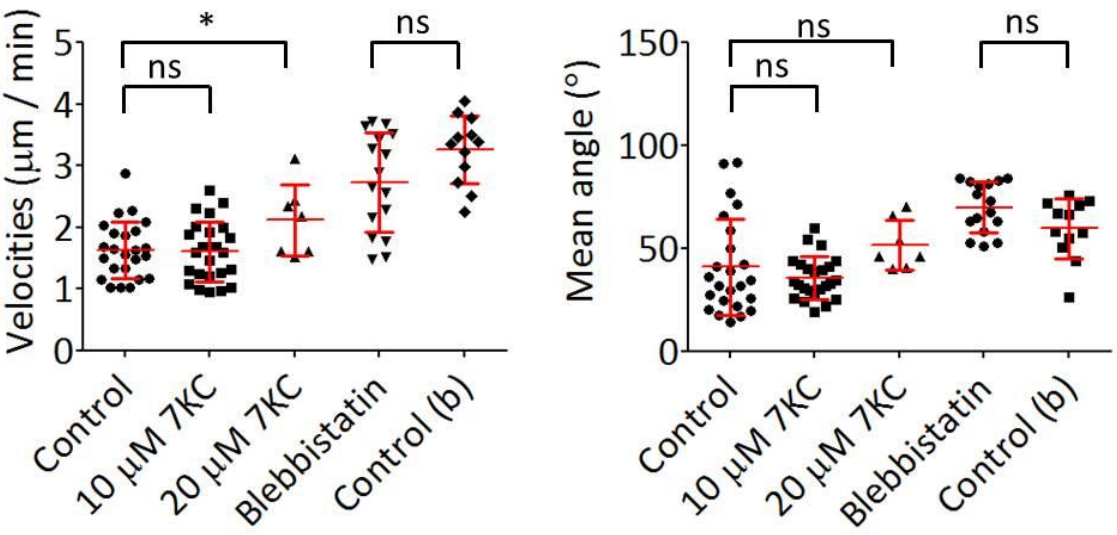

Figure 5.14 Scatterplots of mean cell velocities (left) and angles (right) for F-actin in the dSMAC. Compared to control cells, disruption of membrane order with 10 µM 7KC had no significant effect on the speed or directionality (p = 0.88 and 0.32), while increased disruption through 20 M 7KC did significantly affect actin speeds (p = 0.03). Disruption of myosin IIA with blebbistatin had no effect on actin flow speed or directionality (p = 0.06 and 0.05). ns = non-significant, * p < 0.05.

These results demonstrate cells may rely on balancing lipid order within the membrane to modulate or sustain actin polymerisation during synapse formation. With higher levels of disruption with 7KC disrupting both actin speed within the dSMAC and overall actin architecture as demonstrated by radial profile plots.

Though LifeAct has been shown not to interfere with actin dynamics (Riedl et al., 2008), it labels F-actin by transiently binding to multiple monomers and also binds to monomeric actin with 30 times higher affinity than filaments, potentially transiently stabilising fibres. Therefore control and drug treatment experiments were repeated with cells expressing monomeric actin-GFP to label actin structures without transient binding (Figure 5.15 & Figure 5.16). Control and drug treatment results were both similar to LifeAct data, with cyto-D significantly slowing actin flow ($p < 0.003$) and disrupting actin directionality ($p < 0.0005$). Jasplakinolide treated cells were not significantly different for either flow speed (0.07) or direction ($p = 0.1$) versus controls. Control results differ slightly from LifeAct results with higher retrograde flow speeds, possibly due to the overexpression of monomeric actin within the cells. This would also explain why jasplakinolide treatment (which increases polymerisation rates) reduces the mean angles of F-actin flow in actin-GFP experiments (Figure 5.16), as there is a greater amount of monomers contained within the cell, to continue driving retrograde flow, even after fibre stabilisation.

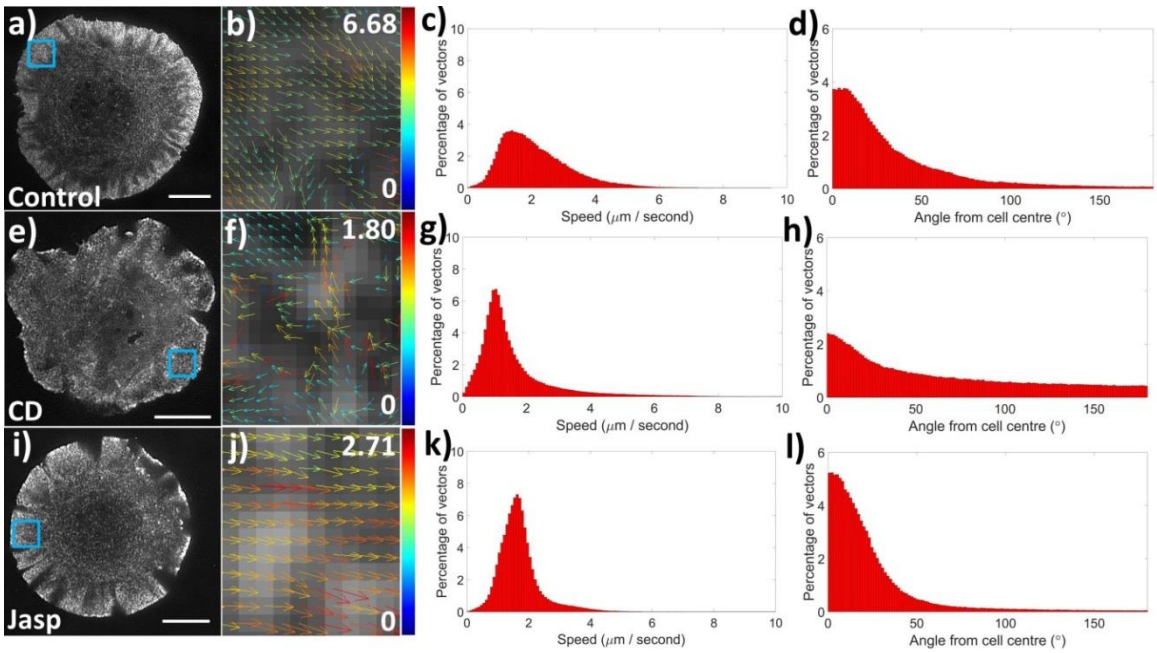

Figure 5.15 Actin-GFP flow characterised using TIRF-SIM and STICS analysis. Images show characterisation of monomeric actin flow in Jurkat T cells, shown are TIRF-SIM images (a, e, i) of cells 5 mins after contact with a stimulatory coverslip and following different treatments (labelled bottom left of images). ROI's within the blue boxes show output vector maps from STICS analysis (b, f, j). Scale bar = 5 µm. Graphs show STICS outputs of normalised F-actin flow speeds (c, g, k) or directionality (d, h, l). Controls: 2.15 ± 0.76 µm, n = 13. Cytochalasin-D (C-D): 1.39 ± 0.42 µm, n= 15. Jasplakinolide (Jasp): 1.63 ± 0.43 µm, n = 10.

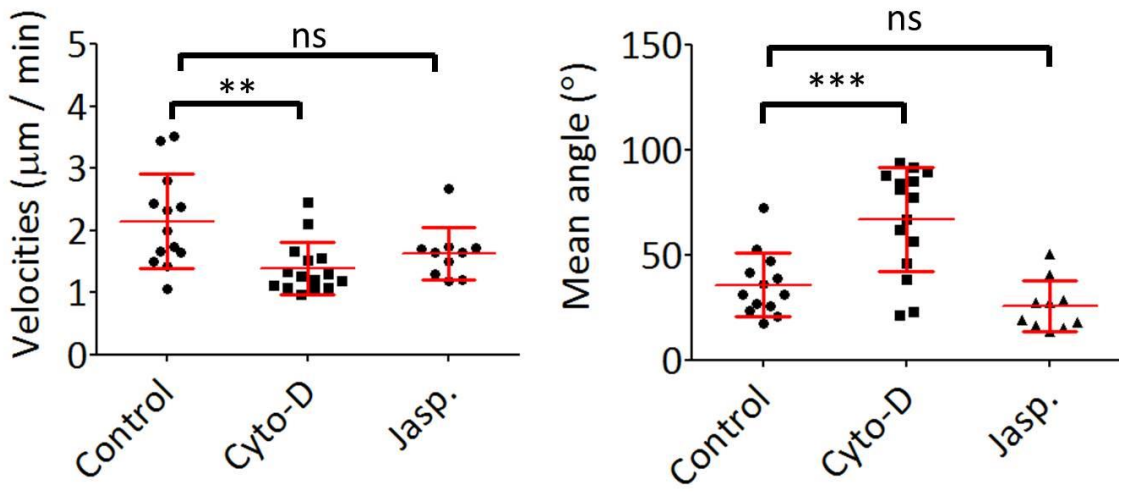

Figure 5.16 Scatterplots of mean cell velocities (left plot) and angles (right plot) for different drug treatments. Compared to control cells, cytochalasin-D treated cells had significantly slower ($p < 0.005$) average speeds. For directionality, the actin-modulating cytochalasin-D increased the mean angle significantly ($p < 0.001$). Increasing actin polymerisation and stabilising actin fibres had no significant effect on the speed or directionality of cell means ($p = 0.07$ and 0.1). ns = non-significant, ** $p < 0.005$, *** $p < 0.001$.

Together these results build on previous findings that dSMAC cortical actin flow speed is based on polymerisation (Babich et al. 2012; Bunnell et al. 2001; Yi et al. 2012), here this has been

extended with the findings that directionality is also dependent on regulated actin polymerisation, possibly due to the critical concentration of G-actin. Here analysis of the entire synapse periphery was quantified, providing cell-level characterisation of vectors representing sub-diffraction scale correlations. This retrograde flow was independent of myosin IIA activity but, for the first time, was linked to membrane order, as seen by 7KC treatments. These findings highlight a potential link between the actin cortex and plasma membrane regarding maintenance and sustainability of actin dynamics.

To establish whether the control speeds and retrograde flow observed in Jurkat T cells were similar to primary human T cells, experiments were repeated using cells isolated from human blood (Figure 5.17). Compared to quantification from Jurkat T cells, primary human T cells expressing LifeAct-GFP exhibited F-actin flow speeds of 1.86 ± 0.26 µm/min (n.s.) and a mean angle of 52.8 ± 10.6 ° (n.s.) with 54.9 % being retrograde in nature. The mean angle was reduced and flow less retrograde compared to Jurkat T cells (which exhibited 40.8 ± 23.4 ° and 72.9 %).

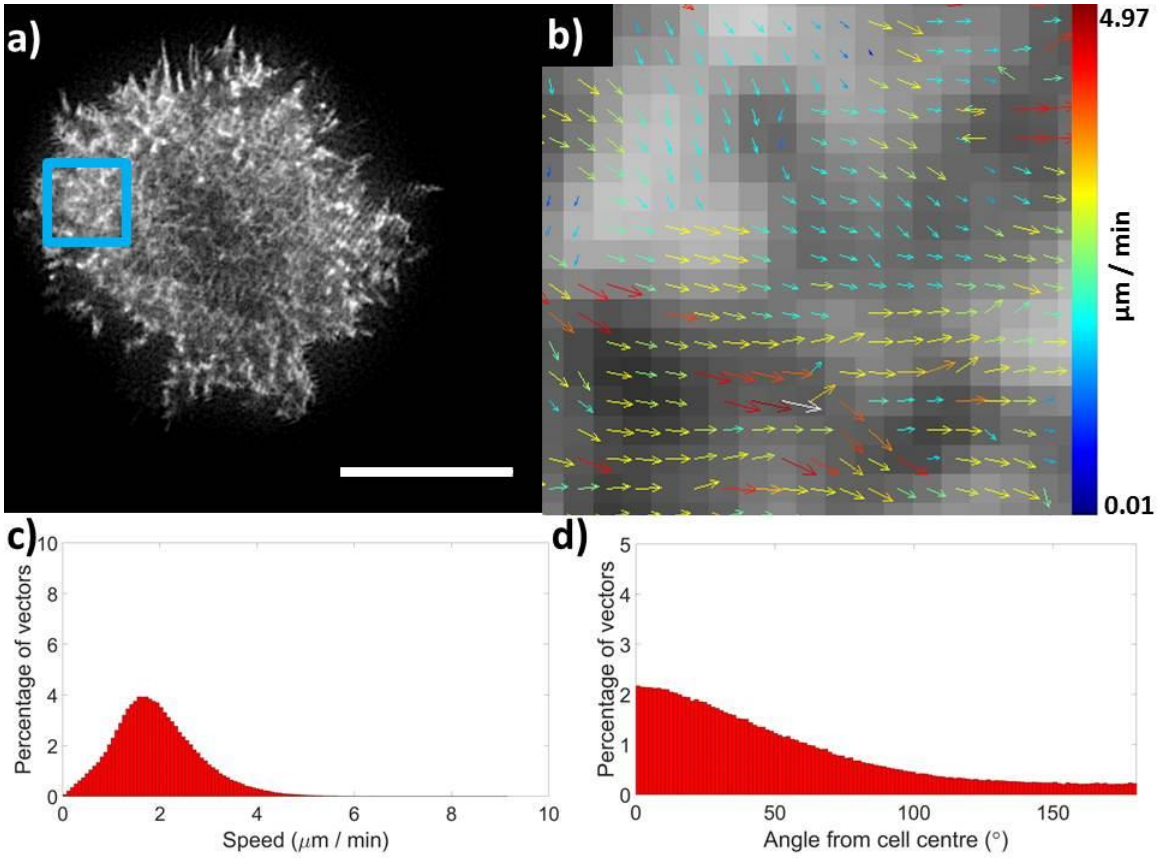

Figure 5.17 TIRF-SIM datasets analysed by image correlation. a) F-actin in primary human T cell forming immunological synapse is labelled by LifeAct-GFP, after STICS analysis vector maps (b) are generated from selected ROI's in the distal region of cell synapse and displayed as histograms reporting mean speed (c, 1.86 ± 0.26 µm) and mean flow directionality (d, 52.8 ± 10.6 °). n = 14. Scale bar = 5 µm.

These discrepancies may be due to the structural differences of F-actin between cell types, as seen in §4.2, primary T cells have more cortical actin made up of less radial fibres, with more structures akin to asters which would exhibit less directed polymerisation derived flow as fibres are orientated in multiple directions. Jurkat cells cortical actin is more radially organised, driven by both actin polymerisation and myosin motors (at least at the pSMAC).

As many T cell studies make use of the Jurkat cell lines (Schneider et al. 1977); these cells allow researchers to study the fundamental biophysics and TCR signalling during stimulation and synapse formation. However the differences seen here between Jurkat and primary human T cells could be due to several other factors; Jurkat T cells exhibit strong stimulation and IL-2 production upon stimulation by CD3 antibodies (Bunnell et al. 2002; Gillis & Watson 1980). They also have higher Ca^{2+} flux during activation, and increased phosphorylation of PLCγ1 and Vav1 (Bartelt et al. 2009); both important for actin reorganisation. As covered in §1.2, Jurkat T cells are bigger than primary cells, allowing larger surface areas when forming synapses. Jurkats also do not possess the lipid phosphatases SHIP2 or PTEN (Astoul et al. 2001; Shan et al. 2000; Wang et al. 2000), though the implications of these deficiencies are still poorly understood in the context of TCR signalling.

These differences highlight the importance of studying both the imaging favourable Jurkat T cells, before applying these findings to primary T cells, especially in the context of molecular organisation and cytoskeletal architecture nuances.

5.4. Does the membrane at the immunological synapse flow?

The actin cortex and plasma membrane are linked via numerous factors including transmembrane and ERM proteins (Figure 5.18), with actin flow driving clustering and lateral mobility of membrane residing microclusters of proteins such as TCR (Babich et al. 2012; Yi et al. 2012; Yu et al. 2010).

The evolution of membrane theories presented in §1.5.4 demonstrates the progress made on experimental techniques, with novel findings driven by new imaging and analysis methods. Not all these models are mutually exclusive, and it is likely membrane organisation relies in part on lipid composition and cytoskeletal forces, with membrane-bound molecules transiently trapped by or to the juxtaposed cortex. Upon certain stimulations these molecules could be actively brought together via actin polymerisation or depolymerisation, as well as through disengagement of actin - membrane linkers (discussed in §1.6) which would decompartmentalise these segregated molecules.

The main limitations of these models is the simplified experimental setups; implemented in a reductionist lipid bilayer: not in cells, often using fixed samples or selective labelling, while the dynamics and interactions between all cellular molecules is what creates the balancing act to form and stabilise membrane heterogeneity.

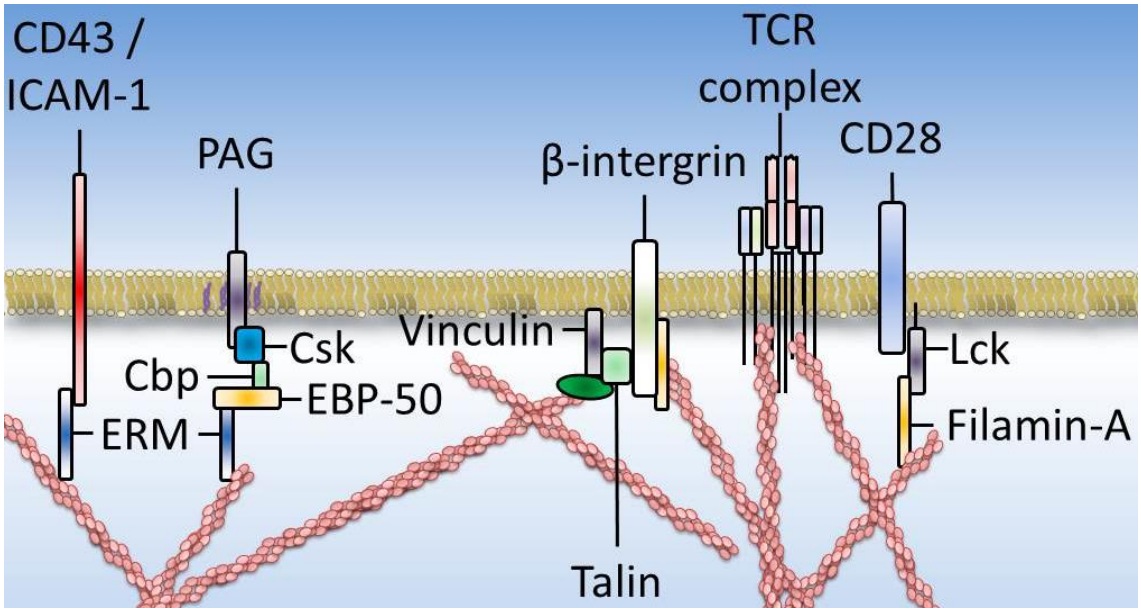

Figure 5.18 Actin-membrane interaction molecules. Modified from §1, this shows the potential transmembrane and membrane residing proteins which could transfer dynamic forces from the flowing actin cytoskeleton to the plasma membrane. Potential candidates may require a structured cytoskeleton for this force to be efficiently transferred.

To test whether the retrograde flow seen in F-actin is transferred to or coupled with the plasma membrane, T cells were imaged; repeating previous F-actin experimental conditions but with the lipophilic dye DiO incorporated into the membrane (Figure 5.19a). Analysis was run on both dSMAC and cSMAC regions, to investigate whether actin-poor regions of the cSMAC exhibit flow when compared with actin-rich dSMAC regions. STICS results of reconstructed TIRF-SIM datasets indicated dSMAC membrane flowed at comparable speeds to actin (3.98 ± 1.61 µm/min) with mean angles of 56.1 ± 17.0 ° and 63.3% of vectors flowing in a retrograde fashion (Figure 5.19b & Figure 5.19d). In comparison, cSMAC regions exhibited similar flow speeds (3.55 ± 1.09 µm/min, $p = 0.39$), however these regions exhibited a significant reduction of flow directionality, with mean angles of 82.4 ± 12.0 °, $p < 0.0001$, and 30.7 % of vectors flowing in a retrograde fashion (Figure 5.19c & Figure 5.19d).

Membrane flow is detected if any fluorescence signal exhibited non-Brownian motion, as such this flow characterises a summation of flowing membrane dye, possibly due to flowing lipids. As these regions were also shown to be devoid of actin flow directionality these results may demonstrate flow of the membrane is actin-mediated.

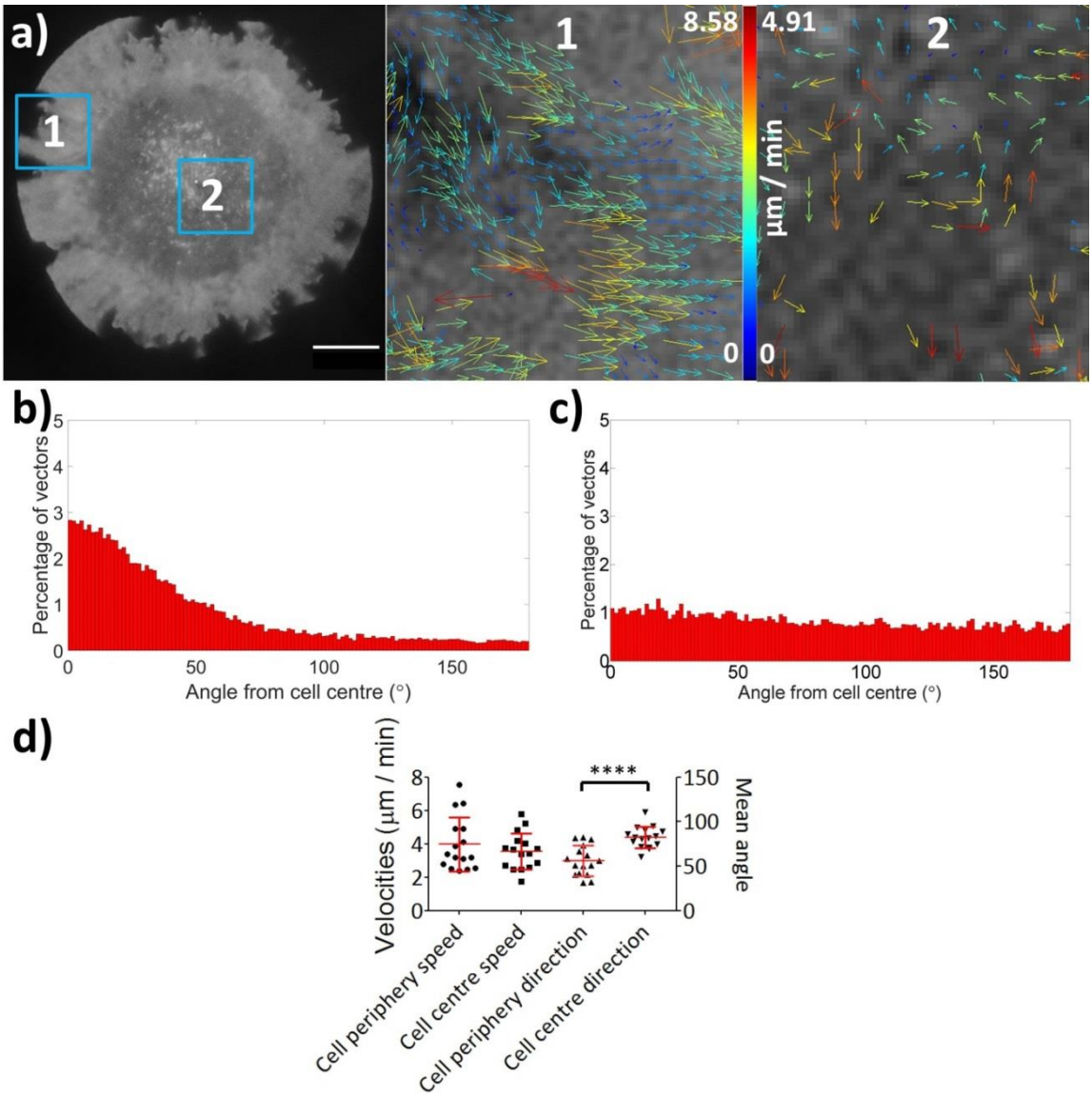

Figure 5.19 Image correlation of the plasma membrane imaged by TIRF-SIM in Jurkat T cell forming immunological synapse. a) The plasma membrane was labelled with the lipophilic dye DiO, and imaged 5 mins after contact with an antibody coated coverslip. Shown is a representative TIRF-SIM image with the magnified ROI within the blue box showing 1) the dSMAC and 2) cSMAC regions, indicating the output vector map from STICS analysis. Scale bar = 5 µm. Histograms show the normalised directionality of the b) dSMAC and c) cSMAC regions of plasma membrane flow. d) Scatterplots of cell averages comparing speeds in the distal and central regions (left: 3.98 ± 1.61 and 3.55 ± 1.09 µm) and directionality (56.1 ± 17.0 and 82.4 ± 12.0 °) of generated vectors (n = 16). **** = p < 0.0001.

To investigate whether disrupting cortical actin flow also disrupted the apparent flow of the plasma membrane, drug treatments from the actin experiments were repeated for cells with a labelled membrane. After TIRF-SIM imaging and STICS analysis (Figure 5.20a & b) and compared to controls (3.98 ± 1.09 µm/min), cyto-D treatment did not affect the speeds of membrane flow (Figure 5.20c, 4.82 ± 1.12 µm/min, p = 0.09), and while reducing the

percentage of vectors exhibiting retrograde flow from 63.3 % to 44.1 % overall directionality was not affected, with mean angles of 82.8 ± 16.9 ° (Figure 5.20d, p = 0.94 versus control cells: 82.4 ± 12.0 °).

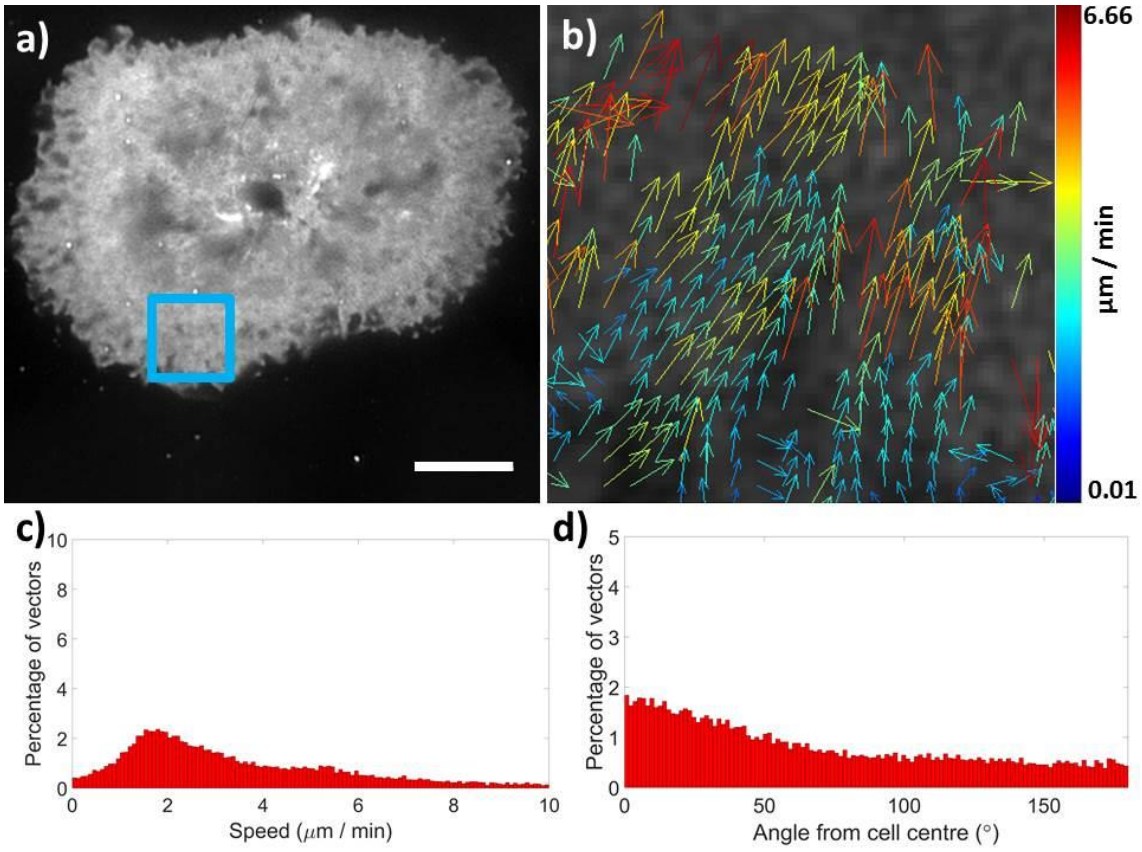

Figure 5.20 Image correlation of the plasma membrane imaged by TIRF-SIM in Jurkat T cell forming immunological synapse treated with cytochalasin-D. a) The plasma membrane was labelled with the lipophilic dye DiO, and imaged 5 mins after contact with an antibody coated coverslip and 1 minute after drug treatment. b) Shows the output vector map from STICS analysis of the magnified ROI within the dSMAC. Scale bar = 5 µm. Histograms show c) the normalised speed within the dSMAC (4.82 ± 1.12 µm) and d) directionality (82.8 ± 16.9 °) n = 17.

Next jasplakinolide treatments, which stabilises actin fibres and also increases actin polymerisation were trialled for membrane flow modulation after TIRF-SIM imaging and STICS analysis (Figure 5.21a & b). Compared to controls (3.98 ± 1.09 µm/min), jasplakinolide treatment did not affect the speeds of membrane flow (Figure 5.21c, 4.16 ± 2.01 µm/min, p = 0.80), and while reducing the percentage of vectors exhibiting retrograde flow from 63.3 % to 41.8 %, overall directionality was not affected, with mean angles of 76.8 ± 15.0 ° (Figure 5.22d, p = 0.29 versus control cells: 82.4 ± 12.0 °).

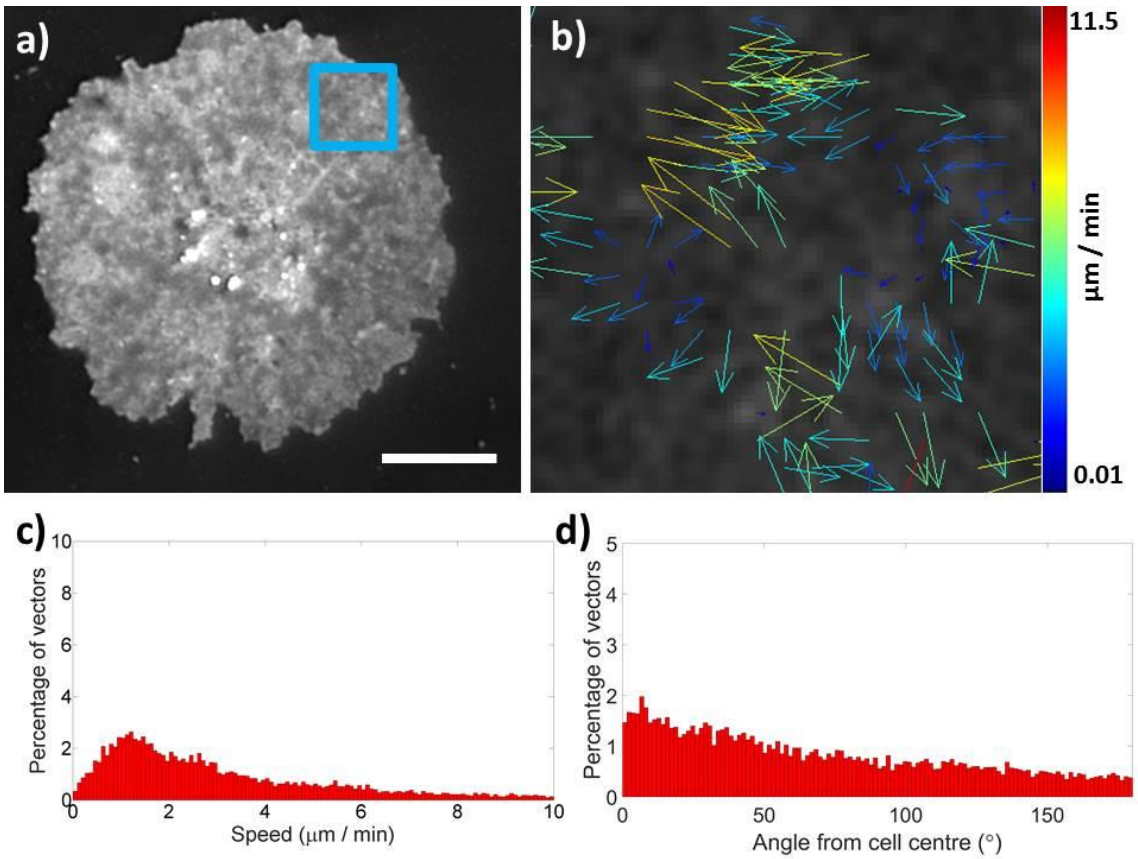

Figure 5.21 Image correlation of the plasma membrane imaged by TIRF-SIM in Jurkat T cell forming immunological synapse treated with jasplakinolide. a) The plasma membrane was labelled with the lipophilic dye DiO, and imaged 5 mins after contact with an antibody coated coverslip and 1 minute after drug treatment. b) Shows the output vector map from STICS analysis of the magnified ROI within the dSMAC. Scale bar = 5 µm. Histograms show c) the normalised speed within the dSMAC (4.16 ± 2.01 µm) and d) directionality (76.8 ± 15.0) n = 11.

Finally, to investigate any role for plasma membrane order in membrane flow, 7KC treatments were carried out. After TIRF-SIM imaging and STICS analysis (Figure 5.22a & b, compared to controls (3.98 ± 1.09 µm/min), 10 µM 7KC treatment did not affect the speeds of membrane flow (Figure 5.22c, 2.95 ± 0.66 µm/min, p = 0.23), and reduced the percentage of vectors exhibiting retrograde flow from 63.3 % to 43.7 %, and overall directionality, with mean angles of 61.6 ± 2.7 ° (Figure 5.22d, p = 0.004 versus control cells: 82.4 ± 12.0 °).

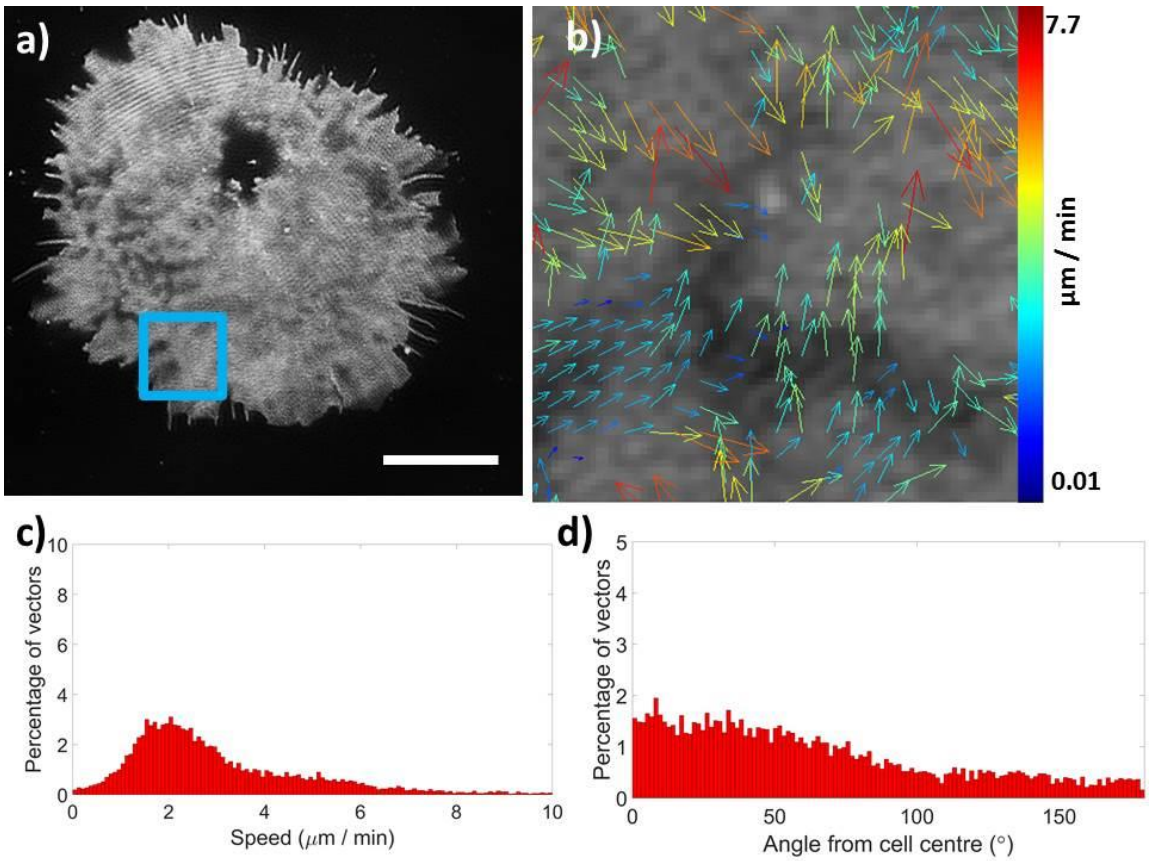

Figure 5.22 Image correlation of the plasma membrane imaged by TIRF-SIM in Jurkat T cell forming immunological synapse treated with 7KC. a) The plasma membrane was labelled with the lipophilic dye DiO, and imaged 5 mins after contact with an antibody coated coverslip and 1 minute after drug treatment. b) Shows the output vector map from STICS analysis of the magnified ROI within the dSMAC. Scale bar = 5 µm. Histograms show c) the normalised speed within the dSMAC (2.95 ± 0.66 µm) and d) directionality (61.6 ± 2.70) n = 4.

These data are summarised below, compared to control cells, detected plasma membrane flow was not significantly changed for either speed or directionality for cyto-D ($p = 0.08$ and 0.94), jasplakinolide ($p = 0.80$ and 0.29), or flow speed in 7KC treated cells ($p = 0.23$), however directionality was significantly changed ($p < 0.005$).

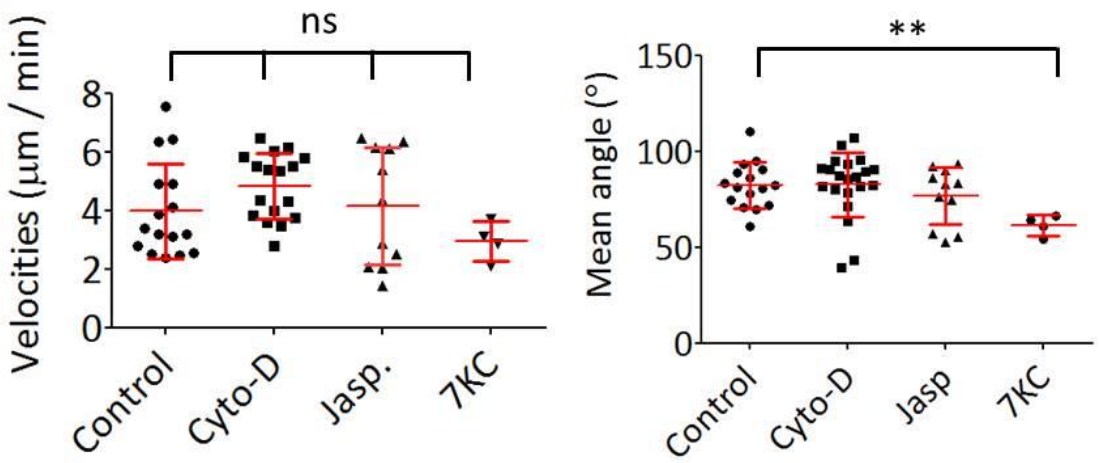

Figure 5.23 Scatterplots of dSMAC plasma membrane speed and directionality following drug treatments. Individual cell averages of vector speed and directionality are shown for each condition. ns = non-significant, ** p < 0.005.

Overall these results show reducing or increasing actin polymerisation through small molecule drugs did not affect the flow of the membrane regarding speed, or directionality. While reducing membrane order did not alter membrane flow speed, it did increase the directionality of membrane flow. These results demonstrate any linkage between the actin and membrane does not influence flow dynamics within the membrane itself, but rather the flow of proteins within the membrane. However these results are difficult to interpret, highlighting the limitations of single channel image data, as it is impossible to run correlations between the observed system (membrane) and the unobserved system (actin).

In an attempt to overcome these limitations two-channel TIRF-SIM data was acquired, and analysed using the cross-correlation variant of STICS.

5.5. Are cortical actin and plasma membrane flow correlated?

Simultaneously imaging actin and membrane flow within the same cell followed by cross-correlation analysis allowed investigation of any coupling between the two systems flow, this was achieved on the custom-build system outlined in §3.7.2. Cells expressing LifeAct-GFP had their membranes labelled 5 minutes prior to imaging via the membrane dye DiI. Cells then formed synapses on a CD3 and CD28 antibody coated coverslip, with serial excitation from the 488 and 561 nm laser permitting imaging of the actin and plasma membrane.

Images were run through STICCS (the cross-correlation variant of the software). Figure 5.24 shows representative data and analysis, Figure 5.24a shows the merged channels, with the ROI magnified for vector maps of the F-actin and plasma membrane. Cross-correlation outputs vectors show where flow between the two channels exhibited co-transportation.

Figure 5.24b shows a set of representative heat maps for both the speed and directionality correlations, while Figure 5.24c shows the mean ratio of the flow velocities at the synapse periphery was 1.02 ± 0.39 indicating the flows have a similar velocity (>1 indicates channel *a* [actin] flows faster than channel *b* [membrane], 1 indicates perfect correlation, <1 indicates channel *b* flows faster than channel *a*). The correlation between the directionality also demonstrated some positive correlation; 0.57 ± 0.27 (where 1 indicates collinear flow, 0 no correlation and -1 perfect negative correlation).

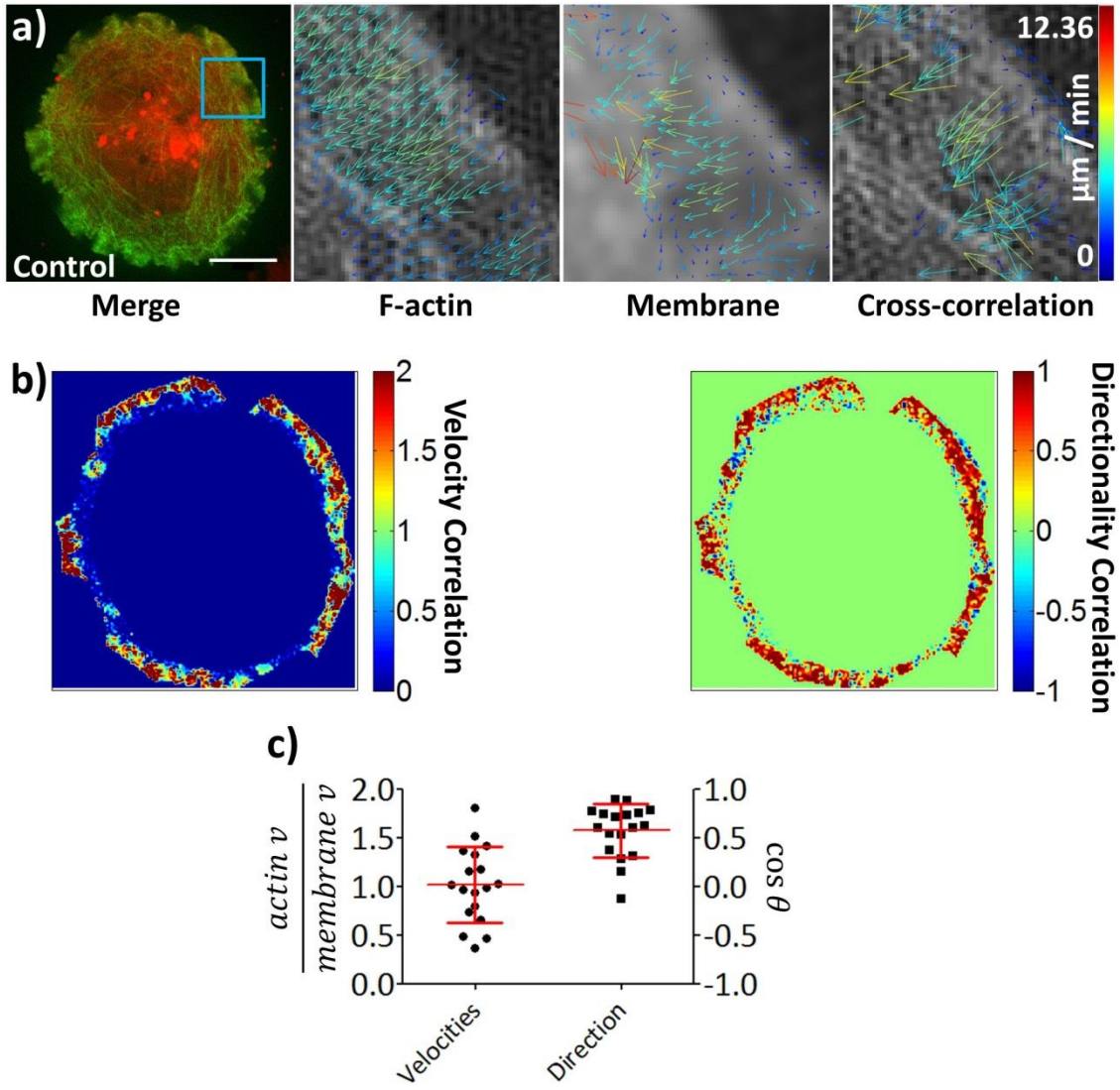

Figure 5.24 Cross-correlation analysis of F-actin and plasma membrane flow. a) Jurkat T cells imaged using two-colour TIRF-SIM (left). Single channel correlation outputs for actin and the plasma membrane (middle images) and the cross-correlation vectors showing flow vectors for cotransported actin and the plasma membrane (right). Scale bar = 5 μm. b) Heatmaps show regions of greater and lesser correlation for subregion velocities (left) and directionality (right). c) Scatter plots of whole cell mean velocities (left; 1.02 ± 0.39) and directionalities (right; 0.57 ± 0.27) n = 18.

After establishing regions of the dSMAC did exhibit cotransportation between actin and the plasma membrane, drug treatments to modulate the cortical actin and its flow were applied to

cells. This permitted investigation of whether the actin-membrane correlation was changed. Figure 5.25 shows how cyto-D (p = 0.57) and jasplakinolide (p = 0.65) did not significantly affect the velocity correlation between actin and the plasma membrane. However there was a significant reduction for both treatments when assessing the directionality of the plasma membrane, compared to controls. This may indicate that cortical actin flow does control membrane flow speed but does not maintain bulk directional dynamics during synapse formation.

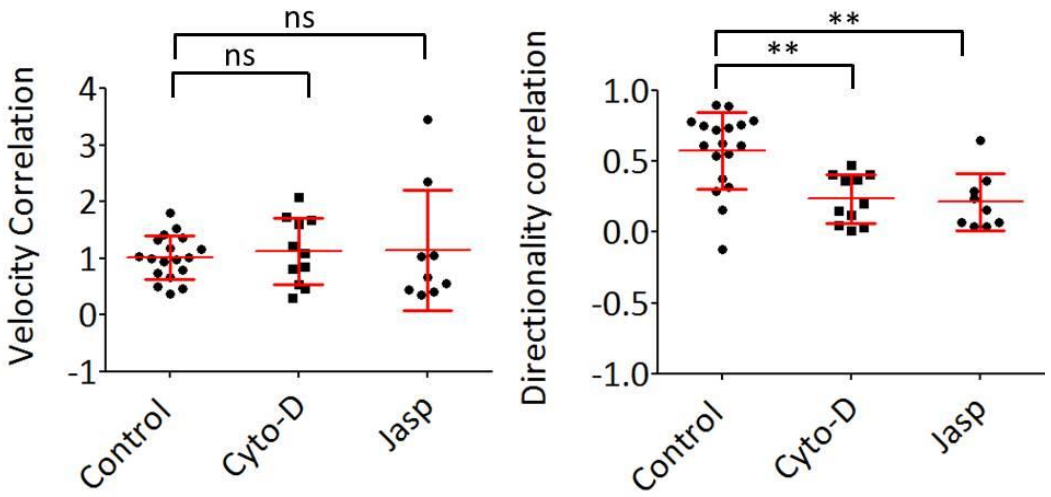

Figure 5.25 Scatterplots of correlations between actin and the plasma membrane after drug treatments. Velocities (left) of both cytochalasin-D and jasplakinolide treated cells (n = 11 and 9) showed no significant difference compared to control cells (p = 0.57 and 0.65), while the directionality correlation (right plot) was reduced for both conditions versus controls (p < 0.05). ns = non-significant, ** p < 0.005.

Two-channel TIRF-SIM results here demonstrate the flowing actin cortex and labelled plasma membrane are correlated for both speed and directionality, in Jurkat T cell synapses. Upon actin disruption, flow speed by small molecule drugs continue to be correlated; demonstrating velocity modulation of actin is mirrored within the plasma membrane. This highlights the potential that the two systems may be linked either directly, through linker proteins or indirectly through transmembrane proteins. Interestingly disrupting the actin cytoskeleton leads to a significant drop in correlated directionality, these observations would not be possible using other correlative techniques which only observe diffusion speed such as FCS.

Disruption of directional correlation may indicate plasma membrane flow organised by an actively flowing actin cortex may require sites of specific interaction, rather than bulk actin flow, which would agree with findings in vitro (Raghupathy et al. 2015; Köster et al. 2016). This may also be indicative of actin forming barrier-type fences (Kusumi, Ike, et al. 2005), which may not actively drive protein flow speeds within the membrane but could control directionality if transmembrane proteins reside between actin fibres of the dSMAC meshwork.

These studies observe nanoscale clustering of membrane lipids and proteins which are passively modulated by actin or actively organise the cortical network. Koster et al (2016) reported disruption of clusters upon cessation of actin flow. As specific subpopulations within the plasma membrane may exhibit higher correlations with actin flow this was investigated using two-channel TIRF-SIM.

5.6. Cross-correlation analysis of F-actin and lipids within the outer membrane leaflet

To explore the possibility of specific components within the plasma membrane correlating with the flowing actin cortex, T cells expressing GPI-GFP together with LifeAct-mCherry were imaged. GPI-anchored proteins are located on the outer leaflet of the plasma membrane and are believed to preferentially segregate into lipid ordered compartments of the membrane (Goswami et al. 2008; Saha et al. 2015). The extracellular GPI-anchored proteins can indirectly associate with cortical actin filaments via interleaflet tail coupling and transbilayer interactions (Gowrishankar et al. 2012; Raghupathy et al. 2015; Köster et al. 2016).

It was therefore hypothesised that markers for ordered components of the plasma membrane may display correlated flow with actin, if actin corrals proteins residing in membrane-ordered domains, or if GPI-anchored proteins are indirectly interacting with the actin cytoskeleton. As such GPI-GFP and LifeAct-mCherry were imaged in transfected Jurkat T cells forming an immunological synapse against a stimulatory coverslip, using TIRF-SIM.

STICCS analysis showed some subregions were cotransported (Figure 5.26a), with the most correlated flows occurring at the dSMAC region of the synapse depicted by heatmaps (Figure 5.26b). Figure 5.26c shows average cell correlation, with GPI-GFP and LifeAct-mCherry correlated for both speed (1.05 ± 0.35) and directionality (0.39 ± 0.13). Compared to correlations from LifeAct-GFP and DiI control cells, flow speeds was non-significant ($p = 0.79$) while directionality was less correlated ($p < 0.05$). These results demonstrate the correlation of flow may extend to both plasma membrane leaflets. This transmission to extracellular leaflet components is in agreement with the active composite model of actin-coupled advection of embedded proteins (Gowrishankar et al. 2012; Raghupathy et al. 2015; Köster et al. 2016).

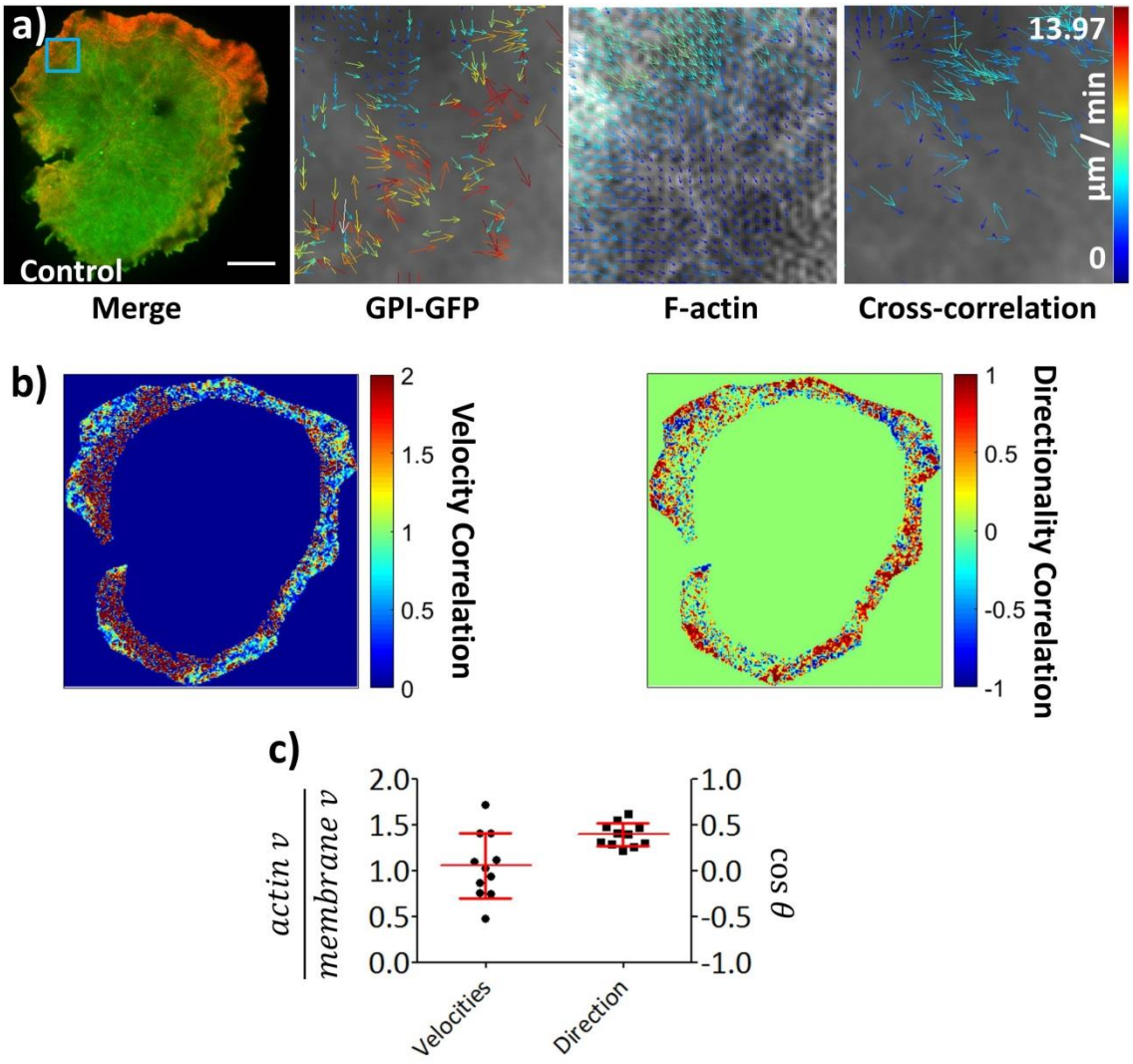

Figure 5.26 Cross-correlation analysis of F-actin and extracellular residing GPI-GFP. a) show the ordered-residing membrane marker GPI-GFP alongside LifeAct-mCherry with using two-colour TIRF-SIM (left), the single channel correlations for actin and the plasma membrane (middle images) and the cross-correlation vectors between the two channels (right). Scale bar = 5 µm. b) Heatmaps show regions of greater and lesser correlation for subregion velocities (left) and directionality (right). c) showing an average correlated speed of 1.05 ± 0.35, and correlated directionality 0.39 ± 0.13, n = 11.

Figure 5.27 shows how drug treatments affect the cross-correlation between actin and GPI-GFP. Compared to controls speed (1.05 ± 0.35) and directionality (0.39 ± 0.13) correlations, cyto-D exhibited less correlated velocities (1.69 ± 0.64, $p = 0.006$) and directionality (0.15 ± 0.19, $p < 0.0001$), while jasplakinolide did not significantly alter correlated speed (1.23 ± 0.63, $p = 0.39$) or directionality (0.34 ± 0.15, $p = 0.31$). As with previous analysis, >1 means channel *a* (in this case GPI-GFP) is flowing faster than channel *b* (actin).

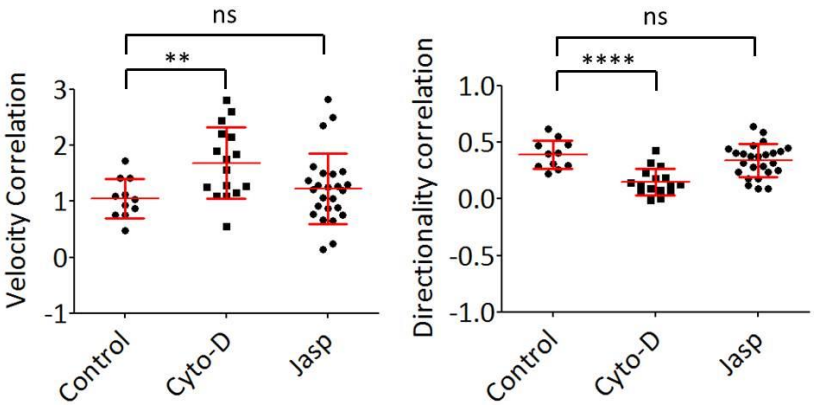

Figure 5.27 Scatterplots of cross-correlation analysis for F-actin and extracellular residing GPI-GFP following drug treatments. Mean correlations of velocities (left plot) and angles (right plot) for different drug treatments. Compared to control cells, cytochalasin-D treated cells had significantly different velocity ($p = 0.006$) and directionality ($p < 0.0001$) correlations ($n = 16$). Increasing actin polymerisation and stabilising actin fibres had no significant effect on the speed or directionality correlations ($p = 0.39$ and 0.31; $n = 25$). ns = non-significant, ** $p < 0.005$, **** $p < 0.0005$.

To compare these cross-correlations with negative control conditions a Jurkat T cell forming a synapse expressing cytosolic-GFP was imaged and correlated to the membrane dye DiI (Figure 5.28a). These results showed spurious regions of correlation (Figure 5.28b), with cytosolic-GFP exhibiting reduced correlation with the membrane dye. Compared to control conditions cell averages showed non-significant changes in speed (1.31 ± 0.52, $p = 0.11$) and significantly reduced directionality correlation (0.10 ± 0.13, $p < 0.0001$; Figure 5.28c).

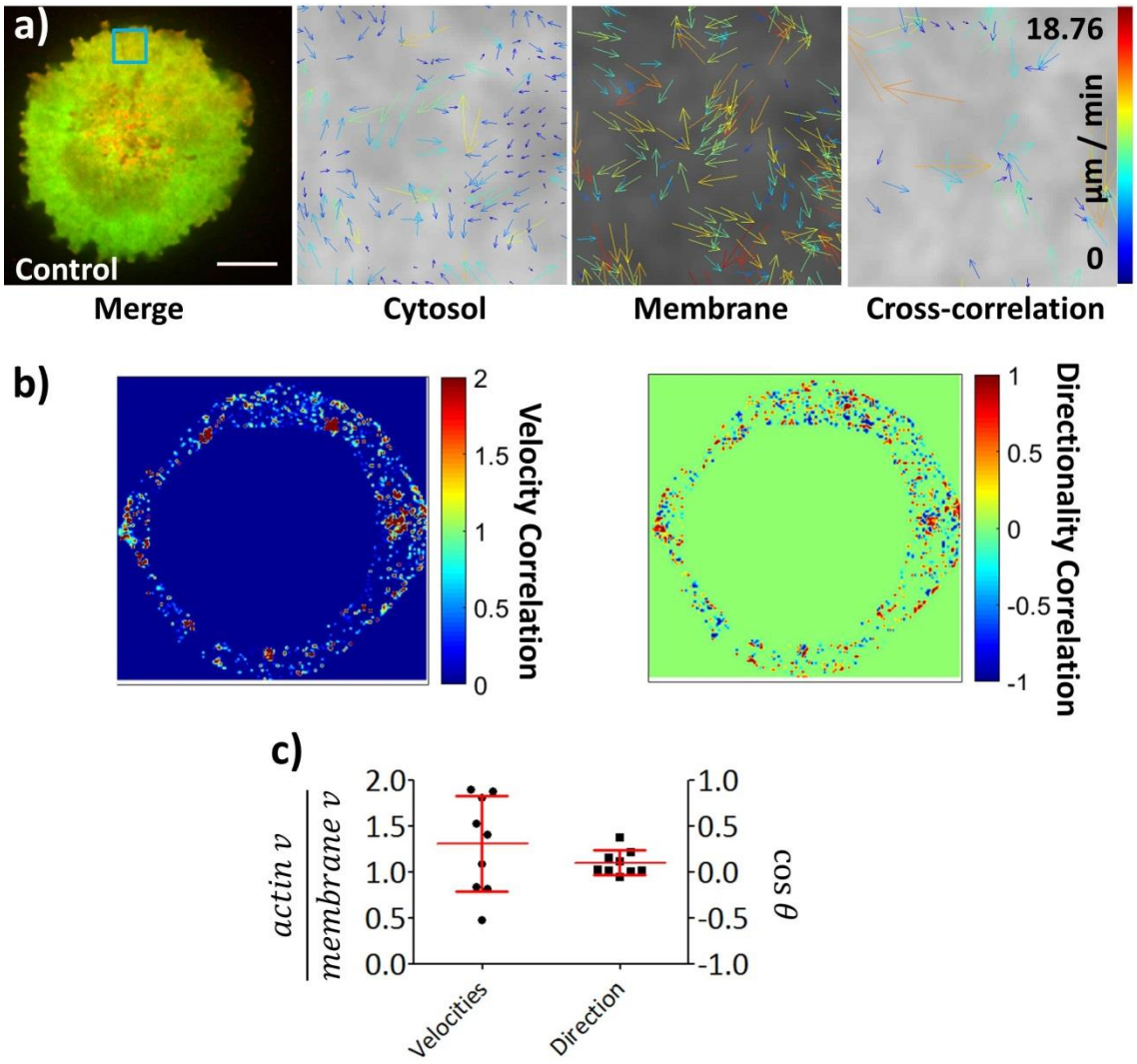

Figure 5.28 Cross-correlation analysis of the cytosol and the plasma membrane. a) show the cytosolic-GFP and plasma membrane marker DiI using two-colour TIRF-SIM (left), the single channel correlations for the cytosol and the plasma membrane (middle images) and the cross-correlation vectors between the two channels (right). Scale bar = 5 µm. b) Heatmaps show regions of greater and lesser correlation for subregion velocities (left) and directionality (right). c) Showing average correlated speed as 1.31 ± 0.52, and correlated directionality is 0.10 ± 0.13, n = 9.

Overall, these results show components of the plasma membrane appear to flow, and are correlated with the retrograde flow of cortical actin at the T cell synapse. Additionally, lipids which associate within the outer leaflet of the plasma membrane and are known to reside in liquid ordered domains exhibit, in part, correlated flow.

The correlated flow between actin and GPI-GFP agrees with in vitro experiments showing active actin flow may drive nanoclustering within the outer leaflet of the plasma membrane due to coupling with the inner leaflet. This leaflet mirroring between PS and GPI lipids takes place in an actin dependent manner through interactions between the lipids long acyl-chains (Raghupathy et al. 2015; Gowrishankar et al. 2012).

5.7. Actin crosslinker α-actinin at the immunological synapse

To better understand what could be driving the apparent transmission of flow between actin and the plasma membrane, F-actin was correlated with the candidate protein α-actinin. If correlated flows between the actin and plasma membrane seen in §5.5 & §5.6 are indeed due to actin forming 'tracks' or meshworks which transmembrane proteins can follow and are trapped by, molecules which form these longer lived structures may have a role in membrane flow transmission. α-actinin both bundles and crosslinks F-actin fibres together and binds several transmembrane proteins (Hoessli et al. 1980; Geiger & Singer 1979), as such it may allow actin to transfer forces and flow through to the membrane. This could occur through the transmission of flow from crosslinked actin in the dSMAC to transmembrane proteins directly or indirectly, as speculated by the picket fence and active composite models (Kusumi, Nakada, et al. 2005; Köster et al. 2016). These transmembrane proteins may include those which actively orchestrate actin dynamics such as the TCR or CD28, or those which interact with actin through long cytosolic tails; for example LAT or integrins.

TIRF-SIM imaging followed by STICCS analysis (Figure 5.29a) showed near-perfect correlation of flowing signal (Figure 5.29b & c) indicating this linker protein could be involved in transferring forces between actin and the plasma membrane. Normalised actin radial intensity profiles (Figure 5.29d) show actin fluorescence reduces towards the synapse centre relative to α-actinin fluorescence.

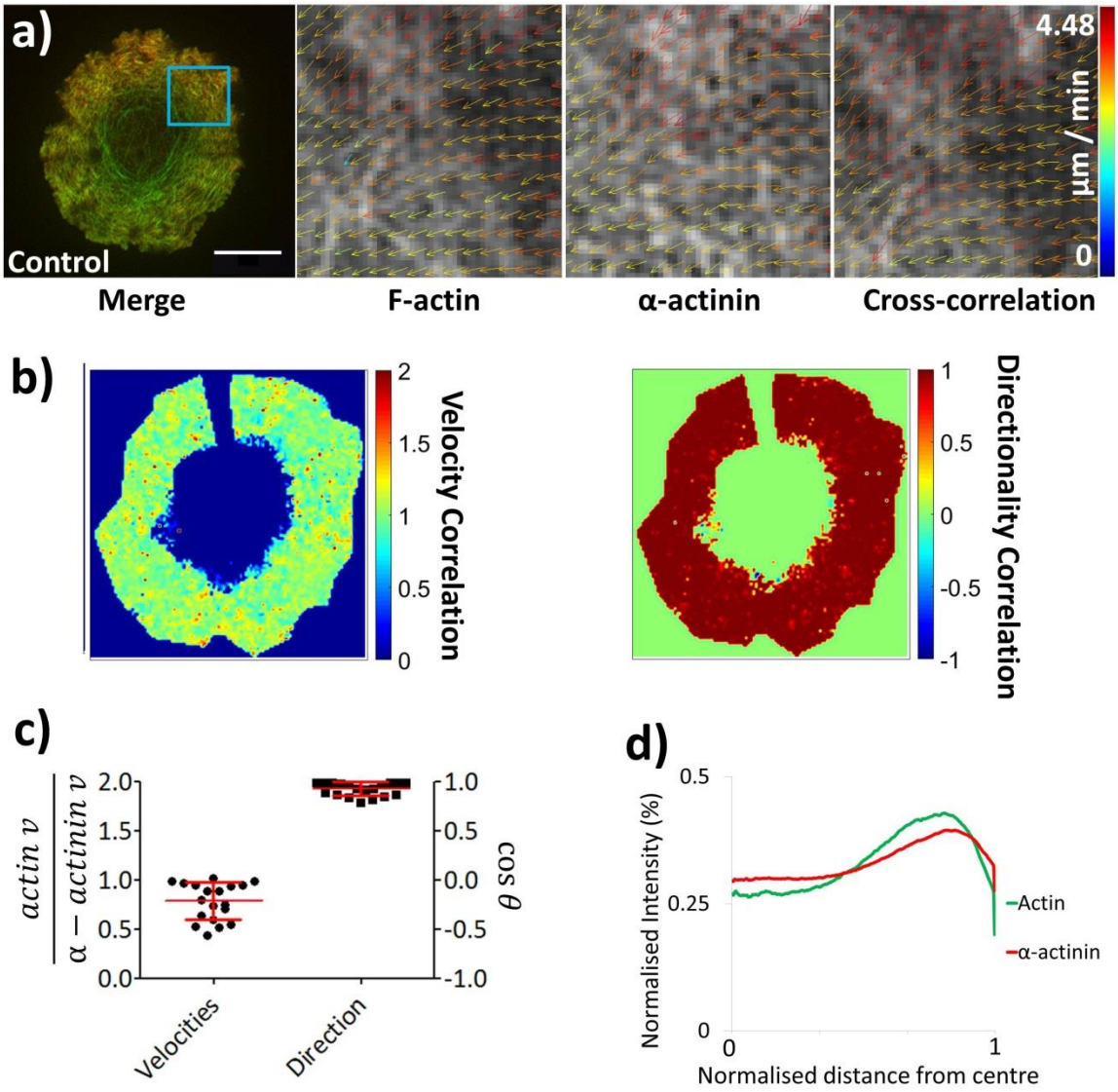

Figure 5.29 Cross-correlation analysis of actin and α-actinin. a) Shows a Jurkat T cells expressing LifeAct-GFP and α-actinin mCherry imaged by TIRF-SIM, with the separated correlated channels and corresponding vector maps from within the blue ROI. Scale bar = 5 µm. b) Heatmaps demonstrate the extent of regions of correlation with cell averages plotted in c), giving an average velocity correlation of 0.78 ± 0.19, and directionality of 0.92 ± 0.07. d) Demonstrates the fluorescent intensity of both actin and α-actinin, at the synapse interface (n = 19).

This data demonstrates that in the regions of highest actin-membrane cotransportation, α-actinin is also present, and this flow is significantly correlated to the actin cortex. As such it was hypothesized this actin crosslinking protein could in some way be responsible for translating actin flow forces to the membrane potentially via transmembrane proteins trapped within the dense and flowing meshwork of the dSMAC. This was investigated by TIRF-SIM imaging and STICS analysis of α–actinin CRISPR knockout of the gene of interest (ACTN1) which encodes α-actinin, these cells were obtained from Dr. David Williamson (Owen lab).

After CRISPR editing, cells were split down to single cell cultures, ensuring cells where CRISPR interference was successful would lead to a fully homogeneous culture. Western Blot was used

to establish in which cultures CRISPR had been successful (Figure 5.30a) and to ensure the knockout did not affect the housekeeping protein glyceraldehyde-3-phosphate dehydrogenase (GAPDH), as is shown in Figure 5.30b, when normalised to wild-type Jurkat T cells, knockouts showed reduced α–actinin expression.

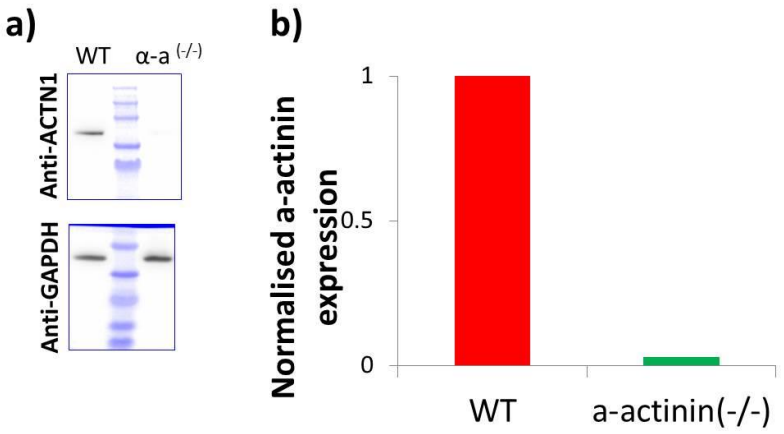

Figure 5.30 α-actinin CRIPSR knockout quantification. a) Compared to wild type Jurkat T cells α-actinin expression was successfully knocked out, but this process did not affect GAPDH. α-actinin expression in CRISPR cells was then quantified relative to wild type Jurkat T cells (b).

This selected cell culture was used for the investigation into α–actinin's role during synapse formation, with actin and membrane flow quantified as before. To determine what effect α–actinin had on the actin network, knockout cells were transiently transfected with LifeAct-GFP. Actin flow is shown in Figure 5.31 and was found to flow faster compared to control cells with mean actin flow of 2.23 ± 0.39 μ/min ($p < 0.0001$), while directionality analysis showed actin flow was disrupted with a mean angle of 79.4 ± 7.5 ° ($p < 0.0001$, $n = 17$).

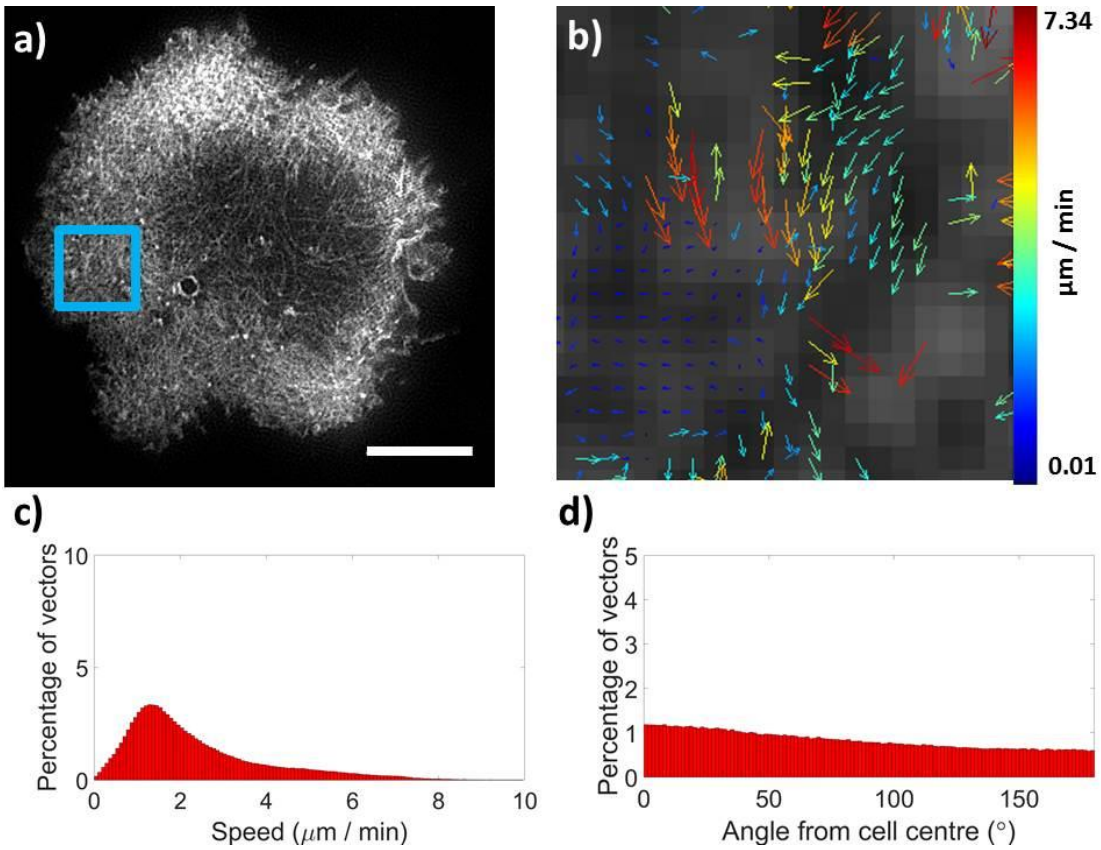

Figure 5.31 Image correlation of cortical actin imaged by TIRF-SIM in Jurkat T cell forming immunological synapse after CRISPR knockout. a) Actin labelled with LifeAct-GFP was imaged 5 mins after contact with an antibody coated coverslip. b) Shows the output vector map from STICS analysis of the magnified ROI within the dSMAC. Scale bar = 5 µm. Histograms show c) the normalised speed within the dSMAC (2.23 ± 0.39 µm) and d) directionality (79.4 ± 7.5) n = 17.

After staining the plasma membrane using DiO, these cells were imaged and analysed (Figure 5.32a & b). Compared to controls these cells exhibited a non-significant decrease in mean membrane flow speeds 2.8 ± 0.67 µ/min ($p = 0.06$, Figure 5.32c), while directionality analysis showed the plasma membrane flow was significantly disrupted with a mean angle of 80.4 ± 19.7 ° ($p < 0.005$, Figure 5.32d, $n = 8$). These results demonstrate the crosslinking function of α-actinin may facilitate directed flow of the plasma membrane.

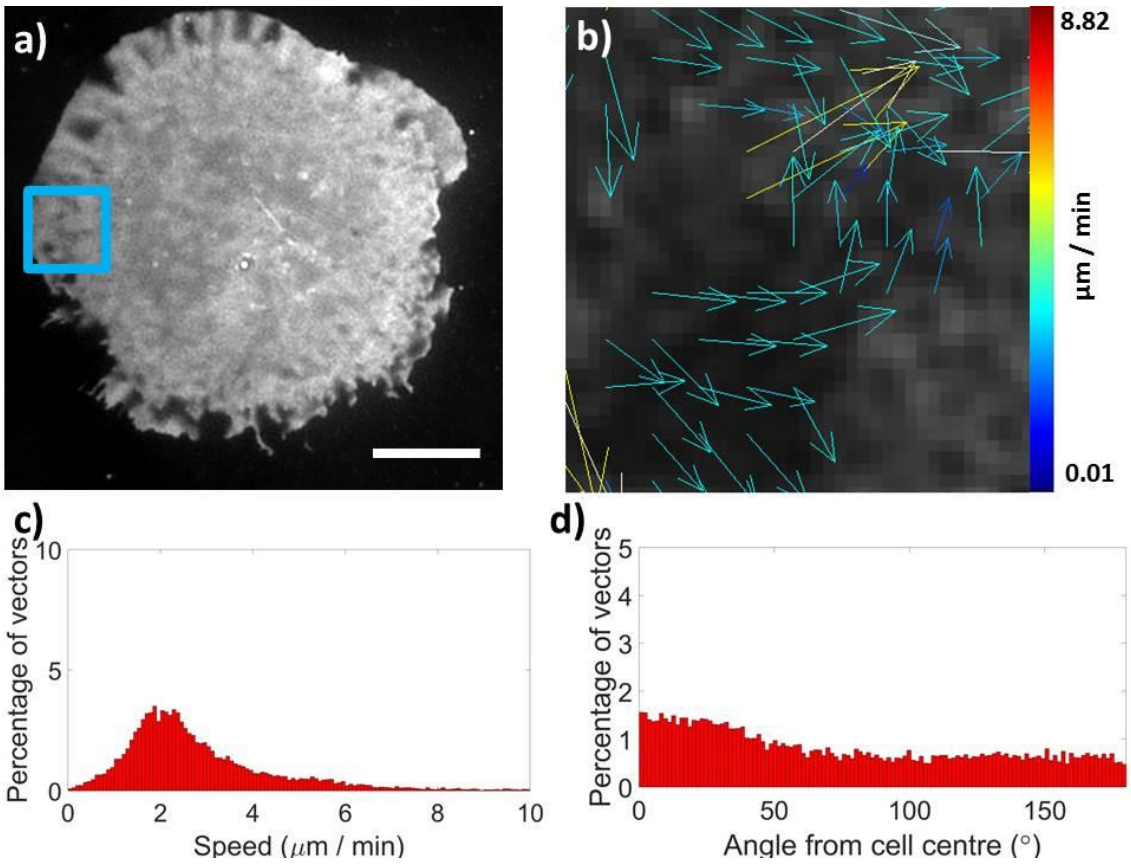

Figure 5.32 Image correlation of the plasma membrane imaged by TIRF-SIM in Jurkat T cell forming immunological synapse after CRISPR knockout of α-actinin. a) The plasma membrane was labelled with the lipophilic dye DiO, and imaged 5 mins after contact with an antibody coated coverslip. b) Shows the output vector map from STICS analysis of the magnified ROI within the dSMAC. Scale bar = 5 µm. Histograms show c) the normalised speed within the dSMAC (2.8 ± 0.67 µm) and d) directionality (80.4 ± 19.7) n = 8.

These results are summarised as individual cell means in Figure 5.33, where α–actinin knockout by CRISPR did not affect plasma membrane flow speed but did reduce the retrograde nature of the plasma membrane flow.

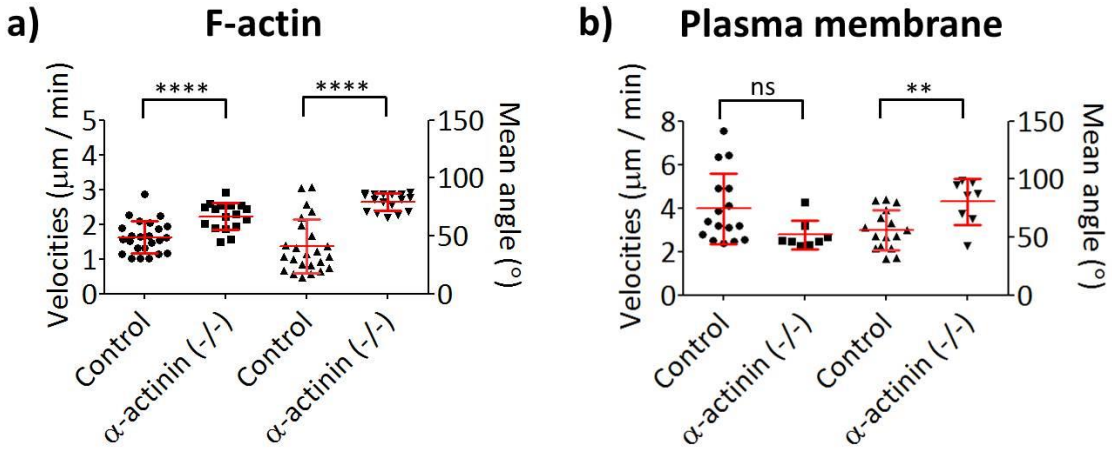

Figure 5.33 Scatterplots of single cell means for α-actinin$^{-/-}$ cells. a) Single cell mean velocities and angles for plasma membrane flow, n = 16 (controls) and 8 (-/-). b) Single cell mean velocities and angles for cortical actin flow, n = 24 (controls) and 17 (-/-). n.s. = non-significant, ** = p < 0.005, **** = p < 0.0001.

Through its cross-linking ability to F-actin, knocking out α-actinin demonstrated a significant reduction in the orderedness of cortical actin retrograde flow and the plasma membrane itself; indicating the tight meshwork structure partially formed by α-actinin may contribute to plasma membrane dynamics.

5.8. Membrane topography within the dSMAC

Cells are not 2D structures and their morphology in 3D is thought to be important for their interactions with the surrounding environment. Within the T cell synapse, these 3D morphologies include membrane ruffles which may play a role in T cell signalling, shown before in NK cells (Benninger et al. 2009). Speculated to limit diffusion via the kinetic segregation model, these ruffles are controlled by the actin modulating enzymes (e.g. GRB2 in macrophages and the Rho-GTPase Ras-related C3 botulinum toxin substrate 2 [Rac2] (Mahankali et al. 2011)) and are thought to signify areas of newly polymerised actin meshwork (Ridley 1994), which also contain α-actinin (Bretscher & Lynch 1985).

The membrane flow seen within the dSMAC could be in part due to ruffling, with the membrane oscillating within or out of the exponentially decaying evanescent wave, creating fluctuations in signal picked up as membrane flow. To test this hypothesis T cells were imaged using IRM. While a predominantly qualitative method, it provides nanometer resolution in the z-plane, with grayscale images denoting the distance of structures from the coverslip. T cells forming synapses were imaged with dark regions (indicating structures close to the coverslip) seen primarily in the synapse centre while more peripheral structures appeared as both lighter and darker regions (indicating ruffling).

Figure 5.34a demonstrates data from a Jurkat T cell exhibiting membrane ruffling when imaged by IRM, upon STICS analysis these regions of lighter and darker intensities were shown to flow within the dSMAC in a retrograde manner akin to previous actin and the plasma membrane results. Quantification revealed vector speeds were nonsignificant compared with correlated actin ($p = 0.43$ and 0.24) and membrane ($p = 0.19$) flow (Figure 5.34b).

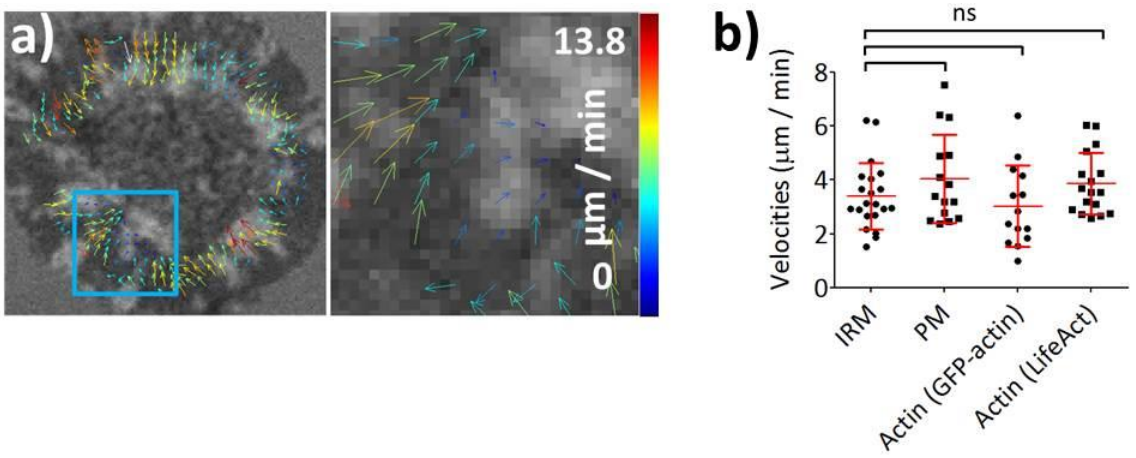

Figure 5.34 IRM image of Jurkat T cell forming an immunological synapse, imaged by IRM. a) STICS analysis revealed membrane ruffles translocate in a retrograde fashion from the dSMAC towards the cSMAC, these ruffle speeds were nonsignificant versus plasma membrane, or actin flow (b); p = 0.19, 0.43, 0.24), n = 21, 15, 14 and 17.

Imaging the membrane topography by IRM and STICS analysis demonstrates ruffling within the dSMAC; these ruffled regions are also shown to flow in a retrograde manner towards the unruffled cell centre. These results agree with similar ruffled structures seen in synapse forming NK cells (Benninger et al. 2009). Whether these structures are formed as part of the kinetic segregation model (Davis & van der Merwe 2006), where larger downregulatory molecules such as CD43 are excluded from active signalling sites such as actin and TCR rich membrane protrusions is yet to be fully investigated.

5.9. Discussion

This chapter investigated the causes and effects of actin flow on synapse dynamics and architecture. Correlation analysis agreed with previous findings that actin polymerisation drives actin flow speeds at the immunological synapse (Babich et al. 2012; Yi et al. 2012). Here, super-resolution imaging and correlative analysis techniques were used, extending the findings beyond single dimensional analysis thus enabling the extraction of directional information. This provided findings that actin polymerisation is important for the directionality of the flow, with actin modulating drugs scrambling the retrograde nature of cortical actin. Many studies highlight the importance of the actin-membrane interface in maintaining lipid order (Dinic et al. 2013; Gaus et al. 2003), while actin NPF's are located in, and activated at, the plasma membrane, (including the WASp/Arp2/3 complex) such as PI(3,4)P_2 rich domains (Sasahara et al. 2002). As such, 7KC treatments, which disrupt membrane order, were investigated; lower (10 µM) concentrations did not affect the speed or retrograde nature of the actin. However, higher (20 µM) concentrations sped up this flow of actin, whether these are due to disruption of nanodomains such as lipid raft like structures, the clustering of regulatory molecules, lower membrane viscosity or other factors is yet to be understood.

This chapter then quantified how components of the plasma membrane itself flowed in a similar direction and speed to the actin cortex. While previous studies have reported flow does not appear in cells (Lee et al. 1990; Kucik et al. 1990), these studies used nanoparticles attached to the membrane of migrating cells. Here actin flow would also be linked to static integrin complexes, additionally these studies utilised diffraction-limited imaging techniques and FRAP analysis techniques which may be less sensitive to flowing rather than diffusive components within the membrane.

Next, the plasma membrane was imaged using the same drug treatments as with the cortical actin experiments. These results showed little change in the mean velocities or angles compared to controls (Figure 5.23) and were less retrograde in nature. As the plasma membrane was imaged while using actin modulating drugs these results were inconclusive, as it was not known whether the actin was exhibiting flow changes within cells. Alternatively differences between the actin and membrane flow may indicate a degree of elastic interaction between the actin cortex, the membrane and its associated proteins. This relationship has been observed before using static barriers to halt or trap actin-transported TCR microclusters; described as ‘slippage’ and ‘frictional coupling’ (Kaizuka et al. 2007; DeMond et al. 2008)

To study actin-membrane interactions further, two-channel TIRF-SIM of actin and the plasma membrane was analysed by cross-correlation. Results demonstrated flowing components of the plasma membrane exhibited regions of similar speeds and directionality to the actin cortex (Figure 5.24). When actin modulating drugs were added, the flow speed correlations were not significantly changed, however directionality correlation was significantly reduced. This indicates any actin flow that transfers to the plasma membrane may control membrane flow speed but does not maintain bulk directional dynamics during synapse formation.

As actin-membrane cotransportation exhibited heterogeneity, specific components linked to the plasma membrane where investigated to establish whether these are more susceptible to the flow of cortical actin. GPI-GFP, which is trafficked to the outer leaflet of the plasma membrane, forms nanoclusters and is believed to be transiently trapped within lipid ordered regions (Sharma et al. 2004; Eggeling et al. 2009). GPI-GFP was correlated against the retrograde flow of the actin cortex; results (Figure 5.26) demonstrated a similar level of correlation as the labelled plasma membrane (Figure 5.24). Scatterplots of correlation scores following drug treatments demonstrated cyto-D significantly disrupted the flow of GPI-GFP relative to actin flow while increasing actin polymerisation and stabilising existing fibres did not significantly affect this correlation. These results agree with the active composite model whereby GPI-AP’s interact with flowing actin in areas of liquid order through membrane leaflet

coupling due to lipids long acyl-chain interactions (Raghupathy et al. 2015; Gowrishankar et al. 2012).

As actin may drive membrane flow through lipid and protein interactions, the role of the candidate protein, α-actinin, was investigated. While ERM proteins are known to mediate interactions between transmembrane proteins and actin (Fehon et al. 2010), the role of actin organising proteins is less well known. This may be important; especially for proteins known to bundle and crosslink actin to generate meshworks. Arrangement may increase and control protein clustering, as seen by FRET (Chichili & Rodgers 2007) and hypothesised by the picket fence and active composite models (Kusumi, Nakada, et al. 2005; Köster et al. 2016).

α-actinin showed highly correlated flow with actin upon synapse formation within the dSMAC (Figure 5.29), where the actin meshwork is most dense and was also localised to regions where the highest correlation between the plasma membrane and actin were seen. As such CRISPR knockouts were generated to investigate this protein as a potential mediator of actin dynamics. By knocking out α–actinin it was demonstrated the retrograde nature of flow, quantified within both the plasma membrane and actin cortex, was disrupted at dSMAC regions. Whether this is due to a reduction in the actin-meshwork density, and therefore its ability to trap transmembrane proteins and translate lateral forces through them, a reduction in overall actin flow or another process remains to be elucidated.

The highest regions of correlation between the actin cortex and plasma membrane within wild-type Jurkat synapses also correlated with membrane ruffling imaged using IRM. This suggests actin meshwork-derived membrane ruffles also flow inwards from the dSMAC before diminishing in the actin and α-actinin poor pSMAC (Figure 5.29d). IRM results showed membrane ruffle speeds were not significantly different from plasma membrane flow, or labelled actin. These ruffles may be important for the modulation of signalling and synapse stability if they contain downregulatory molecules with large extracellular regions such as CD43-45, and integrins such as LFA-1. These molecules would be limited to these regions of larger interface partitioning due to their larger extracellular domains, as predicted by the kinetic segregation model (Anton van der Merwe et al. 2000) and shown via in vitro vesicle systems (Schmid et al. 2016).

Conflicting results between the single channel actin and plasma membrane following drug treatments may highlight a potential limitation of the imaging technique. With a frame rate of 1 s^{-1} and imaging of the comparatively homogeneous plasma membrane (versus F-actin labelled structures for example) the imaging and analysis may lack the sensitivity required to pick up a slowing of membrane flow. Additionally, as STICS correlates flowing populations, and

rejects static and diffusive signal within regions, only populations which are still exhibiting active and directed dynamics will be correlated. This is highlighted in §4.6 where significantly fewer vectors were generated for non-flowing samples. As such, if modulated actin flow leads to reduced membrane dynamics, STICS could reject these regions as diffusive signal.

Overall, this chapter demonstrates how the dynamics of the actin cytoskeleton can lead to a correlation between itself and the plasma membrane, while disrupting its retrograde flow leads to reduced directionality correlations. This correlation was also observed within the outer leaflet and could be due, in part, to the high levels of actin and α-actinin within the dSMAC region of the synapse, with α-actinin known to cluster and move lymphocyte membrane receptors (Hoessli et al. 1980). Finally, IRM data demonstrated a ruffling within the dSMAC with regions of membrane flowing in a retrograde fashion towards the cSMAC.

Chapter 6 – Subsynaptic vesicles at the immune synapse

While previous chapters focused on the flow and dynamics of the actin cytoskeleton within the immunological synapse, this chapter investigates the transportation and cargo of subsynaptic vesicles at the immunological synapse. In particular, the functional roles of the cytoskeleton and membrane order in controlling vesicle dynamics are studied. As shown in Figure 6.1, vesicle distribution has previously been shown to correlate with different stages of the $CD8^+$ T cell synapse, relating to both actin and microtubule dynamics (Ritter et al. 2015). Vesicles have also been shown to be important for cargo delivery and uptake in $CD4^+$ T cells (Soares et al. 2013). This chapter investigated the distribution and dynamics of vesicles during synapse formation; looking exclusively at those vesicles at the synapse interface with TIRF and confocal microscopy.

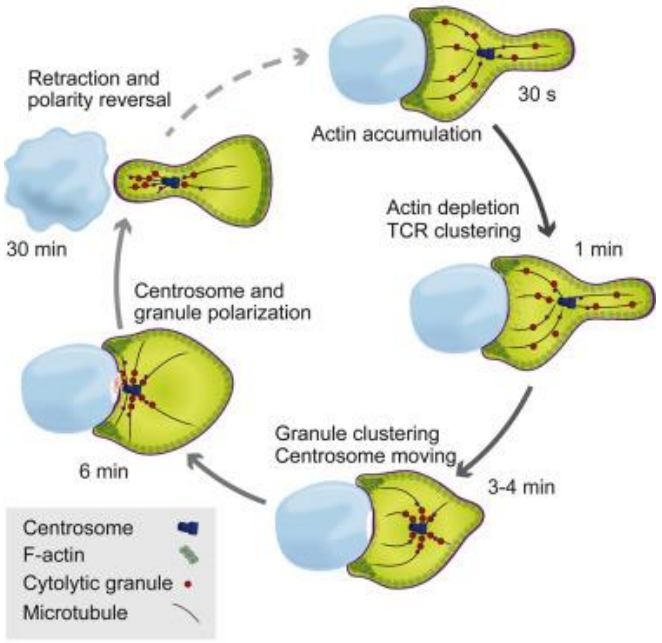

Figure 6.1 Vesicle distribution at the immunological synapse. Depending on the time after TCR engagement, vesicles (red spots) can be distributed at different regions of the cell, associated with the repolarisation of the MTOC. (Source: Ritter et al., 2015)

Vesicles are transported through various pathways including along actin tracks (Neco et al. 2003) and transported via myosin V and VI for short range motion (DePina & Langford 1999) and along microtubules through dynein and kinesin for long-range movement (Sheetz & Martenson 1991). More recent work using oocytes has revealed a long-range, actin-exclusive mechanism for vesicle dynamics; controlled by nucleation promoting factors (NPF's) (Schuh 2011).

As vesicles have been shown to distribute to different regions of the synapse (Soares et al. 2013) this may be controlled through their interaction with cortical actin and/or microtubules. F-actin has been shown to modulate vesicle behaviour serving both as tracks for delivery via myosin motors (Lang et al. 2000) and barriers of fusion (Wang & Richards 2011) with the cytoskeleton also creating hotspots of vesicle exocytosis, and disruption of either actin or microtubule networks halting this process (Yuan et al. 2015). Lang et al also found cortical actin had opposing actions, both trapping and driving vesicle diffusion, confusing previous reports as to the role of cortical actin regarding vesicle mobility.

This apparent confusion was previously addressed through the study of cellular Ca^{2+} influx, this modulated the cyclical recruitment of neuronal-WASp and $PI(4,5)P_2$ to the plasma membrane (Wollman & Meyer 2012). The study found these oscillations controlled vesicle trafficking through fluctuations in cortical actin; with actin firstly capturing vesicles when levels were high, passing them through the cortex when levels were low before aiding vesicular fusion upon the next peak in actin polymerisation.

Additionally, preformed T cell synapses have been shown to rely on the MTOC – not actin - for directed vesicle localisation, including targeted cytokine release, with disruption of the actin cytoskeleton not having the same effect (Ueda et al. 2015). This agrees with findings that the MTOC motor protein dynein may contribute, through direct interaction, with membrane-bound TCR microclusters, aiding dynamics within the actin poor cSMAC (Hashimoto-Tane et al. 2011). As such this chapter investigated the complex relationship between subsynaptic vesicle distribution, their dynamics in T cell synapses, and their relationship to the actin and microtubule cytoskeletal components.

To establish whether different cytoskeletal components affected specific populations of vesicles with specific membrane orders, drug treatments which modulate actin and microtubule dynamics were applied to T cells. As lipid order has a role in modulating the heterogeneous nature of the plasma membrane, both in terms of structure and the proteins they contain, this work was also carried out using environmentally sensitive dyes. Firstly, vesicle populations were analysed to determine whether different membrane order cohorts existed. After optimisation, this work was moved on to study vesicular dynamics within primary human T cells. Finally, 3 channel imaging of fixed cells was carried out to deduce whether vesicle populations with different membrane orders were present on different cytoskeletal structures (e.g. actin or microtubules) and whether these vesicle populations preferentially contain different cargos, as is hypothesized in the lipid raft model for the plasma membrane (Simons & Ikonen 1997).

6.1. Imaging of subsynaptic vesicles and membrane order

Firstly, the protocol was demonstrated in Jurkat T cells, after being incubated with the environmentally sensitive dye; di-4-ANEPPDHQ (§3.5 and §3.7.3). T cells were imaged forming an immunological synapse against a CD3 and CD28 antibody coated coverslip, providing evidence of more ordered (white arrow) and disordered (blue arrow) vesicles (Figure 6.2a). By splitting the green- and red-shifted emission spectra from di-4-ANEPPDHQ (Figure 6.2b & c) a ratiometric measurement was generated by GP analysis, giving a grayscale and pseudo-colour image (Figure 6.2d & e). The grayscale image provided a means to quantify vesicular GP values for evidence that there were vesicles exhibiting different degrees of orderedness (Figure 6.2f) which could then be tracked for dynamics.

Vesicles were tracked using an autoregressive motion algorithm which allows the automated tracking of vesicles which exhibit acceleration and deceleration, but does provide improved tracking accuracy of linear motion, compared with a Brownian motion model.

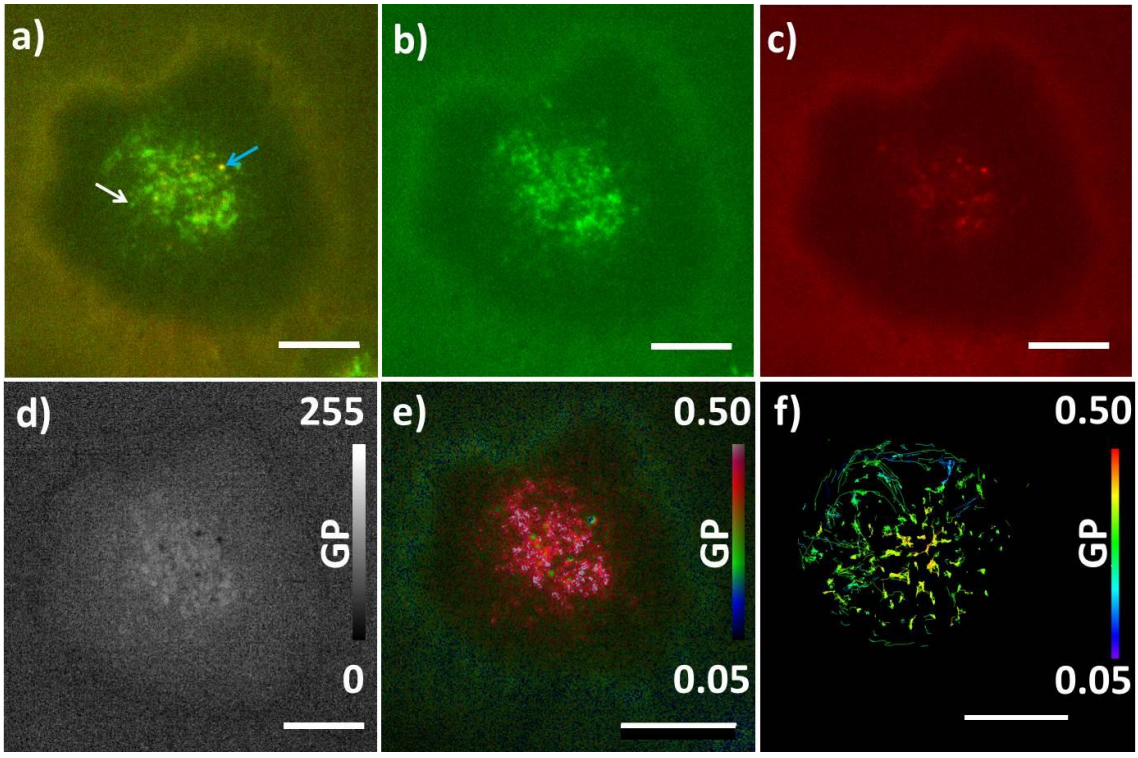

Figure 6.2 Subsynaptic vesicles imaged by di-4-ANEPPDHQ for quantification. To quantify the orderedness of vesicles at the Jurkat T cell synapse the environmentally sensitive dye di-4-ANEPPDHQ was used to stain the membrane, with T cells stimulated into forming a synapse against an antibody coated coverslip (a) two channel imaging provided raw data which demonstrated vesicles of higher (white arrow) and lower (blue arrow) order. This data was split into ordered (b) and disordered (c) channels based on the dyes spectra before GP analysis provided a grayscale image (d) and psuedo-coloured images (e) both representing membrane order. f) These vesicles were then tracked, with mean GP values for the whole dataset attributed to each vesicle track. Information on their membrane order could then be attributed to each vesicles dynamics. Scale bars = 10 µm.

As shown in §4.2 using SMLM techniques, actin forms a dense meshwork at the dSMAC region of the synapse, which in NK cells is thought to act as a barrier for vesicle transport to these regions, limiting vesicle trafficking to the centre for better targeted cell killing (Rak et al. 2011; Mace & Orange 2014). Additionally actin clearing at the synapse centre allows MTOC reorientation, for transportation of more vesicles and sustaining late-stage signalling in $CD8^+$ T cells (Ritter et al. 2015).

As individual vesicles exhibited different levels of membrane order these values were plotted (Figure 6.3), here total vesicle populations demonstrated a slight but significant change ($p < 0.0001$) from a GP value of 0.29 ± 0.07 for early synapses (Figure 6.3a) to 0.30 ± 0.09 in mature synapses (Figure 6.3b). This difference is in line with those previously reported for imaging of T cell plasma membranes during stimulation by CD3 coated beads; where mean GP values at sites of T cell activation exhibit a two-Gaussian fit with peaks 3 minutes after stimulation of 0.228 and 0.406 and after 7 minutes of 0.201 and 0.456 (Gaus et al. 2005). Though quantification of GP values at the bead contact sites before and after stimulation was significant, others have reported non-significant shifts in plasma membrane order after stimulation by CD3 in solution (Dinic et al. 2015). Results here demonstrate similarities with previous plasma membrane findings; where individual GP values of subsynaptic vesicles resulted in significant differences, but mean shifts are small due to the range of values quantified.

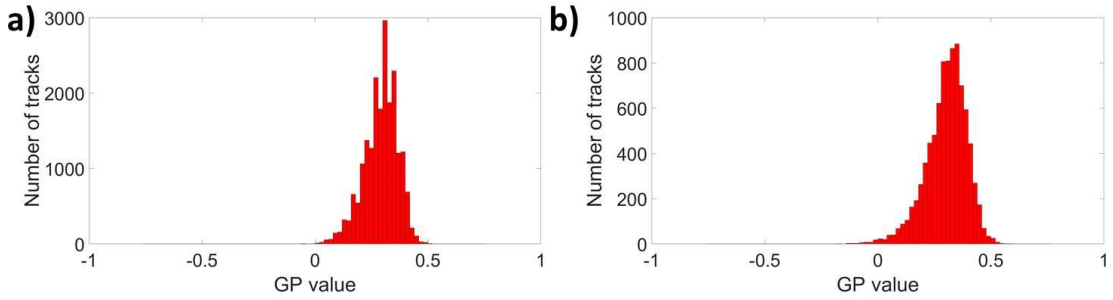

Figure 6.3 Vesicle tracks plotted for membrane order through GP analysis. After synapse formation stained vesicles were identified using Imaris spot tracker software before quantifying individual order values. a) Shows the distribution of GP values for early synapses (5-10 minutes after stimulation) and b) the orderedness of vesicles in mature synapses (10-20 minutes after stimulation) (n = 20,612 and 8,640 vesicles [24 and 20 cells]).

This data demonstrates lipid order varies within vesicle populations, and that this technique is sensitive enough to quantify these populations. The data collected includes track statistics which could be important for characterising different populations of vesicles and their dynamics at the synapse. Vesicle GP values were therefore correlated with vesicle track

dynamics to establish the relationships between membrane order and vesicle behaviour using primary human T cells.

6.2. Vesicle characteristics in primary human T cell synapses

To fully characterise the vesicular populations of the immunological synapse, datasets were taken 10 minutes after synapse formation. This permitted the imaging of vesicles associated with both actin fibres and microtubules; as the MTOC polarises towards the synapse after 7 minutes (Ritter et al. 2015). Analysis of vesicles was therefore undertaken on mature (> 10 minute) synapses. Vesicles were tracked for 30 seconds, collecting ordered and disordered channels (Figure 6.4a-c); at 4 frames per second with track statistics correlated to individual GP values (Figure 6.4d). Finally, as GP values are given as means across the whole tracking event the GP value of an individual vesicle was plotted through time to ensure these means were representative of the vesicles order through the tracking event (Figure 6.4e). This plot demonstrated small fluctuations in vesicle order about the means (0.06 ± 0.01 [red plot], 0.06 ± 0.03 [blue plot] and 0.07 ± 0.02 [green plot]), thus reporting mean GP values from vesicle tracks is a valid method – though these fluctuations could be investigated in the future.

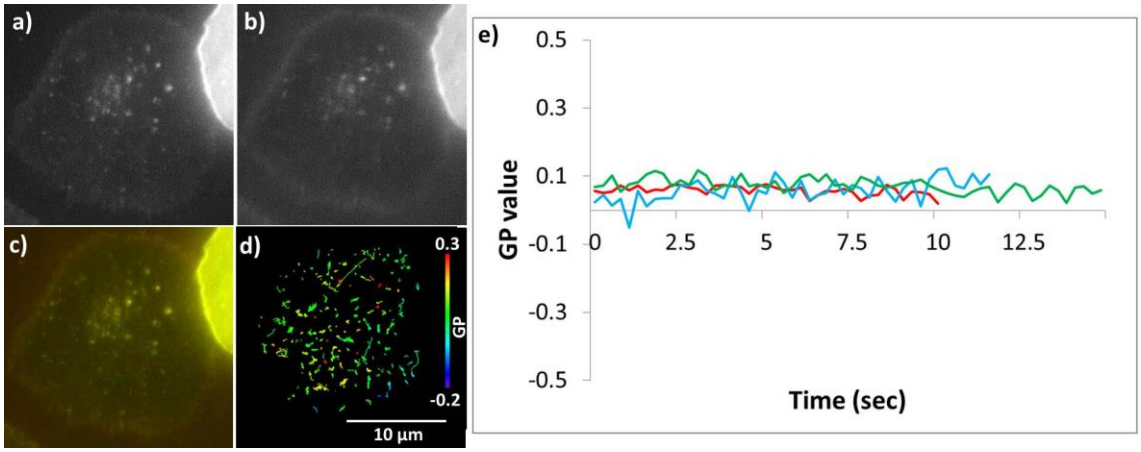

Figure 6.4 Vesicle order and track characteristics in primary human T cells. Representative T cell stained with the membrane dye di-4-ANEPPDHQ forming an immunological synapse, for identification of a) ordered and b) disordered emission from the membrane dye. c) Merged ordered and disordered channel and d) Tracking of individual vesicles with corresponding tracks coloured for each GP value, e) demonstrates an individual vesicles GP value through the entire tracking event (n = 3).

After Pearson's correlation analysis of GP values and track statistics, results demonstrated a significant correlation between individual vesicle membrane order and their speeds ($r = -0.22$, Figure 6.5a), track duration ($r = 0.26$, Figure 6.5b) and track length ($r = 0.18$, Figure 6.5c) and track straightness ($r = -0.12$, Figure 6.5d, $p < 0.0001$ in all cases).

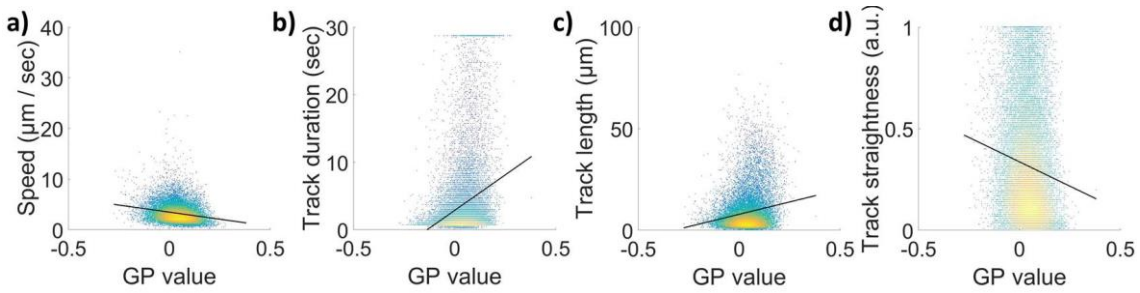

Figure 6.5 Vesicle order and track correlation in primary human T cells. Tracking statistics from individual vesicles GP values were correlated against vesicle a) speed, b) track duration c) track length and d) track straightness. N = 20,240 vesicles (from 20 cells).

These findings demonstrate more ordered vesicles move slower while residing at the synapse for longer periods of time, exhibiting more stability with longer tracks but exhibit lower directionality and therefore less straightness. Vesicles are known to travel along different cytoskeletal components using different mechanisms; for example, long-range microtubule based locomotion requires dynein and kinesin and actin based travel relies on myosin V (DePina & Langford 1999) and potentially actin polymerisation itself (Schuh 2011). Findings here agree with previous data that vesicle populations may use different cytoskeletal methods for different transportation dynamics, but with the novel possibility that the membrane order is correlated with these dynamics. To elucidate the role of the cytoskeleton with vesicle dynamics and membrane order, further investigation was carried out using drug treatments which modulate the polymerisation and stability of different cytoskeletal structures.

If aspects of the cytoskeleton regulate vesicle dynamics, disruption of specific components may change vesicle behaviour. Any vesicle sub-populations using actin or microtubules based on their order - signified by GP analysis - may exhibit quantifiable changes in dynamic behaviour compared to control conditions.

Firstly, drug treatments were repeated as in §5.2, with cytochalasin-D (CD; 2 µM) added to cells after the formation of synapses. As shown in §5.2, actin fibres and polymerisation are disrupted upon its addition due to reduced binding of G-actin to the fast growing barbed end of F-actin and severing of existing fibres (Wegner 1976; Brown & Spudich 1981; Schliwa 1982). Collected ordered and disordered channels (Figure 6.6a-c), were used to track vesicle dynamics and correlated to individual GP values (Figure 6.6d).

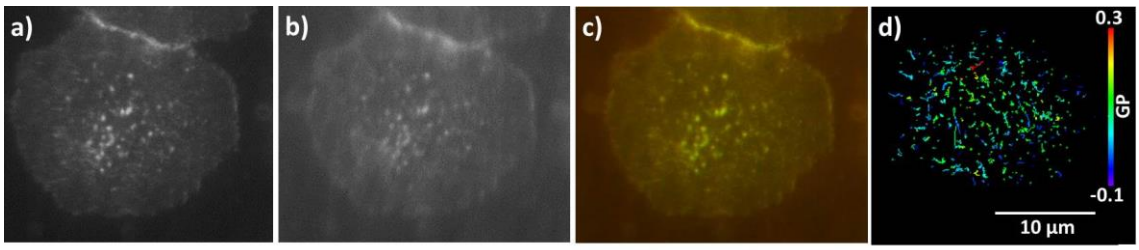

Figure 6.6 Vesicle order and track characteristics after cytochalasin-D treatment of primary human T cells. a) Representative T cell stained with the membrane dye di-4-ANEPPDHQ forming an immunological synapse, for identification of a) ordered and b) disordered emission from the membrane dye. c) Merged ordered and disordered channel and d) Tracking of individual vesicles with corresponding tracks coloured for each GP value.

GP values within CD treated cells were analysed for tracked vesicles with individual membrane order correlated against speeds (r = -0.12, Figure 6.7a), track duration (r = 0.24, Figure 6.7b) and track length (r = 0.19, Figure 6.7c) and track straightness (r = -0.07, Figure 6.7d, $p < 0.0001$ in all cases).

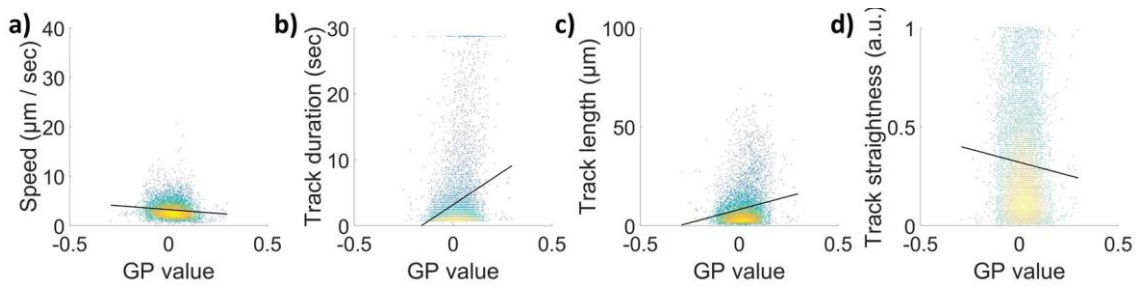

Figure 6.7 Vesicle order and track correlation in primary human T cells following cytochalasin-D treatment. Tracking statistics from individual vesicles GP values were correlated against vesicle a) speed, b) track duration c) track length and d) track straightness. N = 8350 vesicles (from 19 cells).

Next, as in §5.2, the drug jasplakinolide (2 µM) was added to cells after the formation of synapses; this drug enhances actin nucleation thereby increasing F-actin polymerisation and stabilisation (Bubb et al. 2000). This is in agreement with results in §5.2 where jasplakinolide was shown to stabilise existing fibres and scramble the retrograde nature of the meshwork. Here, vesicles were tracked for 30 seconds, collecting ordered and disordered channels (Figure 6.8a-c); track statistics were correlated to individual GP values (Figure 6.8d).

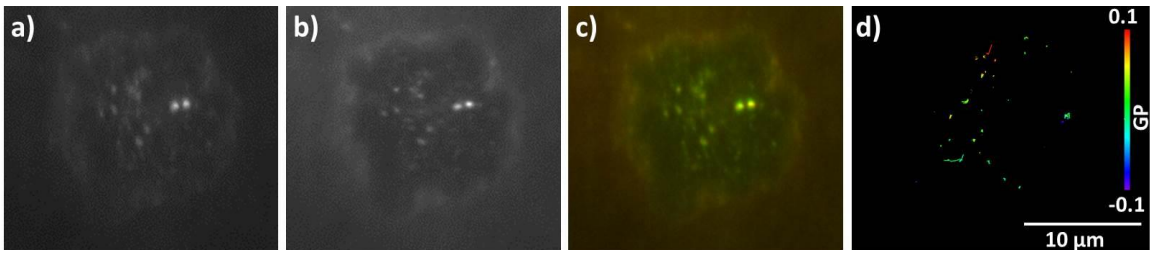

Figure 6.8. Vesicle order and track characteristics in primary human T cells following jasplakinolide treatment. Representative T cell stained with the membrane dye di-4-ANEPPDHQ forming an immunological synapse, for identification of a) ordered and b) disordered emission from the membrane dye. c) Merged ordered and disordered channel and d) Tracking of individual vesicles with corresponding tracks coloured for each GP value.

Treated cells were analysed (Figure 6.9) and individual membrane orders of vesicles were correlated against vesicle speeds (r = -0.17 Figure 6.9a), track duration (r = 0.21, Figure 6.9b) track length (r = 0.14, Figure 6.9c) and track straightness (r = -0.13, Figure 6.9d, $p < 0.0001$ in all cases).

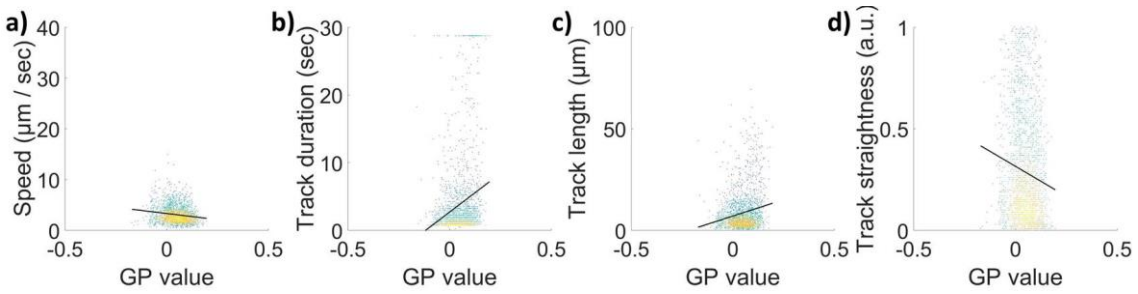

Figure 6.9 Vesicle order and track correlation in primary human T cells following jasplakinolide treatment. Tracking statistics from individual vesicles GP values were correlated against vesicle a) speed, b) track duration c) track length and d) track straightness. N = 2213 vesicles (from 9 cells).

Finally, nocodazole (2 µM) was added to cells after synapse formation; this drug depolymerises microtubules (Vasquez et al. 1997) including the MTOC, so may result in reduced delivery of vesicles to the immunological synapse. Vesicles were tracked for 30 seconds, collecting ordered and disordered channels (Figure 6.10a-c); with track statistics correlated to individual GP values (Figure 6.10d).

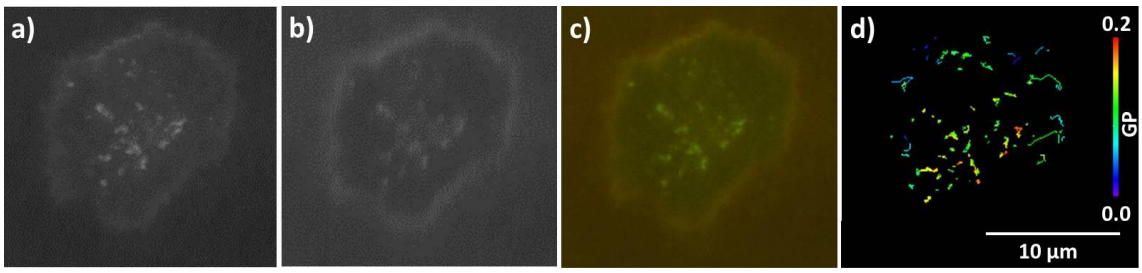

Figure 6.10. Vesicle order and track characteristics after nocodazole treatment of primary human T cells. T cell stained with the membrane dye di-4-ANEPPDHQ forming an immunological synapse, for identification of a) ordered and b) disordered emission from the membrane dye. c) Merged ordered and disordered channel and d) Tracking of individual vesicles with corresponding tracks coloured for each GP value.

Treated cells were analysed (Figure 6.11) and individual membrane orders of vesicles were correlated against vesicle speeds (r = -0.12 Figure 6.11a), track duration (r = 0.14, Figure 6.11b) and track length (r = 0.11, Figure 6.11c) and track straightness (r = -0.06, Figure 6.11d, $p < 0.0001$ in all cases).

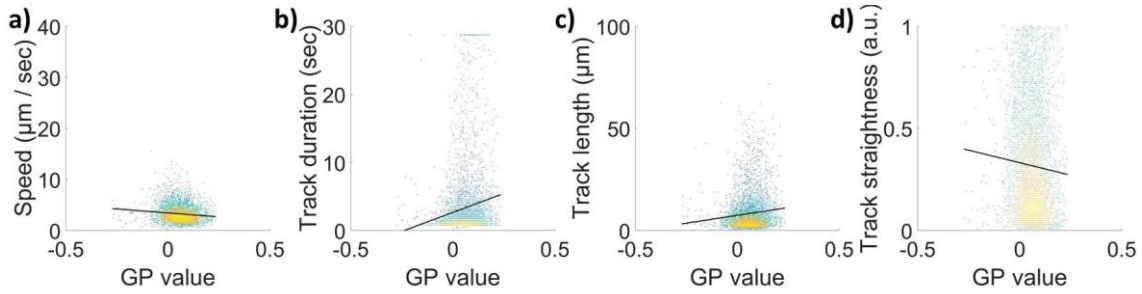

Figure 6.11 Vesicle order and track correlation in primary human T cells following nocodazole treatment. Tracking statistics from individual vesicles GP values were correlated against vesicle a) speed, b) track duration c) track length and d) track straightness. N = 4569 (from 18 cells).

These experiments investigated any effect drug treatments had on vesicle trafficking to the synapse and whether perturbing cytoskeletal components control specific membrane order subpopulations. Figure 6.12 shows results of overall vesicle GP values. Compared to control cells (Figure 6.12a, 0.041 ± 0.07), membrane order was reduced upon disruption of F-actin with CD (0.021 ± 0.06, $p < 0.0001$), but increased upon F-actin stabilisation with jasplakinolide (0.048 ± 0.06, $p < 0.0001$). Disruption of microtubules increased the GP values of vesicles at the synapse (0.058 ± 0.06, $p < 0.0001$). Figure 6.12b shows the number of tracks per cell, compared to control conditions (492.5 ± 188.0) CD did not affect the number of tracks (439.5 ± 176.2, $p = 0.3$), while increasing F-actin polymerisation and its stability reduced the number of tracks (276.6 ± 193.8, $p = 0.005$). The most significant reduction in tracked vesicles at the synapse came when microtubules were disrupted (228.5 ± 101.1, $p < 0.0001$).

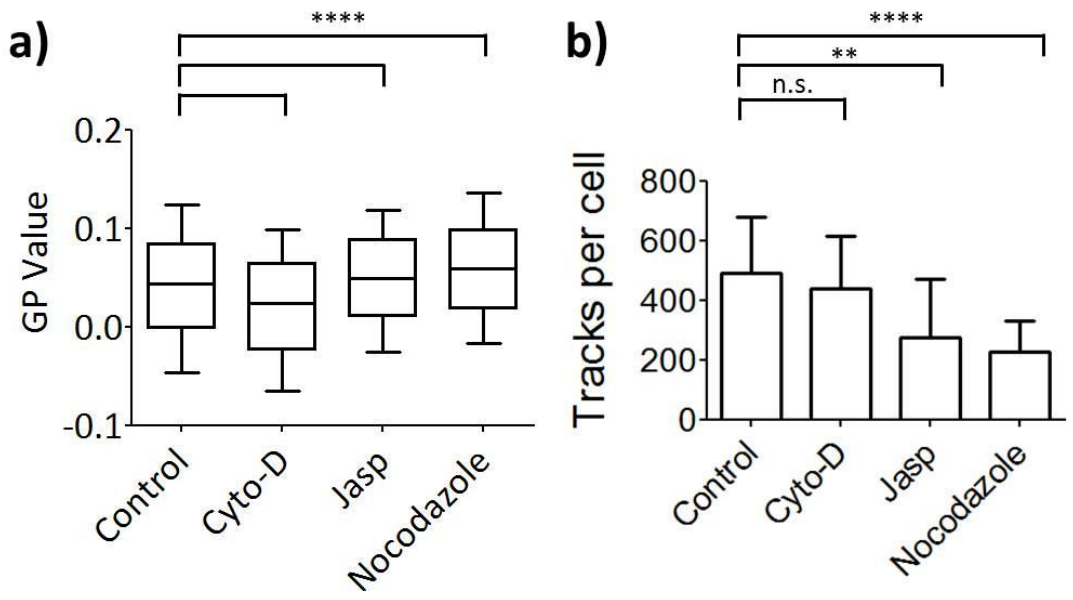

Figure 6.12 Vesicle order and trafficking following drug treatments. After synapse formation cytoskeletal modulating drugs were added and vesicles membrane order was measured (a). Compared to control cells GP values 0.041 ± 0.07, Cytochalasin-D treatment reduced membrane order 0.021 ± 0.06, while stabilising F-actin or disrupting microtubules with jasplakinolide and nocodazole respectively both increased vesicle order, 0.048 ± 0.06 and 0.058 ± 0.06. b) The total numbers of tracks were quantified, compared to controls 492.5 ± 188.0, the number of tracks were unaffected by cytochalasin-D (439.5 ± 176.2, p = 0.3), but increasing F-actin stability or reducing microtubule stability both reduced track numbers (276.6 ± 193.8, p = 0.005 and 228.5 ± 101.1, p < 0.0001).

This data demonstrates more ordered vesicles may rely in part on the actin cytoskeleton, as reducing F-actin lowers the presence of more ordered vesicles at the synapse interface, while increasing fibre polymerisation and stabilising them increased vesicle order in the subsynaptic region. These results also point to actin functioning as a barrier, with F-actin stabilisation reducing the number of quantified tracks. This leads to the hypothesis that ordered vesicles are reliant on actin dynamics for their transportation to the immunological synapse, while disordered vesicles rely on microtubules for delivery to the synapse interface.

These changes in GP value appear small due to the large variation in individual vesicle GP values, but these trends agree with previous findings, where the actin depolymerising drug latrunculin-B reduced plasma membrane order in Jurkat T cells by 0.2, while jasplakinolide increased membrane order by the same amount (Dinic et al. 2013).

Tracked vesicles after drug treatments were then compared with box plots (Figure 6.13). Compared to control cell track speeds (0.52 ± 0.28 µm / sec; Figure 6.13a), disruption of F-actin with CD (0.51 ± 0.26 µm / sec, $p < 0.005$), or F-actin stabilisation with jasplakinolide (0.50 ± 0.26 µm / sec, $p < 0.0001$) reduced these. Disruption of microtubules had no effect on vesicle speed (0.52 ± 0.26 µm / sec, $p = 0.94$). Figure 6.13b plots track duration, showing, compared to

control conditions (3.72 ± 5.56 seconds) neither CD or jasplakinolide affected vesicle track durations (3.60 ± 5.29 seconds, $p > 0.05$ and 3.80 ± 5.95 seconds, $p > 0.5$ respectively). When microtubules were disrupted durations were significantly reduced (3.29 ± 5.02 seconds, $p < 0.0001$).

When track lengths (Figure 6.13c) were compared with controls (1.42 ± 1.45 µm) F-actin disruption led to non-significant changes for CD (1.40 ± 1.42 µm, $p = 0.27$) and jasplakinolide (1.40 ± 1.47 µm, $p = 0.19$), while nocodazole treatment significantly reduced track length (1.33 ± 1.39 µm, $p < 0.0001$). Finally track straightness was analysed, compared to controls (0.32 ± 0.26) neither disruption of the actin cytoskeleton by CD (0.32 ± 0.26, $p = 0.52$), or microtubules (0.32 ± 0.26, $p = 0.99$) significantly affected this, however stabilising actin with jasplakinolide did (0.29 ± 0.26, $p < 0.0001$).

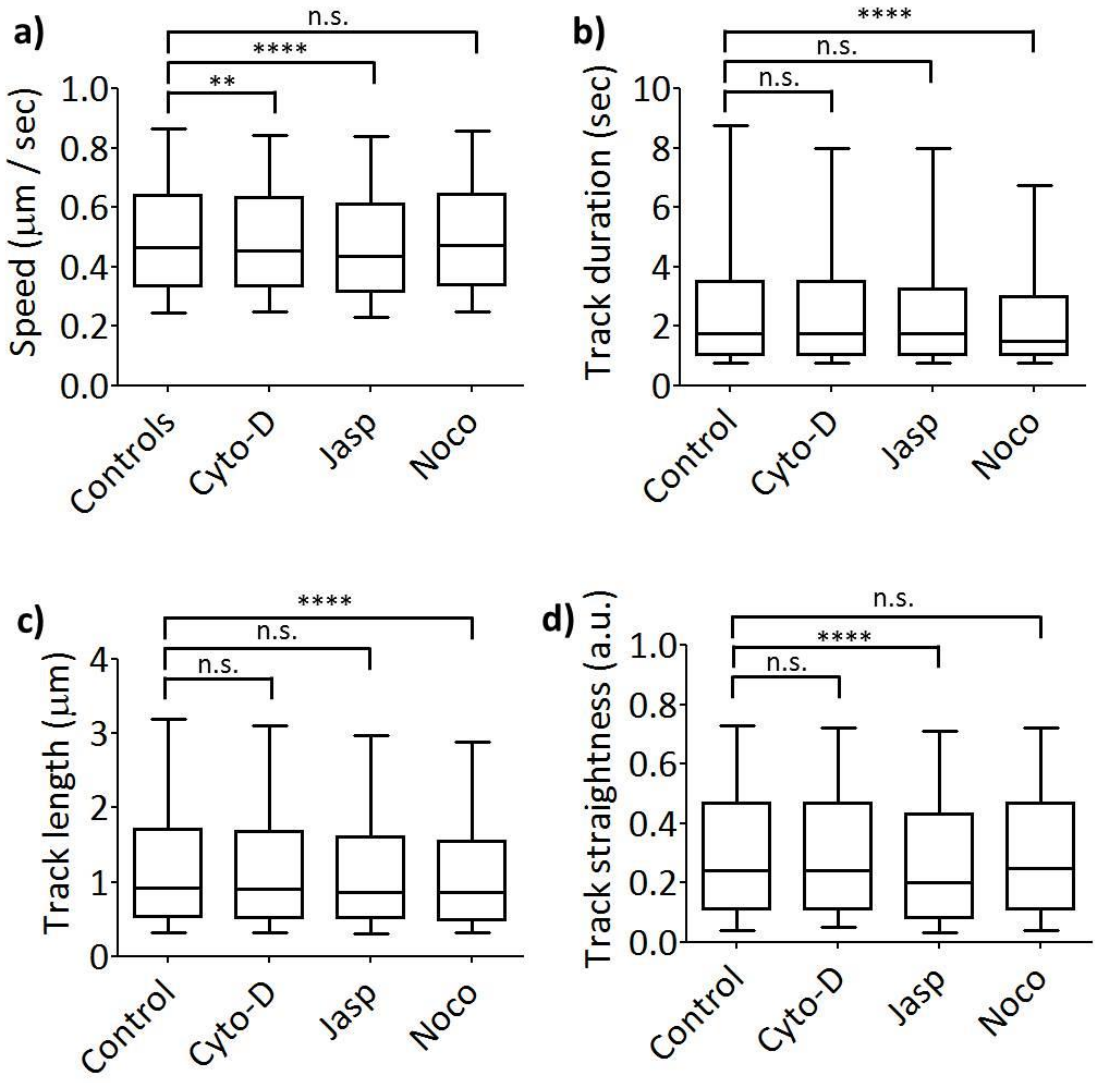

Figure 6.13 Vesicle track characteristics of primary human T cells. Box plots of vesicles for control and drug treatment conditions for track a) speed, b) duration, c) length and d) straightness. Whiskers show the 10 and 90 percentile range for clarity. ns = non-significant, ** $p < 0.005$, **** $p < 0.0001$.

This data shows disruption of polymerised actin reduced the speed of vesicle movement, but did not affect the time vesicles spent at the synapse interface, nor the length or straightness of vesicle tracks. These data suggest actin polymerisation and turnover; potentially through retrograde flow of cortical actin or through polymerisation events including 'actin tails' - based on vesicle composition - is in some way important for vesicle dynamics. Reduced track straightness may demonstrate vesicles unable to efficiently fuse with the plasma membrane, causing undirected motion to and from the synapse interface, as was shown by the reduced number of vesicles per cell in Figure 6.12b.

Surprisingly disruption of microtubules had no effect on vesicle speed or track straightness, two categories associated with vesicle trafficking of microtubules due to their morphology. This may be due to tracked vesicles no longer being associating with microtubules; however no imaging of microtubules was carried out in this work so drug concentrations and incubation times were based on previous studies.

These results together show subsynaptic vesicle populations exhibit different dynamics, based on their membrane order, and when disrupting the cytoskeleton during T cell synapse formation, these dynamics can be modulated. Ordered vesicle dynamics and localisation appear more sensitive to F-actin modulation, while disordered vesicles are more reliant on the microtubule network (Figure 6.14).

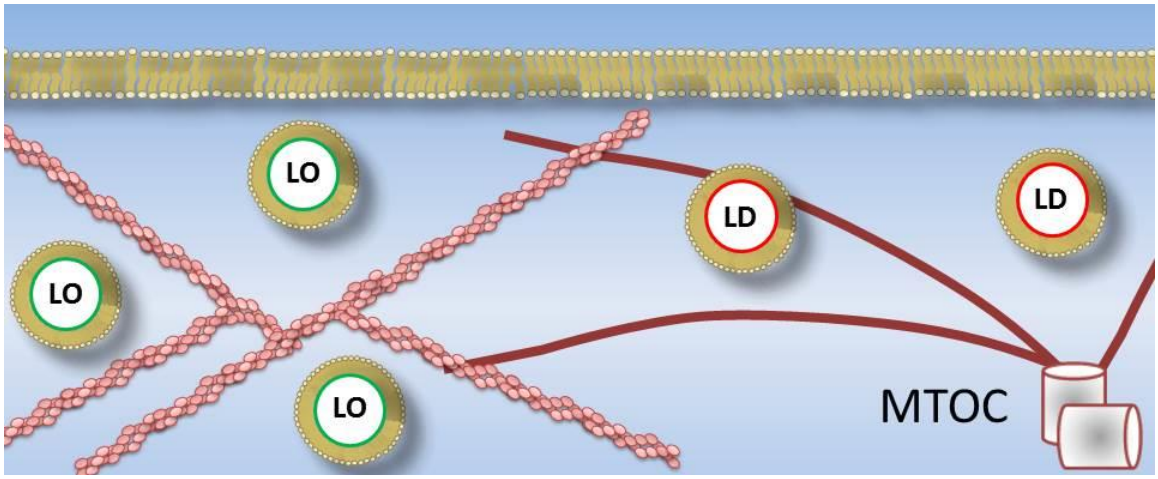

Figure 6.14 Schematic of vesicle and cytoskeleton interplay at the immunological synapse. F-actin acts as a dynamic barrier for more ordered vesicles at the synapse interface, as stabilising actin fibres reduces the number of vesicles tracked in this region, additionally lipid order of remaining vesicles is reduced upon F-actin disruption. Interestingly, upon microtubule disruption vesicle numbers were also reduced, with remaining vesicles exhibiting higher orders compared to controls.

To investigate whether these changes were indeed due to different vesicle populations residing on or proximal to different cytoskeletal structures, 3-channel imaging was carried out.

6.3. Vesicle order and the cytoskeleton

As shown here, and previously, vesicle dynamics and their directed transportation by the cytoskeleton may exist through actin tracks (Neco et al. 2003), actin polymerisation (Schuh 2011) or microtubules for long range transportation (Ritter et al. 2015). Most trafficking processes require vesicles to recruit specific proteins to organise their own transportation, for example NPF's can generate actin polymerisation on vesicles themselves, as observed in oocytes (Schuh 2011).

F-actin modulates both vesicle delivery via myosin motors (Lang et al. 2000) and fusion (Wang & Richards 2011). The cytoskeleton also creates hotspots of vesicle exocytosis, in an actin and microtubule dependent manner (Yuan et al. 2015). Within the T cell synapse, vesicles distribute to different synaptic regions (Soares et al. 2013) this may be controlled through their interaction with cortical actin. Based on these findings, lipid order of subsynaptic vesicles was correlated to specific cytoskeletal components in the context of the immunological synapse, to deduce intersystem relationships.

Jurkat T cell membranes were stained with di-4-ANEPPDQ and stimulated to form synapses as described in the methods section. 10 minutes post-stimulation cells were fixed and either actin or microtubules were labelled with AlexaFluor-647 conjugated to phalloidin, or α-tubulin antibody followed by secondary antibody labelling conjugated to AlexaFluor-647. 3-channel imaging of di-4-ANEPPDHQ stained vesicles followed by sequential imaging of either actin or microtubules was then carried out on the Nikon A1R confocal microscope §3.7.5.

To further investigate the hypothesised role for actin as a dynamic barrier for ordered vesicle trafficking, F-actin was imaged along with stained vesicles (Figure 6.15), as with previous imaging, vesicles demonstrated both ordered (Figure 6.15a) and disordered (Figure 6.15b) populations, while actin formed a dense meshwork at the dSMAC which gave way to resolvable fibres within the pSMAC, and punctate actin structures were detected in the cSMAC (Figure 6.15c). When overlaid these imaged showed vesicles close to actin structures (Figure 6.15d).

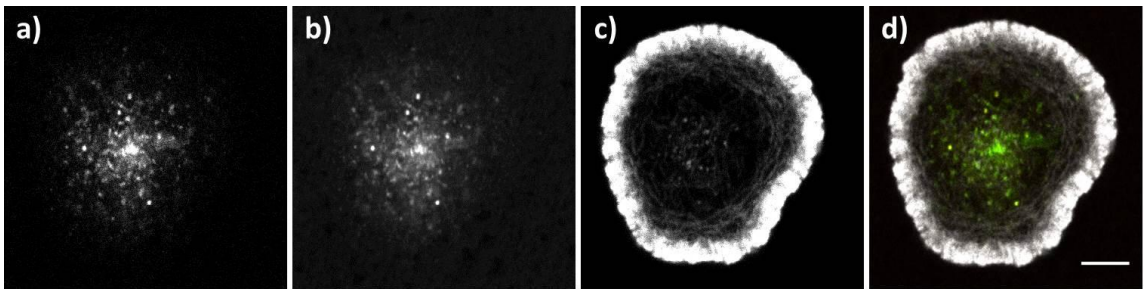

Figure 6.15 Vesicle order and actin structure at the immunological synapse. Vesicles were stained with di-4-ANEPPDHQ to permit imaging of both a) ordered and b) disordered emission spectra, actin c) was visualised allowing overlay d) with vesicle data for analysis. Scale bar = 5 µm.

To assess the distribution of vesicles and actin and whether there was any overlap a single line profile was taken of a representative cell (Figure 6.16a). The normalised intensity profile showed that towards the synapse centre some actin intensity peaks appeared negatively correlated to vesicles while others may be proximal to these cytoskeletal structures (Figure 6.16b).

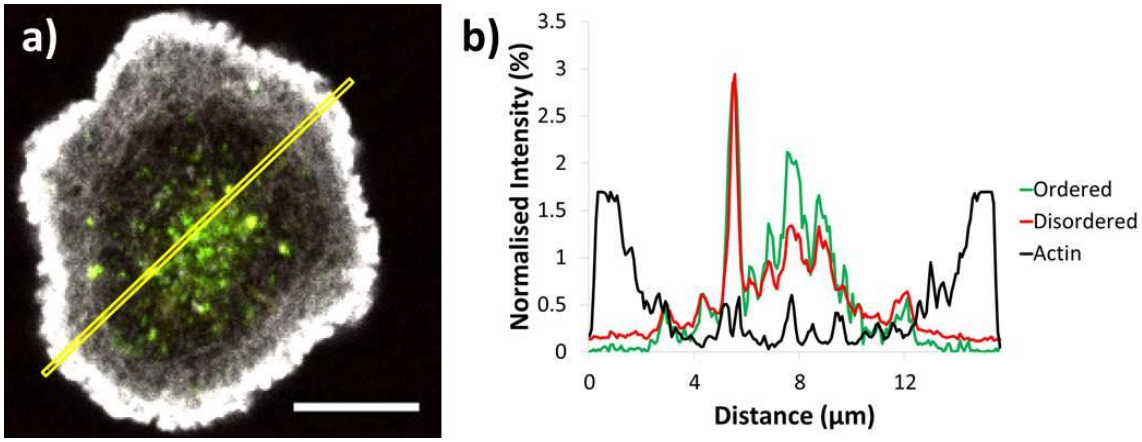

Figure 6.16 Line profile plots of vesicle order and actin. a) Single pixel width line plots were taken through the synapse and the 3 channels intensities were normalied and b) plotted. Line plots demonstrate actin resides in more peripheral regions, with vesicle intensities peaking in regions devoid of actin. Scale bar = 5 µm.

To investigate these findings further, ROI's were taken of the pSMAC and cSMAC area from multiple cells, with membrane intensity values quantified and correlated to the intensity of actin (Figure 6.17). Correlation analysis revealed individual vesicle intensities were anti-correlated with local actin density ($r = 0.05$, $p = 0.6$, $n = 153$).

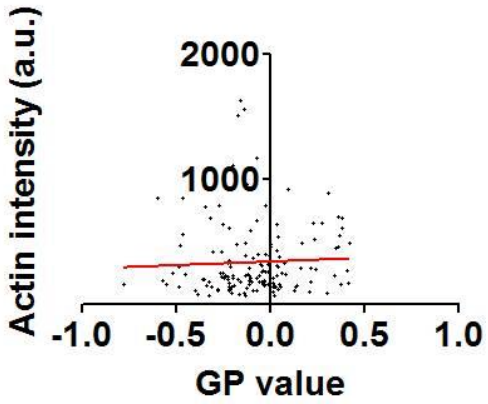

Figure 6.17 Vesicle order and actin intensity correlation in Jurkat T cells. Individual vesicle GP values were correlated against actin intensity within the same ROI providing a non-significant Pearson's correlation (r = 0.05, p = 0.6), n = 153.

As vesicles were not correlated with actin **s**tructures within the pSMAC or cSMAC this implies these are possible sites of vesicle endocytosis or exocytosis, with actin poor regions permitting vesicle fusion with the plasma membrane. This agrees with previous findings using fixed NK cells and SIM imaging that actin forms holes within the cSMAC with dimensions to allow vesicles through (Brown et al. 2011). Findings here demonstrate for the first time using fluorescence microscopy this is the case for T cells. These results may demonstrate vesicles are trapped within the peripheral actin network, between fibres of the pSMAC, resulting in reduced correlation of vesicles to overall actin intensity.

Next, microtubules were imaged sequentially with stained vesicles, as this cytoskeletal component was hypothesized in the previous section to influence disordered vesicle trafficking to the synapse interface and is known to aid transportation of vesicles to both murine and human T cell synapses (Ritter et al. 2015; Hashimoto-Tane et al. 2011). Stained vesicles were imaged for both their ordered (Figure 6.18a) and disordered (Figure 6.18b) components, along with microtubules (Figure 6.18c), the MTOC was localised near the synapse centre, which is where the actin-poor central region is also located, as previously reported for $CD8^+$ murine cells (Ritter et al. 2015). Microtubules radiated outwards towards the dSMAC, with the majority of vesicular signal found in the region of the MTOC, indicating vesicles may be located on these structures.

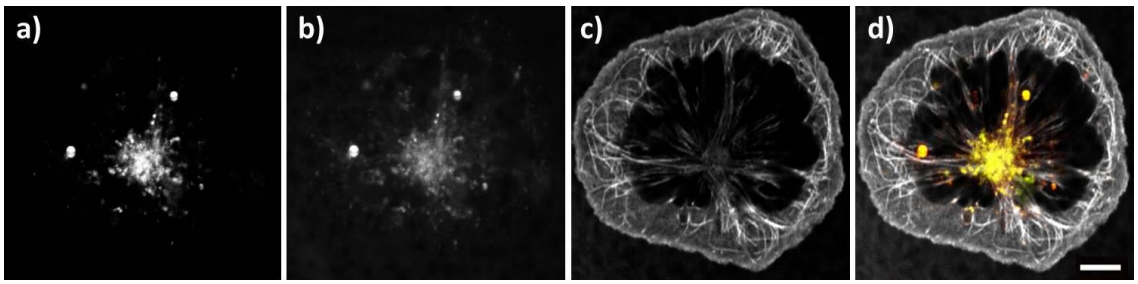

Figure 6.18 Vesicle order and microtubule structure at the immunological synapse. Vesicles were stained with di-4-ANEPPDHQ to permit imaging of both a) ordered and b) disordered emission spectra, microtubules c) were visualised allowing overlay d) with vesicle data for analysis. Scale bar = 5 µm.

A single line profile was taken (Figure 6.19a). A normalised intensity profile demonstrated vesicle intensity peaks around the centre of the MTOC structure (Figure 6.19b). Though these findings were more difficult to interpret than the actin line profiles as MTOC fibres were less bright than peripheral regions, and fibres were located more along ROI's than passing through them as with actin; which when normalised gave spikes of phalloidin-647 intensity.

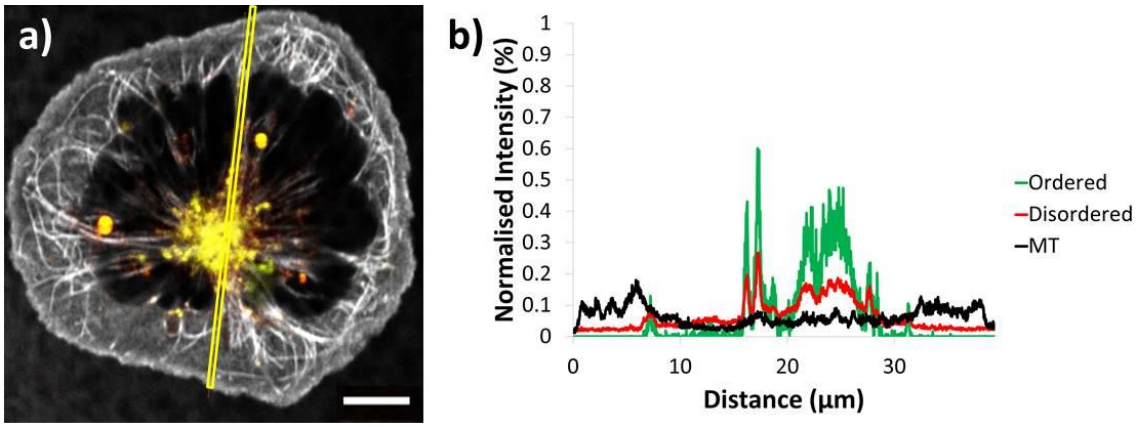

Figure 6.19 Line profile plots of vesicle order and microtubules. a) Single pixel width line plots were taken through the synapse and the 3 channels intensities were normalied and b) plotted. Line plots demonstrate increased intensity for microtubules around the synapse periphery and centre, with vesicles residing in more central regions. Scale bar = 5 µm.

To clarify these results, correlation analysis was carried out (Figure 6.20), this revealed individual vesicle GP intensities were negatively correlated to local microtubule density ($r = -0.19$, $p < 0.0001$, $n = 795$).

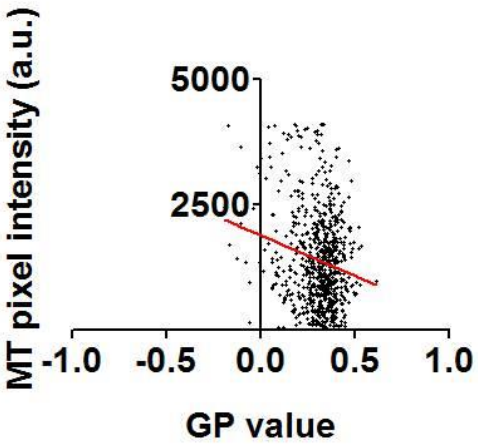

Figure 6.20 Vesicle order and microtubule intensity correlation in Jurkat T cells. Individual vesicle GP values were correlated against microtubule intensity within the same ROI providing a significantly non-zero Pearson's correlation (r = -0.19, p < 0.0001), n = 795.

Here, vesicles were anti-correlated with F-actin within the pSMAC, and therefore had GP value dependence on their colocalisation. However vesicles did show some correlation to microtubules, with more disordered vesicles preferentially colocalising with this cytoskeletal component. Together these results demonstrated more disordered vesicles preferentially localise with microtubules, which agrees with the hypothesized model of the previous section (Figure 6.14) where nocodazole treatment led to a decrease in the number of disordered vesicles (i.e. increased mean GP values of remaining subsynaptic vesicles).

6.4. Vesicle order and cargo

Lipid order has been established as a contributing factor in determining the heterogeneity of molecules within the plasma membrane, including T cells (Owen et al. 2012; Dinic et al. 2015). It has also been shown through lipidomic studies that lipid raft-like molecules including cholesterol, sphingomyelin and saturated phosphatidylcholine are associated with the TCR (Zech et al. 2009). The interplay between lipid order and protein composition is clearly a complicated area and with the findings in this chapter that vesicles exhibit order heterogeneity akin to the plasma membrane it was next established whether vesicles of different orders contain different cargo proteins.

Phosphorylated LAT is known to be contained within vesicles and is located at the synapse after TCR signalling, where it is thought to create a signalosome complex, dependent on the vesicle associated membrane protein (VAMP)-7 (Larghi et al. 2013; Williamson et al. 2011). LAT is also palmitoylated, aiding membrane localisation and has also been shown to reside in more ordered membrane compartments such as DRM's (Zhang et al. 1998). Furthermore, Lck, TCR-ζ and LAT reside in different vesicular compartments based on trafficking components: Lck

colocalised with MAL and Rab11b, TCR-ζ with Rab3, Rab8 and VAMP while LAT is found with Rab27a and VAMP containing vesicles (Soares et al. 2013).

Cells were stained with di-4-ANEPPDHQ and fixed before immunostaining for LAT and imaged on the Nikon confocal A1R as in the previous section. This permitted the imaging of both vesicle order (Figure 6.21a) and disorder (Figure 6.21b), along with endogenous LAT (Figure 6.21c). Images of LAT demonstrated populations of LAT did not fully overlay with vesicle staining (Figure 6.21d); as LAT is known to reside both in the plasma membrane and vesicles this agrees with previous data (Balagopalan et al. 2013; Williamson et al. 2011).

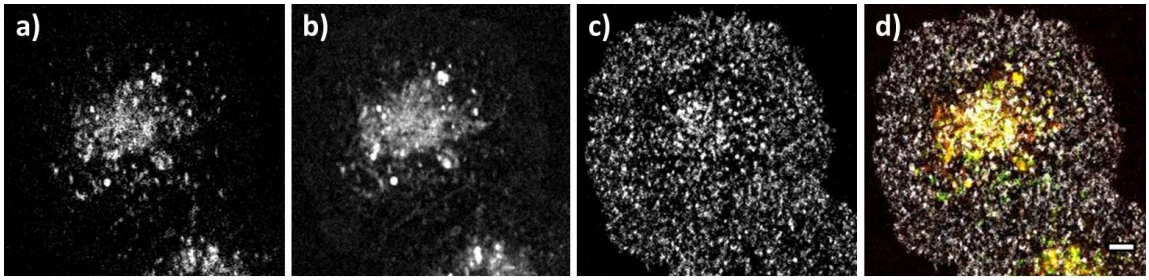

Figure 6.21 Vesicle order and LAT at the immunological synapse. Vesicles were stained with di-4-ANEPPDHQ to permit imaging of both a) ordered and b) disordered emission spectra; LAT c) was visualised allowing overlay d) with vesicle data for analysis. Scale bar = 5 µm.

Overlaying stained vesicle images with LAT (Figure 6.22a), showed regions where these intensities peaked together (Figure 6.22b), however much of the LAT was uncorrelated with vesicle staining.

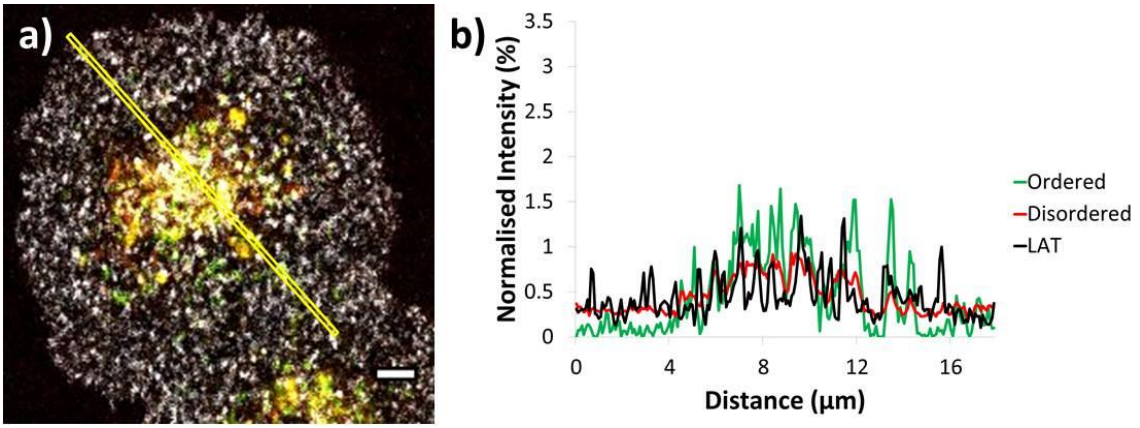

Figure 6.22 Line profile plots of vesicle order and LAT. a) Single pixel width line plots were taken through the synapse and the 3 channels intensities were normalised and b) plotted. Line plots demonstrate increased intensity for LAT both in regions of vesicles and no vesicles. Scale bar = 5 µm.

To better quantify these results correlation analysis was performed of individual vesicular structures, upon selecting ROI's based on membrane labelling and measuring LAT intensity within these regions, individual vesicle GP intensities were correlated with local LAT intensity.

Interestingly LAT was shown to weakly but significantly segregate to disordered vesicles ($r = -0.25$, $p < 0.0001$, $n = 308$). Together these results demonstrated LAT may reside in vesicles, but the sparsity of the vesicle staining coupled with the large amount of endogenous LAT that resides at the plasma membrane made results here inconclusive.

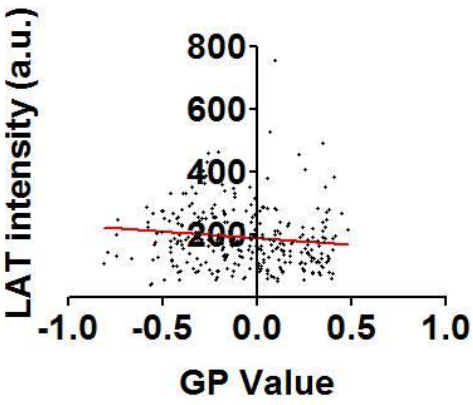

Figure 6.23 Vesicle order and LAT intensity correlation in Jurkat T cells. Individual vesicle GP values were correlated against LAT intensity within the same ROI providing a significantly non-zero Pearson's correlation ($r = -0.25$, $p < 0.0001$), with LAT residing in more disordered vesicles, $n = 308$.

Next, MAL, a protein which is known to mediate the transportation of vesicles to the synapse interface and segregates into ordered membrane domains was imaged. MAL has also been shown, using detergent analysis and Laurdan imaging, to both reside in and maintain glycosphingolipid rich, ordered plasma membrane domains and aid LAT and Lck trafficking to the cSMAC (Frank 2000; Anton et al. 2011). Here imaging of both vesicle order (Figure 6.24a) and disorder (Figure 6.24b), along with labelled MAL (Figure 6.24c) with a subpopulation of MAL colocalising with stained vesicles (Figure 6.24d). This data also agreed with previous findings that MAL segregates to the cSMAC (Anton et al. 2011).

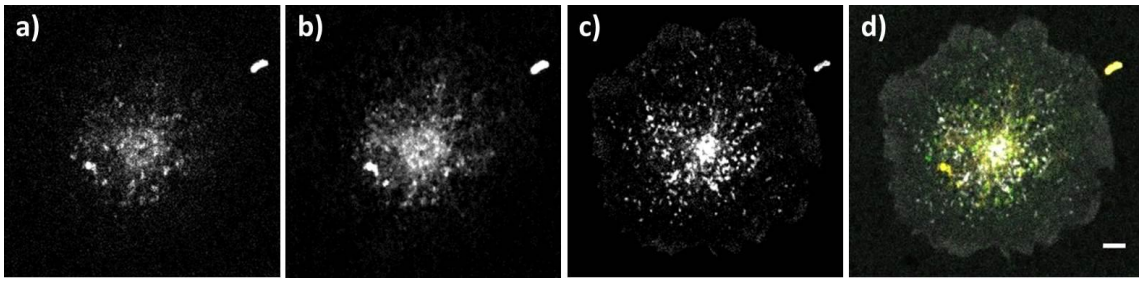

Figure 6.24 Vesicle order and MAL at the immunological synapse. Vesicles were stained with di-4-ANEPPDHQ to permit imaging of both a) ordered and b) disordered emission spectra; MAL c) was visualised allowing overlay d) with vesicle data for analysis. Scale bar = 5 µm.

Overlaying stained vesicle images with MAL and selecting a single pixel line profile (Figure 6.25a), demonstrated regions where their intensities peaked together (Figure 6.25b), with a potential for MAL to preferentially segregate to more ordered vesicles.

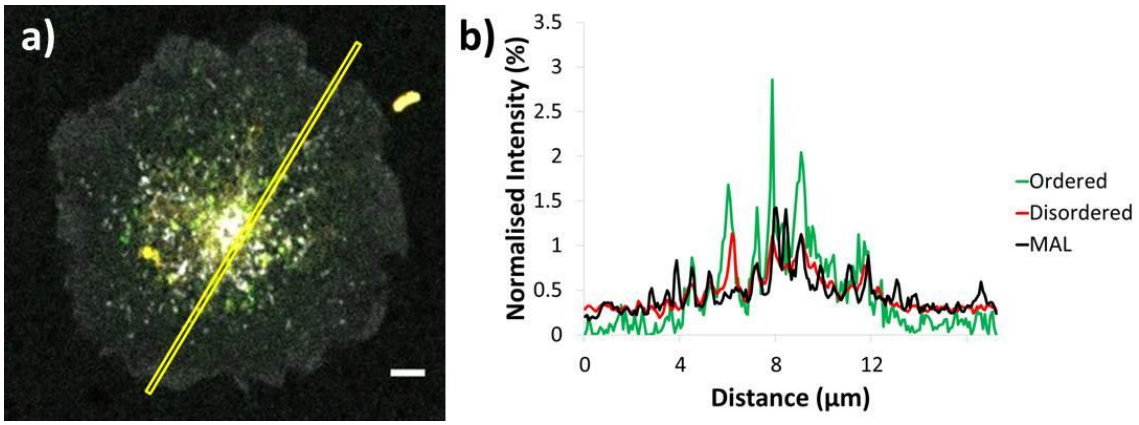

Figure 6.25 Line profile plots of vesicle order and MAL. a) Single pixel width line plots were taken through the synapse and the 3 channels intensities were normalised and b) plotted. Line plots demonstrate increased intensity for MAL in vesicles residing regions. Scale bar = 5 µm.

Correlation analysis was performed by selecting regions of increased vesicle signal intensity (as with the above LAT data), this revealed where individual vesicle GP intensities were correlated with local MAL intensity, MAL demonstrated a preference towards more ordered vesicular structures at the immunological synapse, ($r = 0.16$, $p < 0.05$, $n = 164$). This agrees with previous literature where MAL is known to aid trafficking of vesicles to the synapse and resides in more ordered membrane domains (Soares et al. 2013; Frank 2000; Anton et al. 2011).

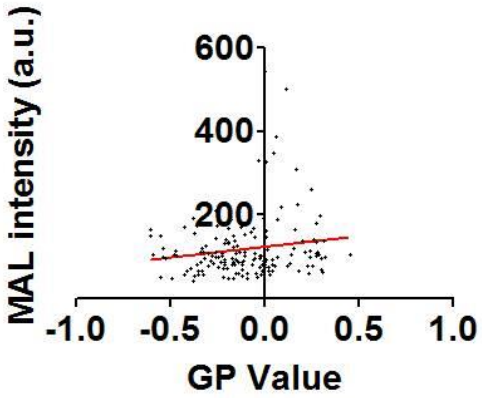

Figure 6.26 Vesicle order and MAL intensity correlation Jurkat T cells. Individual vesicle GP values were correlated against microtubule intensity within the same ROI providing a significantly non-zero Pearson's correlation ($r = 0.16$, $p < 0.05$), with MAL residing in more ordered vesicles, $n = 164$.

Overall, vesicle structures were shown to be anti-correlated with actin fibres, while being partially correlated with microtubules as shown by line profiling. When measuring GP values, correlation with microtubule intensities showed a preference for more disordered vesicles.

Upon imaging of vesicles and labelled cargo it was shown MAL preferentially segregated into more ordered vesicles, agreeing with previous biochemical analysis (Frank 2000), however LAT demonstrated a slight preference to more disordered vesicles (Figure 6.27).

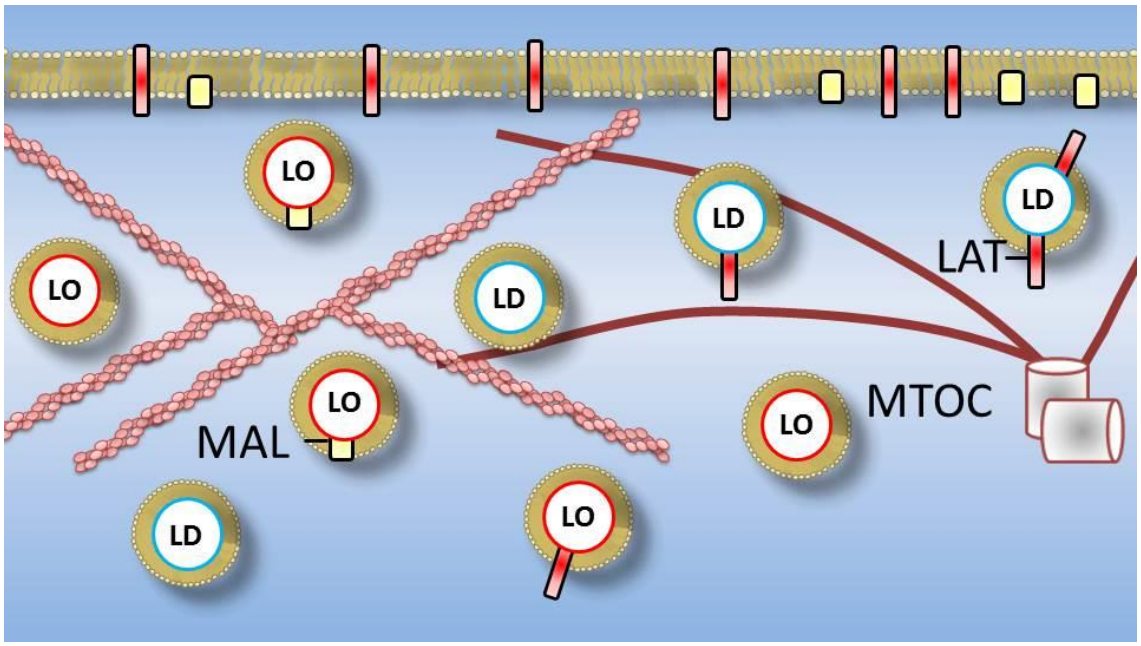

Figure 6.27 Schematic of vesicle order and cargo at the immunological synapse. Subsynaptic vesicles close to the immunological synapse interface display both ordered and disordered populations, with more ordered vesicles preferentially containing MAL, while LAT appears to be contained within more disordered vesicles. Vesicles were also anticorrelated to labelled actin, suggesting vesicles reside between actin fibres, while more disordered vesicles were correlated to microtubules.

6.5. Discussion

This chapter has outlined a combination of live-cell imaging and analysis techniques for the novel quantification of vesicle lipid order and dynamics within the T cell synapse. The use of drug treatments and fixed cell, 3-channel imaging has elucidated subsynaptic vesicle properties with regard to their relationship with the cytoskeleton and vesicular cargo.

Subsynaptic vesicles exhibited correlations between their membrane order and track dynamics, with more ordered vesicles exhibiting slower dynamics and residing at the synapse for longer periods of time, generating longer and more stable tracks.

Through inhibiting polymerisation of actin with cytochalasin-D it was found subsynaptic vesicles exhibited reduced order but did not reduce in number. Increasing actin polymerisation and stability with jasplakinolide increased vesicle order and reduced the number of vesicles tracked. These results agree with previous findings of actin drug treatments and plasma membrane order in Jurkat T cells, where the actin depolymerising drug latrunculin-B and polymerising drug jasplakinolide respectively led to reduced and increased membrane order

(Dinic et al. 2013). Results here also show maintaining or increasing the cortical actin meshwork reduces vesicle tracks at the synapse, possibly indicating actins role as a barrier to vesicle fusion at the membrane, as has been speculated before for NK cells (Rak et al. 2011; Mace & Orange 2014).

Both actin modulating treatments reduced the speed of tracked vesicles at the synapse, with no effect on the time vesicles were present at the interface, suggesting actin polymerisation, potentially through the flow of cortical actin, could be important for vesicle dynamics. Reduction of vesicle speed after jasplakinolide treatments correlate with results in §5.2, where the finite pool of actin potentially dropped below the critical concentration required for polymerisation. The reduced track straightness and reduced number of vesicles at the membrane during jasplakinolide treatments may demonstrate vesicles unable to efficiently fuse with the plasma membrane.

Disrupting microtubules led to an increase in subsynaptic vesicle population order, and the most significant reduction in the number of tracked vesicles. This data agrees with findings that microtubules form an important structure for vesicle delivery to the synapse (Ritter et al. 2015). Together these results demonstrated subpopulations of vesicles are excluded from the synapse during cytoskeletal modulation based on their membrane order.

Tracking data showed no effect on vesicle speed or track straightness during nocodazole treatment, with both track lengths and durations significantly reduced this may indicate tracked vesicles were following shorter tubule tracks. A potential pitfall of this technique is the finding that, when used at 100 μM concentrations, nocodazole inhibits TCR downstream signalling of Lck and Fyn in Jurkat T cells, and that this is independent of MT depolymerisation (Huby et al. 1998). Whether this is a partial cause of the reduction seen in vesicle transport to the synapse interface is not known.

Previous work demonstrated abolition of actin networks or myosin motors in bovine chromaffin cells caused disruption of vesicle dynamics, but not during microtubule inhibitors (Neco et al. 2003), these results agree with work here using primary human T cells. However this work demonstrated vesicles were associated with both actin and microtubule networks; it was therefore hypothesized lipid order may influence vesicular distribution on the cytoskeletal network. For example it was shown NPF's such as WASp become activated in lipid ordered domains within the membrane (Sasahara et al. 2002) and that the NPF's can control actin driven dynamics in oocytes (Schuh 2011). As such more ordered vesicles, which are shown here to possibly rely on the actin cytoskeleton for synapse localisation, may preferentially colocalise with actin fibres.

Using line profile plots it was shown that vesicles were anti-correlated with both actin fibres of the pSMAC and actin foci within the cSMAC. GP analysis and colocalisation confirmed these findings, with all vesicles anti-correlated with actin rich regions.

Colocalisation analysis was then carried out to establish whether vesicles were instead located on microtubules. Data suggested the majority of disordered vesicles were located on microtubules agreeing with the drug treatment data where using nocodazole to disrupt microtubules, increased order of vesicles still present at the synapse interface.

Together colocalisation and tracking results demonstrate lipid order does not appear to control vesicle distribution on actin components. With more disordered vesicles segregated with and relying upon microtubules for immunological synapse localisation.

Finally this chapter investigated whether lipid order of individual vesicles influenced their cargos. Vesicles have been shown to contain molecules that increase their transportation to the synapse interface (e.g. vesicle associated protein 7 (VAMP7) and MAL). With VAMP7 promoting the recruitment of vesicular LAT, while MAL increases Lck trafficking to the synapse (Larghi et al. 2013; Soares et al. 2013).

Within the plasma membrane, LAT resides in more ordered membrane compartments (Zhang et al. 1998), and may form signalosomes with the TCR complex from within vesicles (Williamson et al. 2011). These findings disagree with data here where LAT was found to weakly but significantly correlate with less ordered vesicles. Whether this was due to the large percentage of plasma membrane residing LAT resulting in non-vesicular 'background' signal is not known. As such staining for phosphorylated LAT may result in a better indication of active signalling sites in the future.

MAL preferentially localised with more ordered vesicles, agreeing with biochemical analysis (Frank 2000). It has been previously reported that MAL traffics Lck to the synapse interface and also increases the recruitment of LAT containing vesicles to form nanoterritories (Soares et al. 2013). Data in this chapter highlighting membrane order based segregation within vesicles, may indicate a mechanism for reduced spontaneous signalosome formation and T cell activation.

One limitation of this work is the selective nature of the vesicles imaged, as only those present at the synapse interface were analysed. This may account for data here, where GP values are more homogeneous than in previous studies investigating the heterogeneity of the plasma membrane (Owen et al. 2011), as this population of vesicles may be preferentially trafficked to the synapse. Other vesicles may be trafficked towards the distal regions of the synapse,

containing downregulatory proteins such as CD43 which are accumulated there in an ERM dependent manner (Cullinan et al. 2002).

Overall these finding demonstrate a complex interplay between subsynaptic vesicles, membrane order, and their localisation to the cytoskeleton and how the cargo they contain may modulate synaptic delivery and localisation (Table 6.1).

Table 6.1 Summary of different vesicle parameters correlated to individual membrane orders, determined by GP analysis. Positive ((+)ive) correlations indicate preferential segregation to more ordered vesicles, negative ((-)ive) to more disordered vesicles. + - +++ indicate the relative size of the correlation.

Correlation to vesicle GP value:					
Cytoskeleton		**Cargo**		**Track statistics**	
Actin	**Microtubules**	**MAL**	**LAT**	**Speed**	**Duration**
None p = 0.06	(-)ive p < 0.0001	(+)ive p < 0.05	(-)ive p < 0.0001	(-)ive p < 0.0001	(+)ive p < 0.0001
	++	++	+	+	+++

Whether vesicles anticorrelated with actin (i.e. between actin fibres) are carried in towards the cSMAC during any transient signalosome formation is unknown, however it has been shown in T cells using a stimulatory coverslip, that vesicular LAT slows at regions of ZAP-70 microclusters (Purbhoo et al. 2010). It could be that these LAT containing vesicles are then carried up into the cell by actin retrograde flow (as both actin modulating treatments used here reduced vesicle speeds), ceasing contact with membrane-localised microclusters and recycled to the dSMAC-pSMAC interface for repeat signalling. This may account for the reduced TCR signalling reported in the cSMAC and the fact active signalling occurs within the pSMAC and agrees with previous finding that VAMP7 increases signalosome assembly after TCR engagement, without fusion to the membrane, allowing vesicles to become signalling platforms in their own right (Larghi et al. 2013).

Chapter 7 – Conclusions

This thesis has outlined work aimed at understanding the biophysical processes that occur within T cells during synapse formation. This was undertaken using a series of advanced and super-resolution microscopy techniques on both fixed and live-cells to enable analysis of cytoskeletal and membranous systems.

7.1. F-actin and the plasma membrane

First, SMLM was used to characterise the nanostructure of cortical F-actin within fixed T cells. Results agreed with previous diffraction-limited (Babich et al. 2012; Yi et al. 2012; Yu et al. 2010) and fixed-cell structured illumination imaging (Ritter et al. 2015; Brown et al. 2011) where, upon synapse formation, F-actin creates a dense ring-like meshwork within the dSMAC. The actin cortex then reduced in density towards the pSMAC where individual fibres were resolved. Results were then presented using the novel combination of TIRF-SIM and image correlation analysis; this permitted the quantification of velocity and directionality of nanometer scale subregions for greater characterisation of F-actin retrograde flow within the dSMAC. Compared to other tracking and correlative techniques, STICS' additional directionality statistics resulted in the characterisation of individual subregion flow orientations.

Next, using drug treatments to modulate actin and myosin IIA, it was shown flow within the dSMAC was almost exclusively driven by actin-polymerisation. Cytochalasin-D and jasplakinolide were shown to decrease and increase F-actin flow respectively, agreeing with their respective roles as F-actin disrupters and stabilisers. Additional information from directionality results showed disrupting actin polymerisation also reduced the retrograde nature of the flow within the dSMAC. Both cytochalasin-D and jasplakinolide have been found to stop Ca^{2+} signalling (Rivas et al. 2004; Babich et al. 2012) resulting in reduced TCR induced cell spreading and downstream signalling from TCR microclusters within the synapse periphery both driven by actin. Results here also demonstrate that pre-formed synapses require controlled actin retrograde flow speed and directional persistence for characteristic actin structure. Additionally, the persistence of the actin flow maintains the morphology of the synapse.

Flow within the dSMAC has been speculated to be partially dependent on myosin IIA contractility in the past (Yi et al. 2012). However others using confocal microscopy (Babich et al. 2012) and TIRF-SIM (Murugesan et al. 2016) have shown similar findings to data presented here, with F-actin flow speed relatively unchanged upon myosin IIA inhibition. Murugesen did report however that myosin IIA inhibition led to different pSMAC morphologies including

higher actin accumulation and fibres orientated radially rather than tangentially. These data suggest the retrograde nature of cortical actin within the immunological synapse may be driven by both the 'pulling' of myosin motors on tangential 'actomyosin arc' structures within the pSMAC, and 'pushing' from polymerisation of formin derived radial fibres in the dSMAC. It would be interesting to study the interplay between actin fibre orientations and how motor proteins are segregated into different fibre populations or whether they actively control fibre organisation. This may mediate understanding as to how these structures and their dynamics contribute to protein distribution at the plasma membrane, leading to molecular clustering and ultimately macroscale organisation.

Many of the molecules controlling actin and myosin motors have been shown to rely on liquid ordered domains for changes to their activity status. Indeed, membrane order has been speculated to control membrane protein clustering, including those domains containing T cell signalling molecules (Saarikangas et al. 2010; Dinic et al. 2015; Owen et al. 2012). Conversely, disruption of the cytoskeleton reduces membrane order and the clustering of order-dependent signalling molecules including Lck (Chichili et al. 2012). Higher membrane order may also imply higher lipid packing in these regions and so could demonstrate higher viscosities; with the dSMAC exhibiting higher membrane order than the cSMAC (Dylan M Owen et al. 2010). As such membrane-actin interactions; particularly with transmembrane proteins spanning more ordered, viscous regions, were speculated to result in slower actin flow and disrupted directionality. To test this, 7KC was used to disrupt membrane order before imaging with TIRF-SIM and STICS analysis.

At higher 7KC concentration actin flow speed was increased; possibly indicating a reduction in membrane viscosity, with no significant changes to actin flow directionality. It would be interesting to see if even greater 7KC concentrations lead to further increases in speed, or whether they reduce actin polymerisation and therefore flow speed due to disruption of ordered membrane domains which are known to contain active NPF's such as the WASp/Arp2/3 complex (Sasahara et al. 2002). These findings indicate actin-membrane interactions may form a feedback loop, whereby actin forms more ordered domains, leading to increased protein packing within these regions, leading to greater interactions with the actin cortex through transmembrane and linker proteins. This could indicate an important biophysical mechanism for the generation and sustainability of membrane order, protein clustering and molecular segregation.

Higher concentrations of 7KC have been shown to reduce primary T cells ability to form coverslip attachments (Miguel et al. 2011) and reduce IL-2 secretion in Jurkat T cells,

potentially due to disruption of LAT signalling complexes but not due to changes in Ca^{2+} signalling (Rentero et al. 2008). This demonstrates actin-membrane interactions may be in part reliant on membrane order. It has, for example, been shown *in vitro* how the actin cytoskeleton can modulate membrane domains (Köster et al. 2016; Dinic et al. 2013); this evidence points to a role for the membrane in modulating actin dynamics during synapse formation.

As actin and the plasma membrane possess direct and indirect means of contact through transmembrane and linker proteins it was speculated the retrograde flow of actin may be transmitted to the membrane itself. To test this, membrane dyes were incorporated into cells and imaged. Results showed components of the membrane were flowing in a retrograde fashion at the actin-rich synapse periphery but not the actin-poor synapse centre.

To test whether this flow was indeed due to actin dynamics, actin modulating drug treatments were applied to cells while imaging actin and the plasma membrane using two-channel TIRF-SIM imaging. Firstly, cross-correlation analysis in control cells revealed, for the first time, that cortical actin and the plasma membrane were correlated for speed and directionality. Actin modulating drug treatments showed no significant differences when correlated with membrane flow; as the actin cytoskeleton exhibits modulated flow this may indicate similar changes within the membrane. Interestingly, both drug treatments demonstrated a significant reduction in directional correlation compared to control conditions. Together these results show actin driven flow within the membrane leads to similar flow speeds, but not directionality. Whether this highlights actin as an ordering mechanism, where the breakdown of active flow leads to reduced membrane flow needs further investigation.

This flow has been speculated to transfer to both membrane leaflets in simulations (Gowrishankar et al. 2012) and recent studies, demonstrating outer-membrane GPI-anchored proteins are organised into clusters via transmembrane lipid linkages to the actin cytoskeleton *in vitro* (Köster et al. 2016). This was investigated here using GPI-GFP expressing T cells to provide information on whether any membrane flow present was also linked to the outer leaflet and whether these classically 'lipid ordered' residing molecules were sensitive to changes in actin flow modulation.

Control conditions demonstrated non-significant correlations compared with membrane dye imaging for speed; however directionality was significantly reduced for GPI-GFP. This could demonstrate GPI-molecules and the outer leaflet of the membrane itself exhibits more 'slipping' than the stained membrane which will be reporting on both leaflets. These findings support the idea that membrane-actin interactions, could exist in T cells through

transmembrane proteins where the diffusion of MHC, integrins and TCR microclusters are controlled by actin dynamics (Lavi et al. 2012; Comrie et al. 2015; Dushek et al. 2008).

These findings demonstrate evidence that a combination of various actin-membrane theories may be most accurate when describing the T cell synapse. For example active flow does appear to order the plasma membrane in some way, both for flow speed and directionality, this agrees with *in vitro* findings from the Mayor group (Raghupathy et al. 2015; Köster et al. 2016). Additionally, actin disruption reduces the directional correlation of membrane-actin flow, which points to the requirement of an active actin flow. If the membrane and its components continue to flow when actin is disrupted this may demonstrate actin has a role in forming a flexible or dynamic barrier for transmembrane proteins, rather than lipids themselves; agreeing with the picket fence model (Kusumi, Ike, et al. 2005).

Many proteins are known to form links between the actin cortex and transmembrane proteins, including ERM proteins (Gautreau et al., 2000; Yonemura et al., 1998). The dSMAC and pSMAC of T cells are also sites where, during synapse formation, transmembrane proteins known to interact with the cytoskeleton are located; including CD43, CD44 and ICAM-1 proteins (Yonemura et al. 1998; Allenspach et al. 2001; Delon et al. 2001; Roumier et al. 2001). Where ERM and transmembrane proteins which control cortical actin-membrane interactions and as speculated by the picket fence model (Kusumi, Ike, et al. 2005), trap membrane residing proteins is unknown. While this has been studied in neurons, where single particle tracking deduced the spatial organisation of GPI-GFP (Albrecht et al. 2016) this has not been fully investigated in T cell synapses.

Studies which have shown actin-membrane coupling in T cells have demonstrated protein-protein interactions including LAT mediated clustering, though this was reported to be independent of both actin and raft-like liquid ordered domains as these clusters could form within the cSMAC (Douglass & Vale 2005)**.** Intriguingly this group did later report TCR microclusters move centripetally inwards in line with actin dynamics (Kaizuka et al. 2007) which agrees with others (Yu et al. 2010; Yi et al. 2012) including simulations deducing lipid-protein assembly is cytoskeleton- and cholesterol-dependent with transmembrane proteins generating increased lipid order around them (Gómez-Llobregat et al. 2013; Machta et al. 2011).

To investigate whether actin crosslinking and actin-protein interactions contributed to the flow of actin and the membrane, α-actinin, which bundles and crosslinks F-actin fibres as well as binding transmembrane proteins (Hoessli et al. 1980; Geiger & Singer 1979), was studied. A-actinin was found to reside in the dSMAC, where the dense actin meshwork and highest actin-

membrane correlation was found. This highlights the potential for the actin meshwork to translate polymerisation driven flow to the plasma membrane via α-actinin or transmembrane proteins. As lipid density is speculated to be highest around these transmembrane proteins; termed 'lipid shells', this more viscous membrane may translate flow of actin more efficiently.

Using α-actinin CRISPR knockout cells, it was demonstrated the actin cortex flow speed was increased but with reduced retrograde directionality, while plasma membrane directionality was also scrambled. This may demonstrate when α-actinin's crosslinking ability is lost, uncoordinated polymerisation driven flow occurs. The uncoordinated nature of actin flow is also seen in the plasma membrane, consistent with a loss of coupling between actin and the membrane.

Findings presented here highlight some challenges, including the spatial and temporal resolution permitted by SIM imaging which make it difficult to deduce small (< 100 nm) or faster fluorescent fluctuations within the membrane. As has been shown previously using scanning-STED-FCS, labelled lipids can form 80 nm domains with transiently trapped lipids exhibiting diffusion coefficients of ~ 0.5 $\mu m^2 / s^{-1}$ (Honigmann et al. 2014), less than the spatial and temporal resolution of TIRF-SIM. These findings also demonstrate transient trapping on the scale of milliseconds, whereas the temporal resolution of TIRF-SIM may not fully elucidate these faster interactions.

Correlation between actin and the membrane could be captured by FCS-STED systems, but while this data would show whether faster moving membrane populations were correlated for speed and were transiently trapped around actin rich domains it would not permit directional correlation between actin and the membrane. As with neurons (Albrecht et al. 2016) single particle tracking may also be utilised during lipid investigations, however some lipids within the plasma membrane will exhibit Brownian motion so would limit the analysis of those lipid populations which are flowing.

This work demonstrates that while a link between actin and the membrane may be present during synapse formation in T cells, there is still much to be done to fully reveal which molecules are involved. Whether actin organising proteins; classed as 'active' proteins in the active composite model (Raghupathy et al. 2015; Köster et al. 2016) have a role in any membrane flow remains inconclusive. There is still controversy for the roles of actin and / or lipid rafts in T cell signalling complex formation, including raft associated proteins (Lck, LAT) which have exhibited increased diffusion compared to CD2 (a non-raft protein); therefore indicating liquid ordered domains do not contribute to signalling clusters (Douglass & Vale 2005).

7.2. Subsynaptic Vesicles

Much like the plasma membrane, vesicles are also known to contain signalling molecules involved in the downstream activation of T cells (Larghi et al. 2013; Williamson et al. 2011; Soares et al. 2013) work here characterised the subsynaptic population at the synapse interface.

Vesicles have been shown to rely on both microtubules and actin for their transportation in other cell types (Schuh 2011; Neco et al. 2003), and within the T cell are indirectly reliant on actin depletion at the cSMAC, for MTOC polarisation and microtubule dependent vesicle delivery (Ritter et al. 2015). Vesicles distribute to different SMAC regions (Soares et al. 2013) so it was thought interactions with cortical actin may control this, with F-actin serving as tracks for delivery via myosin motors (Lang et al. 2000) and barriers of fusion (Wang & Richards 2011).

Due to the confusing nature of whether membrane order has a role in facilitating the heterogeneous distribution of molecules within the plasma membrane it was firstly investigated whether subsynaptic vesicles exhibit different liquid orders and whether their trafficking to the synapse is preferentially controlled by the actin or microtubule networks. GP analysis using di-4-ANEPPDHQ led to the observation that different vesicle populations do exist at the synapse interface.

Actin disruption led to a reduction of lipid order, but total numbers of subsynaptic vesicle tracking events was unchanged, while stabilising the actin cortex or disrupting microtubules increased the mean lipid order of remaining vesicles and significantly reduced vesicle numbers. This suggested more ordered vesicles may rely on the actin cytoskeleton for directed transportation to the synapse, as reducing F-actin lowered remaining vesicle order. It is also possible the dynamics of F-actin are required for this process, with actin stabilisation reducing the number of tracks. This would agree with previous finding that an active cortex is required to both trap, transport and release vesicles for fusion to the plasma membrane (Wollman & Meyer 2012).

Microtubule disruption had no effect on vesicle speed, but did reduce track duration, track length and total number of tracking events, confirming longer range vesicle transportation relies on the microtubule network at the T cell synapse (Ritter et al. 2015). Interestingly here; microtubule disruption also increased the mean lipid order of subsynaptic vesicles, suggesting more disordered vesicles may segregate onto the MTOC network for synapse relocation.

3-channel imaging of stained vesicles with di-4-ANEPPDHQ and colocalisation with labelled actin or microtubule networks in fixed cells demonstrated actin was anti-correlated with all vesicles. These findings demonstrate actin's role in T cells may be one of a barrier, where directed fusion or trafficking happens between rather than on fibres, while disordered vesicles were found to be correlated within areas of labelled microtubules, agreeing with drug treatments highlighted earlier. This has also been shown previously in preformed T cell synapses, where the MTOC was key for directed vesicle delivery not the actin cytoskeleton (Ueda et al. 2015).

It was speculated more ordered vesicles, which are removed from the synapse interface upon F-actin disruption, and anti-correlated with actin intensity within the pSMAC, may constitute vesicles containing cargo associated with TCR microclusters. These microclusters are known to follow the retrograde flow of F-actin and also reside between actin filaments (Murugesan et al. 2016). If these vesicles contain signalling proteins such as LAT, which transiently bind to signalling microclusters (Purbhoo et al. 2010) they may also be carried inwards towards the cSMAC between actin filaments.

LAT is known to reside in lipid ordered regions of the membrane as demonstrated by DRM analysis and environmentally sensitive dyes (Zhang et al. 1998; Gaus et al. 2005). As such imaging was undertaken using di-4-ANEPPDHQ to deduce whether membrane order had any effect on the cargo contained within vesicles. Imaging was also undertaken after labelling the vesicle protein MAL which controls vesicle docking and fusion, including those respectively containing Lck (Soares et al. 2013).

LAT containing vesicles were found to have a negative correlation with GP values; this indicates that although these proteins may reside in more ordered domains of the plasma membrane, they reside in less ordered populations of subsynaptic vesicles. This may be explained by the fact subsynaptic vesicles only represent a fraction of the total population; while other subpopulations may include those molecules known to downregulate TCR signalling, as has been shown with plasma membrane-residing CD43 which localises away from the synapse interface in an ERM-actin dependent manner (Delon et al. 2001; Allenspach et al. 2001). These other subpopulations may exhibit different membrane orders and different cargos to those at the synapse interface, which could be studied in the future.

It has also been observed that although LAT preferentially resides in lipid ordered domains it is not known whether LAT controls the order of the membrane; which is thought to be driven by the actin cytoskeleton (Dinic et al. 2013). As subsynaptic vesicles here were not associated

with actin, this may demonstrate further proof actin, rather than transmembrane proteins, form lipid ordered domains.

MAL containing vesicles demonstrated a significant positive correlation between intensity and GP value, agreeing with previous findings this protein preferentially segregates into lipid ordered domains (Frank 2000). These findings are summarised in Figure 7.1, where: 1) Actin retrograde flow leads to correlated membrane flow speed, directionality and ruffling. 2) α-actinin crosslinking helps control F-actin's directed retrograde nature, thereby maintaining membrane flow. 3) Cortical actin is anti-correlated with vesicles. 4) Vesicles are not reliant on membrane order for their molecular cargo, but more disordered vesicles do segregate onto microtubules.

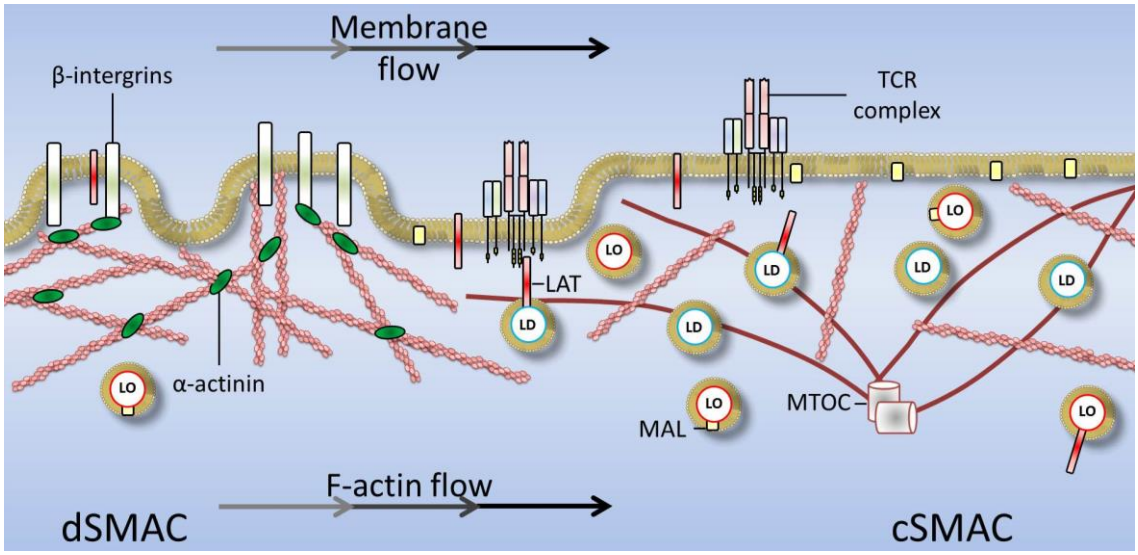

Figure 7.1 Schematic model demonstrating actins dynamic and structurally dependent role in the organisation and flow of membranous systems. α–actinin controlled F-actin dynamics lead to directed membrane flow potentially through α–actinin – integrin linkages. Vesicle trafficking to the synapse interface relies on a dynamic and permissive F-actin network, with ordered vesicles preferentially containing MAL and more disordered vesicles preferentially containing LAT while localising onto microtubules.

These results demonstrate vesicle populations are trafficked to or from the immunological synapse, partially controlled by either the actin or microtubule networks. These may in turn help generate the heterogeneous makeup of the plasma membrane, both in terms of lipid and protein composition. Whether cells are capable of directing this delivery based on environmental conditions remains unclear but could provide a significant mechanism for other cell types such as neurons and migrating cells.

This preferential segregation of different cargos into different vesicles also demonstrates a potential mechanism for controlling where and when signalling proteins can interact, which would result in the reduction of spurious signalling.

Chapter 8 – Future direction

Much of the current knowledge into how T cells initiate, maintain and ultimately balance immunological synapse signalling and architecture is based on either biochemical or image analysis of fixed cells, capturing a point in time or live-cell imaging methods confined to two-dimensions with one or two molecules of interest labelled. The findings here describe a new technique which utilises advanced imaging and analysis methods to elucidate how actin, the plasma membrane itself and their components interact during synapse formation. Assessing membrane composition and behaviour continues to be a provocative area of research due to its dynamic nature.

Outcomes from this work do however lead to some immediate questions, which if answered has the potential to validate or broaden the proposed model.

Findings here have implemented 2D super-resolution imaging, through time. Extending this imaging into four-dimensions (x, y, z, t) will allow better understanding of cell behaviours and nanoscale dynamics. This will become particularly interesting when looking at synapse formation on supported lipid bilayers, cell-cell interactions and eventually *in-vivo*. Additionally, simultaneous multi-channel imaging will permit the quantification of correlated structure, including those exhibiting faster dynamics.

The use of lattice light sheet would enable faster imaging in 4D with reduced phototoxicity and background signal compared with standard imaging methods. This technique would also allow whole-cell imaging to deduce whether different cytoskeletal, vesicle, and protein populations preferentially segregate to different regions of the cytosol or plasma membrane, and how flow dynamics may change in a volume. These imaging techniques require the implementation of 3D and 4D analysis techniques, potentially using a combination of advanced image correlation and single molecule datasets. For example the current development of Bayesian cluster analysis combined with live-cell SMLM imaging datasets will provide robust and unbiased identification of clusters from pointillist datasets.

Regarding the data from this thesis, the nanoscale regions analysed during this work demonstrated areas of variable actin flow speeds; it would be interesting to see if these are correlated or colocalised with signalling molecules or regions of higher membrane order. Whether these regions are functionally important, and whether bound integrins could result in a slowing of the actin flow within these regions is another avenue for enquiry.

The generation of α-actinin knockout cells using CRISPR also permits further investigation of this crosslinking protein, and its contribution to the formation of the immunological synapse. Further investigation of the proteins role and the importance of actin crosslinking could be achieved by expressing a mutant form of α-actinin within T cells. A mutant which lacks one of the actin binding domains would reduce its ability to crosslink actin fibres and allow analysis of actin flow, plasma membrane dynamics and protein organisation as well as vesicle trafficking to the synapse.

Additionally, these cells could be used to study the role of the actin cortex in enabling or preventing invasion by parasites or viruses. As α-actinin has been shown to reduce the infection rate of HIV-1, potentially through its ability to form a dense crosslinked meshwork (Gordón-Alonso et al. 2012) it would be interesting to image this process using live-cell super-resolution techniques and the α-actinin$^{-/-}$ cells to investigate any differences in actin dynamics and the speed of infection or transmission between cells.

Looking ahead there is still much to investigate to fully understand the role and mechanics of the immunological synapse using super-resolution microscopy. For example imaging actin-membrane linkers such as ERM proteins to characterise their nanoscale organisation and modulation of the actin-membrane interface could uncover whether these systems control membrane residing molecules. With the characterisation of the actin cortex comes questions as to how they are made to form intricate structures. Actin modulating proteins such as coronin-1, cofilin, profilin and other NPF's (some known to be modulated by lipid composition of the plasma membrane) may contribute to synapse structure.

Image correlation of the plasma membrane shown in this study demonstrated certain components followed the retrograde flow of the F-actin cortex. Further investigation of whether individual components of the plasma membrane preferentially flow could be achieved through the use of labelled lipids such as PI(4,5)P_2 labelled with GFP. These molecules have been delivered into cells before using polymersomes, with PIP2 following the retrograde flow of actin in adherent cells (Chierico et al. 2014).

Beyond the T cell synapse, techniques demonstrated here could be applied to other biological systems, particularly those involving the interplay between the cytoskeleton, membrane and vesicles, within cells residing close to the coverslip sample interface.

Additionally, other cells of the immune system could be investigated, including NK cells, whose vesicles contain molecules to destroy target cells, and whose actin cytoskeleton needs to tightly regulate their release to prevent untargeted killing. The techniques here would allow

researchers to better understand the temporal as well as spatial mechanisms the cytoskeleton contributes to, while also investigating whether vesicle lipid order and their cargo have a role in synapse trafficking and secretion. Lymphocytes can also be engineered to migrate against coverslips, where the polymerisation of actin and subsequent retrograde flow is thought to be a mechanism for propulsion and engagement respectively. Through the labelling of molecules associated with these sites of engagement or actin itself and the nanoscale size of analysed subregions, any changes in molecular speed around these sites could be quantified.

Neurons are another biological system to investigate, with synaptic junctions of these cells known to rely on the dynamics and recycling of vesicles to sustain their signalling potential. The current hypothesised role of actin as a slow moving or static structure (rather than a reorganising network) and its interaction with outer leaflet membrane residing GPI-linked molecules, this lends itself to the live-cell imaging and analysis demonstrated here. Due to the crowded nature of the synaptic regions in neurons, the live-cell super-resolution imaging, combined with the selective nature of fluorescence microscopy may elucidate a greater understanding of the dynamics controlling signalling between neuronal cells. Overall, any research using adherent cells will benefit from the imaging and analysis described in this thesis.

Together the application of sample-friendly, multi-channel super-resolution imaging in 4D and advanced analysis, will allow interdisciplinary researchers to investigate the true biophysics of the cell in its natural environment.

References

Abbas, A.K., Lichtman, A.H. & Pillai, S., 2012. *Cellular and Molecular Immunology*, Saunders.

Abraham, R.T. & Weiss, A., 2004. Jurkat T cells and development of the T-cell receptor signalling paradigm. *Nature Reviews Immunology*, 4(4), pp.301–308. Available at: http://www.nature.com/doifinder/10.1038/nri1330 [Accessed January 5, 2017].

Aguilar, L.F. et al., 2012. Differential Dynamic and Structural Behavior of Lipid-Cholesterol Domains in Model Membranes P. Butko, ed. *PLoS ONE*, 7(6), p.e40254. Available at: http://dx.plos.org/10.1371/journal.pone.0040254 [Accessed November 8, 2016].

Airy, G.B., 1834. On the Diffraction of an Object-glass with a Circular Aperture. *Transactions of the Cambridge Philosophical Society*, 5, pp.283–291. Available at: http://adsabs.harvard.edu/abs/1835TCaPS...5..283A [Accessed November 8, 2016].

Aitken, C.E., Marshall, R.A. & Puglisi, J.D., 2008. An Oxygen Scavenging System for Improvement of Dye Stability in Single-Molecule Fluorescence Experiments. *Biophysical Journal*, 94(5), pp.1826–1835.

Albrecht, D. et al., 2016. Nanoscopic compartmentalization of membrane protein motion at the axon initial segment. *Journal of Cell Biology*, 215(1).

Alivisatos, A.P., 1996. Perspectives on the Physical Chemistry of Semiconductor Nanocrystals.

Allenspach, E.J. et al., 2001. ERM-dependent movement of CD43 defines a novel protein complex distal to the immunological synapse. *Immunity*, 15(5), pp.739–50. Available at: http://www.ncbi.nlm.nih.gov/pubmed/11728336 [Accessed November 8, 2016].

Anchisi, L. et al., 2013. Cholesterol homeostasis: a key to prevent or slow down neurodegeneration. *Frontiers in Physiology*, 3. Available at: http://journal.frontiersin.org/article/10.3389/fphys.2012.00486/abstract [Accessed November 8, 2016].

Antes, P., Schwarzmann, G. & Sandhoff, K., 1992. Detection of protein mediated glycosphingolipid clustering by the use of resonance energy transfer between fluorescent labelled lipids. A method established by applying the system ganglioside GM1 and cholera toxin B subunit. *Chemistry and physics of lipids*, 62(3), pp.269–80. Available at: http://www.ncbi.nlm.nih.gov/pubmed/1468126 [Accessed November 8, 2016].

Anton, O.M. et al., 2011. MAL Protein Controls Protein Sorting at the Supramolecular

Activation Cluster of Human T Lymphocytes. *The Journal of Immunology*, 186(11), pp.6345–6356. Available at: http://www.ncbi.nlm.nih.gov/pubmed/21508261 [Accessed January 23, 2017].

Anton van der Merwe, P. et al., 2000. Cytoskeletal polarization and redistribution of cell-surface molecules during T cell antigen recognition. *Seminars in immunology*, 12(1), pp.5–21. Available at: http://www.ncbi.nlm.nih.gov/pubmed/10723794 [Accessed November 25, 2016].

Astoul, E. et al., 2001. PI 3-K and T-cell activation: limitations of T-leukemic cell lines as signaling models. *Trends in immunology*, 22(9), pp.490–6. Available at: http://www.ncbi.nlm.nih.gov/pubmed/11525939 [Accessed November 8, 2016].

Aureli, M. et al., 2016. Isolation and Analysis of Detergent-Resistant Membrane Fractions. In pp. 107–131. Available at: http://link.springer.com/10.1007/978-1-4939-3170-5_10 [Accessed November 7, 2016].

Axelrod, D., 1981. Cell-substrate contacts illuminated by total internal reflection fluorescence. *The Journal of cell biology*, 89(1), pp.141–5. Available at: http://www.ncbi.nlm.nih.gov/pubmed/7014571 [Accessed November 8, 2016].

Axelrod, D., 2001. Selective imaging of surface fluorescence with very high aperture microscope objectives. *Journal of Biomedical Optics*, 6(1), p.6. Available at: http://biomedicaloptics.spiedigitallibrary.org/article.aspx?doi=10.1117/1.1335689 [Accessed November 8, 2016].

Babich, A. et al., 2012. F-actin polymerization and retrograde flow drive sustained PLCγ1 signaling during T cell activation. *The Journal of cell biology*, 197(6), pp.775–87. Available at: http://jcb.rupress.org/content/197/6/775.abstract [Accessed January 18, 2016].

Balagopalan, L. et al., 2013. Cutting edge: cell surface linker for activation of T cells is recruited to microclusters and is active in signaling. *Journal of immunology (Baltimore, Md. : 1950)*, 190(8), pp.3849–53. Available at: http://www.ncbi.nlm.nih.gov/pubmed/23487428 [Accessed December 16, 2016].

Barda-Saad, M. et al., 2005. Dynamic molecular interactions linking the T cell antigen receptor to the actin cytoskeleton. *Nature Immunology*, 6(1), pp.80–89. Available at: http://www.nature.com/doifinder/10.1038/ni1143 [Accessed November 7, 2016].

Bartelt, R.R. et al., 2009. Comparison of T cell receptor-induced proximal signaling and

downstream functions in immortalized and primary T cells D. Unutmaz, ed. *PLoS ONE*, 4(5), p.e5430. Available at: http://dx.plos.org/10.1371/journal.pone.0005430 [Accessed November 25, 2016].

Baumgart, T. et al., 2007. Large-scale fluid/fluid phase separation of proteins and lipids in giant plasma membrane vesicles. *Proceedings of the National Academy of Sciences*, 104(9), pp.3165–3170. Available at: http://www.pnas.org/cgi/doi/10.1073/pnas.0611357104 [Accessed November 8, 2016].

Benninger, R.K.P. et al., 2009. Live cell linear dichroism imaging reveals extensive membrane ruffling within the docking structure of natural killer cell immune synapses. *Biophysical journal*, 96(2), pp.L13-5. Available at: http://www.sciencedirect.com/science/article/pii/S0006349508000490 [Accessed January 19, 2016].

Betzig, E. et al., 2006. Imaging Intracellular Fluorescent Proteins at Nanometer Resolution. *Science*, 313(5793).

Blanchoin, L. et al., 2000. Direct observation of dendritic actin filament networks nucleated by Arp2/3 complex and WASP/Scar proteins. *Nature*, 404(6781), pp.1007–11. Available at: http://www.ncbi.nlm.nih.gov/pubmed/10801131 [Accessed November 7, 2016].

Bonello, G. et al., 2004. Dynamic recruitment of the adaptor protein LAT: LAT exists in two distinct intracellular pools and controls its own recruitment. *Journal of Cell Science*, 117(7).

Bretscher, A. & Lynch, W., 1985. Identification and localization of immunoreactive forms of caldesmon in smooth and nonmuscle cells: a comparison with the distributions of tropomyosin and alpha-actinin. *The Journal of cell biology*, 100(5), pp.1656–63. Available at: http://www.ncbi.nlm.nih.gov/pubmed/2985624 [Accessed November 25, 2016].

Brown, A.C.N. et al., 2011. Remodelling of cortical actin where lytic granules dock at natural killer cell immune synapses revealed by super-resolution microscopy. *PLoS biology*, 9(9), p.e1001152. Available at: http://journals.plos.org/plosbiology/article?id=10.1371/journal.pbio.1001152 [Accessed January 18, 2016].

Brown, C.M. et al., 2006. Probing the integrin-actin linkage using high-resolution protein velocity mapping. *Journal of Cell Science*, 119(24).

Brown, D.A., 2007. Analysis of Raft Affinity of Membrane Proteins by Detergent-Insolubility. In pp. 9–20. Available at: http://link.springer.com/10.1007/978-1-59745-513-8_2 [Accessed November 8, 2016].

Brown, S.S. & Spudich, J.A., 1981. Mechanism of action of cytochalasin: evidence that it binds to actin filament ends. *The Journal of cell biology*, 88(3), pp.487–91. Available at: http://www.ncbi.nlm.nih.gov/pubmed/6894300 [Accessed September 16, 2016].

Bruchez, M. et al., 1998. Semiconductor Nanocrystals as Fluorescent Biological Labels. *Science*, 281(5385).

Bubb, M.R. et al., 2000. Effects of jasplakinolide on the kinetics of actin polymerization. An explanation for certain in vivo observations. *The Journal of biological chemistry*, 275(7), pp.5163–70. Available at: http://www.ncbi.nlm.nih.gov/pubmed/10671562 [Accessed September 16, 2016].

Bunnell, S.C. et al., 2001. Dynamic actin polymerization drives T cell receptor-induced spreading: A role for the signal transduction adaptor LAT. *Immunity*, 14(3), pp.315–329. Available at: http://www.ncbi.nlm.nih.gov/pubmed/11290340 [Accessed November 7, 2016].

Bunnell, S.C. et al., 2002. T cell receptor ligation induces the formation of dynamically regulated signaling assemblies. *The Journal of Cell Biology*, 158(7).

van der Burg, M. & Gennery, A.R., 2011. Educational paper. *European Journal of Pediatrics*, 170(5), pp.561–571. Available at: http://link.springer.com/10.1007/s00431-011-1452-3 [Accessed November 7, 2016].

Burnet, F.M., 1976. A modification of Jerne's theory of antibody production using the concept of clonal selection. *The Australian Journal of Science*, 20(3), pp.67–69. Available at: http://www.ncbi.nlm.nih.gov/pubmed/816431 [Accessed November 7, 2016].

Campi, G., Varma, R. & Dustin, M.L., 2005. Actin and agonist MHC-peptide complex-dependent T cell receptor microclusters as scaffolds for signaling. *The Journal of experimental medicine*, 202(8), pp.1031–6. Available at: http://www.pubmedcentral.nih.gov/articlerender.fcgi?artid=1373686&tool=pmcentrez&rendertype=abstract [Accessed December 24, 2015].

Carlsson, L. et al., 1977. Actin polymerizability is influenced by profilin, a low molecular weight protein in non-muscle cells. *Journal of molecular biology*, 115(3), pp.465–83. Available at:

http://www.ncbi.nlm.nih.gov/pubmed/563468 [Accessed November 7, 2016].

Cartwright, A.N.R., Griggs, J. & Davis, D.M., 2014. The immune synapse clears and excludes molecules above a size threshold. *Nature Communications*, 5, p.5479. Available at: http://www.nature.com/doifinder/10.1038/ncomms6479 [Accessed November 8, 2016].

Chang, V.T. et al., 2016. Initiation of T cell signaling by CD45 segregation at "close contacts." *Nature Immunology*, 17(5), pp.574–582. Available at: http://www.nature.com/doifinder/10.1038/ni.3392 [Accessed November 7, 2016].

Chichili, G.R., Cail, R.C. & Rodgers, W., 2012. Cytoskeletal modulation of lipid interactions regulates Lck kinase activity. *The Journal of biological chemistry*, 287(29), pp.24186–94. Available at: http://www.jbc.org/content/287/29/24186.long [Accessed January 18, 2016].

Chichili, G.R. & Rodgers, W., 2007. Clustering of membrane raft proteins by the actin cytoskeleton. *The Journal of biological chemistry*, 282(50), pp.36682–91. Available at: http://www.jbc.org/content/282/50/36682.long [Accessed January 18, 2016].

Chierico, L. et al., 2014. Live cell imaging of membrane/cytoskeleton interactions and membrane topology. *Scientific reports*, 4, p.6056. Available at: http://www.nature.com/articles/srep06056 [Accessed January 16, 2017].

Comrie, W.A. et al., 2015. The dendritic cell cytoskeleton promotes T cell adhesion and activation by constraining ICAM-1 mobility. *The Journal of Cell Biology*, 208(4), pp.457–473. Available at: http://jcb.rupress.org/content/208/4/457.long [Accessed January 19, 2016].

Cooper, G.M. & Hausman, R.E., 2013. *The cell : a molecular approach*, Sinauer Associates.

Crites, T.J. et al., 2014. TCR Microclusters pre-exist and contain molecules necessary for TCR signal transduction. *Journal of immunology (Baltimore, Md. : 1950)*, 193(1), pp.56–67. Available at: http://www.ncbi.nlm.nih.gov/pubmed/24860189 [Accessed November 8, 2016].

Cullinan, P., Sperling, A.I. & Burkhardt, J.K., 2002. The distal pole complex: a novel membrane domain distal to the immunological synapse. *Immunological Reviews*, 189(1), pp.111–122. Available at: http://doi.wiley.com/10.1034/j.1600-065X.2002.18910.x [Accessed December 19, 2016].

Das, V. et al., 2004. Activation-induced polarized recycling targets T cell antigen receptors to

the immunological synapse; involvement of SNARE complexes. *Immunity*, 20(5), pp.577–88. Available at: http://www.ncbi.nlm.nih.gov/pubmed/15142526 [Accessed November 7, 2016].

Davis, S.J. & van der Merwe, P.A., 2006. The kinetic-segregation model: TCR triggering and beyond. *Nature Immunology*, 7(8), pp.803–809. Available at: http://www.nature.com/doifinder/10.1038/ni1369 [Accessed November 8, 2016].

Delon, J., Kaibuchi, K. & Germain, R.N., 2001. Exclusion of CD43 from the immunological synapse is mediated by phosphorylation-regulated relocation of the cytoskeletal adaptor moesin. *Immunity*, 15(5), pp.691–701. Available at: http://www.ncbi.nlm.nih.gov/pubmed/11728332 [Accessed November 8, 2016].

DeMond, A.L. et al., 2008. T cell receptor microcluster transport through molecular mazes reveals mechanism of translocation. *Biophysical journal*, 94(8), pp.3286–92. Available at: http://www.ncbi.nlm.nih.gov/pubmed/18199675 [Accessed November 25, 2016].

Dempsey, G.T. et al., 2011. Evaluation of fluorophores for optimal performance in localization-based super-resolution imaging. *Nature Methods*, 8(12), pp.1027–1036. Available at: http://www.nature.com/doifinder/10.1038/nmeth.1768 [Accessed November 8, 2016].

DePina, A.S. & Langford, G.M., 1999. Vesicle transport: The role of actin filaments and myosin motors. *Microscopy Research and Technique*, 47(2), pp.93–106. Available at: http://www.ncbi.nlm.nih.gov/pubmed/10523788 [Accessed December 16, 2016].

Derivery, E. et al., 2009. The Arp2/3 Activator WASH Controls the Fission of Endosomes through a Large Multiprotein Complex. *Developmental Cell*, 17(5), pp.712–723.

Deschamps, J., Mund, M. & Ries, J., 2014. 3D superresolution microscopy by supercritical angle detection. *Optics Express*, 22(23), p.29081. Available at: https://www.osapublishing.org/oe/abstract.cfm?uri=oe-22-23-29081 [Accessed November 8, 2016].

Dinic, J. et al., 2011. Laurdan and di-4-ANEPPDHQ do not respond to membrane-inserted peptides and are good probes for lipid packing. *Biochimica et Biophysica Acta (BBA) - Biomembranes*, 1808(1), pp.298–306.

Dinic, J. et al., 2015. The T cell receptor resides in ordered plasma membrane nanodomains that aggregate upon patching of the receptor. *Scientific reports*, 5, p.10082. Available at: http://www.ncbi.nlm.nih.gov/pubmed/25955440 [Accessed September 16, 2016].

Dinic, J., Ashrafzadeh, P. & Parmryd, I., 2013. Actin filaments attachment at the plasma membrane in live cells cause the formation of ordered lipid domains. *Biochimica et Biophysica Acta (BBA) - Biomembranes*, 1828(3), pp.1102–1111. Available at: http://www.sciencedirect.com/science/article/pii/S0005273612004294 [Accessed October 2, 2015].

Douglass, A.D. & Vale, R.D., 2005. Single-Molecule Microscopy Reveals Plasma Membrane Microdomains Created by Protein-Protein Networks that Exclude or Trap Signaling Molecules in T Cells. *Cell*, 121(6), pp.937–950. Available at: http://www.ncbi.nlm.nih.gov/pubmed/15960980 [Accessed December 20, 2016].

Dushek, O. et al., 2008. Effects of intracellular calcium and actin cytoskeleton on TCR mobility measured by fluorescence recovery. *PloS one*, 3(12), p.e3913. Available at: http://www.ncbi.nlm.nih.gov/pubmed/19079546 [Accessed November 7, 2016].

Dushek, O. & Coombs, D., 2008. Analysis of serial engagement and peptide-MHC transport in T cell receptor microclusters. *Biophysical journal*, 94(9), pp.3447–60. Available at: http://www.ncbi.nlm.nih.gov/pubmed/18227132 [Accessed January 5, 2017].

Eggeling, C. et al., 2009. Direct observation of the nanoscale dynamics of membrane lipids in a living cell. *Nature*, 457(7233), pp.1159–1162. Available at: http://www.nature.com/doifinder/10.1038/nature07596 [Accessed November 8, 2016].

Ehrlich, L.I.R. et al., 2002. Dynamics of p56lck translocation to the T cell immunological synapse following agonist and antagonist stimulation. *Immunity*, 17(6), pp.809–22. Available at: http://www.ncbi.nlm.nih.gov/pubmed/12479826 [Accessed November 8, 2016].

Eibert, S.M. et al., 2004. Cofilin peptide homologs interfere with immunological synapse formation and T cell activation. *Proceedings of the National Academy of Sciences*, 101(7), pp.1957–1962. Available at: http://www.pnas.org/lookup/doi/10.1073/pnas.0308282100 [Accessed November 7, 2016].

Esue, O. et al., 2008. The Filamentous Actin Cross-Linking/Bundling Activity of Mammalian Formins. *Journal of Molecular Biology*, 384(2), pp.324–334. Available at: http://linkinghub.elsevier.com/retrieve/pii/S0022283608011698 [Accessed November 8, 2016].

Fehon, R.G., McClatchey, A.I. & Bretscher, A., 2010. Organizing the cell cortex: the role of ERM proteins. *Nature reviews. Molecular cell biology*, 11(4), pp.276–87. Available at: http://www.pubmedcentral.nih.gov/articlerender.fcgi?artid=2871950&tool=pmcentrez&

rendertype=abstract.

Feng, Y. & Walsh, C.A., 2004. The many faces of filamin: A versatile molecular scaffold for cell motility and signalling. *Nature Cell Biology*, 6(11), pp.1034–1038. Available at: http://www.nature.com/doifinder/10.1038/ncb1104-1034 [Accessed November 8, 2016].

Foger, N., 2006. Requirement for Coronin 1 in T Lymphocyte Trafficking and Cellular Homeostasis. *Science*, 313(5788), pp.839–842. Available at: http://www.sciencemag.org/cgi/doi/10.1126/science.1130563 [Accessed November 7, 2016].

Fölling, J. et al., 2008. Fluorescence nanoscopy by ground-state depletion and single-molecule return. *Nature Methods*, 5(11), pp.943–945. Available at: http://www.nature.com/doifinder/10.1038/nmeth.1257 [Accessed September 16, 2016].

Fooksman, D.R. et al., 2010. Functional Anatomy of T Cell Activation and Synapse Formation. *Annual Review of Immunology*, 28(1), pp.79–105. Available at: http://www.annualreviews.org/doi/10.1146/annurev-immunol-030409-101308 [Accessed November 8, 2016].

Forscher, P. & Smith, S.J., 1988. Actions of cytochalasins on the organization of actin filaments and microtubules in a neuronal growth cone. *The Journal of cell biology*, 107(4), pp.1505–16. Available at: http://www.ncbi.nlm.nih.gov/pubmed/3170637 [Accessed November 25, 2016].

Frank, M., 2000. MAL, a proteolipid in glycosphingolipid enriched domains: functional implications in myelin and beyond. *Progress in neurobiology*, 60(6), pp.531–44. Available at: http://www.ncbi.nlm.nih.gov/pubmed/10739088 [Accessed December 16, 2016].

Fujiwara, T. et al., 2002. Phospholipids undergo hop diffusion in compartmentalized cell membrane. *The Journal of Cell Biology*, 157(6).

Gaus, K. et al., 2005. Condensation of the plasma membrane at the site of T lymphocyte activation. *The Journal of cell biology*, 171(1), pp.121–31. Available at: http://www.ncbi.nlm.nih.gov/pubmed/16203859 [Accessed September 16, 2016].

Gaus, K. et al., 2003. Visualizing lipid structure and raft domains in living cells with two-photon microscopy. *Proceedings of the National Academy of Sciences of the United States of America*, 100(26), pp.15554–9. Available at: http://www.ncbi.nlm.nih.gov/pubmed/14673117 [Accessed November 8, 2016].

Gaus, K., Zech, T. & Harder, T., 2006. Visualizing membrane microdomains by Laurdan 2-photon microscopy (Review). *Molecular Membrane Biology*, 23(1), pp.41–48. Available at: http://www.tandfonline.com/doi/full/10.1080/09687860500466857 [Accessed November 8, 2016].

Gautreau, A., Louvard, D. & Arpin, M., 2000. Morphogenic Effects of Ezrin Require a Phosphorylation-Induced Transition from Oligomers to Monomers at the Plasma Membrane. *The Journal of Cell Biology*, 150(1).

Geiger, B. & Singer, S.J., 1979. The participation of alpha-actinin in the capping of cell membrane components. *Cell*, 16(1), pp.213–22. Available at: http://www.ncbi.nlm.nih.gov/pubmed/369707 [Accessed November 8, 2016].

Gillis, S. & Watson, J., 1980. Biochemical and biological characterization of lymphocyte regulatory molecules. V. Identification of an interleukin 2-producing human leukemia T cell line. *The Journal of experimental medicine*, 152(6), pp.1709–19. Available at: http://www.ncbi.nlm.nih.gov/pubmed/6778951 [Accessed November 25, 2016].

Goldsmith, M.A. & Weiss, A., 1988. Early signal transduction by the antigen receptor without commitment to T cell activation. *Science (New York, N.Y.)*, 240(4855), pp.1029–31. Available at: http://www.ncbi.nlm.nih.gov/pubmed/3259335 [Accessed November 8, 2016].

Goley, E.D. & Welch, M.D., 2006. The ARP2/3 complex: an actin nucleator comes of age. *Nature Reviews Molecular Cell Biology*, 7(10), pp.713–726. Available at: http://www.nature.com/doifinder/10.1038/nrm2026 [Accessed November 8, 2016].

Golfetto, O., Hinde, E. & Gratton, E., 2013. Laurdan fluorescence lifetime discriminates cholesterol content from changes in fluidity in living cell membranes. *Biophysical journal*, 104(6), pp.1238–47. Available at: http://www.ncbi.nlm.nih.gov/pubmed/23528083 [Accessed November 8, 2016].

Gómez-Llobregat, J., Buceta, J. & Reigada, R., 2013. Interplay of cytoskeletal activity and lipid phase stability in dynamic protein recruitment and clustering. *Scientific reports*, 3, p.2608. Available at: http://www.nature.com/articles/srep02608 [Accessed November 8, 2016].

Gordón-Alonso, M. et al., 2012. EWI-2 association with α-actinin regulates T cell immune synapses and HIV viral infection. *Journal of immunology (Baltimore, Md. : 1950)*, 189(2), pp.689–700. Available at: http://www.jimmunol.org/content/189/2/689.full [Accessed

January 18, 2016].

Goswami, D. et al., 2008. Nanoclusters of GPI-Anchored Proteins Are Formed by Cortical Actin-Driven Activity. *Cell*, 135(6), pp.1085–1097. Available at: http://linkinghub.elsevier.com/retrieve/pii/S0092867408015079 [Accessed November 8, 2016].

Gowrishankar, K. et al., 2012. Active Remodeling of Cortical Actin Regulates Spatiotemporal Organization of Cell Surface Molecules. *Cell*, 149(6), pp.1353–1367.

Grant, I., 1997. Particle image velocimetry: A review. *Proceedings of the Institution of Mechanical Engineers, Part C: Journal of Mechanical Engineering Science*, 211(1), pp.55–76. Available at: http://pic.sagepub.com/lookup/doi/10.1243/0954406971521665 [Accessed November 8, 2016].

Gustafsson, M.G., 2000. Surpassing the lateral resolution limit by a factor of two using structured illumination microscopy. *Journal of microscopy*, 198(Pt 2), pp.82–7. Available at: http://www.ncbi.nlm.nih.gov/pubmed/10810003 [Accessed September 16, 2016].

Ha, T. & Tinnefeld, P., 2012. Photophysics of fluorescent probes for single-molecule biophysics and super-resolution imaging. *Annual review of physical chemistry*, 63, pp.595–617. Available at: http://www.ncbi.nlm.nih.gov/pubmed/22404588 [Accessed September 16, 2016].

Hampton, C.M., Taylor, D.W. & Taylor, K.A., 2007. Novel structures for alpha-actinin:F-actin interactions and their implications for actin-membrane attachment and tension sensing in the cytoskeleton. *Journal of molecular biology*, 368(1), pp.92–104. Available at: http://www.sciencedirect.com/science/article/pii/S0022283607001362 [Accessed January 18, 2016].

Han, J. & Burgess, K., 2010. Fluorescent Indicators for Intracellular pH. *Chemical Reviews*, 110(5), pp.2709–2728. Available at: http://pubs.acs.org/doi/abs/10.1021/cr900249z [Accessed November 8, 2016].

Harke, B. et al., 2008. Resolution scaling in STED microscopy. *Optics Express*, 16(6), p.4154. Available at: https://www.osapublishing.org/abstract.cfm?URI=oe-16-6-4154 [Accessed September 16, 2016].

Hashimoto-Tane, A. et al., 2011. Dynein-Driven Transport of T Cell Receptor Microclusters Regulates Immune Synapse Formation and T Cell Activation. *Immunity*, 34(6), pp.919–

931. Available at: http://linkinghub.elsevier.com/retrieve/pii/S1074761311002287 [Accessed November 7, 2016].

Hayashi, K. & Altman, A., 2006. Filamin A is required for T cell activation mediated by protein kinase C-theta. *Journal of immunology (Baltimore, Md. : 1950)*, 177(3), pp.1721–8. Available at: http://www.ncbi.nlm.nih.gov/pubmed/16849481 [Accessed November 8, 2016].

Hebert, B., Costantino, S. & Wiseman, P.W., 2005. Spatiotemporal image correlation spectroscopy (STICS) theory, verification, and application to protein velocity mapping in living CHO cells. *Biophysical journal*, 88(5), pp.3601–14. Available at: http://www.pubmedcentral.nih.gov/articlerender.fcgi?artid=1305507&tool=pmcentrez&rendertype=abstract [Accessed January 18, 2016].

Hedde, P.N. et al., 2013. Stimulated emission depletion-based raster image correlation spectroscopy reveals biomolecular dynamics in live cells. *Nature Communications*, 4. Available at: http://www.nature.com/doifinder/10.1038/ncomms3093 [Accessed November 15, 2016].

Heilemann, M. et al., 2008. Subdiffraction-Resolution Fluorescence Imaging with Conventional Fluorescent Probes. *Angewandte Chemie International Edition*, 47(33), pp.6172–6176. Available at: http://doi.wiley.com/10.1002/anie.200802376 [Accessed September 16, 2016].

Heintzmann, R. & Cremer, C.G., 1999. <title>Laterally modulated excitation microscopy: improvement of resolution by using a diffraction grating</title> In I. J. Bigio et al., eds. International Society for Optics and Photonics, pp. 185–196. Available at: http://proceedings.spiedigitallibrary.org/proceeding.aspx?articleid=972650 [Accessed September 16, 2016].

Hell, S.W. & Wichmann, J., 1994. Breaking the diffraction resolution limit by stimulated emission: stimulated-emission-depletion fluorescence microscopy. *Optics Letters*, 19(11), p.780. Available at: https://www.osapublishing.org/abstract.cfm?URI=ol-19-11-780 [Accessed September 16, 2016].

Henson, J.H. et al., 1999. Two components of actin-based retrograde flow in sea urchin coelomocytes. *Molecular biology of the cell*, 10(12), pp.4075–90. Available at: http://www.ncbi.nlm.nih.gov/pubmed/10588644 [Accessed November 25, 2016].

Herndon, T.M. et al., 2001. ZAP-70 and SLP-76 regulate protein kinase C-theta and NF-kappa B

activation in response to engagement of CD3 and CD28. *Journal of immunology (Baltimore, Md. : 1950)*, 166(9), pp.5654–64. Available at: http://www.ncbi.nlm.nih.gov/pubmed/11313406 [Accessed November 7, 2016].

Hine, R., 1999. *The Facts on File dictionary of biology* 3rd ed., Facts On File.

Hoessli, D. et al., 1980. Lymphocyte alpha-actinin. Relationship to cell membrane and co-capping with surface receptors. *The Journal of cell biology*, 84(2), pp.305–14. Available at: http://www.ncbi.nlm.nih.gov/pubmed/6991509 [Accessed November 8, 2016].

Honigmann, A. et al., 2014. Scanning STED-FCS reveals spatiotemporal heterogeneity of lipid interaction in the plasma membrane of living cells. *Nature communications*, 5, p.5412. Available at: http://www.nature.com/doifinder/10.1038/ncomms6412 [Accessed November 8, 2016].

Huby, R.D.J., Weiss, A. & Ley, S.C., 1998. Nocodazole Inhibits Signal Transduction by the T Cell Antigen Receptor. *Journal of Biological Chemistry*, 273(20), pp.12024–12031. Available at: http://www.jbc.org/cgi/doi/10.1074/jbc.273.20.12024 [Accessed December 16, 2016].

Itoh, K. et al., 2002. Cutting edge: negative regulation of immune synapse formation by anchoring lipid raft to cytoskeleton through Cbp-EBP50-ERM assembly. *Journal of immunology (Baltimore, Md. : 1950)*, 168(2), pp.541–4. Available at: http://www.ncbi.nlm.nih.gov/pubmed/11777944 [Accessed November 8, 2016].

Jaiswal, J.K. & Simon, S.M., 2004. Potentials and pitfalls of fluorescent quantum dots for biological imaging. *Trends in Cell Biology*, 14(9), pp.497–504.

Jin, L. et al., 2005. Cholesterol-enriched lipid domains can be visualized by di-4-ANEPPDHQ with linear and nonlinear optics. *Biophysical journal*, 89(1), pp.L04-6. Available at: http://www.ncbi.nlm.nih.gov/pubmed/15879475 [Accessed September 16, 2016].

Jost, A. & Heintzmann, R., 2013. Superresolution Multidimensional Imaging with Structured Illumination Microscopy. *Annual Review of Materials Research*, 43(1), pp.261–282. Available at: http://www.annualreviews.org/doi/10.1146/annurev-matsci-071312-121648 [Accessed September 16, 2016].

Jungmann, R. et al., 2014. Multiplexed 3D cellular super-resolution imaging with DNA-PAINT and Exchange-PAINT. *Nature methods*, 11(3), pp.313–8. Available at: http://www.ncbi.nlm.nih.gov/pubmed/24487583 [Accessed September 16, 2016].

Jungmann, R. et al., 2016. Quantitative super-resolution imaging with qPAINT. *Nature*

methods, 13(5), pp.439–42. Available at: http://www.ncbi.nlm.nih.gov/pubmed/27018580 [Accessed September 16, 2016].

Kaizuka, Y. et al., 2007. Mechanisms for segregating T cell receptor and adhesion molecules during immunological synapse formation in Jurkat T cells. *Proceedings of the National Academy of Sciences of the United States of America*, 104(51), pp.20296–301. Available at: http://www.ncbi.nlm.nih.gov/pubmed/18077330 [Accessed November 7, 2016].

Katsuno, H. et al., 2015. Actin migration driven by directional assembly and disassembly of membrane-anchored actin filaments. *Cell Reports*, 12(4), pp.648–660. Available at: http://linkinghub.elsevier.com/retrieve/pii/S2211124715006749 [Accessed November 7, 2016].

Kelly, D.F. et al., 2006. Structure of the α-Actinin–Vinculin Head Domain Complex Determined by Cryo-electron Microscopy. *Journal of Molecular Biology*, 357(2), pp.562–573.

Kiuchi, T. et al., 2015. Multitarget super-resolution microscopy with high-density labeling by exchangeable probes. *Nature methods*, 12(8), pp.743–6. Available at: http://www.ncbi.nlm.nih.gov/pubmed/26147917 [Accessed September 16, 2016].

Klymchenko, A.S. & Kreder, R., 2014. Fluorescent Probes for Lipid Rafts: From Model Membranes to Living Cells. *Chemistry & Biology*, 21(1), pp.97–113. Available at: http://linkinghub.elsevier.com/retrieve/pii/S1074552113004183 [Accessed November 8, 2016].

Kolin, D.L., Ronis, D. & Wiseman, P.W., 2006. k-Space image correlation spectroscopy: a method for accurate transport measurements independent of fluorophore photophysics. *Biophysical journal*, 91(8), pp.3061–75. Available at: http://www.ncbi.nlm.nih.gov/pubmed/16861272 [Accessed November 8, 2016].

Köster, D.V. et al., 2016. Actomyosin dynamics drive local membrane component organization in an in vitro active composite layer. *Proceedings of the National Academy of Sciences*, 113(12), pp.E1645–E1654. Available at: http://www.pnas.org/lookup/doi/10.1073/pnas.1514030113 [Accessed November 8, 2016].

Kovács, M. et al., 2004. Mechanism of blebbistatin inhibition of myosin II. *The Journal of biological chemistry*, 279(34), pp.35557–63. Available at: http://www.ncbi.nlm.nih.gov/pubmed/15205456 [Accessed November 23, 2016].

Krause, M. et al., 2000. Fyn-Binding Protein (Fyb)/Slp-76–Associated Protein (Slap), Ena/Vasodilator-Stimulated Phosphoprotein (Vasp) Proteins and the Arp2/3 Complex Link T Cell Receptor (Tcr) Signaling to the Actin Cytoskeleton. *The Journal of Cell Biology*, 149(1).

Kucik, D.F., Elson, E.L. & Sheetz, M.P., 1990. Cell migration does not produce membrane flow. *The Journal of cell biology*, 111(4), pp.1617–22. Available at: http://www.pubmedcentral.nih.gov/articlerender.fcgi?artid=2116247&tool=pmcentrez&rendertype=abstract [Accessed January 18, 2016].

Kumari, S. et al., 2015. Actin foci facilitate activation of the phospholipase C-γ in primary T lymphocytes via the WASP pathway. *eLife*, 2015(4), pp.1–31. Available at: http://www.ncbi.nlm.nih.gov/pubmed/25758716 [Accessed December 19, 2016].

Kusumi, A. et al., 2012. Membrane mechanisms for signal transduction: The coupling of the meso-scale raft domains to membrane-skeleton-induced compartments and dynamic protein complexes. *Seminars in Cell & Developmental Biology*, 23(2), pp.126–144. Available at: http://linkinghub.elsevier.com/retrieve/pii/S1084952112000286 [Accessed November 8, 2016].

Kusumi, A., Nakada, C., et al., 2005. Paradigm Shift of the Plasma Membrane Concept from the Two-Dimensional Continuum Fluid to the Partitioned Fluid: High-Speed Single-Molecule Tracking of Membrane Molecules. *Annual Review of Biophysics and Biomolecular Structure*, 34(1), pp.351–378. Available at: http://www.annualreviews.org/doi/10.1146/annurev.biophys.34.040204.144637 [Accessed November 8, 2016].

Kusumi, A., Ike, H., et al., 2005. Single-molecule tracking of membrane molecules: plasma membrane compartmentalization and dynamic assembly of raft-philic signaling molecules. *Seminars in immunology*, 17(1), pp.3–21. Available at: http://www.sciencedirect.com/science/article/pii/S1044532304000594 [Accessed January 18, 2016].

de la Fuente, M.A. et al., 2007. WIP is a chaperone for Wiskott-Aldrich syndrome protein (WASP). *Proceedings of the National Academy of Sciences of the United States of America*, 104(3), pp.926–31. Available at: http://www.ncbi.nlm.nih.gov/pubmed/17213309 [Accessed November 7, 2016].

Lakowicz, J.R. ed., 2006. *Principles of Fluorescence Spectroscopy*, Boston, MA: Springer US.

Available at: http://link.springer.com/10.1007/978-0-387-46312-4 [Accessed September 16, 2016].

Lang, T. et al., 2000. Role of Actin Cortex in the Subplasmalemmal Transport of Secretory Granules in PC-12 Cells. *Biophysical Journal*, 78(6), pp.2863–2877. Available at: http://linkinghub.elsevier.com/retrieve/pii/S0006349500768287 [Accessed November 8, 2016].

Larghi, P. et al., 2013. VAMP7 controls T cell activation by regulating the recruitment and phosphorylation of vesicular Lat at TCR-activation sites. *Nature Immunology*, 14(7), pp.723–731. Available at: http://www.nature.com/doifinder/10.1038/ni.2609 [Accessed November 8, 2016].

Lavi, Y. et al., 2012. Lifetime of Major Histocompatibility Complex Class-I Membrane Clusters Is Controlled by the Actin Cytoskeleton. *Biophysical Journal*, 102(7), pp.1543–1550.

Lee, J. et al., 1990. The direction of membrane lipid flow in locomoting polymorphonuclear leukocytes. *Science*, 247(4947).

Lee, K.-H. et al., 2003. The Immunological Synapse Balances T Cell Receptor Signaling and Degradation. *Science*, 302(5648). Available at: http://science.sciencemag.org/content/302/5648/1218 [Accessed January 5, 2017].

Leupin, O. et al., 2000. Exclusion of CD45 from the T-cell receptor signaling area in antigen-stimulated T lymphocytes. *Current Biology*, 10(5), pp.277–280.

Li, D. et al., 2015. Extended-resolution structured illumination imaging of endocytic and cytoskeletal dynamics. *Science*, 349(6251).

Lichtenberg, D., Goñi, F.M. & Heerklotz, H., 2005. Detergent-resistant membranes should not be identified with membrane rafts. *Trends in Biochemical Sciences*, 30(8), pp.430–436. Available at: http://linkinghub.elsevier.com/retrieve/pii/S0968000405001830 [Accessed November 8, 2016].

Lillemeier, B.F. et al., 2006. Plasma membrane-associated proteins are clustered into islands attached to the cytoskeleton. *Proceedings of the National Academy of Sciences of the United States of America*, 103(50), pp.18992–7. Available at: http://www.pubmedcentral.nih.gov/articlerender.fcgi?artid=1681352&tool=pmcentrez&rendertype=abstract [Accessed January 18, 2016].

Lillemeier, B.F. et al., 2010. TCR and Lat are expressed on separate protein islands on T cell

membranes and concatenate during activation. *Nature immunology*, 11(1), pp.90–6. Available at: http://www.ncbi.nlm.nih.gov/pubmed/20010844 [Accessed August 16, 2016].

Lipkowitz, S. et al., 1984. Expression of receptors for interleukin 2: Role in the commitment of T lymphocytes to proliferate. *Journal of immunology (Baltimore, Md. : 1950)*, 132(1), pp.31–7. Available at: http://www.ncbi.nlm.nih.gov/pubmed/6418801 [Accessed November 8, 2016].

Love, P.E. & Hayes, S.M., 2010. ITAM-mediated signaling by the T-cell antigen receptor. *Cold Spring Harbor perspectives in biology*, 2(6), p.a002485. Available at: http://www.ncbi.nlm.nih.gov/pubmed/20516133 [Accessed November 7, 2016].

Lyons, M.A. & Brown, A.J., 1999. 7-Ketocholesterol. *The International Journal of Biochemistry & Cell Biology*, 31(3), pp.369–375.

Ma, Z. et al., 2008. Surface-Anchored Monomeric Agonist pMHCs Alone Trigger TCR with High Sensitivity P. Marrack, ed. *PLoS Biology*, 6(2), p.e43. Available at: http://dx.plos.org/10.1371/journal.pbio.0060043 [Accessed November 8, 2016].

Mace, E.M. et al., 2010. Elucidation of the integrin LFA-1-mediated signaling pathway of actin polarization in natural killer cells. *Blood*, 116(8), pp.1272–1279. Available at: http://www.bloodjournal.org/cgi/doi/10.1182/blood-2009-12-261487 [Accessed November 7, 2016].

Mace, E.M. & Orange, J.S., 2014. Lytic immune synapse function requires filamentous actin deconstruction by Coronin 1A. *Proceedings of the National Academy of Sciences of the United States of America*, 111(18), pp.6708–13. Available at: http://www.pubmedcentral.nih.gov/articlerender.fcgi?artid=4020046&tool=pmcentrez&rendertype=abstract [Accessed January 18, 2016].

Machta, B.B. et al., 2011. Minimal model of plasma membrane heterogeneity requires coupling cortical actin to criticality. *Biophysical journal*, 100(7), pp.1668–77. Available at: http://www.sciencedirect.com/science/article/pii/S0006349511002475 [Accessed December 10, 2015].

Magde, D., Elson, E. & Webb, W.W., 1972. Thermodynamic Fluctuations in a Reacting System—Measurement by Fluorescence Correlation Spectroscopy. *Physical Review Letters*, 29(11), pp.705–708. Available at: http://link.aps.org/doi/10.1103/PhysRevLett.29.705 [Accessed November 8, 2016].

Mahankali, M. et al., 2011. The mechanism of cell membrane ruffling relies on a phospholipase D2 (PLD2), Grb2 and Rac2 association. *Cellular signalling*, 23(8), pp.1291–8. Available at: http://www.ncbi.nlm.nih.gov/pubmed/21419846 [Accessed November 25, 2016].

Martín-Cófreces, N.B. et al., 2008. MTOC translocation modulates IS formation and controls sustained T cell signaling. *The Journal of Cell Biology*, 182(5), pp.951–962. Available at: http://www.jcb.org/lookup/doi/10.1083/jcb.200801014 [Accessed November 7, 2016].

Massey, J.B. & Pownall, H.J., 2005. The polar nature of 7-ketocholesterol determines its location within membrane domains and the kinetics of membrane microsolubilization by apolipoprotein A-I. *Biochemistry*, 44(30), pp.10423–33. Available at: http://www.ncbi.nlm.nih.gov/pubmed/16042420 [Accessed September 16, 2016].

Mattila, P.K., Batista, F.D. & Treanor, B., 2016. Dynamics of the actin cytoskeleton mediates receptor cross talk: An emerging concept in tuning receptor signaling. *The Journal of Cell Biology*, 212(3).

Mattila, P.K. & Lappalainen, P., 2008. Filopodia: molecular architecture and cellular functions. *Nature Reviews Molecular Cell Biology*, 9(6), pp.446–454. Available at: http://www.nature.com/doifinder/10.1038/nrm2406 [Accessed November 7, 2016].

Metcalf, D.J. et al., 2013. Test samples for optimizing STORM super-resolution microscopy. *Journal of visualized experiments : JoVE*, (79). Available at: http://www.ncbi.nlm.nih.gov/pubmed/24056752 [Accessed September 16, 2016].

Miguel, L. et al., 2011. Primary Human CD4+ T Cells Have Diverse Levels of Membrane Lipid Order That Correlate with Their Function. *The Journal of Immunology*, 186(6), pp.3505–3516. Available at: http://www.jimmunol.org/cgi/doi/10.4049/jimmunol.1002980 [Accessed November 8, 2016].

Milovanovic, D. et al., 2015. Hydrophobic mismatch sorts SNARE proteins into distinct membrane domains. *Nature communications*, 6, p.5984. Available at: http://www.nature.com/doifinder/10.1038/ncomms6984 [Accessed November 8, 2016].

Mitxitorena, I., Saavedra, E. & Barcia, C., 2015. Kupfer-type immunological synapses in vivo: Raison D'être of SMAC. *Immunology and Cell Biology*, 93(1), pp.51–56. Available at: http://www.nature.com/doifinder/10.1038/icb.2014.80 [Accessed November 7, 2016].

Mohrmann, K. & van der Sluijs, P., 1999. Regulation of membrane transport through the endocytic pathway by rabGTPases. *Mol Membr Biol*, 16(1), pp.81–87. Available at:

http://www.ncbi.nlm.nih.gov/pubmed/10332741 [Accessed November 8, 2016].

Mondal, S. et al., 2013. Membrane Driven Spatial Organization of GPCRs. *Scientific Reports*, 3, p.2909(1-9). Available at: http://www.nature.com/articles/srep02909 [Accessed November 8, 2016].

Monks, C.R. et al., 1998. Three-dimensional segregation of supramolecular activation clusters in T cells. *Nature*, 395(6697), pp.82–86. Available at: http://www.nature.com/doifinder/10.1038/25764 [Accessed November 7, 2016].

Murugesan, S. et al., 2016. Formin-generated actomyosin arcs propel t cell receptor microcluster movement at the immune synapse. *Journal of Cell Biology*, 215(3), pp.383–399.

Neco, P. et al., 2003. Differential participation of actin- and tubulin-based vesicle transport systems during secretion in bovine chromaffin cells. *The European journal of neuroscience*, 18(4), pp.733–42. Available at: http://www.ncbi.nlm.nih.gov/pubmed/12924999 [Accessed December 16, 2016].

Neisch, A.L. & Fehon, R.G., 2011. Ezrin, Radixin and Moesin: key regulators of membrane-cortex interactions and signaling. *Current opinion in cell biology*, 23(4), pp.377–82. Available at: http://www.ncbi.nlm.nih.gov/pubmed/21592758 [Accessed November 8, 2016].

Niggli, V. & Rossy, J., 2008. Ezrin/radixin/moesin: Versatile controllers of signaling molecules and of the cortical cytoskeleton. *The International Journal of Biochemistry & Cell Biology*, 40(3), pp.344–349. Available at: http://linkinghub.elsevier.com/retrieve/pii/S1357272507000593 [Accessed November 8, 2016].

Obaid, A.L. et al., 2004. Novel naphthylstyryl-pyridium potentiometric dyes offer advantages for neural network analysis. *Journal of neuroscience methods*, 134(2), pp.179–90. Available at: http://www.ncbi.nlm.nih.gov/pubmed/15003384 [Accessed September 16, 2016].

Olsen, B.N. et al., 2013. The structural basis of cholesterol accessibility in membranes. *Biophysical journal*, 105(8), pp.1838–47. Available at: http://www.ncbi.nlm.nih.gov/pubmed/24138860 [Accessed November 8, 2016].

Ostašov, P. et al., 2013. FLIM studies of 22- and 25-NBD-cholesterol in living HEK293 cells:

Plasma membrane change induced by cholesterol depletion. *Chemistry and Physics of Lipids*, 167–168, pp.62–69. Available at: http://www.ncbi.nlm.nih.gov/pubmed/23466534 [Accessed November 8, 2016].

Otey, C.A. & Carpen, O., 2004. Alpha-actinin revisited: a fresh look at an old player. *Cell motility and the cytoskeleton*, 58(2), pp.104–11. Available at: http://www.ncbi.nlm.nih.gov/pubmed/15083532 [Accessed November 8, 2016].

Otey, C.A., Pavalko, F.M. & Burridge, K., 1990. An interaction between alpha-actinin and the beta 1 integrin subunit in vitro. *The Journal of cell biology*, 111(2), pp.721–9. Available at: http://www.ncbi.nlm.nih.gov/pubmed/2116421 [Accessed November 8, 2016].

Owen, D.M., Oddos, S., et al., 2010. High plasma membrane lipid order imaged at the immunological synapse periphery in live T cells. *Molecular Membrane Biology*, 27(4–6), pp.178–189. Available at: http://www.tandfonline.com/doi/full/10.3109/09687688.2010.495353 [Accessed January 18, 2016].

Owen, D.M. et al., 2010. High plasma membrane lipid order imaged at the immunological synapse periphery in live T cells. *Molecular membrane biology*, 27(4–6), pp.178–89. Available at: http://www.ncbi.nlm.nih.gov/pubmed/20540668 [Accessed September 16, 2016].

Owen, D.M., Magenau, A., et al., 2010. Imaging membrane lipid order in whole, living vertebrate organisms. *Biophysical journal*, 99(1), pp.L7–L9.

Owen, D.M. et al., 2011. Quantitative imaging of membrane lipid order in cells and organisms. *Nature Protocols*, 7(1), pp.24–35. Available at: http://www.nature.com/doifinder/10.1038/nprot.2011.419 [Accessed November 8, 2016].

Owen, D.M. et al., 2012. Sub-resolution lipid domains exist in the plasma membrane and regulate protein diffusion and distribution. *Nat Commun*, 3, p.1256. Available at: http://www.nature.com/doifinder/10.1038/ncomms2273 [Accessed November 25, 2016].

Panchuk-Voloshina, N. et al., 1999. Alexa dyes, a series of new fluorescent dyes that yield exceptionally bright, photostable conjugates. *The journal of histochemistry and cytochemistry : official journal of the Histochemistry Society*, 47(9), pp.1179–88. Available at: http://www.ncbi.nlm.nih.gov/pubmed/10449539 [Accessed September 16, 2016].

Pandžić, E., Rossy, J. & Gaus, K., 2015. Tracking molecular dynamics without tracking: image correlation of photo-activation microscopy. *Methods and Applications in Fluorescence*, 3(1), p.14006. Available at: http://stacks.iop.org/2050-6120/3/i=1/a=014006?key=crossref.bb8ed8ceff5d268221ce294f40f320c0 [Accessed November 8, 2016].

Parasassi, T. et al., 1991. Quantitation of lipid phases in phospholipid vesicles by the generalized polarization of Laurdan fluorescence. *Biophysical journal*, 60(1), pp.179–89. Available at: http://www.ncbi.nlm.nih.gov/pubmed/1883937 [Accessed September 16, 2016].

Patterson, G.H., 2002. A Photoactivatable GFP for Selective Photolabeling of Proteins and Cells. *Science*, 297(5588), pp.1873–1877. Available at: http://www.sciencemag.org/cgi/doi/10.1126/science.1074952 [Accessed November 8, 2016].

Patterson, G.H. et al., 1997. Use of the green fluorescent protein and its mutants in quantitative fluorescence microscopy. *Biophysical journal*, 73(5), pp.2782–90. Available at: http://www.ncbi.nlm.nih.gov/pubmed/9370472 [Accessed November 8, 2016].

Pawley, J.B., 2006. Fundamental Limits in Confocal Microscopy. In *Handbook Of Biological Confocal Microscopy*. Boston, MA: Springer US, pp. 20–42. Available at: http://link.springer.com/10.1007/978-0-387-45524-2_2 [Accessed November 8, 2016].

Petersen, N.O. et al., 1993. Quantitation of membrane receptor distributions by image correlation spectroscopy: concept and application. *Biophysical Journal*, 65(3), pp.1135–1146. Available at: http://linkinghub.elsevier.com/retrieve/pii/S0006349593811731 [Accessed November 8, 2016].

Pike, L.J. et al., 2002. Lipid rafts are enriched in arachidonic acid and plasmenylethanolamine and their composition is independent of caveolin-1 expression: a quantitative electrospray ionization/mass spectrometric analysis. *Biochemistry*, 41(6), pp.2075–88. Available at: http://www.ncbi.nlm.nih.gov/pubmed/11827555 [Accessed November 8, 2016].

Pollard, T.D., Blanchoin, L. & Mullins, R.D., 2000. Molecular Mechanisms Controlling Actin Filament Dynamics in Nonmuscle Cells. *Annual Review of Biophysics and Biomolecular Structure*, 29(1), pp.545–576. Available at: http://www.annualreviews.org/doi/10.1146/annurev.biophys.29.1.545 [Accessed April 7,

2017].

Pollard, T.D. & Cooper, J.A., 2009. Actin, a Central Player in Cell Shape and Movement. *Science*, 326(5957), pp.1208–1212. Available at: http://www.sciencemag.org/cgi/doi/10.1126/science.1175862 [Accessed November 7, 2016].

Purbhoo, M.A. et al., 2010. Dynamics of subsynaptic vesicles and surface microclusters at the immunological synapse. *Science signaling*, 3(121), p.ra36. Available at: http://www.ncbi.nlm.nih.gov/pubmed/20460647 [Accessed November 7, 2016].

Raghupathy, R. et al., 2015. Transbilayer lipid interactions mediate nanoclustering of lipid-anchored proteins. *Cell*, 161(3), pp.581–594. Available at: http://www.ncbi.nlm.nih.gov/pubmed/25910209 [Accessed August 8, 2016].

Rak, G.D. et al., 2011. Natural killer cell lytic granule secretion occurs through a pervasive actin network at the immune synapse. *PLoS biology*, 9(9), p.e1001151. Available at: http://journals.plos.org/plosbiology/article?id=10.1371/journal.pbio.1001151 [Accessed January 18, 2016].

Rego, E.H. et al., 2012. Nonlinear structured-illumination microscopy with a photoswitchable protein reveals cellular structures at 50-nm resolution. *Proceedings of the National Academy of Sciences of the United States of America*, 109(3), pp.E135-43. Available at: http://www.ncbi.nlm.nih.gov/pubmed/22160683 [Accessed November 8, 2016].

Rentero, C. et al., 2008. Functional implications of plasma membrane condensation for T cell activation. *PloS one*, 3(5), p.e2262. Available at: http://journals.plos.org/plosone/article?id=10.1371/journal.pone.0002262 [Accessed January 18, 2016].

Reschner, A. et al., 2008. Innate lymphocyte and dendritic cell cross-talk: a key factor in the regulation of the immune response. *Clinical and experimental immunology*, 152(2), pp.219–26. Available at: http://www.ncbi.nlm.nih.gov/pubmed/18336590 [Accessed November 7, 2016].

Ridley, A.J., 1994. Membrane ruffling and signal transduction. *BioEssays*, 16(5), pp.321–327. Available at: http://doi.wiley.com/10.1002/bies.950160506 [Accessed November 25, 2016].

Riedl, J. et al., 2008. Lifeact: a versatile marker to visualize F-actin. *Nature methods*, 5(7),

pp.605–7. Available at: http://www.ncbi.nlm.nih.gov/pubmed/18536722 [Accessed September 16, 2016].

Ritter, A.T. et al., 2015. Actin Depletion Initiates Events Leading to Granule Secretion at the Immunological Synapse. *Immunity*, 42(5), pp.864–876. Available at: http://www.cell.com/article/S1074761315001739/fulltext [Accessed May 21, 2015].

Rivas, F. V et al., 2004. Actin cytoskeleton regulates calcium dynamics and NFAT nuclear duration. *Molecular and cellular biology*, 24(4), pp.1628–39. Available at: http://www.ncbi.nlm.nih.gov/pubmed/14749378 [Accessed December 20, 2016].

Roumier, A. et al., 2001. The membrane-microfilament linker ezrin is involved in the formation of the immunological synapse and in T cell activation. *Immunity*, 15(5), pp.715–28. Available at: http://www.ncbi.nlm.nih.gov/pubmed/11728334 [Accessed November 8, 2016].

Ruan, Q. et al., 2004. Spatial-Temporal Studies of Membrane Dynamics: Scanning Fluorescence Correlation Spectroscopy (SFCS). *Biophysical Journal*, 87(2), pp.1260–1267. Available at: http://linkinghub.elsevier.com/retrieve/pii/S000634950473605X [Accessed November 8, 2016].

Rust, M.J., Bates, M. & Zhuang, X., 2006. Sub-diffraction-limit imaging by stochastic optical reconstruction microscopy (STORM). *Nature methods*, 3(10), pp.793–5. Available at: http://www.ncbi.nlm.nih.gov/pubmed/16896339 [Accessed September 16, 2016].

Saarikangas, J., Zhao, H. & Lappalainen, P., 2010. Regulation of the Actin Cytoskeleton-Plasma Membrane Interplay by Phosphoinositides. *Physiological Reviews*, 90(1).

Sage, P.T. et al., 2012. Antigen Recognition Is Facilitated by Invadosome-like Protrusions Formed by Memory/Effector T Cells. *The Journal of Immunology*, 188(8), pp.3686–3699. Available at: http://www.jimmunol.org/cgi/doi/10.4049/jimmunol.1102594 [Accessed November 8, 2016].

Saha, S. et al., 2015. Diffusion of GPI-anchored proteins is influenced by the activity of dynamic cortical actin. *Molecular biology of the cell*, 26(22), pp.4033–45. Available at: http://www.ncbi.nlm.nih.gov/pubmed/26378258 [Accessed November 8, 2016].

Sakamoto, T. et al., 2005. Blebbistatin, a Myosin II Inhibitor, Is Photoinactivated by Blue Light. *Biochemistry*, 44(2), pp.584–588. Available at: http://pubs.acs.org/doi/abs/10.1021/bi0483357 [Accessed November 17, 2016].

Salazar-Fontana, L.I. et al., 2003. CD28 engagement promotes actin polymerization through the activation of the small Rho GTPase Cdc42 in human T cells. *Journal of immunology (Baltimore, Md. : 1950)*, 171(5), pp.2225–32. Available at: http://www.ncbi.nlm.nih.gov/pubmed/12928366 [Accessed November 7, 2016].

Salojin, K. V, Zhang, J. & Delovitch, T.L., 1999. TCR and CD28 are coupled via ZAP-70 to the activation of the Vav/Rac-1-/PAK-1/p38 MAPK signaling pathway. *Journal of immunology (Baltimore, Md. : 1950)*, 163(2), pp.844–53. Available at: http://www.ncbi.nlm.nih.gov/pubmed/10395678 [Accessed November 7, 2016].

Samstag, Y. et al., 2003. Actin cytoskeletal dynamics in T lymphocyte activation and migration. *Journal of leukocyte biology*, 73(1), pp.30–48. Available at: http://www.ncbi.nlm.nih.gov/pubmed/12525560 [Accessed November 8, 2016].

Sasahara, Y. et al., 2002. Mechanism of recruitment of WASP to the immunological synapse and of its activation following TCR ligation. *Molecular cell*, 10(6), pp.1269–81. Available at: http://www.ncbi.nlm.nih.gov/pubmed/12504004 [Accessed November 7, 2016].

Schliwa, M., 1982. Action of cytochalasin D on cytoskeletal networks. *The Journal of cell biology*, 92(1), pp.79–91. Available at: http://www.ncbi.nlm.nih.gov/pubmed/7199055 [Accessed September 16, 2016].

Schmid, E.M. et al., 2016. Size-dependent protein segregation at membrane interfaces. *Nature Physics*, 12(7), pp.704–711. Available at: http://www.nature.com/doifinder/10.1038/nphys3678 [Accessed November 8, 2016].

Schneider, C.A., Rasband, W.S. & Eliceiri, K.W., 2012. NIH Image to ImageJ: 25 years of image analysis. *Nature Methods*, 9(7), pp.671–675. Available at: http://www.nature.com/doifinder/10.1038/nmeth.2089 [Accessed January 9, 2017].

Schneider, U., Schwenk, H.U. & Bornkamm, G., 1977. Characterization of EBV-genome negative "null" and "T" cell lines derived from children with acute lymphoblastic leukemia and leukemic transformed non-Hodgkin lymphoma. *International journal of cancer*, 19(5), pp.621–6. Available at: http://www.ncbi.nlm.nih.gov/pubmed/68013 [Accessed November 7, 2016].

Schofield, C. et al., 2016. Characterization of IL-17AA and IL-17FF in rheumatoid arthritis and multiple sclerosis. *Bioanalysis*, 8(22), pp.2317–2327. Available at: http://www.future-science.com/doi/10.4155/bio-2016-0207 [Accessed November 7, 2016].

Schuck, S. et al., 2003. Resistance of cell membranes to different detergents. *Proceedings of the National Academy of Sciences of the United States of America*, 100(10), pp.5795–800. Available at: http://www.ncbi.nlm.nih.gov/pubmed/12721375 [Accessed November 8, 2016].

Schuh, M., 2011. An actin-dependent mechanism for long-range vesicle transport. *Nature Cell Biology*, 13(12), pp.1431–1436. Available at: http://www.ncbi.nlm.nih.gov/pubmed/21983562 [Accessed December 16, 2016].

Semrau, S. & Schmidt, T., 2007. Particle image correlation spectroscopy (PICS): retrieving nanometer-scale correlations from high-density single-molecule position data. *Biophysical journal*, 92(2), pp.613–21. Available at: http://www.ncbi.nlm.nih.gov/pubmed/17085496 [Accessed November 8, 2016].

Sevcsik, E. et al., 2015. GPI-anchored proteins do not reside in ordered domains in the live cell plasma membrane. *Nature Communications*, 6, p.6969. Available at: http://www.nature.com/doifinder/10.1038/ncomms7969 [Accessed November 8, 2016].

Shabardina, V. et al., 2016. Mode of Ezrin-Membrane Interaction as a Function of PIP2 Binding and Pseudophosphorylation. *Biophysical Journal*, 110(12), pp.2710–2719. Available at: http://linkinghub.elsevier.com/retrieve/pii/S0006349516302867 [Accessed November 8, 2016].

Shan, X. et al., 2000. Deficiency of PTEN in Jurkat T cells causes constitutive localization of Itk to the plasma membrane and hyperresponsiveness to CD3 stimulation. *Molecular and cellular biology*, 20(18), pp.6945–57. Available at: http://www.ncbi.nlm.nih.gov/pubmed/10958690 [Accessed November 8, 2016].

Sharma, P. et al., 2004. Nanoscale organization of multiple GPI-anchored proteins in living cell membranes. *Cell*, 116(4), pp.577–89. Available at: http://www.ncbi.nlm.nih.gov/pubmed/14980224 [Accessed November 8, 2016].

Shcherbina, A. et al., 1999. Moesin, the major ERM protein of lymphocytes and platelets, differs from ezrin in its insensitivity to calpain. *FEBS Letters*, 443(1), pp.31–36.

Sheetz, M.P. & Martenson, C.H., 1991. Axonal transport: beyond kinesin and cytoplasmic dynein. *Current opinion in neurobiology*, 1(3), pp.393–8. Available at: http://www.ncbi.nlm.nih.gov/pubmed/1726552 [Accessed December 16, 2016].

Sherman, E. et al., 2016. Hierarchical nanostructure and synergy of multimolecular signalling

complexes. *Nature communications*, 7, p.12161. Available at: http://www.nature.com/doifinder/10.1038/ncomms12161 [Accessed November 8, 2016].

Shimomura, O., Johnson, F.H. & Saiga, Y., 1962. Extraction, Purification and Properties of Aequorin, a Bioluminescent Protein from the Luminous Hydromedusan,Aequorea. *Journal of Cellular and Comparative Physiology*, 59(3), pp.223–239. Available at: http://doi.wiley.com/10.1002/jcp.1030590302 [Accessed November 8, 2016].

Shroff, H. et al., 2008. Live-cell photoactivated localization microscopy of nanoscale adhesion dynamics. *Nature Methods*, 5(5), pp.417–423. Available at: http://www.nature.com/doifinder/10.1038/nmeth.1202 [Accessed September 16, 2016].

Siegmund, K. et al., 2015. Novel Protein kinase C θ: Coronin 1A complex in T lymphocytes. *Cell Communication and Signaling*, 13(1), pp.1–8. Available at: http://www.biosignaling.com/content/13/1/22 [Accessed November 7, 2016].

Silvius, J.R., del Giudice, D. & Lafleur, M., 1996. Cholesterol at different bilayer concentrations can promote or antagonize lateral segregation of phospholipids of differing acyl chain length. *Biochemistry*, 35(48), pp.15198–208. Available at: http://www.ncbi.nlm.nih.gov/pubmed/8952467 [Accessed November 8, 2016].

Simons, K. & Ikonen, E., 1997. Functional rafts in cell membranes. *Nature*, 387(6633), pp.569–72. Available at: http://www.ncbi.nlm.nih.gov/pubmed/9177342 [Accessed November 8, 2016].

Simons, K. & van Meer, G., 1988. Lipid sorting in epithelial cells. *Biochemistry*, 27(17), pp.6197–202. Available at: http://www.ncbi.nlm.nih.gov/pubmed/3064805 [Accessed November 8, 2016].

Sims, T.N. et al., 2007. Opposing Effects of PKCθ and WASp on Symmetry Breaking and Relocation of the Immunological Synapse. *Cell*, 129(4), pp.773–785. Available at: http://linkinghub.elsevier.com/retrieve/pii/S0092867407004539 [Accessed November 7, 2016].

Singer, S.J. & Nicolson, G.L., 1972. The fluid mosaic model of the structure of cell membranes. *Science (New York, N.Y.)*, 175(4023), pp.720–31. Available at: http://www.ncbi.nlm.nih.gov/pubmed/4333397 [Accessed November 8, 2016].

Sjöblom, B., Salmazo, A. & Djinović-Carugo, K., 2008. Alpha-actinin structure and regulation.

Cellular and molecular life sciences : CMLS, 65(17), pp.2688–701. Available at: http://www.ncbi.nlm.nih.gov/pubmed/18488141 [Accessed January 18, 2016].

Soares, H. et al., 2013. Regulated vesicle fusion generates signaling nanoterritories that control T cell activation at the immunological synapse. *The Journal of Experimental Medicine*, 210(11), pp.2415–2433. Available at: http://www.jem.org/lookup/doi/10.1084/jem.20130150 [Accessed November 7, 2016].

Stockton, B.M. et al., 1998. Negative regulation of T cell homing by CD43. *Immunity*, 8(3), pp.373–81. Available at: http://www.ncbi.nlm.nih.gov/pubmed/9529154 [Accessed November 7, 2016].

Stossel, T.P. et al., 2001. Filamins as integrators of cell mechanics and signalling. *Nature Reviews Molecular Cell Biology*, 2(2), pp.138–145. Available at: http://www.nature.com/doifinder/10.1038/35052082 [Accessed November 8, 2016].

Sun, Z. et al., 2000. PKC-theta is required for TCR-induced NF-kappaB activation in mature but not immature T lymphocytes. *Nature*, 404(6776), pp.402–7. Available at: http://www.ncbi.nlm.nih.gov/pubmed/10746729 [Accessed November 7, 2016].

Svitkina, T.M. & Borisy, G.G., 1999. Arp2/3 complex and actin depolymerizing factor/cofilin in dendritic organization and treadmilling of actin filament array in lamellipodia. *The Journal of cell biology*, 145(5), pp.1009–26. Available at: http://www.ncbi.nlm.nih.gov/pubmed/10352018 [Accessed November 15, 2016].

Takenawa, T. & Suetsugu, S., 2007. The WASP–WAVE protein network: connecting the membrane to the cytoskeleton. *Nature Reviews Molecular Cell Biology*, 8(1), pp.37–48. Available at: http://www.nature.com/doifinder/10.1038/nrm2069 [Accessed November 8, 2016].

Tavano, R. et al., 2006. CD28 interaction with filamin-A controls lipid raft accumulation at the T-cell immunological synapse. *Nature cell biology*, 8(11), pp.1270–6. Available at: http://www.ncbi.nlm.nih.gov/pubmed/17060905 [Accessed August 17, 2016].

Tee, Y.H. et al., 2015. Cellular chirality arising from the self-organization of the actin cytoskeleton. *Nature Cell Biology*, 17(4), pp.445–457. Available at: http://www.nature.com/doifinder/10.1038/ncb3137 [Accessed November 7, 2016].

Thauland, T.J. & Parker, D.C., 2010. Diversity in immunological synapse structure. *Immunology*, 131(4), pp.466–72. Available at: http://www.ncbi.nlm.nih.gov/pubmed/21039474

[Accessed November 7, 2016].

Thompson, R.E., Larson, D.R. & Webb, W.W., 2002. Precise nanometer localization analysis for individual fluorescent probes. *Biophysical journal*, 82(5), pp.2775–83. Available at: http://www.ncbi.nlm.nih.gov/pubmed/11964263 [Accessed September 16, 2016].

Tomas, E.M., Chau, T.A. & Madrenas, J., 2002. Clustering of a lipid-raft associated pool of ERM proteins at the immunological synapse upon T cell receptor or CD28 ligation. *Immunology Letters*, 83(2), pp.143–147.

Tong, J. et al., 2004. CD43 regulation of T cell activation is not through steric inhibition of T cell-APC interactions but through an intracellular mechanism. *The Journal of experimental medicine*, 199(9), pp.1277–83. Available at: http://www.ncbi.nlm.nih.gov/pubmed/15117976 [Accessed November 7, 2016].

Turro, N.J., Ramamurthy, V. & Scaiano., J.C., 2010. *Modern Molecular Photochemistry of Organic Molecules*, University Science Books. Available at: http://doi.wiley.com/10.1002/anie.201003826 [Accessed September 16, 2016].

Ueda, H. et al., 2015. Distinct Roles of Cytoskeletal Components in Immunological Synapse Formation and Directed Secretion. *The Journal of Immunology*, 195(9), pp.4117–4125. Available at: http://www.ncbi.nlm.nih.gov/pubmed/26392461 [Accessed December 16, 2016].

Valensin, S. et al., 2002. F-actin dynamics control segregation of the TCR signaling cascade to clustered lipid rafts. *European Journal of Immunology*, 32(2), pp.435–446. Available at: http://doi.wiley.com/10.1002/1521-4141%28200202%2932%3A2%3C435%3A%3AAID-IMMU435%3E3.0.CO%3B2-H [Accessed November 8, 2016].

Valitutti, S. et al., 1995. Serial triggering of many T-cell receptors by a few peptide-MHC complexes. *Nature*, 375(6527), pp.148–51. Available at: http://www.ncbi.nlm.nih.gov/pubmed/7753171 [Accessed November 7, 2016].

Varma, R. et al., 2006. T cell receptor-proximal signals are sustained in peripheral microclusters and terminated in the central supramolecular activation cluster. *Immunity*, 25(1), pp.117–27. Available at: http://www.sciencedirect.com/science/article/pii/S1074761306002974 [Accessed January 6, 2016].

Vasquez, R.J. et al., 1997. Nanomolar concentrations of nocodazole alter microtubule dynamic

instability in vivo and in vitro. *Molecular biology of the cell*, 8(6), pp.973–85. Available at: http://www.ncbi.nlm.nih.gov/pubmed/9201709 [Accessed November 23, 2016].

Vicidomini, G. et al., 2013. STED Nanoscopy with Time-Gated Detection: Theoretical and Experimental Aspects G. Chirico, ed. *PLoS ONE*, 8(1), p.e54421. Available at: http://dx.plos.org/10.1371/journal.pone.0054421 [Accessed November 8, 2016].

Viola, A. & Gupta, N., 2007. Tether and trap: regulation of membrane-raft dynamics by actin-binding proteins. *Nature Reviews Immunology*, 7(11), pp.889–896. Available at: http://www.nature.com/doifinder/10.1038/nri2193 [Accessed November 8, 2016].

Vogelsang, J. et al., 2008. A Reducing and Oxidizing System Minimizes Photobleaching and Blinking of Fluorescent Dyes. *Angewandte Chemie International Edition*, 47(29), pp.5465–5469. Available at: http://doi.wiley.com/10.1002/anie.200801518 [Accessed September 16, 2016].

Wang, J. & Richards, D.A., 2011. Spatial Regulation of Exocytic Site and Vesicle Mobilization by the Actin Cytoskeleton M. Bezanilla, ed. *PLoS ONE*, 6(12), p.e29162. Available at: http://dx.plos.org/10.1371/journal.pone.0029162 [Accessed November 8, 2016].

Wang, X. et al., 2000. The tumor suppressor PTEN regulates T cell survival and antigen receptor signaling by acting as a phosphatidylinositol 3-phosphatase. *Journal of immunology (Baltimore, Md. : 1950)*, 164(4), pp.1934–9. Available at: http://www.ncbi.nlm.nih.gov/pubmed/10657643 [Accessed November 8, 2016].

Ward, E.S. et al., 2005. From sorting endosomes to exocytosis: association of Rab4 and Rab11 GTPases with the Fc receptor, FcRn, during recycling. *Molecular biology of the cell*, 16(4), pp.2028–38. Available at: http://www.ncbi.nlm.nih.gov/pubmed/15689494 [Accessed November 8, 2016].

Watanabe, N. & Mitchison, T.J., 2002. Single-molecule speckle analysis of actin filament turnover in lamellipodia. *Science (New York, N.Y.)*, 295(5557), pp.1083–6. Available at: http://www.ncbi.nlm.nih.gov/pubmed/11834838 [Accessed November 8, 2016].

Wawrezinieck, L. et al., 2005. Fluorescence correlation spectroscopy diffusion laws to probe the submicron cell membrane organization. *Biophysical journal*, 89(6), pp.4029–42. Available at: http://www.ncbi.nlm.nih.gov/pubmed/16199500 [Accessed November 8, 2016].

Wegner, A., 1976. Head to tail polymerization of actin. *Journal of Molecular Biology*, 108(1),

pp.139–150.

Wen, K.-K. et al., 2011. Mutant profilin suppresses mutant actin-dependent mitochondrial phenotype in Saccharomyces cerevisiae. *The Journal of biological chemistry*, 286(48), pp.41745–57. Available at: http://www.ncbi.nlm.nih.gov/pubmed/21956104 [Accessed November 7, 2016].

Wernimont, S.A. et al., 2011. Contact-Dependent T Cell Activation and T Cell Stopping Require Talin1. *The Journal of Immunology*, 187(12), pp.6256–6267. Available at: http://www.jimmunol.org/cgi/doi/10.4049/jimmunol.1102028 [Accessed November 7, 2016].

Westphal, V. et al., 2008. Video-rate far-field optical nanoscopy dissects synaptic vesicle movement. *Science (New York, N.Y.)*, 320(5873), pp.246–9. Available at: http://www.ncbi.nlm.nih.gov/pubmed/18292304 [Accessed September 16, 2016].

Wiedemann, A. et al., 2005. T-cell activation is accompanied by an ubiquitination process occurring at the immunological synapse. *Immunology Letters*, 98(1), pp.57–61.

Williamson, D.J. et al., 2011. Pre-existing clusters of the adaptor Lat do not participate in early T cell signaling events. *Nature Immunology*, 12(7), pp.655–662. Available at: http://www.nature.com/doifinder/10.1038/ni.2049 [Accessed August 16, 2016].

Willig, K.I. et al., 2007. STED microscopy with continuous wave beams. *Nature Methods*, 4(11), pp.915–918. Available at: http://www.nature.com/doifinder/10.1038/nmeth1108 [Accessed November 8, 2016].

Wiseman, P.W., 2013. Image correlation spectroscopy: mapping correlations in space, time, and reciprocal space. *Methods in enzymology*, 518, pp.245–67. Available at: http://www.ncbi.nlm.nih.gov/pubmed/23276542 [Accessed November 8, 2016].

Wollman, R. & Meyer, T., 2012. Coordinated oscillations in cortical actin and Ca2+ correlate with cycles of vesicle secretion. *Nature Cell Biology*, 14(12), pp.1261–1269. Available at: http://www.nature.com/doifinder/10.1038/ncb2614 [Accessed November 8, 2016].

Wu, J. et al., 1997. The Vav Binding Site (Y315) in ZAP-70 Is Critical for Antigen Receptor–mediated Signal Transduction. *Journal of Experimental Medicine*, 185(10).

Yahara, I. et al., 1982. Correlation between effects of 24 different cytochalasins on cellular structures and cellular events and those on actin in vitro. *The Journal of cell biology*, 92(1), pp.69–78. Available at: http://www.ncbi.nlm.nih.gov/pubmed/7199054 [Accessed

September 16, 2016].

Yi, J. et al., 2012. Actin retrograde flow and actomyosin II arc contraction drive receptor cluster dynamics at the immunological synapse in Jurkat T cells. *Molecular biology of the cell*, 23(5), pp.834–52. Available at: http://www.ncbi.nlm.nih.gov/pubmed/22219382 [Accessed November 7, 2016].

Yokosuka, T. et al., 2005. Newly generated T cell receptor microclusters initiate and sustain T cell activation by recruitment of Zap70 and SLP-76. *Nature immunology*, 6(12), pp.1253–62. Available at: http://dx.doi.org/10.1038/ni1272 [Accessed December 15, 2015].

Yokosuka, T. et al., 2008. Spatiotemporal regulation of T cell costimulation by TCR-CD28 microclusters and protein kinase C theta translocation. *Immunity*, 29(4), pp.589–601. Available at: http://www.ncbi.nlm.nih.gov/pubmed/18848472 [Accessed November 7, 2016].

Yonemura, S. et al., 1998. Ezrin/Radixin/Moesin (ERM) Proteins Bind to a Positively Charged Amino Acid Cluster in the Juxta-Membrane Cytoplasmic Domain of CD44, CD43, and ICAM-2. *The Journal of Cell Biology*, 140(4).

Yonemura, S. et al., 2002. Rho-dependent and -independent activation mechanisms of ezrin/radixin/moesin proteins: an essential role for polyphosphoinositides in vivo. *Journal of cell science*, 115(Pt 12), pp.2569–80. Available at: http://www.ncbi.nlm.nih.gov/pubmed/12045227 [Accessed November 8, 2016].

Yu, C. et al., 2010. Altered actin centripetal retrograde flow in physically restricted immunological synapses. *PloS one*, 5(7), p.e11878. Available at: http://journals.plos.org/plosone/article?id=10.1371/journal.pone.0011878 [Accessed January 18, 2016].

Yuan, T. et al., 2015. Spatiotemporal detection and analysis of exocytosis reveal fusion "hotspots" organized by the cytoskeleton in endocrine cells. *Biophysical journal*, 108(2), pp.251–60. Available at: http://www.ncbi.nlm.nih.gov/pubmed/25606674 [Accessed November 8, 2016].

Zech, T. et al., 2009. Accumulation of raft lipids in T-cell plasma membrane domains engaged in TCR signalling. *The EMBO Journal*, 28(5), pp.466–476. Available at: http://www.ncbi.nlm.nih.gov/pubmed/19177148 [Accessed December 16, 2016].

Zeissig, S. et al., 2015. Early-onset Crohn’s disease and autoimmunity associated with a variant

in CTLA-4. *Gut*, 64(12), pp.1889–1897. Available at: http://gut.bmj.com/lookup/doi/10.1136/gutjnl-2014-308541 [Accessed November 7, 2016].

Zhang, W., Trible, R.P. & Samelson, L.E., 1998. LAT Palmitoylation: Its Essential Role in Membrane Microdomain Targeting and Tyrosine Phosphorylation during T Cell Activation. *Immunity*, 9(2), pp.239–246.

Appendix A

Publications

Ashdown GW., Burn GL., Williamson, DJ., Pandžić E., Peters R., Holden M., Ewers H., Shao L., Wiseman PW., and Owen DM. Live-cell super-resolution reveals F-actin and plasma membrane dynamics at the T cell synapse *Biophysical Journal,* Vol. 112, Issue 8, p1703–1713 http://dx.doi.org/10.1016/j.bpj.2017.01.038

R. Peters, M. Bentham-Muňiz, J. Griffié, D.J. Williamson, **G.W. Ashdown**, C.D. Lorenz and D.M. Owen. Quantification of fibrous spatial point patterns from single-molecule localisation microscopy (SMLM) data. *Bioinformatics* (Online pre-print: doi: 10.1093/bioinformatics/btx026)

Burn, GL., Cornish, G., Potrzebowska K., Samuelsson, M., Griffié, J., Minoughan, S., Yates, M., **Ashdown, GW**., Pernodet, N., Morrison, VL., Sanchez-Blanco, C., Purvis, H., Clarke, F., Brownlie, RJ., Vyse, TJ., Zamoyska, R., Owen, DM., Svensson, LM., and Cope, AP. Superresolution imaging of the cytoplasmic phosphatase PTPN22 links integrin-mediated T cell adhesion with autoimmunity. *Sci. signal*, Vol. 9, Issue 448, pp. ra99. doi: 10.1126/scisignal.aaf2195

Gustafsson, N., Culley, S., **Ashdown, GW**., Owen, DM., Pereira, PM., and Henriques, R. Fast live-cell conventional fluorophore nanoscopy with ImageJ through Super-Resolution Radial Fluctuations. *Nature Communications* 7, 12471. Doi: 10.1038/ncomms12471

Ashdown GW., Pandžić E., Cope A., Wiseman PW., and Owen DM. (2015) Cortical Actin Flow in T Cells Quantified by Spatio-Temporal Image Correlation Spectroscopy of Structured Illumination Microscopy Data. *J. Vis. Exp.* doi:10.3791/53749

Ashdown GW., Cope A., Wiseman PW., and Owen DM. (2014) Molecular flow quantified beyond the diffraction limit by spatiotemporal image correlation of structured illumination microscopy data. *Biophysical Journal.* Vol. 107, Issue 9, L21-3. doi: 10.1016/j.bpj.2014.09.018

Book chapters and articles

Ashdown GW., and Owen DM. (2014) Imaging membrane order using environmentally sensitive fluorophores. *Methods in Molecular Biology.* Edited by DM Owen. Vol 1232, pp. 115-122.

Ashdown GW., Griffié J., Shannon M., and Owen DM. Image analysis: colocalisation and correlation. *Correlations and colocalisation. Working with Imaging Data in the Biosciences: A Primer.* Edited by Anne Wheeler and Ricardo Henriques, Wiley, Chichester, UK (In preparation)

Ashdown GW., Burn, GL., Griffié J., Shannon M., and Owen DM (2015) Quantifying structure and motion in super-resolution microscopy. *Microscopy and Analysis.* Issue 18, pp9-12.

Conference posters and talks

2016

EMBL, Heidelberg. Actin in Action, 'Live-cell super-resolution reveals F-actin and plasma membrane dynamics at the T cell synapse' (**Selected speaker**)

Tridivisional Symposium (Randall Division) 'Molecular dynamics of the T cell synapse by super-resolution'

Guest speaker: University of Cambridge, University of Oxford and Imperial College London.

2015

T cell molecular dynamics revealed during synapse formation using super-resolution microscopy (**Selected speaker**) MMC2015, Manchester.

Dynamics of the actin cytoskeleton and plasma membrane at the immunological synapse using live cell super resolution microscopy (**Speaker**) London Super-resolution group meeting, Imperial College London.

Dynamics of the actin cytoskeleton and plasma membrane at the immunological synapse using live cell super resolution microscopy (**Poster**) Biophysical Congress, Baltimore, USA.

2014

The use of environmentally-sensitive fluorescent dyes to probe membrane organization during T cell signaling (**poster**) MMC2014, Manchester.

Immunological synapse, a role for F-actin during structural and dynamic changes in T-cells (**poster**) SMLMS2014, King's College, London.

Dynamics of the actin cytoskeleton and plasma membrane at the immunological synapse using live cell super resolution microscopy (**poster**) UCL Super resolution meeting.

Immunological synapse, a role for F-actin during structural and dynamic changes in T-cells (**poster**) Randall Division of Cell and Molecular Biophysics Retreat

Postgraduate support (under primary supervisor)

2016

Nathan Day MSci student: Analysis of membrane order at the immunological synapse and vesicle distribution in the context of the cytoskeleton

2015

Michael Holden MSci student: Quantifying filamentous-actin dynamics in live T cells during formation of the immunological synapse

2014

Gary HM Soh MRes student: The role of membrane biophysical properties in regulating T cell signalling studied by advanced fluorescence microscopy techniques.